SUB-SYNCHRONOUS CONTROL INTERACTION – MODELING AND DETECTION

By

FARSHID SALEHI

Presented to the Faculty of the Graduate School of

The University of Texas at Arlington in Partial Fulfillment of the Requirements

for the Degree of

DOCTOR OF PHILOSOPHY

THE UNIVERSITY OF TEXAS AT ARLINGTON

December 2018

Acknowledgements

I am extremely grateful to my advisor Prof. Wei-Jen Lee for his tremendous support throughout my graduate study. I would also like to thank Dr. David Wetz, Dr. Ali Davoudi, Dr. Ramtin Madani, and Dr. Rasool Kenarangui for being part of my defense committee. I would like to acknowledge the members of EE department especially Dr. Allen Davis and Gail Paniuski for their assistance.

Also, I would like to express my gratitude to many others who helped me during my PHD Dissertation including, GL PowerSolutions Inc., particularly Dr. Hamed Khalilinia and Dr. Mandhir Sahni for their support to this effort.

Finally, this Dissertation is dedicated to my wonderful family, friends and specially my beloved wife whose unconditional compassion and support has sustained me through difficult times.

December 2018

Abstract

SUB-SYNCHRONOUS CONTROL INTERACTION – MODELING AND DETECTION

Farshid Salehi, PHD.

The University of Texas at Arlington, 2018

Supervising Professor: Wei-Jen Lee

Power systems have recently become more susceptible to Sub-Synchronous Control Interaction (SSCI) due to the increasing penetration of renewable generation resources and series compensated lines. Any contingency which results in a radial condition between renewable generation resources and near-by series compensated lines might trigger an undamped SSCI oscillation. This is a purely electrical phenomenon which has potential to grow rapidly. Undamped SSCI oscillation can cause serious damage to the renewable generation resources and transmission elements and consequently leads to cascading outages. Due to the importance of the phenomena and its potential impacts, this research has focused on two aspects of this event as listed below:

- Detail modeling of Doubly-Fed Induction Generators (DFIGs) as the most vulnerable type of wind generator to SSCI

- Proposing a novel algorithm for the detection of SSCI

Firstly, a novel state-space based modeling approach for Doubly Fed Induction Generator (DFIG) is proposed which allows for the inclusion of the Phase Locked Loop (PLL) controller in a detail dual *d-q* state-space model. Eigenvalue analysis as well as time domain transient simulations are performed using the proposed nonlinear state-space model to study the impact of PLL parameters on SSCI oscillations. The results are indicative that faster PLL control parameters can increase the risk and severity of SSCI. To validate and interpret the results, the closed loop *d-q* sub-synchronous impedance model of the DFIG including impedance transfer function of the proposed PLL model is extracted. Bode diagrams of the DFIG and transmission system are then plotted for different scenarios utilizing different PLL parameters. In line with the eigenvalue and time domain transient analysis, the impedance model depicts that faster PLL control parameters leads to smaller phase margin and consequently higher SSCI risk.

Secondly, an effective algorithm is proposed to detect SSCI within 45ms and reliably send a trip signal within 95ms. Initially, a comprehensive SSCI analysis is suggested to improve the pre-processing of the measured signal. The proposed algorithm then utilizes mode identification approaches in conjunction with a moving FFT to capture the frequency and magnitude of oscillations and process them to issue a reliable trip command in the case of a SSCI event. To

evaluate the algorithm, a portion of ERCOT grid with relatively higher penetration of renewable resources is utilized to simulate the SSCI phenomenon. The proposed detection algorithm was implemented on a real-time target device. The SSCI signal observed in the detailed EMT simulation of the ERCOT grid was injected to the device to test the algorithm under real-time operating conditions. The results indicate the efficiency and accuracy of the method in successful detection within the acceptable time frame.

Table of Contents

List of Illustrations

List of Tables

Chapter 1

Theory and Background of Sub-Synchronous Oscillation

1.1 Introduction

The first incident of Sub-Synchronous Oscillation (SSO) occurred in the Mohave coal-fired power plant in 1970 [1]. In this event, a gradually growing oscillation at sub-synchronous frequency fractured the shaft of the turbine generator. The first investigation incorrectly identified the root cause of the event as a mechanical issue. However, after a second incident in 1971, the torsional interaction between the mechanical mode of the turbine-generator shaft and a near-by series compensated line was identified as the cause for undamped oscillation. In this case, the natural frequency of the series compensated network at 30.5 Hz excited the torsional mode of turbine generator at 30.1 Hz. After this incident, extensive investigation and research was performed to analyze the phenomena and determine appropriate solutions and mitigation options to prevent occurrence of similar events.

In 2009, another SSO event was reported within the ERCOT grid (South Texas) between a wind farm in radial connection with a series compensated line. Primary investigation of this event highlighted the differences between this event and the traditional concept of SSO phenomena. This time, the frequency of

oscillation did not align with the torsional modes of the wind turbine drive train and oscillation magnitude increased rapidly. Within 200 ms, the voltage reached to 1.5 pu (520kV) and caused series damage to the wind farm and the respective series capacitor [1]-[6]. In this case, the voltage continued to increase to 2 pu and was finally mitigated by bypassing the series capacitor after 1.5 seconds. This presented another serious concern with respect to protection system design. None of the voltage/current protection schemes operated under this critical incident. Further investigation identified that the oscillation was the result of a resonance between the series compensated line and poorly tuned control system of the respective wind farm.

The event in the ERCOT grid introduced new concerns with respect to Sub-Synchronous Oscillation phenomena and lead to comprehensive research on this topic to understand all aspects and possibilities associated with SSO occurrence within a modern power system [1]-[15]. The ensuing section of this chapter outline and describe the event in detail.

1.2 Classification of SSO Phenomena

In general, SSO is the result of the energy exchange between two or more elements of a power system within the sub-synchronous frequency range [1]-[11]. The elements involved in the sub-synchronous oscillation as well as the nature of the phenomenon can be classified as depicted in Figure 1-1 [6].

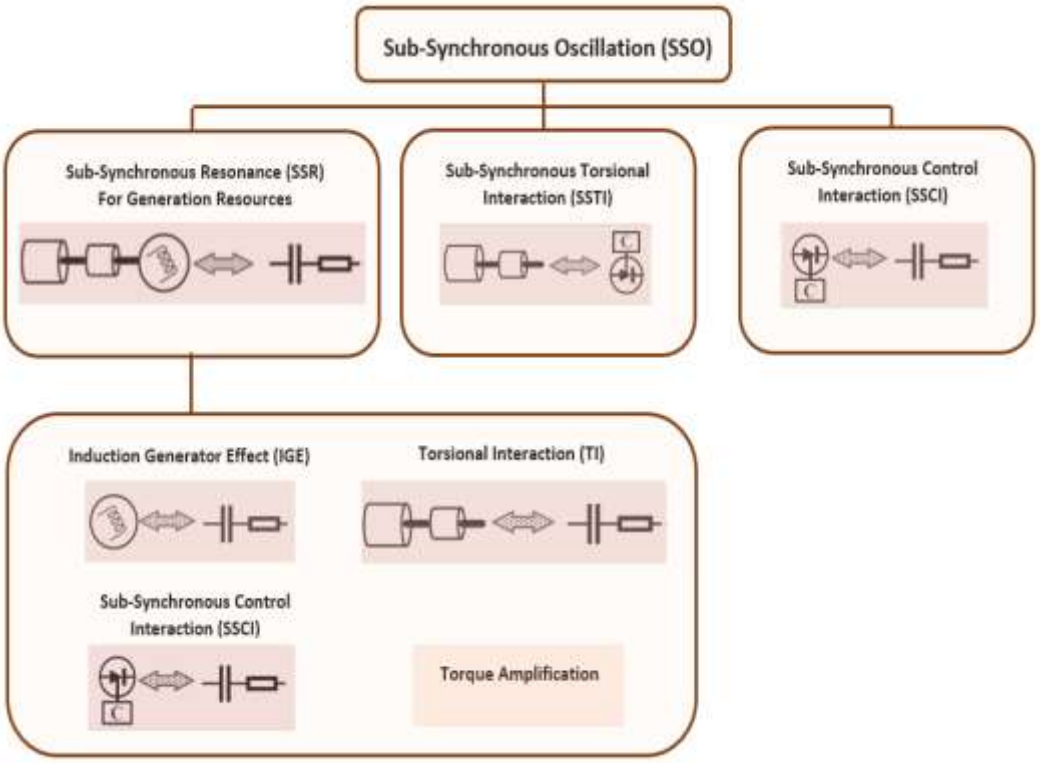

Figure 1-1 Sub-Synchronous Oscillation Classification

The details regarding each category is provided in ensuing subsections.

1.2.1 Sub-Synchronous Resonance

Sub-synchronous resonance (SSR) occurs when a generation resource and a series compensated line experiences sub-synchronous interaction. Depending on the type of generation resource as well as the nature of interaction the type of SSR can be classified as follows [6],[11]:

- Induction Generator Effect (IGE)
- Torsional Interaction (TI)

- Sub-Synchronous Control Interaction (SSCI)
- Torque Amplification (TA)

1.2.1.1 Induction Generator Effect (IGE)

A series compensated line has a natural frequency at $f_{ssr} = f_s\sqrt{X_c/X_L}$, where f_s is the synchronous frequency of the system (in this case 60 Hz), and X_c and X_L are the reactance associated with the series capacitor and the transmission line, respectively [14]. For this sub-synchronous frequency, the slip is given as:

$$S_{ssr} = \frac{f_{ssr} - f_r}{f_{ssr}} \tag{1.1}$$

Where, f_r is the electrical frequency of rotor.

Normally, the sub-synchronous natural frequency (f_{ssr}) is less than the rotor electrical frequency. Therefore, the slip at this natural frequency is negative. Considering the steady state equivalent circuit of the machine (DFIG) as depicted in Figure 1-2, the equivalent resistance of the rotor at sub-synchronous frequency is negative. If the magnitude of this negative resistance exceeds the summation of the transmission line and stator resistance, negative damping will occur at the sub-synchronous resonant frequency. This negative damping can lead to self-excitation of the machine and consequently undamped SSO. This electrical phenomenon is called Induction Generator Effect (IGE) and typically occurs in Type 3 wind farms [14].

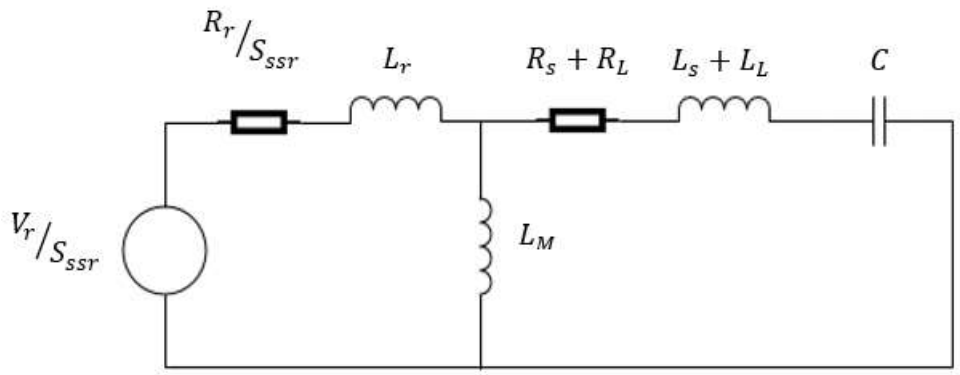

Figure 1-2 Simplified Sub-Synchronous Equivalent Model of DFIG

The frequency components for a DFIG in a radial connection with series compensated line is given in Table 1-1 [14].

Table 1-1 Frequency component of DFIG

Stator Current	Rotor Current
I_{s1} at f_s	I_{r1} at $(f_s - f_r)$
I_{s2} at f_{ssr}	I_{r2} at $(f_{ssr} - f_r)$

Interaction between these currents results in four different torques in a DFIG as depicted in Table 1-2 [14].

Table 1-2 Torque component of DFIG

Torque	Interaction	Frequency
T_1	I_{s1} & I_{r1}	0
T_2	I_{s1} & I_{r2}	$(f_s - f_{ssr})$
T_3	I_{s2} & I_{r1}	$(f_s - f_{ssr})$
T_4	I_{s2} & I_{r2}	0

1.2.1.2 Torsional Interaction

Torsional interaction is a condition in which a series compensated line exchanges energy with the turbine-generator shaft at the sub-synchronous frequency. In this case, the complementary frequency of the transmission line natural frequency $(f_{er} = 60 - f_{ssr})$ coincide with one of the mechanical modes of the mass drive train. This oscillation is the interaction between the mechanical and electrical system and has a frequency corresponding to the torsional modes of the turbine generator drive train. Conventional generation units are mainly susceptible to torsional interaction. Wind farms also contain the mass drive train, however; torsional interaction is less likely. Because, slightly damped mechanical modes of wind farms exist at low frequencies and consequently high amounts of compensation is required to excite them [6], [14].

1.2.1.3 Sub-Synchronous Control Interaction

SSCI involves the interaction of renewable generation resources controls and series compensated lines at sub-synchronous frequency (<60 Hz). This is a purely electrical phenomena which manifests and increases rapidly. In this case, the frequency of oscillation is not fixed and varies under different operational conditions of the system and control system parameters [4].

1.2.1.4 Torque Amplification

Severe disturbances in vicinity of series compensated lines result in electro-mechanical torque at a frequency of $(f_s - f_{ssr})$. If the frequency of the transient torque matches or is close to the torsional modes of the turbine-generator shaft, the amplitude of the transient torque is much larger as compared to the disturbances without coincidence between torsional modes and electro-mechanical torque. This is a transient phenomenon and can lead to severe damages to transmission elements and generation resources [6], [14].

1.2.2 Sub-Synchronous Torsional Interaction (SSTI)

SSTI describes the interaction between a power electronic controller near a turbine-generator mass drive-train in which the mechanical system resonates with the negative damping of the control system at sub-synchronous frequencies [6]. Power electronic controllers (such as HVDC lines and control systems of FACTS devices) can exhibit negative damping at sub-synchronous frequencies which can

cause undamped oscillations in the fixed mechanical torsional modes of drive-train systems. It should be noted that SSTI is not associated with series compensation [6].

1.2.3 Sub-Synchronous Control Interaction

This incident is identical to SSCI in generation resources, however; the control system can be the control system of any power electronic devices. In SSCI the control system of power electronic devices presents negative damping at the sub-synchronous resonant frequency of the network [6], [8].

1.3 SSO Countermeasure

In order to avoid any damage and/or negative effects of SSO in a power system, different countermeasures have been proposed to mitigate SSO and protect the affected elements from damage. These measures fall in two main group as listed below [1]:

Mitigation Measures (or Countermeasure) – These are Preventative measures which are implemented in the case of SSO risk. These approaches mitigate the SSO without tripping the affected elements.

Protection Measures – These measures involve the tripping of the affected elements and can be applied as a back-up to mitigation.

Based on the location of implementation, the countermeasures can be divided in to Network-based or Generator-based measures. The summary and classification of SSO countermeasures are depicted in Figure 1-3.

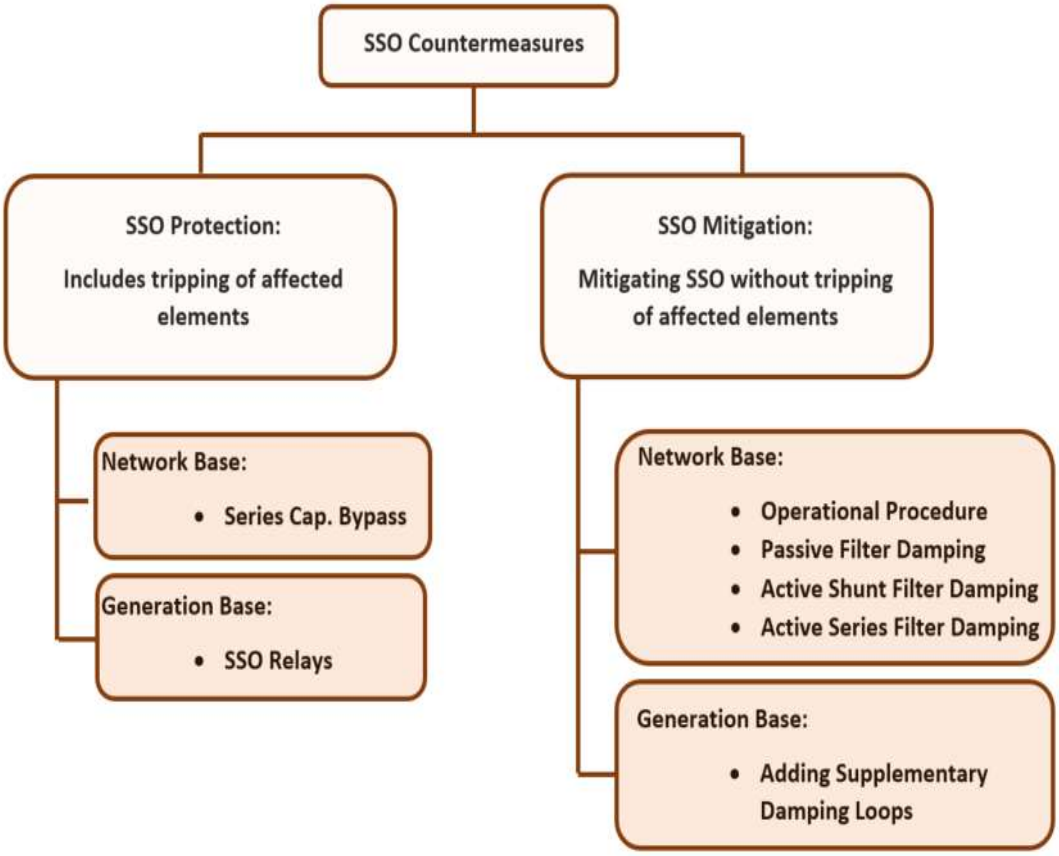

Figure 1-3 Different SSO countermeasures

Chapter 2

ERCOT Nodal Protocol for SSR Study

2.1 Introduction

Power grids have always been facing different types of reliability challenges and at mean time variety of solutions such as optimization, operational approaches, new mitigating options, protection and control designs have been proposed to overcome these problems [16]-[25]. Recently, ERCOT grid has become more susceptible to the sub-synchronous resonance due to the introduction of series capacitors for voltage support and also high penetration of renewable resources with power electronic devices [11]. Without reliable mitigation and detection solution, sub-synchronous resonance can quickly build up and destroy transmission elements and generation resources and lead to the cascading outage. Therefore, it is a critical concern to carefully study the risk and vulnerability of the system to sub-synchronous interaction. In this regard, ERCOT has developed nodal protocol named NPRR562 to address sub-synchronous resonant risk and clarify the responsibility of the various involved entities. This chapter is mainly focused on the approach of ERCOT for sub-synchronous study and utilizes a portion of ERCOT grid as an example to perform a detail sub-synchronous resonant study based on the ERCOT protocol.

2.2 ERCOT Protocol for Sub-Synchronous Resonance Vulnerability Assessment

2.2.1 Vulnerability Assessment of Existing Generation Resources

ERCOT performs one-time SSR study for all existing generation. A generation is considered as an existing unit if it is in service or has met the requirements of planning guide section 6.9. This study includes the following steps [11].

2.2.1.1 Topology Check

As the first step, all contingencies with outage count equal to N-14 or less which result in radial connection between generation and nearby series compensation lines are identified. In this process, each transmission circuit is considered as single outage. Here outage of double circuit line or common tower outage of two circuits will be considered as two transmission outages [11].

2.2.1.2 Screening Study (Frequency Scan)

At this stage, a comprehensive frequency scan will be performed for all contingencies with outage count equal to N-14 or less. The results of frequency scan will be reported to the affected entities. The screening stage can also be performed by eigenvalue analysis [11].

2.2.1.3 Detail Sub-Synchronous Resonant Study

If the results of screening study show any potential risk of SSR, the Transmission Service Provider (TSP) that owns the affected series compensated line in coordination with interconnecting TSP, shall perform a detail SSR study.

If the detail Electro-Magnetic Transient (EMT) study confirms the results of frequency scan and indicates that the generation resource is susceptible to sub-synchronous resonance in the contingencies with outage count of four or less, the affected entities in coordination with ERCOT shall develop and implement SSR mitigation on transmission system [11].

If the detail study indicates the SSR risk is in the events of five or six concurrent transmission outages, ERCOT considers the SSR monitoring option.

2.2.2 Generation Resource Interconnection SSR Risk Assessment

For any generation interconnection or change request, ERCOT will perform topology check to identifies all contingencies which results in radial connection between generation resource and series compensated line. For all contingencies with concurrent outage count equal to 14 or less, the interconnecting TSP will perform frequency scan and detail SSR study on behalf of Interconnecting Entity (IE). Alternatively, if the interconnecting entity can convince ERCOT and interconnecting TSP that the proposed generation is not vulnerable to SSR, then TSP is not required to perform the SSR study [11].

If the SSR study is indicative of SSR risk in the event of four or less concurrent transmission outages, IE must develop an SSR mitigation and submit tit for ERCOT approval before primary synchronization request. If SSR condition is observed in the event of four concurrent outages, the IE may install SSR detection module instead of SSR mitigation [11].

In line with existing generation approach, if the study shows that generation is susceptible to SSR in the event of N-5 or N-6 contingency, ERCOT will implement SSR monitoring before the synchronization of the unit.

2.2.3 Transmission Project SSR Risk Assessment

The Transmission Project will have an impact on the existing transmission topology in the study region, possibly reducing the proximity of the existing generation facilities in the area with series compensated lines that could result in an increase in Sub Synchronous Resonance (SSR) risk for these generation facilities. Conversely, the addition of the transmission projects may result in a reduction in SSR risk for the generation facilities in the area depending upon their location in relation with the nearby series compensated lines.

Therefore, for any Tier 4 projects that consist of 345Kv transmission elements, TSPs shall perform SSR risk assessment. The analysis starts with the topology check for generation facilities near the proposed transmission project. If the proposed project lead to change or reduction in concurrent outage count of any

generation, further investigation (frequency scan and detail study) is required. Here, the TSP that owns the affected series compensated line, in coordination with TSP proposing the transmission facility should perform the detail assessment. Study approach is same as vulnerability assessment of existing generation [11].

2.3 ERCOT Criteria for SSR Risk Assessment

As it was discussed in previous sections, ERCOT SSR risk assessment includes three steps, topology check, frequency scan and detail EMT simulation. in each step, there are certain criteria which are indicative of SSR risk. The specific criteria for each step are given as follow:

2.3.1 Topology check

In topology check, a generation resource is considered to be potentially at SSR risk if, there is contingency with outage count equal or less than 14 which leads to radial connection between the generation and nearby series compensated line.

2.3.2 Frequency Scan

The results of frequency scan are indicative of SSR risk if, one of the following criteria is met.

2.3.2.1 SSCI and Induction Generation Effect (IGE)

If the cumulative resistance of generation and ERCOT grid at cross-over frequency of cumulative reactance (zero reactance from negative to positive) is

negative, the generation resource is considered to be potentially at SSCI/IGE risk [11].

2.3.2.2 Torsional Interaction

A generation resource is potentially vulnerable to torsional interaction if, the complementary network resonant frequency coincides with the torsional mode of mass drive train. In this case, the summation of mechanical and electrical damping is negative [11].

2.3.2.3 Torque Amplification

When considering the total impedance of the generator and the ERCOT system, if a 5% or greater reactance dip, or a reactance crossover of zero Ohms from negative to positive with increasing frequency, occurs within a +/- 3 Hz complement of the modal frequency, then the generator is considered to be potentially vulnerable to Torque Amplification. The percentage of a reactance dip is on the basis of the reactance maximum at the first inflection point of the dip where the reactance begins to decrease with increasing frequency [11].

2.3.3 Detail SSR Study

Detail SSR study consists of performing Electro-Magnetic Transient simulation. The results of simulation are indicative of potential SSR risk if one of the below conditions happens.

- *The SSR vulnerability results in more than 50% of fatigue life expenditure over the expected lifetime of the unit. If the fatigue life expenditure is not available, the highest torsional torque caused by SSR is more than 110% of the torque experienced during a transmission fault with the series capacitors bypassed [*11].
- Undamped Sub-synchronous oscillation.
- Sub-synchronous oscillation which results in tripping of any transmission or generation facility.

2.4 Example of Detail SSR Study for Generation Interconnection

In order to demonstrate the ERCOT protocol for SSR risk assessment, Interconnection of 200 MW wind farm to a portion of ERCOT grid with series compensated line is selected as an illustrative example. The major steps associated with comprehensive SSR study are listed as below [1], [11]-[12];

- Contingency List (topology check)
    - Extracting all contingencies with concurrent outage counts equal or less than 14 which lead to radial condition between the wind farm and series compensated line
- Frequency Scan Study
    - Perform frequency scans on the Wind Project campus

- Perform frequency scans on the transmission system under various contingency conditions to identify system resonant frequency
- Utilize the transmission system side frequency scans in conjunction with the project side scans to shortlist specific operating conditions depicting SSR risk (in the form of IGE and/or SSCI) for detailed EMT simulations

- EMT Simulations
  - Perform EMT simulations to quantify potential for IGE/SSCI concerns under all conditions of concern, if any
- Evaluate the results of the EMT simulations (in conjunction with the screening study observations) to comment on potential conditions of concerns from a Sub-synchronous oscillation standpoint, if any

2.4.1 Case Study

A portion of ERCOT grid with high penetration of wind generation, which export the power through series compensated line is selected. The ERCOT grid portion is depicted in Figure 2-1. A 200MW wind farm is connected to the 345Kv station #3 (POI) through 34.5/345 kV step-up transformers and a gen-tie line. The impedance data relating to the collection system, transformers and gen-tie lines are given in the Table 2-1.

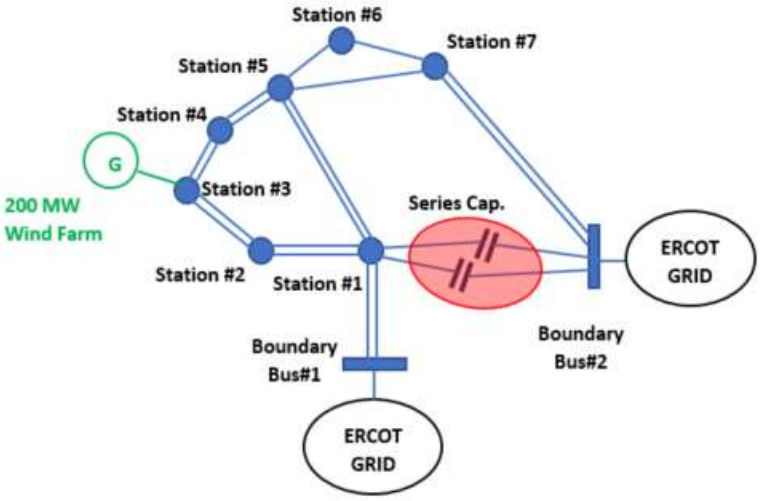

Figure 2-1 Portion of ERCOT grid

Table 2-1 Wind Farm radial test system

Parameters	Collection System	Gen-tie Line	Transmission Line	Equivalent Network
R(Ohm)	0.0492	0.2106	3.17	0.74
X(Ohm)	0.0639	1.9258	39.6	0.828

2.4.2 Contingency List

Any contingency that results in radial condition between the wind farm and series compensated line can leads to SSCI event. The list of all contingencies for the proposed POI and this portion of ERCOT grid is provided in Table 2-2.

Table 2-2 Contingency list

Contingency	Element	From	To	Circuit No.	Contingency Rank
Contingency 1	Transmission Line	Satation#5	Satation#6	Circuit#1	N-4
	Transmission Line	Satation#5	Satation#7	Circuit#1	
	Transmission Line	Satation#1	Boundary Bus#1	Circuit#1	
	Transmission Line	Satation#1	Boundary Bus#1	Circuit#2	
Contingency 2	Transmission Line	Satation#1	Boundary Bus#1	Circuit#1	N-6
	Transmission Line	Satation#1	Boundary Bus#1	Circuit#2	
	Transmission Line	Satation#1	Satation#5	Circuit#1	
	Transmission Line	Satation#1	Satation#5	Circuit#2	
	Transmission Line	Satation#3	Satation#4	Circuit#1	
	Transmission Line	Satation#3	Satation#4	Circuit#2	

2.4.3 Screening Study (Frequency Scan)

2.4.3.1 Wind Farm

The 1st step in the screening study involves frequency scans on the entire Wind campus. The objective of these scans is to measure the resistance and reactance of the entire wind project in the sub-synchronous (<60Hz) frequency range. Frequency scans within a 5-55Hz range have been performed as part of the screening process.

Different scenario of windfarm operation including variation in dispatch level and number of turbines in service is investigated as follow.

- All turbines are in service (100% turbine) and wind farm is in 100% dispatch

- All turbines are in service (100% turbine) and wind farm is in 10% dispatch (Situation, when wind speed drops)
- 10% of turbines are in service and they are in 100% dispatch (This situation occurs during the startup of wind farm)

The sub-synchronous impedance characteristic of wind farm for all abovementioned scenarios are depicted in Figure 2-2 to Figure 2-7.

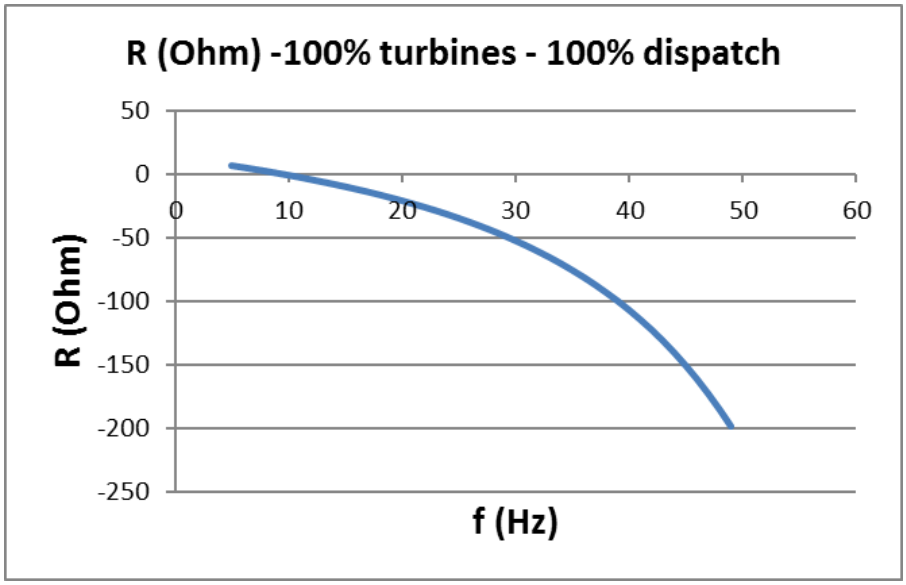

Figure 2-2 Wind farm resistance for scenario of 100% turbine at 100% dispatch

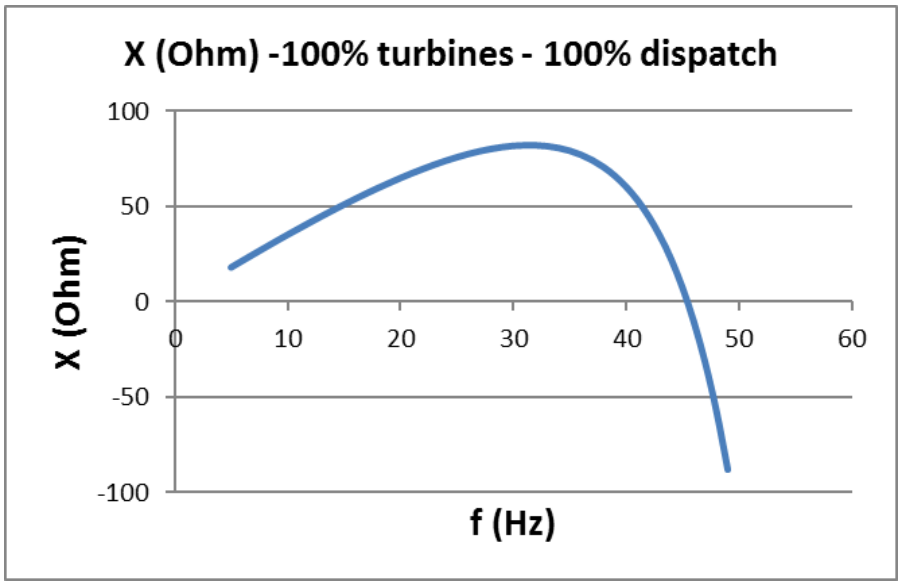

Figure 2-3 Wind farm reactance for scenario of 100% turbine at 100% dispatch

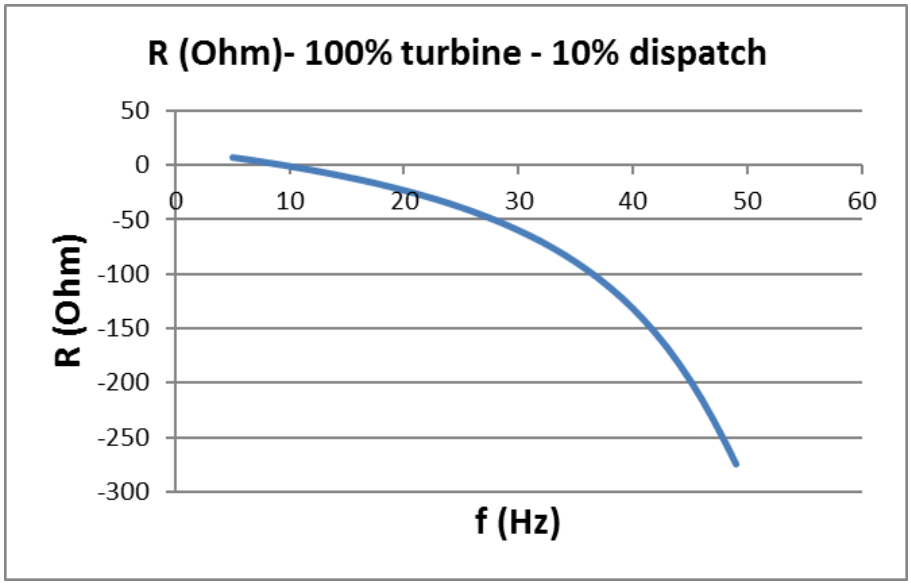

Figure 2-4 Wind farm resistance for scenario of 100% turbine at 10% dispatch

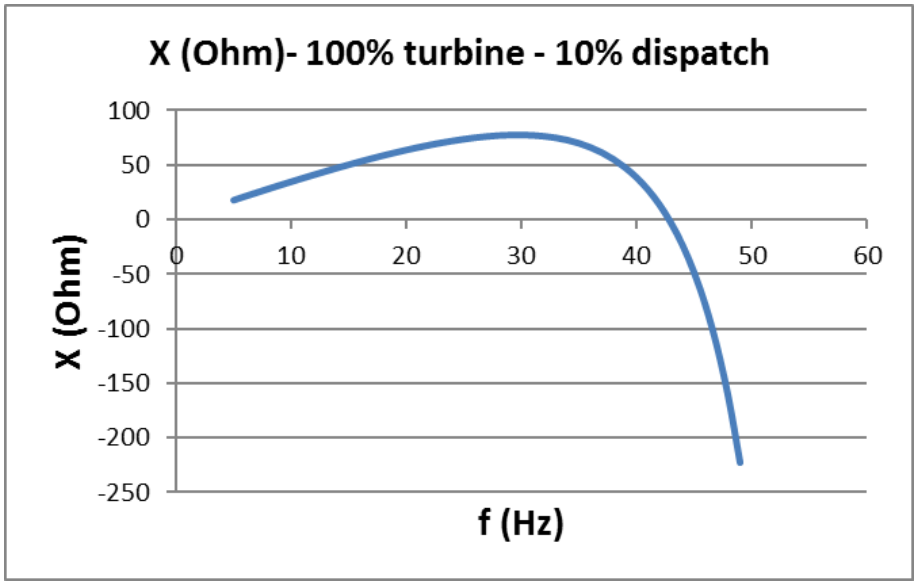

Figure 2-5 Wind farm reactance for scenario of 100% turbine at 10% dispatch

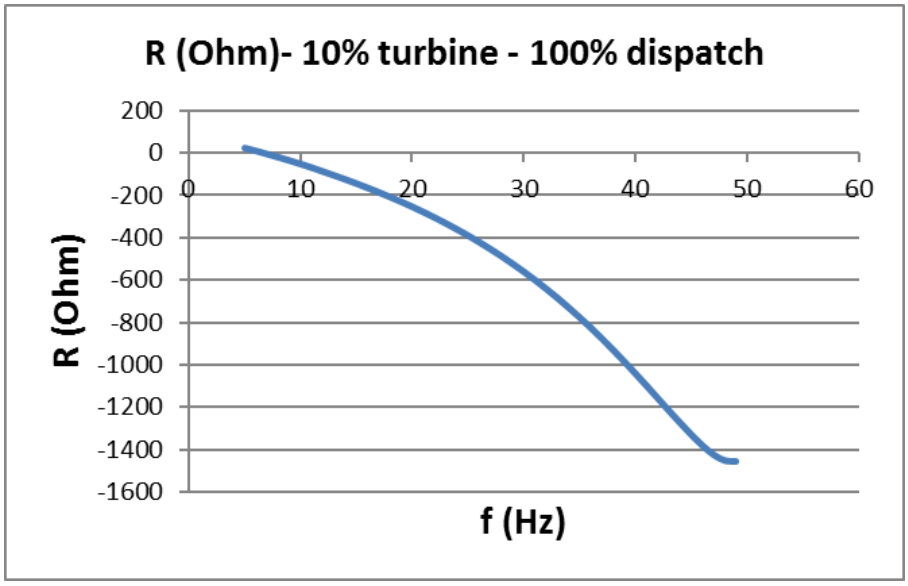

Figure 2-6 Wind farm resistance for scenario of 10% turbine at 100% dispatch

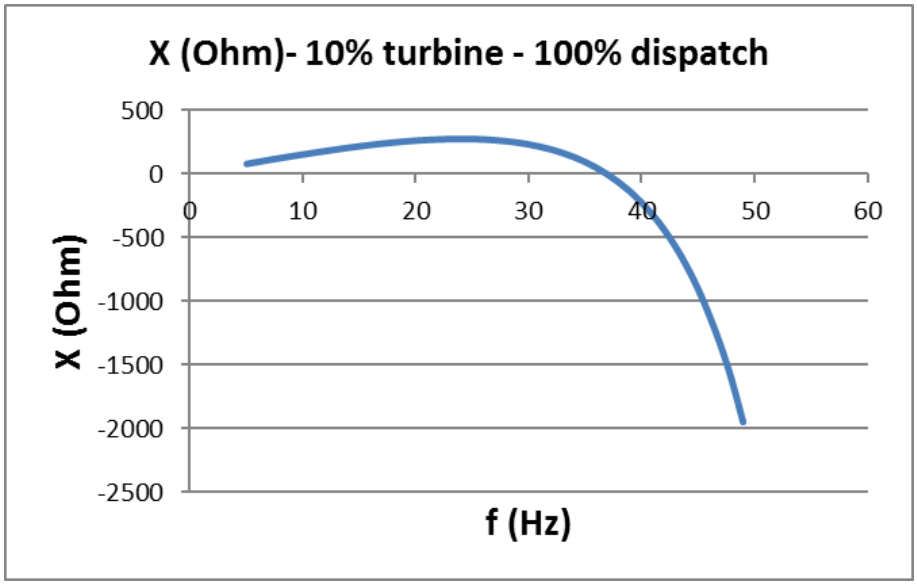

Figure 2-7 Wind farm reactance for scenario of 10% turbine at 100% dispatch

2.4.3.3 Transmission System

The 2nd step in the screening study involves conducting detailed frequency scans on the transmission system. These scans are performed to identify the series resonant frequency of the transmission system under various contingency conditions.

As it was depicted in Table 2-2, two contingencies are identified that lead to a fully radial connection between the wind farm and series compensated line.

Sensitivity around status of critical shunt reactors in the transmission system is considered while performing the system side frequency scan. A shunt reactor is deemed critical if it is located between the project POI and series compensated line

under consideration. Scenarios are defined for each of the two (2) contingency conditions based on the status of critical shunts in the transmission system.

Frequency scans are performed for all scenarios across the two (2) contingencies to identify resonant conditions on the transmission system. These scans are performed for two (2) system side scenarios associated with each contingency. These scenarios cover operating conditions in which either all or none of the critical shunt reactors on the transmission system are in service. Figure 2-8 through Figure 2-11 depict plots of system resistance and reactance as a function of sub-synchronous frequency for the aforementioned two scenarios associated with all contingencies of interest. It is important to note that the series resonant frequency (corresponding to the negative to positive reactance crossover) does not vary based on the status of the critical shunt reactors in this case. However, the status of shunt reactors does impact the parallel resonant frequency (corresponding to the peak in reactance) as measured from the POI.

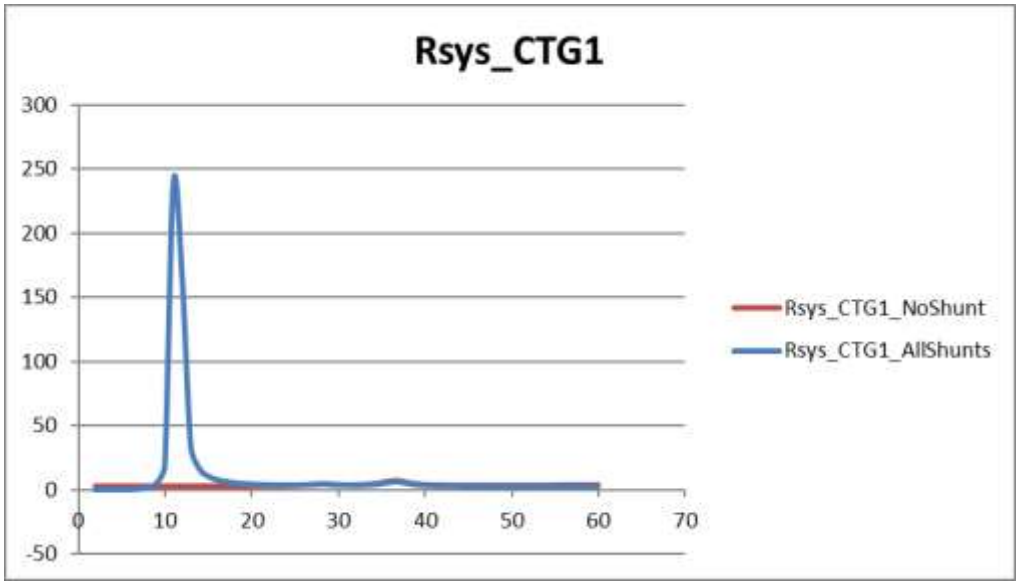

Figure 2-8 System Resistance – Contingency#1

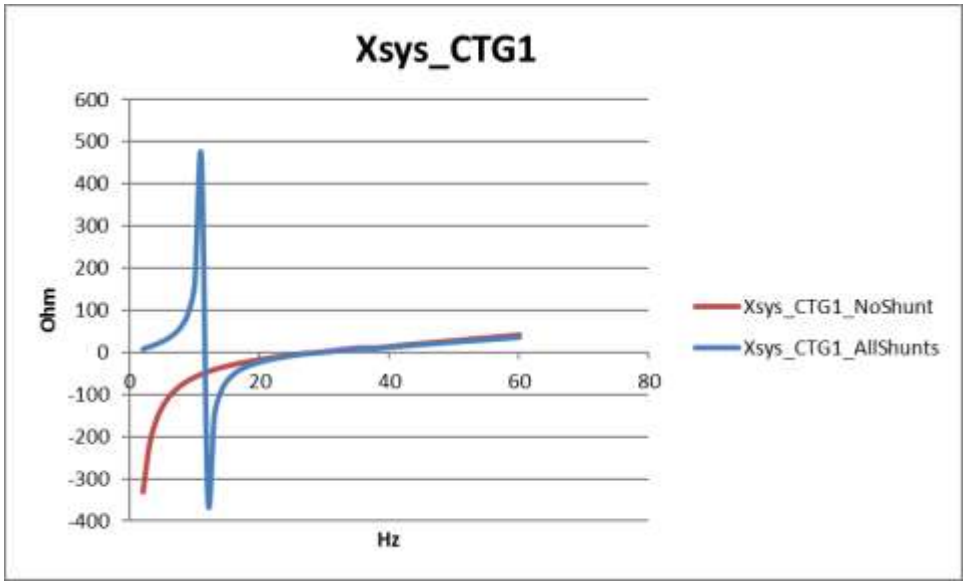

Figure 2-9 System Reactance – Contingency#1

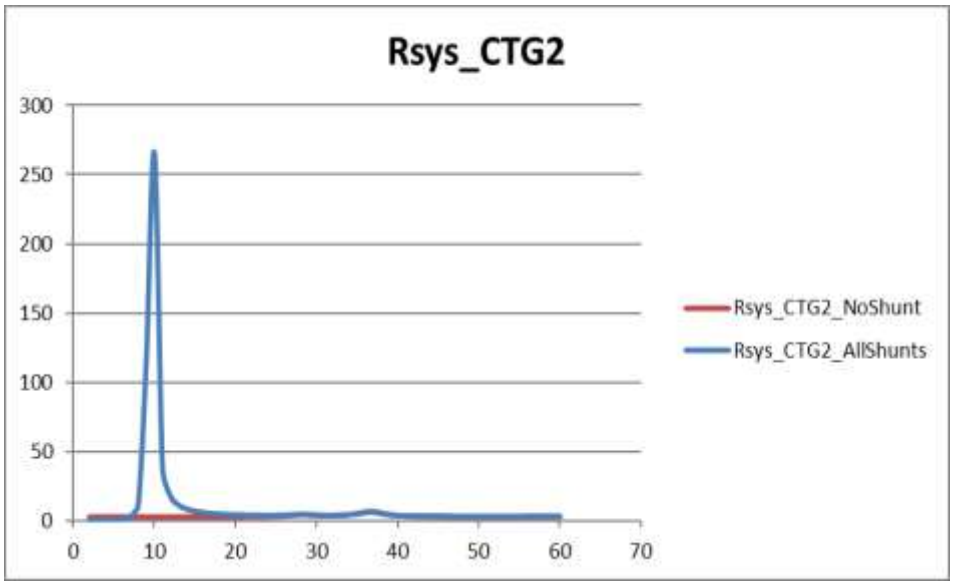

Figure 2-10 System Resistance – Contingency#2

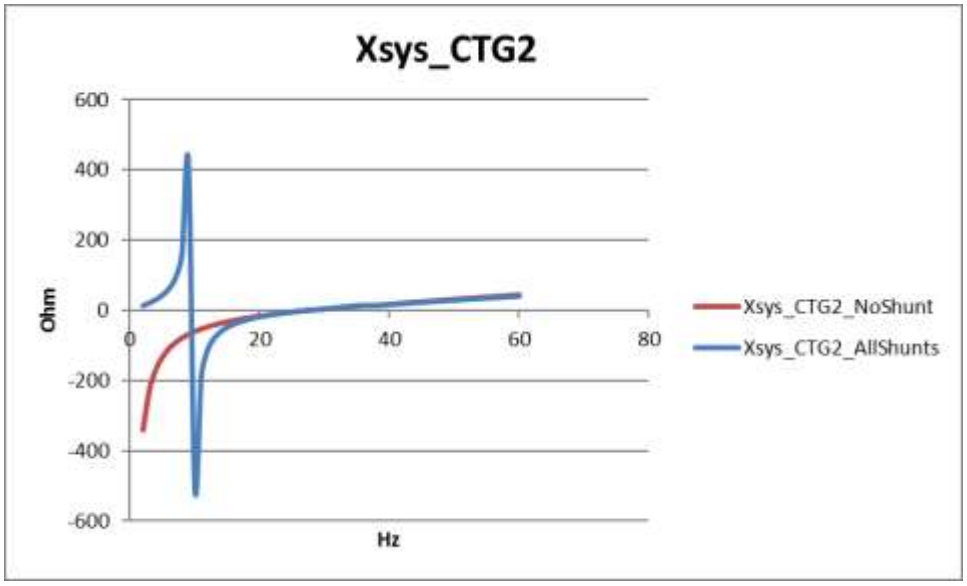

Figure 2-11 System Reactance – Contingency#2

2.4.3.3 Detail Screening Assessment

The 3rd step in the screening study is detailed cumulative frequency scan-based assessment. This assessment involves utilization of frequency scans on the Wind Project campus in conjunction with the transmission system side scans. The cumulative resistance ($R_{cumulative}$) at the 345kV POI station is computed based on the resistance of proposed project and the transmission system resistance under all contingencies of interest. The cumulative reactance ($X_{cumulative}$) is computed in a similar manner. Further, the crossover frequency (from negative to positive) for $X_{cumulative}$ is identified for each scenario. If $R_{cumulative}$ at this frequency is zero/negative, there is a potential for un-damped/negatively damped oscillations.

Cumulative impedance estimation is performed for each contingency with/without critical shunt reactors in-service. Figure 2-12 through Figure 2-15 depict plots of the cumulative impedance for contingency 1 and 2 with all turbines in service operating at full dispatch for both all critical shunt reactors on the transmission system in service or out of service. Similar cumulative impedance estimation is also performed for the operating conditions involving project operation with lower active power dispatch levels/fewer turbines in service. Detailed cumulative impedance plots associated with the aforementioned conditions are provided in Appendix A.

Key observations of the comprehensive SSR screening effort are summarized in Table 2-3.

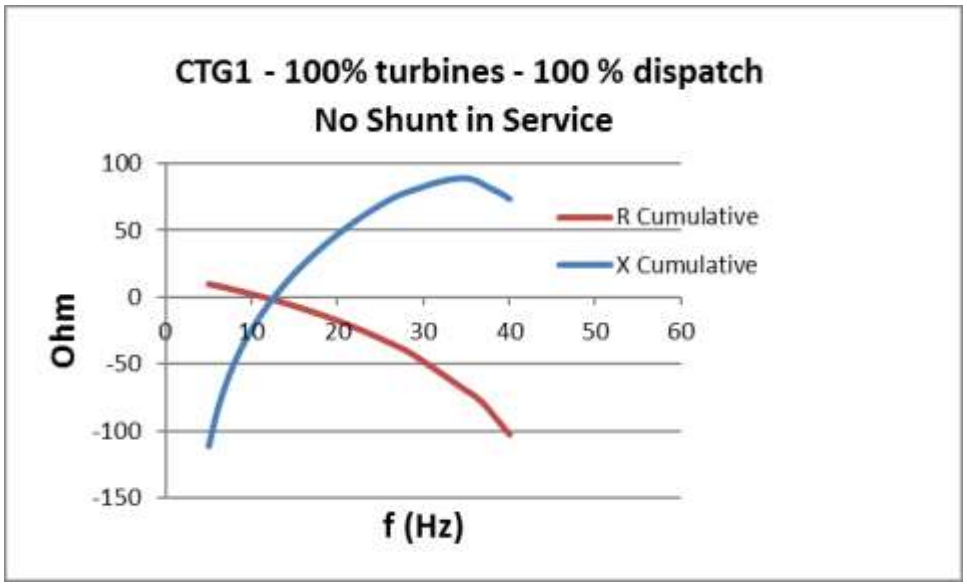

Figure 2-12 Detail Screening – Contingency#1, All Shunts out of service

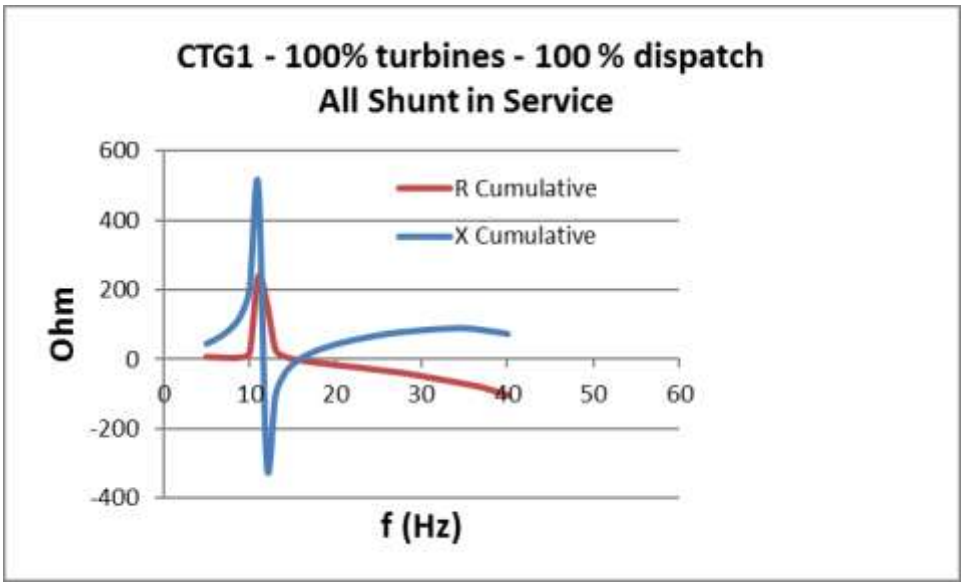

Figure 2-13 Detail Screening – Contingency#1, All Shunts in service

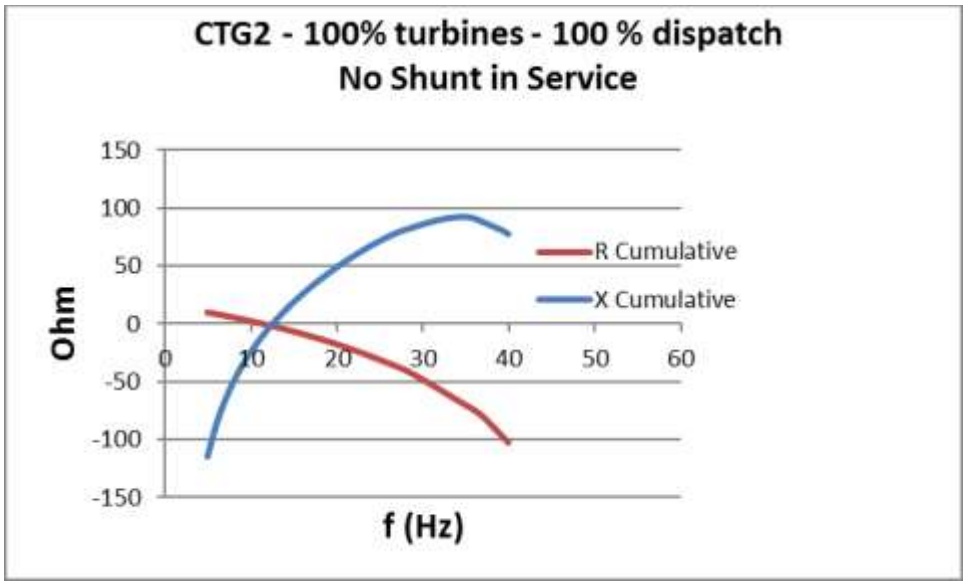

Figure 2-14 Detail Screening – Contingency#2, All Shunts out of service

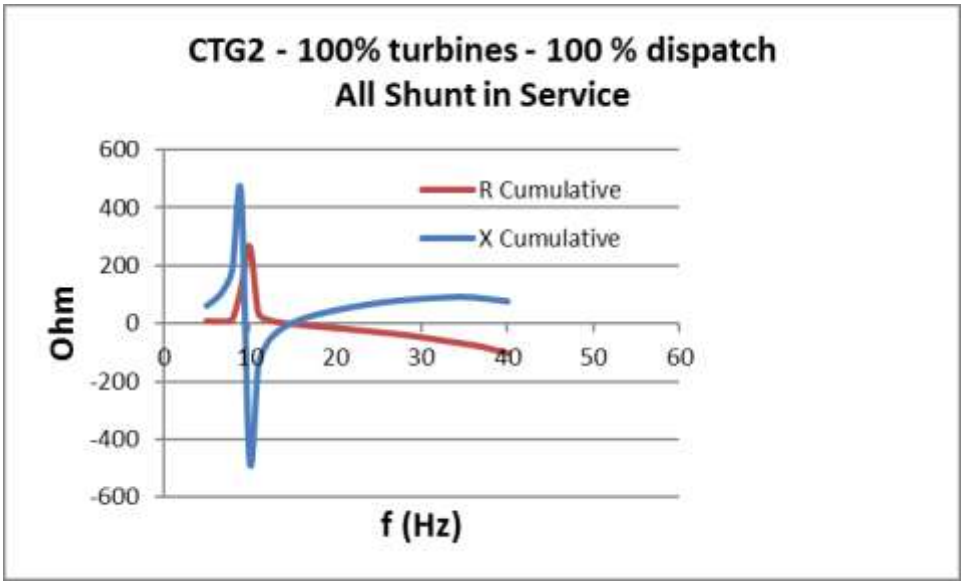

Figure 2-15 Detail Screening – Contingency#2, All Shunts in service

Table 2-3 Summary of Frequency Scan results

WF Scenario	Contingency	N-X	No Shunt in Service		All Shunt in Service	
			Cross-over Freq. for Xcumulative (Hz)	Cumulative R (ohm)	Cross-over Freq. for Xcumulative (Hz)	Cumulative R (ohm)
100% Turbines at 100% Dispatch	1	N-4	12	-2.75	15	-3.39
	2	N-6	12	-2.35	15	2.57
100% Turbines at 10% Dispatch	1	N-4	12	-4.24	15	-5.46
	2	N-6	12	-3.85	14	-4.43
10% Turbines at 100% Dispatch	1	N-4	6	0.78	12	-67.4
	2	N-6	6	1.18	11	-65.9

2.4.4 EMT Simulation

EMT simulations are initiated for CTG#1 and 2 with an outage count equal to or less than N-6. Further, multiple scenarios are developed for each contingency to account for variation in wind farm operating conditions, status of critical shunt reactors and nature of disturbance. Table 2-4 depicts all scenarios that are included as part of detailed EMT simulation-based analysis. Each simulation is executed as per the sequence outlined below:

- Transmission lines in the contingency definition that are remote with respect to the 345kV Wind Project POI station are placed out of service assuming they are under maintenance while initiating the simulation.
- Simulations are executed till 6s so that steady state operation of the wind farm is achieved.

- In case of fault-based simulations, a 3-phase to ground fault is applied on the transmission system at 6s. The fault location is selected such that it is in close vicinity of the POI or series compensated transmission lines included for study. Transmission lines (that are not offline for maintenance) are tripped to clear the fault in 4 cycles thereby establishing a radial connection between proposed project and series compensated transmission lines of interest.
- In case of faultless simulations, appropriate transmission lines are tripped as per the contingency definition at 6.065 s without being preceded by a fault.

Table 2-4 All Scenario of EMT simulation

Scenario	Contingency #	Number of Turbines in Service	Dispatch	Type of Disturbance	Status of Shunt Reactors
1	1	100%	100%	3LG	All Offline
2					All Online
3				Faultless	All Offline
4					All Online
5		100%	10.0%	3LG	All Offline
6					All Online
7				Faultless	All Offline
8					All Online
9		10%	100%	3LG	All Offline
10					All Online
11				Faultless	All Offline
12					All Online
13	2	100%	100%	3LG	All Offline
14					All Online
15				Faultless	All Offline
16					All Online
17		100%	10.0%	3LG	All Offline
18					All Online
19				Faultless	All Offline
20					All Online
21		10%	100%	3LG	All Offline
22					All Online
23				Faultless	All Offline
24					All Online

- The neighboring wind farms are offline while conducting EMT simulation. Fixed current sources are used in place of neighboring wind farms to keep the POI voltage in range for the scenarios with all the critical shunt reactors out of service.

- Following quantities are monitored to assess potential for SSR issues:

- Active and reactive power output from the Wind Project
- Voltage at 345kV Wind Project POI station
- Dominant sub-synchronous frequency component in the output current of the Wind Project (if any)
- Voltage across the series capacitors in transmission system

The key observations obtained from the detailed EMT simulation-based analysis are summarized below:

- Figure 2-16 through Figure 2-18 depict the EMT simulation results for CTG#1 under no fault conditions and with sensitivity around the dispatch level of wind farm and number of turbines in service while all shunts are out of services (Scenarios 3, 7 & 11).
    - Figure 2-16 shows that the project active power, RMS voltage at POI, Instantaneous voltage and current of POI and series capacitor voltage. The outputs exhibit sustained sub-synchronous frequency oscillations after radial connection to 345kV series compensated line is established (i.e. after 6.065s). The simulation results are in agreement with the screening study which indicated negative damping at the crossover of $X_{cumulative}$ for CTG#1.

- EMT simulation results for the condition involving operation of the project at minimum active power dispatch level (10%) under CTG#1 yields similar results. Figure 2-17 depicts oscillations in the project output when the turbines operate under 10% dispatch.
- Another simulation is also conducted for CTG#1 when 10% of the turbines are in-service. As depicted in Figure 2-18, the wind farm active and reactive power show oscillations after the project is radially connected to the series compensated lines. However, this oscillation is damped due to positive resistance at POI.
- As it can be seen, for all scenarios, the results of detail EMT simulations perfectly matches with frequency scan analysis.

- According to the ERCOT protocol, since the wind farm is vulnerable to SSR in the event of 4 concurrent transmission outages, IE should develop and implement an SSR mitigation plan before initial synchronization.
- Simulation results associated with all scenarios for CTG#1 and 2 are depicted in Appendix B.

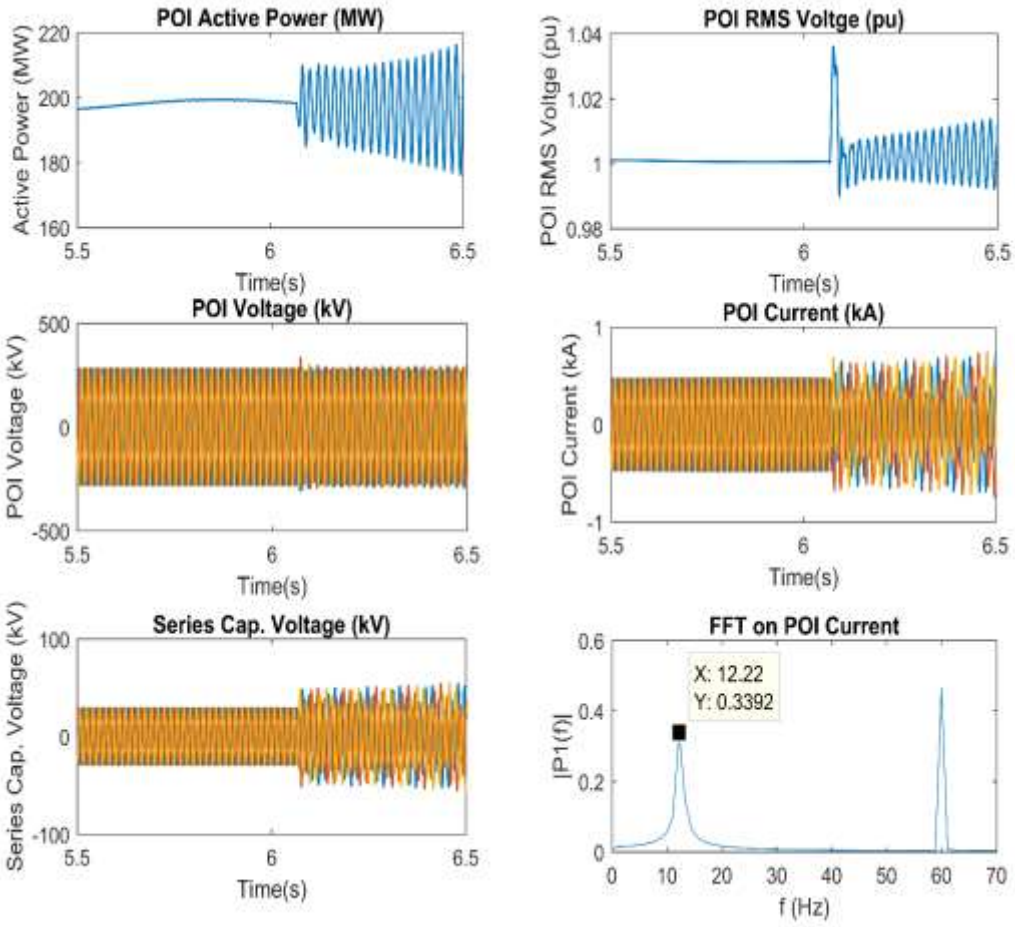

Figure 2-16 EMT simulation results of Scenario #3

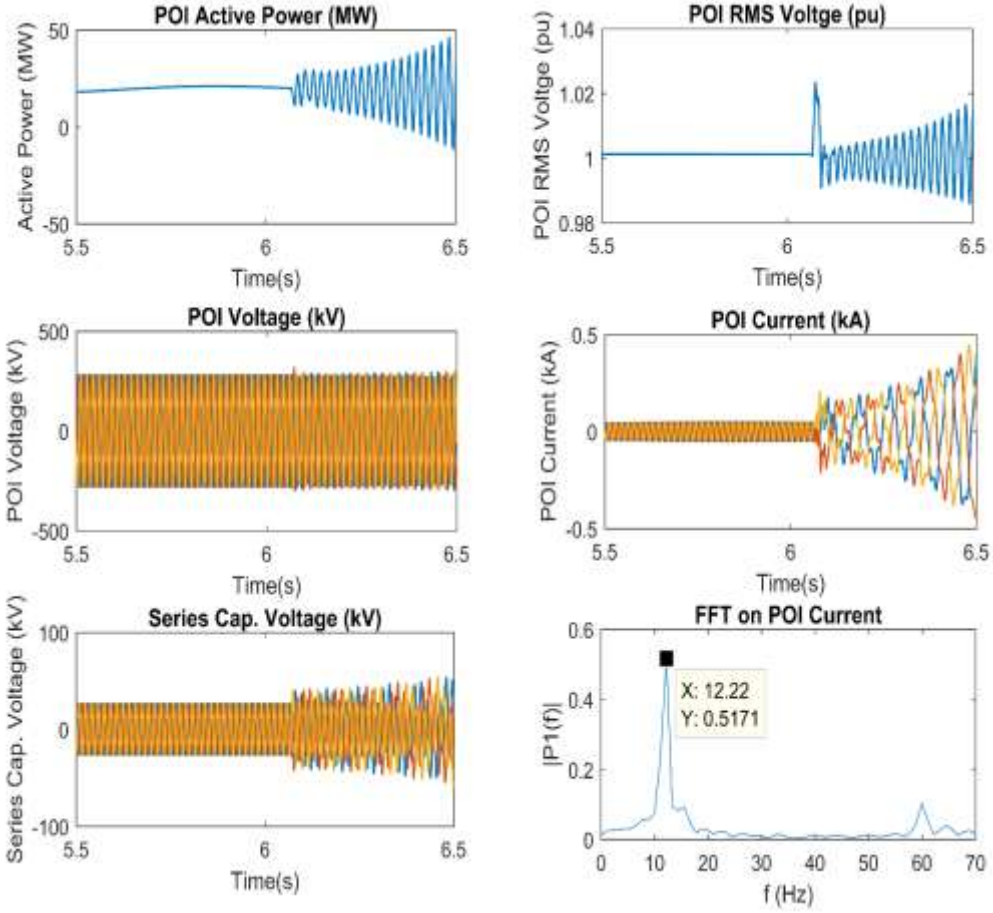

Figure 2-17 EMT simulation results of Scenario #7

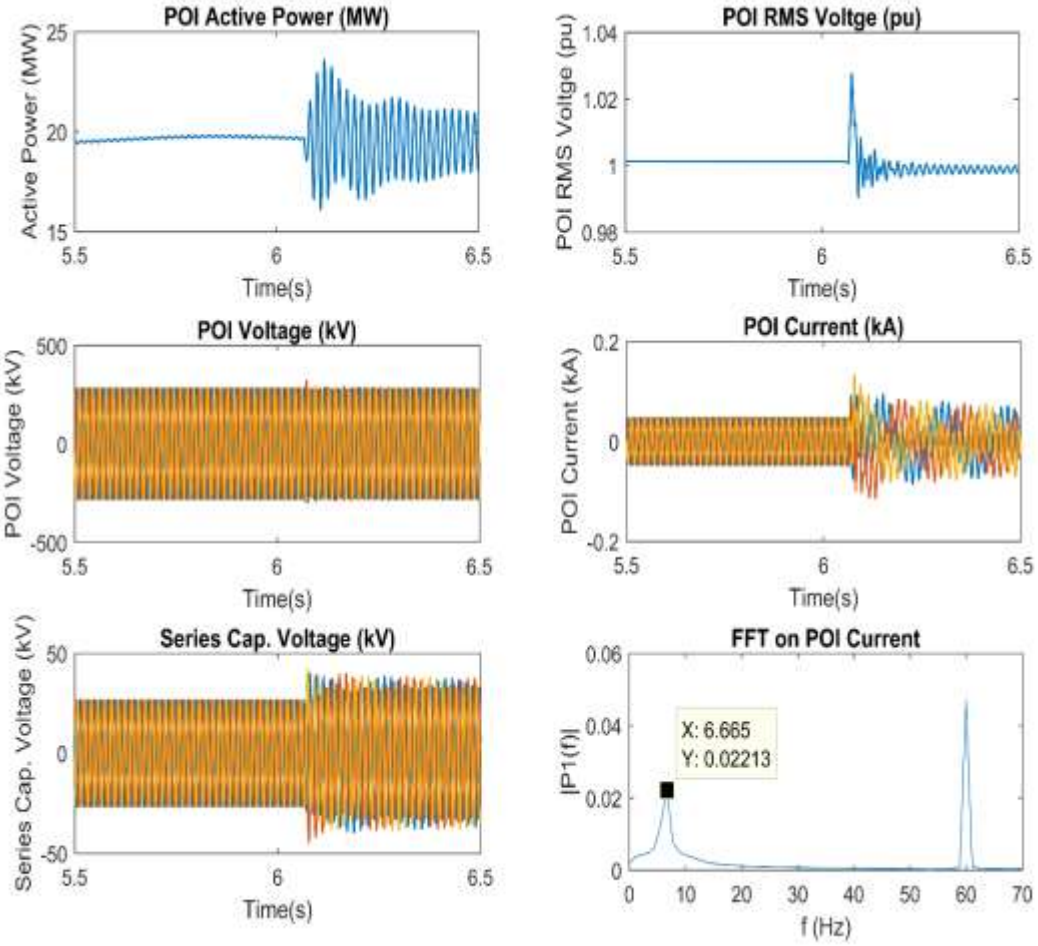

Figure 2-18 EMT simulation results of Scenario #11

Chapter 3

A Detail DFIG Modelling Approach to Study Impact of Phase-Locked Loop (PLL) Controller on Sub-Synchronous Oscillation

3.1 Introduction

Doubly-Fed Induction Generator (DFIG) based wind turbines have been widely used in the power grids. Complex and multi-layer controllers associated with the DFIG wind turbine have introduced challenges in transmission and distribution networks. Some of these challenges such as Sub-Synchronous Control Interaction (SSCI), weak grid interconnection, middle frequency resonance (MFR) and high frequency resonance have received increasing attention by researchers in recent times [1]-[13],[27] . Recent research has also underlined the strong dependency of the nature and extent of these phenomena on the control systems and strategies utilized to parameterize the DFIG controllers.

The most common control strategy for DFIG is vector-oriented control which relies on the accurate angle measurement of stator voltage [13],[26]. Phase-Locked Loop (PLL) is responsible for obtaining a precise angle measurement to be utilized for *d-q* transformation and vector control algorithm. Therefore, PLL plays a very critical role in accurate operation of vector control scheme on both the rotor and grid side closed loop current controllers of DFIG. Significant research has been

conducted on evaluating the impact of PLL dynamics on grid-connected voltage source converter (VSC) under different operating conditions through simulation or small signal impedance modeling. For instance, in [13], the possibility of middle frequency resonance with fast PLL dynamics is investigated through simulation and DFIG impedance model analysis. A small signal impedance model of DFIG with PLL in *abc* reference frame is derived in [28]-[29]. Utilizing the impedance model in conjunction with real time simulation, the effect of PLL parameters on Sub-Synchronous Control Interaction (SSCI) has been investigated. A linearized DFIG modeling approach including the PLL model is introduced in [30] to evaluate the DC-link voltage stability. However, none of these research efforts address the inclusion of PLL in nonlinear *d-q* state space formulation.

Due to the complexity of including PLL model on detail DFIG state-space model, most of the recent research has focused on formulating the DFIG model whilst ignoring PLL controller. An ideal model for the PLL has been considered in all these efforts and the DFIG has been modeled using *d-q* synchronous reference frame by estimating the network voltage angle using the line load flow [14], [31]. The primary limitation of this approach is ignoring the PLL dynamics and its contributions on DFIG response under different events such as SSCI, weak grid situation and MFR. In this work, a detail DFIG modelling approach is proposed which allows for the inclusion of the PLL model in *d-q* state-space equations. Using

this model, the effect of PLL controller on the DFIG dynamic performance during SSCI is investigated.

The proposed model is based on the double synchronous rotating reference frame approach which has capability to include the dynamics of PLL closed loop controller. In this regard, all sets of equations related to DFIG power circuit and mechanical system are written in the synchronous *d-q* frame whilst RSC and GSC controllers are extracted in another *d-axis* aligned PLL coordinate. PLL dynamic equations are adopted to obtain the precise angle of DFIG stator synchronous frames and later this angle utilized to transfer RSC and GSC controller to the PLL reference frame.

For the investigation associated with the impact of the PLL dynamics on SSCI, different scenarios with various PLL parameters have been defined and both eigenvalue analysis and time domain transient analysis are performed for these scenarios. The results confirm that faster PLL parameters can exacerbate the SSCI condition. To support this observation, a sub-synchronous *d-q* impedance model of DFIG including the proposed PLL closed loop is developed and the effects of PLL parameters on phase margin of DFIG have been investigated. In line with the results of the transient and eigenvalue investigations, the impedance model shows that faster PLL loop leads to smaller phase margin in sub-synchronous range and increase the risk of SSCI.

3.2 DFIG Detail State Space Modeling Including PLL

This section presents a comprehensive discussion on the *d-q* state space equation model for a DFIG integrated to the network. The model utilizes two reference frames in order to consider the dynamics of induction generator, turbine model, Grid Side Converter (GSC) controller, Rotor Side Converter (RSC) controller, DC link, grid side filter, pitch control loop, torque control loop, PLL closed loop and transmission system. In this effort, the voltage source converters are assumed to be ideal implying that they are transparent to the power and possess infinite band width (high switching frequency) [32]. The vector-oriented control (VOC) method has been adopted in this work. In addition, the practical limits (electrical and mechanical saturation limits plus ramp rates) and filtering have been accounted for in the model. The level of detail included in the model makes it appropriate for a diverse range of analyses including transient stability study, SSCI study and fault recovery simulations. The proposed model also provides the flexibility to run time domain transient simulation and Eigenvalue analysis on the same model.

The below nomenclature can be utilized as a reference for the formulas of the ensuing subsections.

DFIG	Doubly-fed induction generator
d, q	Subscript for denoting direct and quadrature axis

d, q_PLL	Subscript for denoting PLL direct and quadrature axis
s, r, g	Subscript for denoting stator, rotor and grid
f, L	Subscript for denoting filter and transmission line
dc, IG	Subscript for denoting dc link and induction generator parameter
m, e, sh	Subscript for denoting mechanical, electrical and shaft parameter
V, i	Voltage and current
P, Q, T	Active power, reactive power and torque
U_r, U_g	Rotor and grid voltage in PLL reference frame
$\omega_r, \omega_t, \omega_b$	Rotor, turbine and base angular speed
$\theta_{sh}, \theta_{pitch}, \theta_{PLL}$	Shaft, pitch and PLL angle
K_{sh}, D_m, F	Shaft spring, mutual damping and friction
p	Number of induction machine poles
H_t, H_g	Turbine and generator inertia
K_i, K_p	Integral and proportional coefficients of PI controller
GSC, RSC	Grid side converter and rotor side converter
GSF	Grid side filter
TC	Torque control
R, L, X, C	Resistance, reactance, inductance and capacitor

Z	Impedance
X_M	Magnetizing reactance
L_{ls}, L_{lr}	Stator and rotor leakage inductance
X_{ss}, X_{rr}	Summation of magnetizing reactance and stator/rotor leakage reactance
x, dx	Represent state and derivative of state
FW	Feed forward term
Out_{pitch_Cont}	Output of pitch control loop
Out_{pitch_Comp}	Output of pitch compensation loop
R_g, X_g	Resistance and reactance of grid side filter
net	Subscript for denoting network

3.2.1 Proposed *d-q* Phase-Locked Loop Modeling Approach

Most renewable generation resource technologies utilize voltage source converters (VSC) as grid-connecting interface while using PLL for synchronization with grid [33]. PLL is a closed loop structure that is utilized to estimate the angle of the grid voltage. Although, different PLL techniques have been proposed, the basic model of Synchronous Reference Frame (SRF) PLL has been adopted for the modeling approach presented herein. Without any loss in generality, the same

approach can be applied to the other techniques. The basic SRF-PLL is depicted in Figure 3-1[33].

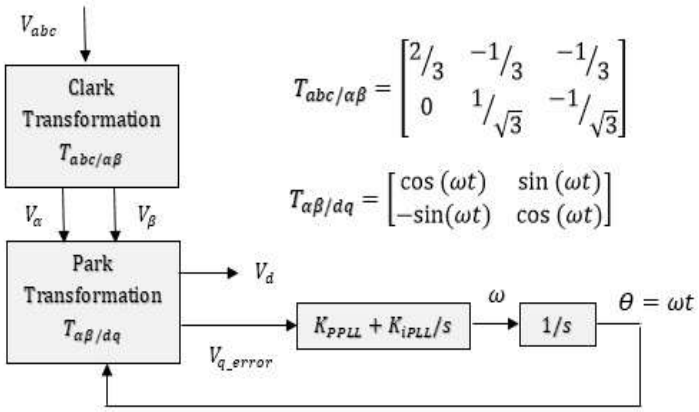

Figure 3-1 Simple synchronous reference frame (SRF) PLL

In the case of grid connected DFIG, PLL synchronizes to the three-phase sinusoidal voltage of DFIG's stator terminal by utilizing the *d-q* coordinates of the voltage [32][32]. The *d* component of the DFIG terminal voltage should be aligned with *d* axis of synchronous rotating reference frame. In other words, the angle must be modified until the *q* axis term of voltage reaches to zero. This can be achieved by a closed loop PI controller at the *q-axis* as shown in Figure 3-1. Firstly, three phase voltage of terminal V_{abc} is converted to the two-phase stationary $V_{\alpha\beta}$ through Clark transformation. Then the Park transformation with the angle feedback, as obtained from PI control loop, is utilized to transform $V_{\alpha\beta}$ to *d-q* synchronous reference frame.

State space *d-q* equations for grid-connected DFIG are intended to represent the electrical and mechanical systems of DFIG and their control loops. PLL plays the crucial role of capturing the precise angle of voltage at terminal of DFIG and utilizing this angle to generate aligned *d-axis* voltage as the input for RSC and GSC controllers. Hence, the dynamics of PLL add another layer of complexity between DFIG voltage/currents and control system and can affect the response of DFIG under various operating conditions.

A novel modelling approach is proposed in this work which allows the inclusion of the PLL control loop in *d-q* state space equations. Based on this approach, two *d-q* reference frames are considered to capture the effect of PLL dynamic loop. In this regard, all set of equations relating to DFIG power circuit and mechanical system are written in one synchronous *d-q* frame and RSC and GSC controllers are implemented in another *d-axis* aligned PLL coordinate. The PLL is responsible for correlating these two reference frames. In this approach, the PLL calculates the precise angle of DFIG and network frame and utilizes this angle to transfer RSC and GSC controller to PLL reference frame. The detail of proposed *d-q* PLL model and corresponding transformation is depicted in Figure 3-2.

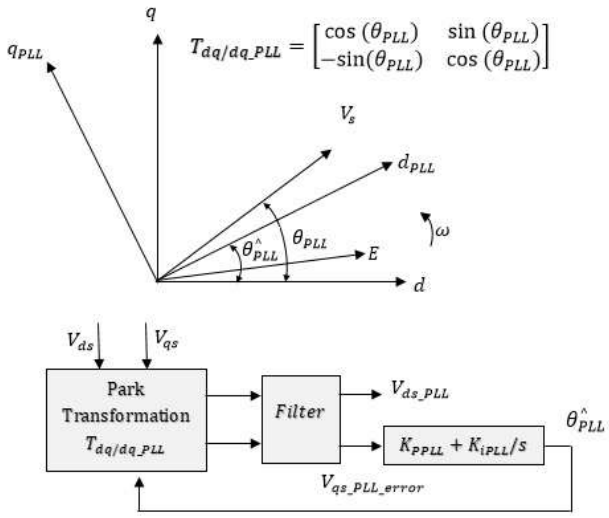

Figure 3-2 Proposed d-q PLL closed loop structure for modeling purpose

The ultimate goal for this loop is to rotate the (d_{PLL}, q_{PLL}) reference frame in such a way that d_{PLL}-*axis* aligns with the stator voltage *Vs*, and $\theta_{PLL} = \hat{\theta_{PLL}}$. Also, the Clark transformation and integrator part of the PI loop controller are ignored in this model as both the V_d and V_q signals are already in synchronous rotating *d-q* reference frame. The simplified proposed PLL without including the filter can be formulated as below:

$$\begin{bmatrix} V_{ds\_PLL} \\ V_{qs\_PLL} \end{bmatrix} = T_{dq/dq\_PLL} \begin{bmatrix} V_{ds} \\ V_{qs} \end{bmatrix} \tag{3.1a}$$

$$\theta_{PLL} = K_{iPLL}\, x_{PLL} + K_{PPLL}\, V_{qs\_PLL} \tag{3.1b}$$

$$dx_{PLL} = V_{qs\_PLL} - 0 \tag{3.1c}$$

The schematic depicting the interaction between the proposed PLL model and DFIG state space equations is depicted in Figure 3-3. The proposed formulation approach is presented in next subsection. Here, all non-linear differential equations corresponding to control system are transferred to the PLL reference frame and the remaining element and control loops are formulated in synchronous reference frame. The subscript determines the reference frame for each set of equation.

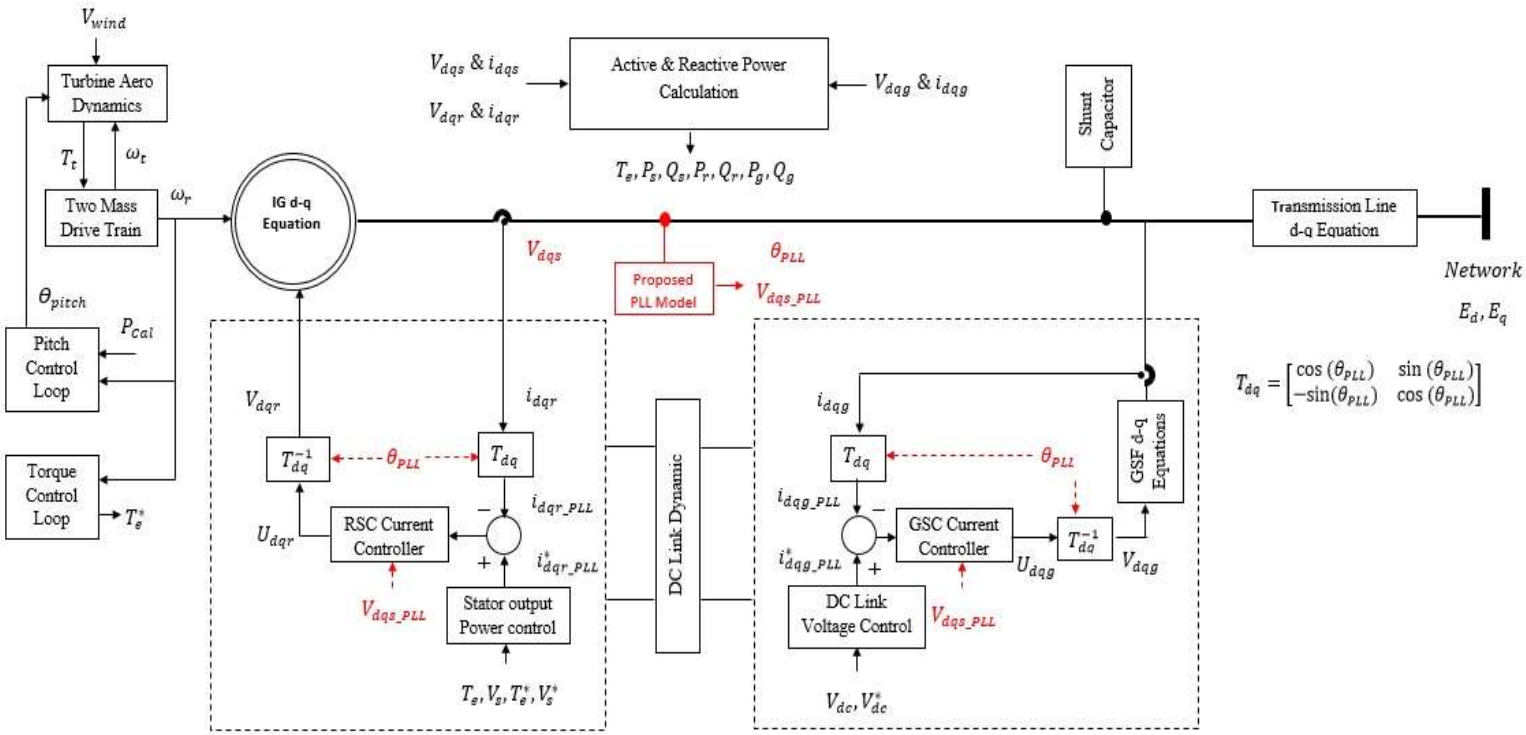

Figure 3-3 Overall interaction block diagram of DFIG with proposed PLL modeling approach

3.2.2 DFIG Dual *d-q* State Space Formulation

3.2.2.1 Power and Torque Calculation in d-q Reference Frame

The algebraic equations for the calculation of electrical torque, active and reactive power in *d-q* reference frame are given as below [32].

$$P_x = \frac{3}{2}\left(V_{dx} i_{dx} + V_{qx} i_{qx}\right) \tag{3.2a}$$

$$Q_x = \frac{3}{2}\left(V_{qx} i_{dx} - V_{dx} i_{qx}\right) \tag{3.2b}$$

Where *x* can be replaced by *s* for stator active and reactive power, *r* for rotor and *g* for grid side converter, respectively.

Electrical torque can be represented as [14]:

$$T_e = X_M \left(i_{qs} i_{dr} - i_{ds} i_{qr}\right) \tag{3.2c}$$

3.2.2.2 Induction Generator

The induction machine is formulated using the six-order state space system [34], [35]. Here current/flux are considered as states and voltages as inputs to the system. The induction machine can be formulated as below.

$$U_{IG} = \begin{bmatrix} V_{qs} \\ V_{ds} \\ V_{0s} \\ V_{qr} \\ V_{dr} \\ V_{0r} \end{bmatrix} \qquad x_{IG} = \begin{bmatrix} i_{qs} \\ i_{ds} \\ i_{0s} \\ i_{qr} \\ i_{dr} \\ i_{0r} \end{bmatrix} \tag{3.3a}$$

$$dx_{IG} = A_{IG} x_{IG} + B_{IG} U_{IG} \tag{3.3a}$$

Where:

$$A_{IG} = -B \times Aux \quad \text{and} \quad B_{IG} = inv(B)$$

Where B matrix is:

$$B = \begin{bmatrix} \frac{X_{ss}}{\omega_b} & 0 & 0 & \frac{X_M}{\omega_b} & 0 & 0 \\ 0 & \frac{X_{ss}}{\omega_b} & 0 & 0 & \frac{X_M}{\omega_b} & 0 \\ 0 & 0 & \frac{X_{ls}}{\omega_b} & 0 & 0 & 0 \\ \frac{X_M}{\omega_b} & 0 & 0 & \frac{X_{rr}}{\omega_b} & 0 & 0 \\ 0 & \frac{X_M}{\omega_b} & 0 & 0 & \frac{X_{rr}}{\omega_b} & 0 \\ 0 & 0 & 0 & 0 & 0 & \frac{X_{lr}}{\omega_b} \end{bmatrix} \tag{3.3b}$$

And *Aux* is equal to

$$\begin{bmatrix} R_s & \frac{\omega_s X_{ss}}{\omega_b} & 0 & 0 & \frac{\omega_s X_M}{\omega_b} & 0 \\ \frac{-\omega_s X_{ss}}{\omega_b} & R_s & 0 & \frac{-\omega_s X_M}{\omega_b} & 0 & 0 \\ 0 & 0 & R_s & 0 & 0 & 0 \\ 0 & \frac{(\omega_s - \omega_r) X_M}{\omega_b} & 0 & R_r & \frac{(\omega_s - \omega_r) \times X_{rr}}{\omega_b} & 0 \\ \frac{-(\omega_s - \omega_r) X_M}{\omega_b} & 0 & 0 & \frac{-(\omega_s - \omega_r) \times X_{rr}}{\omega_b} & R_r & 0 \\ 0 & 0 & 0 & 0 & 0 & R_r \end{bmatrix} \tag{3.3c}$$

3.2.2.3 Grid Side Converter Controller

The grid side converter controller objective is to keep the DC link voltage constant and regulate the grid side AC voltage/reactive power. Constant DC voltage ensures the power balance of RSC and GSC. Using Vector Oriented Control strategy, GSC controller adds 4 states, of which two belong to the outer loop and the others belong to the inner faster current control loop. The final output of this controller is grid side *d-q* voltage. This model also includes a feed forward term which should be considered for the precise performance of model [36], [37]. Considering the proposed PLL transformation, GSC controller is formulated as follow.

$$dx_1 = \frac{(V_{dc}^* - V_{dc})}{V_{dc}^*} \tag{3.4a}$$

$$dx_2 = V_g^* - V_g \tag{3.4b}$$

$$\begin{bmatrix} i_{dg\_PLL} \\ i_{qg\_PLL} \end{bmatrix} = T_{dq/dq\_PLL} \begin{bmatrix} i_{dg} \\ i_{qg} \end{bmatrix} \tag{3.4c}$$

$$dx_3 = i_{dg\_PLL}^* - i_{dg\_PLL} \tag{3.4d}$$

$$dx_4 = i_{qg\_PLL}^* - i_{qg\_PLL} \tag{3.4e}$$

$$i_{dg\_PLL}^* = K_{i1} x_1 + K_{p1} \frac{(V_{dc}^* - V_{dc})}{V_{dc}^*} \tag{3.4f}$$

$$i^*_{qg\_PLL} = K_{i1}x_2 + K_{p1}(V^*_g - V_g) \quad (3.4g)$$

$$U_{dg\_PLL} = (K_{iGSC}x_3 + K_{pGSC}(i^*_{dg\_PLL} - i_{dg\_PLL})) + FW_{dGSC} \quad (3.4h)$$

$$U_{qg\_PLL} = (K_{iGSC}x_4 + K_{pGSC}(i^*_{qg\_PLL} - i_{qg\_PLL})) + FW_{qGSC} \quad (3.4i)$$

$$FW_{dGSC} = V_{ds\_PLL} + X_g\omega_s i^*_{qg\_PLL} - R_g i^*_{dg\_PLL} \quad (3.4j)$$

$$FW_{qGSC} = V_{qs\_PLL} - X_g\omega_s i^*_{dg\_PLL} - R_g i^*_{qg\_PLL} \quad (3.4k)$$

$$\begin{bmatrix} V_{dg} \\ V_{qg} \end{bmatrix} = T_{dq/dq\_PLL}{}^{-1} \begin{bmatrix} U_{dg\_PLL} \\ U_{qg\_PLL} \end{bmatrix} \quad (3.4l)$$

3.2.2.4 Rotor Side Converter Controller

Rotor side converter regulates the generator torque and stator voltage/reactive power exchange between stator and grid by generating voltages at different amplitudes and frequency [36], [37]. The following equations represent the dynamic of this controller with inclusion of PLL control loop's effect.

$$dx_1 = V_s - V^*_s \quad (3.5a)$$

$$\begin{bmatrix} i_{dr\_PLL} \\ i_{qr\_PLL} \end{bmatrix} = T_{dq/dq\_PLL} \begin{bmatrix} i_{dr} \\ i_{qr} \end{bmatrix} \quad (3.5b)$$

$$dx_2 = i^*_{dr\_PLL} - i_{dr\_PLL} \quad (3.5c)$$

$$dx_3 = i^*_{qr\_PLL} - i_{qr\_PLL} \quad (3.5d)$$

$$i^*_{qr\_PLL} = K_{i2}x_1 + K_{p2}(V_s - V^*_s) \tag{3.5e}$$

$$\begin{bmatrix} i_{ds\_PLL} \\ i_{qs\_PLL} \end{bmatrix} = T_{dq/dq\_PLL} \begin{bmatrix} i_{ds} \\ i_{qs} \end{bmatrix} \tag{3.5f}$$

$$i^*_{dr} = \frac{T^*_e}{\left(\frac{X_M}{X_{ss}}\right)\sqrt{\left(\frac{V_{ds}-R_s i_{ds}}{-\omega_s}\right)^2 + \left(\frac{V_{qs}-R_s i_{qs}}{\omega_s}\right)^2}} \tag{3.5g}$$

$$U_{dr\_PLL} = (K_{iRSC}x_2 + K_{pRSC}(i^*_{dr\_PLL} - i_{dr\_PLL})) + FW_{dRSC} \tag{3.5h}$$

$$U_{qr\_PLL} = (K_{iRSC}x_3 + K_{pRSC}(i^*_{qr\_PLL} - i_{qr\_PLL})) + FW_{qRSC} \tag{3.5i}$$

$$FW_{dRSC} = R_r i^*_{dr} + X_{rr}(\omega_s - \omega_r) i^*_{qr} + X_M(\omega_s - \omega_r) i_{qs} \tag{3.5j}$$

$$FW_{qRSC} = R_r i^*_{qr} + X_{rr}(\omega_s - \omega_r) i^*_{dr} + X_M(\omega_s - \omega_r) i_{ds} \tag{3.5k}$$

$$\begin{bmatrix} V_{dr} \\ V_{qr} \end{bmatrix} = T_{dq/dq\_PLL}{}^{-1} \begin{bmatrix} U_{dr\_PLL} \\ U_{qr\_PLL} \end{bmatrix} \tag{3.5l}$$

3.2.2.5 DC Link Dynamic

A DC link with constant voltage is required to control the balance of power flow between RSC and GSC. Based on the energy equation of capacitor comprising the link, the dynamic of the DC link can be represented as [14]:

$$dV_{dc} = \frac{1}{CV_{dc}}(P_g - P_r) \tag{3.6}$$

3.2.2.6 Two Mass Drive Train

Two mass drive train representation has been recommended for wind turbines (Turbine & Generator). Two mass model adds three states to the model which are formulated as shown below [14].

$$d\theta_{sh} = (\omega_t - \omega_r) \times \frac{\omega_b}{p} \tag{3.7a}$$

$$d\omega_t = \frac{(T_t - T_{sh})}{2H_{\omega t}} \tag{3.7b}$$

$$d\omega_r = \frac{(T_e - T_m - F\omega_r)}{2H_g} \tag{3.7c}$$

$$T_{sh} = K_{sh}\,\theta_{sh} + D_m(\omega_t - \omega_r) \tag{3.7d}$$

$$T_m = -T_{sh} \tag{3.7e}$$

3.2.2.7 Pitch Control Loop

For the wind speed above the rated speed, wherein the kinetic energy available from the wind resource is more than rated power of machine, the blades are pitched to decrease the delivered mechanical power of shaft to 1 per unit. This controller adds three states of which one belongs to low pass filter. The pitch control loop and the equations are shown as below [38].

$$dx_1 = \omega_r - \omega_r^* \tag{3.8a}$$

$$dx_2 = P_{Calc} - P^* \tag{3.8b}$$

$$Out_{pitch\_Cont} = K_{ipitch\_Cont}\, x_1 + K_{ppitch\_Cont}(\omega_r - \omega_r^*) \tag{3.8c}$$

$$Out_{pitch\_Comp} = K_{ipitch\_Comp} x_2 + K_{ppitch\_Comp}(P_{Calc} - P^*) \tag{3.8d}$$

$$dx_3 = Out_{pitch\_Cont} + Out_{pitch\_Comp} + \frac{-1}{T_{pitch}} x_3 \tag{3.8e}$$

$$\theta_{pitch} = \frac{1}{T_{pitch}} x_3 \tag{3.8f}$$

Here P_{Calc} is the total power which DFIG delivers to the network through stator and GSC.

$$P_{Calc} = P_s + P_g \tag{3.8g}$$

3.2.2.8 Torque Control Loop

This loop is utilized to determine the desired electrical torque and has one dynamic state:

$$dx_1 = \omega_r - \omega_r^* \tag{3.9a}$$

$$T_e^* = K_{iTC} x_1 + K_{pTC}(\omega_r - \omega_r^*) \tag{3.9b}$$

Based on the turbine that is utilized in this work, the reference speed is 1.2 pu for the power level above 75% of nominal power [39].

3.2.2.9 Grid Side Filter

Interconnection of the AC side of the GSC to the network is buffered through a filter the dynamics of which can be represented as shown below.

$$di_{dg} = \frac{\omega b}{X_g}(-R_g i_{dg} + X_g i_{qg}) + \frac{\omega b}{X_g}(-V_{dg} + V_{ds}) \tag{3.10a}$$

$$di_{qg} = \frac{\omega b}{X_g}(-X_g i_{dg} - R_g i_{qg}) + \frac{\omega b}{X_g}(-V_{qg} + V_{qs}) \tag{3.10b}$$

3.2.2.10 Series Compensated Line

The impact and dynamic of series compensated transmission line, as a part of wind farm integrated into the power system network need to be considered. Here fourth order state space dynamic equations are adopted from [14].

$$dx_L = A_L x_L + B_L U_L \tag{3.11a}$$

$$A_L = \begin{bmatrix} 0 & -\omega_e & X_C & 0 \\ \omega_e & 0 & 0 & X_C \\ \frac{-1}{X_L} & 0 & \frac{-R_L}{X_L} & -\omega_e \\ 0 & \frac{-1}{X_L} & \omega_e & \frac{-R_L}{X_L} \end{bmatrix} \tag{3.11b}$$

$$B_L U_L = -\omega_b \begin{bmatrix} 0 \\ 0 \\ \frac{(V_{qs} - E_q)}{X_L} \\ \frac{(V_{ds} - E_d)}{X_L} \end{bmatrix} \qquad x_L = \begin{bmatrix} V_{cq} \\ V_{cd} \\ i_{qL} \\ i_{dL} \end{bmatrix} \tag{3.11c}$$

3.2.2.11 Terminal Filter

Integration of DFIG to the network through transmission line while considering stator, grid side filter and line current as states is a challenge and requires simplification or the use of an alternative set of equations. Ref [14], [31] mainly focusses on SSCI study and tends to ignore the dynamics of grid side filter due to its higher frequency range compare to the SSCI. Alternatively, a large resistance at the terminal of DFIG is proposed in [8]. In this work, a shunt capacitor at the terminal of DFIG is proposed which can be interpreted as filter or line shunt capacitance. The corresponding dynamic is represented as depicted below.

$$V_{ds} = V_{dcf} \qquad V_{qs} = V_{qcf} \tag{3.12a}$$

$$i_{df} = i_{dl} - i_{ds} - i_{dg} \tag{3.12b}$$

$$i_{qf} = i_{ql} - i_{qs} - i_{qg} \tag{3.12c}$$

$$dV_{ds} = \omega_b V_{qs} + \omega_b X_f i_{df} \tag{3.12d}$$

$$dV_{qs} = -\omega_b V_{ds} + \omega_b X_f i_{qf} \tag{3.12e}$$

3.2.3 Filters and Practical Limits

Consideration of practical hardware limit such as ramp rate, saturation limits and filtering can significantly affect the performance of the developed

models, some of the limits which are taken in to account as part of this effort are as follow:

- Electrical limit: maximum current of RSC and GSC, maximum and minimum limit for PI regulator.
- Mechanical limit: maximum/minimum pitch angle and rate of pitch angle changes.

Proper interaction of different control loops in integrated DFIG, highly depends on the quality of the exchanged signals between these loops and devices. Therefore, appropriate filtering plays an important role in satisfactory performance of developed model. The first order and second order filter can be implemented as follow.

$$dx = \frac{-1}{T_c}x + u \text{ And } y = \frac{1}{T_c}x \tag{3.13a}$$

Where T_c is the time constant of filter and u and y the input and output respectively.

Second order filter:

$$dx = \begin{bmatrix} 0 & 1 \\ -\omega_n^2 & -2\zeta\omega_n \end{bmatrix} x + \begin{bmatrix} 0 \\ 1 \end{bmatrix} u \tag{3.13b}$$

$$y = \begin{bmatrix} \omega_n^2 & 0 \end{bmatrix} x \tag{3.13c}$$

Table 3-1 exhibit the parameters of filters and points of implementation.

Table 3-1 Filter Parameters

Point of implementation	Order of Filter	Characteristic
ω_r^*	1st Order	$T_s = 5$
θ_{pitch}	1st Order	$T_{pitch} = 0.01$
V_{ds_PLL}	2nd Order	$\omega_n = 2\pi \times 100, \zeta = 0.707$
V_{qs_PLL}	2nd Order	$\omega_n = 2\pi \times 100, \zeta = 0.707$

3.3 Solving and Initialization

DFIG wind farm integrated to the network represents a highly nonlinear system. Therefore, solving and initialization of the given equations play an important role in convergence of the system. The initial condition can be calculated by solving state space equation in steady state mode (dx=0). In order to avoid the ill-defined system, the system was solved by three different methods as follow, Runge Kutta, ODE Matlab code and Matlab Simulink. The result for three methods perfectly matched and there is no sign of ill-defined system.

Eigen value analysis also can be performed using Matlab Simulink however, an effective zero Eigen value was observed using linmode command. In order to avoid this mode, Jacobean method is suggested for Eigen value analysis.

3.4 Effects of PLL Closed Loop Parameters on SSCI

This section utilizes the detailed *d-q* model discussed in the preceding section to underline the importance of the PLL controller dynamics in the context of stability studies especially SSCI investigations.

3.4.1 Case Study

In order to demonstrate the contribution of the research documented herein and the significance of the PLL dynamics, the effect of PLL parameters on SSCI has been investigated by means of time domain transient simulation, eigenvalue analysis and impedance model. A utility scale 90 MW wind farm connected to the 345KV network through two step-up transformers and a series compensated line has been utilized for the case study. Information associated with the radial test system including collection system, Gen-tie line, transformers and transmission line is provided in [4].

The wind turbine control parameters, induction generator data are based on a commercial grade utility scale 1.5 MW wind turbine technology [39].

3.4.2 Time domain transient Simulation and Eigenvalue Analysis

Sub-synchronous control interaction (SSCI) is a phenomenon wherein a control system of power electronic device (in this case the wind turbine control etc.) interacts, at a natural frequency below nominal frequency (60 Hz), with the electric power network containing closely located series compensated transmission

facilities [4]. The sub-synchronous currents can increase due to positive feedback between transmission elements and the control systems of the generation resources. DFIG wind turbines have been documented to be vulnerable to SSCI oscillations and several instances of damage are reported in these turbines due to SSCI oscillations [5], [6].

In this section, the proposed model is utilized to perform comprehensive Eigenvalue analysis and time domain transient simulations to evaluate the impact of PLL parameters on SSCI. Various credible study scenarios focusing around variations in the PLL parameters, as utilized for the investigation, are depicted in Table 3-2. The compensation level for series compensated line is assumed to be at 70% for all scenarios.

Table 3-2 Different Scenario of SSCI events

Scenario	Compensation level	PLL parameter
1	70%	K_P=1, K_i=10
2	70%	K_P=10, K_i=100
3	70%	K_P=50, K_i=500
4	70%	K_P=100, K_i=1000
5	70%	K_P=150, K_i=1500

SSCI modes, frequency and damping for each scenario outlined in Table 3-2 are calculated and have been listed in Table 3-3. As evident from the results depicted in Table 3-3, faster PLL parameters exacerbate likelihood of SSCI. This observation is underlined by the presence of more negative damping and more

negative resistance at the DFIG terminal for scenarios characterized by faster PLL control parameters.

Table 3-3 SSCI mode characteristic for different scenario of SSCI event

SSR Modes				
Scenario	Real	Imag	Freq	Damping
SC1	4.557	313.356	49.872	-1.454
	4.557	-313.356	-49.872	-1.454
SC2	4.876	311.696	49.608	-1.564
	4.876	-311.696	-49.608	-1.564
SC3	5.502	310.124	49.358	-1.774
	5.502	-310.124	-49.358	-1.774
SC4	6.526	311.237	49.535	-2.096
	6.526	-311.237	-49.535	-2.096
SC5	6.681	311.729	49.613	-2.143
	6.681	-311.729	-49.613	-2.143

The aforementioned observation is further corroborated by the Eigenvalue locus depicted in Figure 3-4 for the various study scenarios. As evident from Figure 3-4, the SSCI modes move toward right-half plan when faster PLL control loop is in service.

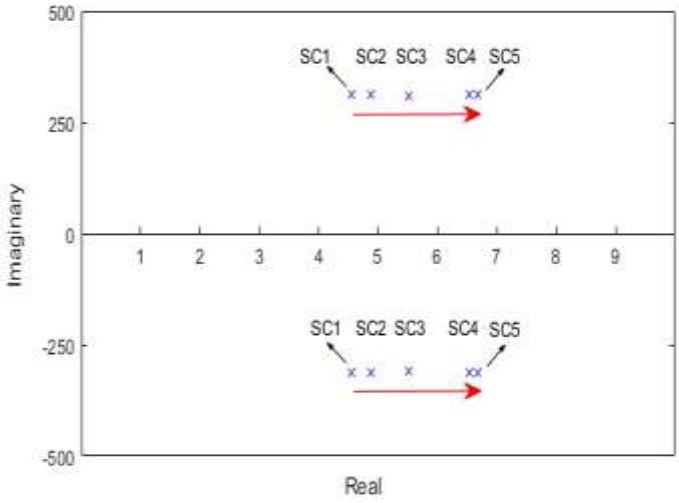

Figure 3-4 Eigenvalue locus for varying PLL parameter

Subsequently, time domain transient simulation for Scenarios 1 and 2 have been implemented to underline the adequacy of model for both Eigenvalue analysis and time domain transient study.

1) *Scenario 1 simulation results*:

In this scenario, the compensation level is set at 70% of line reactance and relatively slower parameters for the PLL have been set based on table I. The series capacitor is placed in service at t=24 sec. The wind farm terminal active power, FFT result on active power, reactive power and DC link voltage are presented in Figure 3-5. The average amplitude and complementary frequency of the oscillations are obtained by applying FFT analysis on 1 second interval of data immediately after the initiation of the oscillations. According to the frequency spectrum, SSCI oscillations on active power have a magnitude as high as 118.6

MW with a 49.8 Hz frequency which aligns perfectly with the Eigenvalue analysis results depicted in Table 3-3. The frequency of the oscillations on the active power is complimentary frequency of the 10.2 Hz SSCI oscillations.

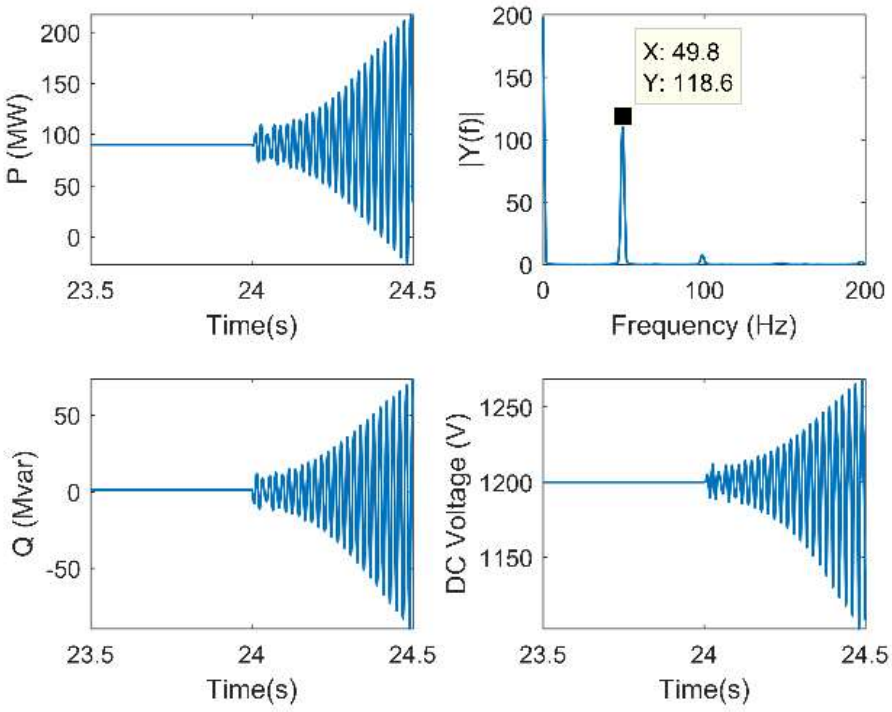

Figure 3-5 Active power, Active Power FFT, reactive power and DC link voltage of scenario 1

2) *Scenario2 simulation results*:

The wind farm terminal active power, FFT result on active power, reactive power and DC link voltage for Scenario 2 are presented in Figure 3-6. According to the frequency spectrum, SSCI oscillations on active power have a magnitude as high as 136.1 MW with a 49.8 Hz frequency.

A comparison of scenario 1 and 2 results is indicative of PLL PI control settings impact on SSCI oscillations. Faster PI controller increases the risk of SSCI by increasing magnitude of the oscillations. The time domain simulation results also confirm the result of Eigenvalue analysis which were indicative of an increase in negative damping and moving of SSCI mode toward right-half plane thereby indicating greater instability from an SSCI perspective.

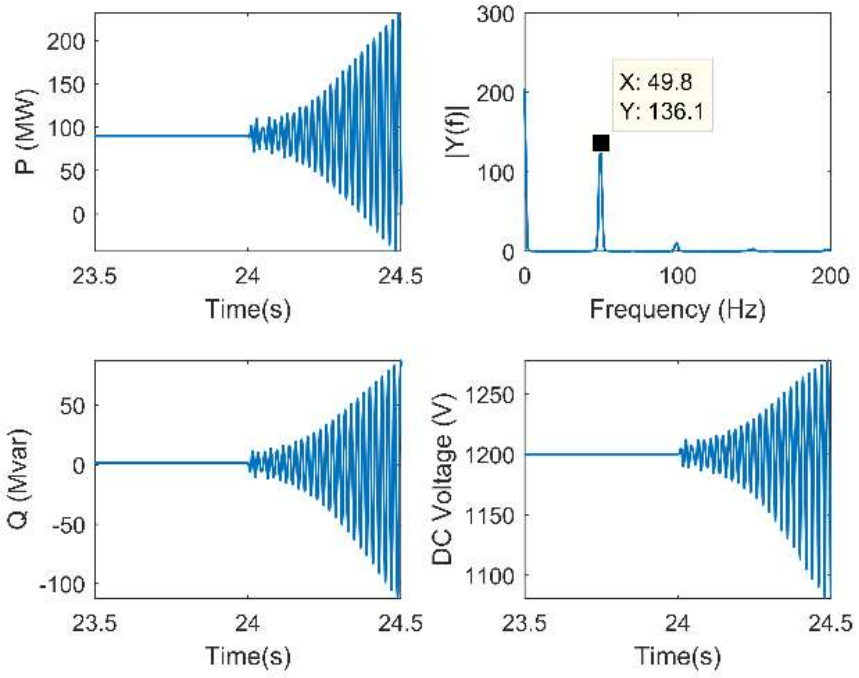

Figure 3-6 Active power, Active Power FFT, reactive power and DC link voltage of scenario 2

3.5 DFIG d-q Sub-Synchronous Impedance Modeling

3.5.1 Impedance Modeling of Proposed PLL Closed Loop Structure

Because of the nonlinear nature of PLL transformation, a small signal model is utilized to extract the closed loop transfer function of proposed PLL [13], [40]. The closed loop transfer function of proposed PLL model can be represented as follows:

$$G_{dq/dqPLL} = \begin{bmatrix} 1 & 0 \\ 0 & 1 - V_{ds\_PLL} T_{PLL} \end{bmatrix} \tag{3.14a}$$

$$G_{dqPLL/dq} = \begin{bmatrix} 1 & 0 \\ 0 & 1 + V_{ds\_PLL} T_{PLL} \end{bmatrix} \tag{3.14b}$$

Where (3.14a) is used to transfer from synchronous *d-q* to PLL *d-q* reference frame and vice-versa for (3.14b). Considering aligned *d-axis* voltage as 1 pu., T_{PLL} is defined as:

$$T_{PLL} = \frac{G_{PLL}(s)}{1 + G_{PLL}(s)} \tag{3.14c}$$

$$G_{PLL}(s) = K_{PPLL} + \frac{K_{iPLL}}{S} \tag{3.14d}$$

This closed loop transfer function comprises of PLL unit information and is capable of reflecting the influence of PLL in DFIG impedance model. This is

important to note that the *d-q* components are decoupled in this model which make the analysis much easier.

3.5.2 Impedance Modeling of Controller and Induction Machine

Both rotor side and grid side controller include PI controller which can be modeled in *d-q* reference frame as shown below.

$$G_{RSC}(s) = K_{pRSC} + \frac{K_{iRSC}}{S} \tag{3.15a}$$

$$G_{GSC}(s) = K_{pGSC} + \frac{K_{iGSC}}{S} \tag{3.15b}$$

Because of the small bandwidth of outer control loops, the dynamics of these controllers are not included in SSCI studies [41]. Therefore, the impedance modeling of these outer loops has been ignored for the purposes of this effort.

The simplified induction machine impedance transfer function while ignoring magnetizing inductance (this inductance is considered much larger in comparison to leakage inductance of stator and rotor) is given as follows [13].

$$Z_{IG} = R_S + R_r + s(L_{lS} + L_{lr}) \tag{3.16a}$$

Then G_{IG} is defined as below:

$$G_{IG} = \frac{1}{Z_{IG}} \tag{3.16b}$$

3.5.3 *d-q* Impedance Modeling of DFIG

The simplified impedance block diagram of rotor side and grid side of DFIG including Induction generator and grid side filter with PLL effect can be depicted as shown Figure 3-7 and Figure 3-8 [13].

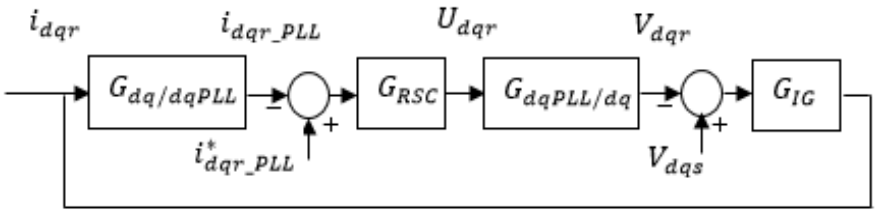

Figure 3-7 Impedance block diagram of rotor side

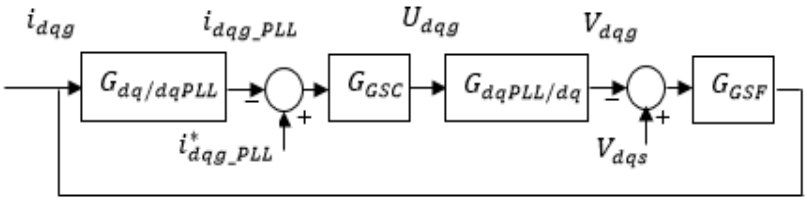

Figure 3-8 Impedance block diagram of grid

Based on Figure 3-7, the impedance of rotor part can be obtained as:

$$Z_r(s)=\frac{V_{dqs}}{-I_{dqs}}=\frac{1+G_{IG}(s)G_{dq/dq\_PLL}(s)G_{RSC}(s)G_{dq\_PLL/dq}(s)}{G_{IG}(s)} \tag{3.17a}$$

Considering the closed loop transfer function of proposed PLL, (3.14a) and (3.14b), the rotor impedance contains *d-q* component and these two components can be represented as follow:

$$Z_{rd}(s)=\frac{1+G_{IG}(s)G_{RSC}(s)}{G_{IG}(s)} \tag{3.17b}$$

$$Z_{rq}(s)=\frac{1+G_{IG}(s)(1-V_{ds}T_{PLL}(s))G_{RSC}(s)(1+V_{ds}T_{PLL}(s))}{G_{IG}(s)} \tag{3.17c}$$

Similarly, based on the Figure 3-8 the grid side impedance of DFIG from stator terminal can be extracted as follows:

$$Z_G(s)=\frac{V_{dqs}}{-I_{dqg}}=\frac{1+G_{GSF}(s)G_{dq/dq\_PLL}(s)G_{GSC}(s)G_{dq\_PLL/dq}(s)}{G_{GSF}(s)} \tag{3.18a}$$

Where the grid side filter transfer function is defined as shown below:

$$G_{GSF}=\frac{1}{R_g+sL_g} \tag{3.18b}$$

And the *d-q* grid side impedances of DFIG from stator terminal are:

$$Z_{Gd}(s)=\frac{1+G_{GSF}(s)G_{GSC}(s)}{G_{GSF}(s)} \tag{3.18c}$$

$$Z_{Gq}(s)=\frac{1+G_{GSF}(s)(1-V_{ds}T_{PLL}(s))G_{GSC}(s)(1+V_{ds}T_{PLL}(s))}{G_{GSF}(s)} \tag{3.18d}$$

The total decoupled impedance of DFIG in *d-q* frame can be calculated as follow:

$$Z_{DFIGd}(s)=\frac{G_{rd}(s)G_{Gd}(s)}{G_{rd}(s)+G_{Gd}(s)} \tag{3.19a}$$

$$Z_{DFIGq}(s)=\frac{G_{rq}(s)G_{Gq}(s)}{G_{rq}(s)+G_{Gq}(s)} \tag{3.19b}$$

3.5.4 Impedance Modeling of Series Compensated Line

The impedance model of series compensated line is formulated as:

$$Z_L = R_L + sL_L + \frac{1}{Cs} \tag{3.20}$$

The bode diagram of series compensated line and DFIG for the Scenarios 2 and 3 are depicted in Figure 3-9 and Figure 3-10 respectively.

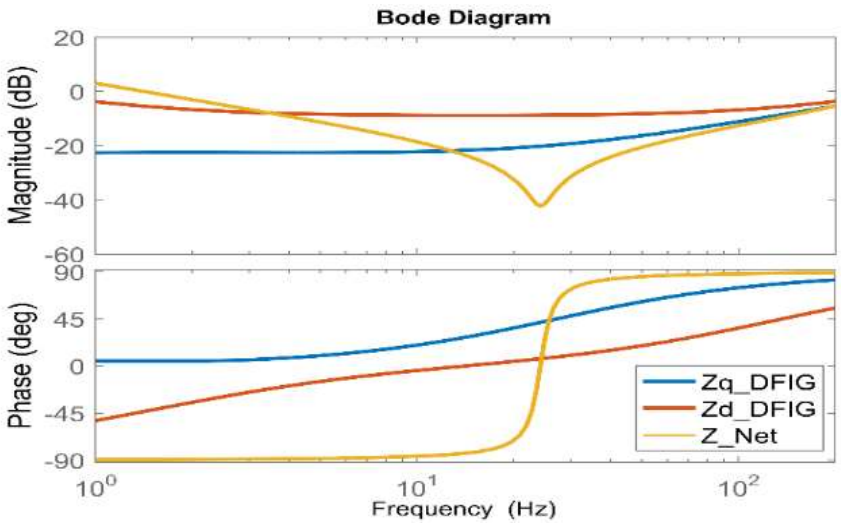

Figure 3-9 Bode diagram of DFIG and Network for PLL parameter SC2

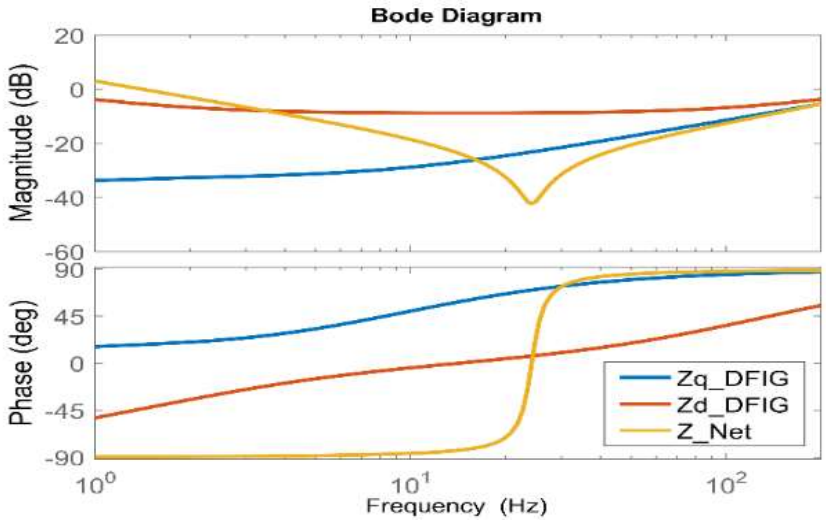

Figure 3-10 Bode diagram of DFIG and Network for PLL parameter SC3

As evident from Figure 3-9 and Figure 3-10, there is a distinct dip in series compensated network with 70% of compensation at 24.1 Hz. This is the resonant frequency of the transmission system which can be calculated as:

$$f_{net} = 60\sqrt{\frac{X_c}{X_L}} \tag{3.21}$$

Here X_L is total reactance of network including collection system, station transformer and transmission line. The relation between sub-synchronous resonant frequency and f_{net} can be given as below [6].

$$f_{SSCI} = 60\sqrt{\frac{X_c}{X_L + X_{DFIG}}} \leq f_{net} \tag{3.22}$$

Where X_{DFIG} is, the total reactance observed from terminal of DFIG and includes rotor and stator reactance of DFIG, grid side filter and control system [6].

The extracted decoupled formulation of sub-synchronous impedance shows that the PLL closed loop impedance mainly affects the *q* component of DFIG impedance. In this regard, as it can be seen in the Figure 3-9 and Figure 3-10 for the range of Sub-synchronous frequency oscillation which is *f<24.1*, by utilizing faster PLL parameters the phase response of DFIG *q-axis* impedance (blue line) increase toward 90 degrees and this results in a decrease in the phase margin between Z_{DFIGq} and network. The smaller the phase margin, the higher the chance of SSCI instability. As expected the results from Impedance modeling is also in tune with Eigenvalues and transient simulation results.

3.6 Conclusion

A unique *d-q* state space modeling methodology that aims to include the dynamic of PLL in detail *d-q* state-space model of DFIG has been presented. Using the proposed modeling approach, the impact of PLL control loop on SSCI is investigated through Eigenvalue analysis and time domain transient simulation. The Eigenvalue analysis results show that faster PLL parameters lead to larger negative damping which exacerbate the risk of SSCI. To further corroborate the modeling approach and findings, the *d-q* impedance model of DFIG consisting of proposed PLL closed loop transfer function is developed for different PLL parameters. In line with Eigenvalue analysis and transient time domain simulation results, impedance analysis shows that faster PLL parameters lead to lower phase margin and higher SSCI risk.

Chapter 4

Sub-Synchronous Oscillation Detection

4.1 Introduction

Sub-Synchronous Control Interaction (SSCI) is the result of energy exchange between power electronic based control systems and series-compensated lines within a sub-synchronous frequency range, usually 5-55Hz in a 60Hz system [4]. SSCI mainly manifests in wind generation resources (WGRs) connected in the vicinity of series-compensated lines in the transmission system. This phenomenon is well documented for wind farms and solar plants [1]-[12] and real-life incidents have been observed in the Electric Reliability Council of Texas (ERCOT) grid and in China power grid [5], [6]. SSCI oscillation introduced by High-Voltage Direct Current (HVDC) systems and voltage source converters is investigated in [44], [46][45]. While the presence of series-compensated lines increases the likelihood of the SSR, the incidence of SSR in the absence of series compensated lines has also been discussed in literature [46]. The higher the penetration of power electronic based control systems in power systems, the higher the risk of SSCI incidents.

One of the main challenges during the occurrence of SSCI is detection of undamped oscillations taking into account protection reliability and system security. Furthermore, unlike torsional interaction SSR, SSCI is a purely electrical

event and grows very fast within a few hundreds of milliseconds and can cause substantial damage to turbines and transmission elements [47], [48]. Hence, there is urgent need for effective mechanisms to detect and mitigate SSCI in a quick and reliable manner.

An SSCI detection approach based on the Fast Fourier Transform (FFT) and Discrete Time Fourier Transform (DTFT) is introduced in [49]. However, the proposed algorithm relies on a single method and has only been tested for one operating condition. Also, the results show the presence of a few oscillations in the detected amplitude that may impact the overall performance of the proposed detection in other conditions. An innovative approach for SSR detection is proposed in [50]. In this method, the envelope of the SSR signal is being utilized to separate the SSR oscillation from the synchronous power signal. However, the author also argues that this approach can result in satisfactory performance only for specific sub-synchronous frequency range. A custom logic-based digital filter and detection system is introduced in [51]. While this solution provides flexibility for implementation in user-programmable relays, two main drawbacks can still be observed: 1) high memory usage of the user logic in the relay; 2) logic adjustments vary by relay internal code. Another approach utilizes the damping ratio for monitoring of torsional SSR signals in conventional generation [52]. This includes ringdown analysis-based algorithms to calculate the frequency and damping of SSR signals. In addition, [52] uses window lengths of 200ms for each processing cycle

resulting in the detection time of around 350ms after fault clearing. A combination of artificial neural network and wavelet transform is proposed in [53]. However, the detection times and realization of the algorithm have not been discussed.

This work proposes an SSCI detection algorithm based on the combination of time-domain and frequency-domain techniques. Two modal identification approaches, namely Prony and Eigensystem Realization Algorithm (ERA), and a moving FFT are used. The three methods work independently and simultaneously monitor the frequency, magnitude and derivative of the magnitude of the input signal. Their parallel operation ensures the detection of undamped SSCI oscillations within an acceptable time frame while preventing misoperation. One of the main challenges associated with these algorithms is the preprocessing of the input signal (i.e. the measurements) to remove the synchronous frequency mode and other unnecessary modes from the input signal. To overcome this issue, a comprehensive SSCI analysis based on frequency scan and electromagnetic transient (EMT) simulations is proposed to identify and extract the expected range of SSCI frequency for any renewable resources. The frequency range with an acceptable margin can be used to enhance the filtering of the input signal in pre-processing block. The preprocessed signal will then allow the application of shorter window lengths for each processing cycle of the algorithm, in this case 45ms, enabling faster detection times while maintaining accuracy. As an illustrative example and in order to validate the proposed approach, a 200MW wind farm

connected to a portion of the ERCOT grid with high penetration of renewable resources is considered to simulate the SSCI phenomenon. The measured signal, active power, from a detailed EMT simulation of the grid was injected to a real-time target device to test the algorithm under real-time conditions.

4.2 Mode Identification Methods (Prony & ERA)

Modal analysis techniques basically utilize system outputs to extract the frequency and magnitude of the signal modes. These methods have the following advantages [48], [54]:

- They are not restricted by the system size and system size reduction is not required for the analysis;
- Any standard time-domain output of the system can be utilized for the study;
- The estimated order for any signal can be lower than the original one while retaining the dominant modes;
- Triggering time of event can be captured.

4.2.1 Prony Method

Any recorded standard output of system including N samples which are evenly spaced by amount of Δt can be represented as below [54]:

$$\hat{P}(t) = \sum_{i=1}^{n} r_i P_{i0} e^{\lambda_i t} + = \sum_{i=1}^{n} A_i e^{\sigma_i t} \cos(\omega_i t + \theta_i) \tag{4.1}$$

Where *n* is the order of the system, r_i is the residue of mode *i*, P_{i0} is the influence of initial condition and λ_i is the mode *i* of state transition matrix, A. The Prony method directly estimate the parameters of exponential term by fitting a function to the recorded output of the system. In other word, it is polynomial method which reconstruct the signal based on the modal information of the signal. At sample t_k the recorded output, *P*, can be discretized as [54]:

$$\hat{P}(t) = \sum_{1}^{n} B_i z_i^k \tag{4.2}$$

Where, $z_i = e^{\lambda_i \Delta t}$ are the roots of polynomial characteristics of the system as follow:

$$z^n - (a_1 z^{n-1} + a_2 z^{n-2} + \ldots + a_{n-1} z^0) = 0 \tag{4.3}$$

Where the factors a_i are unknow and can be calculated from the measurement vector of the system.

Prony method includes the following steps [54].

Step 1: assemble the recorded data elements in to a Toeplitz matrix. A *Toeplitz matrix is a matrix with a constant diagonal in which each descending diagonal from left to right is constant* [54]. For measured vector with *N* sample and the estimated order of *n* the matrix can be represented as below:

$$T = \begin{bmatrix} P_{n-1} & P_{n-2} & \cdots & P_{n-n} \\ P_n & P_{n-1} & \cdots & P_{n-n+1} \\ \vdots & \vdots & \ddots & \vdots \\ P_N & P_{N-1} & \cdots & P_{N-n} \end{bmatrix} \& b = \begin{bmatrix} P_n \\ P_{n+1} \\ \vdots \\ P_N \end{bmatrix} \tag{4.4}$$

Step 2: fitting the recorded data with discrete linear estimated models such as least square [54]. Here pseudo-inverse is utilized to calculate the polynomial coefficients of the system.

$$(T^T T)^{-1} T^T b = \begin{bmatrix} a_1 \\ a_2 \\ \vdots \\ a_n \end{bmatrix} \tag{4.5}$$

Step 3: Solving the polynomial characteristic to find the system modes:

$$z^n - (a_1 z^{n-1} + a_2 z^{n-2} + \ldots + a_{n-1} z^0) = 0 \tag{4.6}$$

Step 4: considering the roots of previous step as the complex modal frequencies for the measured vector, find the amplitude and initial phase for all modes.

4.2.2 Eigen-System Realization Algorithm (ERA)

Eigen-System realization Algorithm (ERA) is another modal identification method which is based on the singular value decomposition of Hankel matrix associated with linear ring-down of the system. This method consists of the following Steps [54].

Step 1: forming the Hankel matrix for the measured output of the system.

$$H_0 = \begin{bmatrix} P_0 & P_1 & \cdots & P_r \\ P_1 & P_2 & \cdots & P_{r+1} \\ \vdots & \vdots & \ddots & \vdots \\ P_r & P_{r+1} & \cdots & P_{N-1} \end{bmatrix} \tag{4.7}$$

$$H_1 = \begin{bmatrix} P_1 & P_2 & \cdots & P_{r+1} \\ P_2 & P_3 & \cdots & P_{r+2} \\ \vdots & \vdots & \ddots & \vdots \\ P_{r+1} & P_{r+2} & \cdots & P_N \end{bmatrix} \tag{4.8}$$

Where, $r = \frac{N}{2} - 1$.

Step 2: performing singular value decomposition of H_0. In this formulation, the singular value decompositions are divided into two components based on their relative size of singular values [54].

$$H_0 = U\ S\ V^T = \begin{bmatrix} U_n & U_z \end{bmatrix} \begin{bmatrix} S_n & 0 \\ 0 & S_z \end{bmatrix} \begin{bmatrix} V_n^T \\ V_z^T \end{bmatrix} \tag{4.9}$$

where, S_n and S_z are diagonal matrices which their elements are ordered by magnitude [54].

$$S_n = diag(\sigma_1, \sigma_1, \ldots, \sigma_n) \tag{4.10}$$

$$S_z = diag(\sigma_{n+1,}\sigma_{n+2,},\ldots,\sigma_N) \tag{4.11}$$

$$\sigma_1 > \sigma_2 > \cdots > \sigma_n > \sigma_{n+1} > \cdots > \sigma_N \tag{4.12}$$

Step 3: Calculating state space transition matrix as below:

$$A = S_n^{-0.5} U_n^T H_1 V_n S_n^{-0.5} \tag{4.13}$$

Step 4: calculating the eigenvalues of matrix A and reconstructing the signal.

4.3 Proposed Detection Algorithm

The detection algorithm consists of three parallel methods (Prony, ERA and moving FFT) which are working independently. Any output of windfarm such as active power, voltage or current can be considered as the input signal for all three methods. The flow chart of the proposed SSO detection algorithm is depicted in Figure 4-1. The proposed detection algorithm comprises three main blocks, namely preprocessing block, monitoring block and decision-making block. Successful and precise performance of these algorithms are highly dependent on the quality of the preprocessed signal. Therefore, as the first step of this design, a comprehensive sub-synchronous resonance analysis is executed on the proposed wind farm to determine the risk of SSCI/IGE, expected sub-synchronous resonant frequency range and also the system damping for frequency of interests. The outputs from this study are then used to tune the preprocessing filter and also to set the decision-

making threshold. The details regarding the sub-synchronous oscillation analysis approach and detection blocks are elaborated in the following subsections.

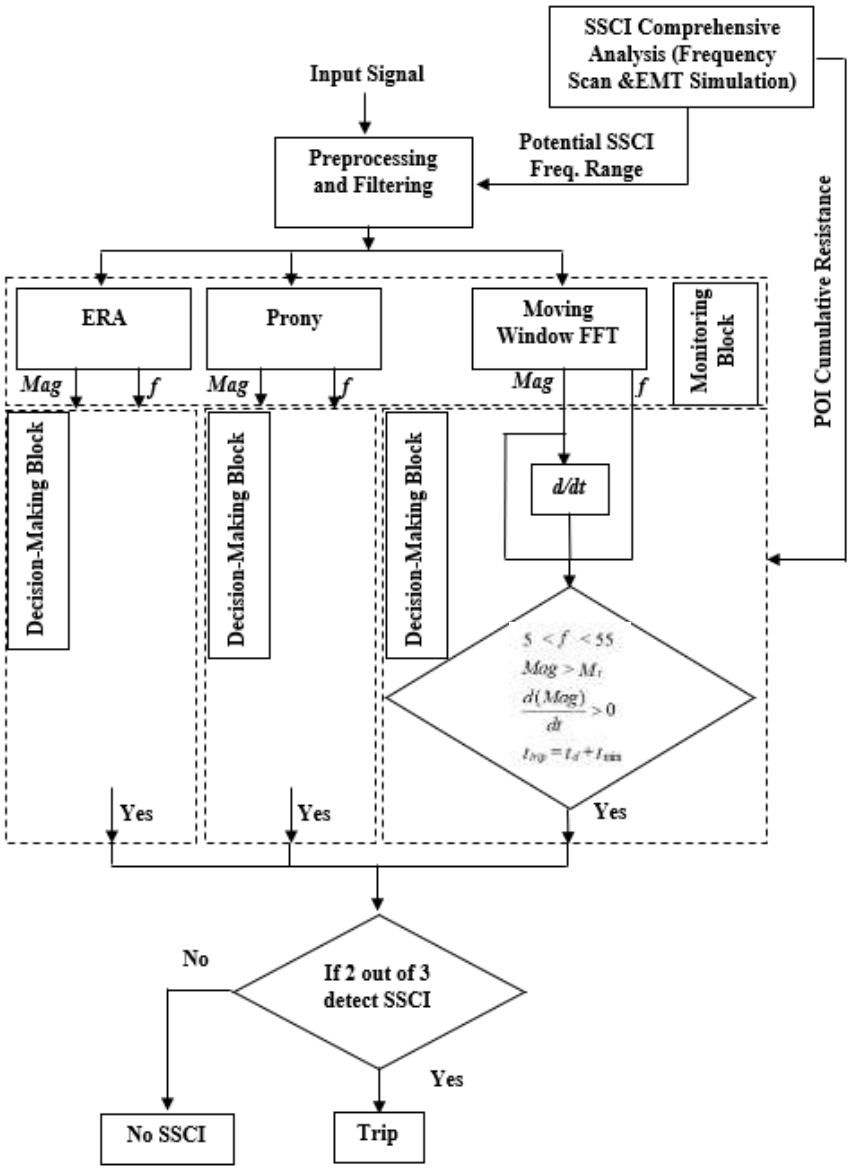

Figure 4-1 Flow chart of SSO detection algorithm

4.3.1 SSO Analysis (Frequency Scan & EMT Simulation)

Frequency scan is a strong tool to evaluate the risk of SSCI and also to estimate the sub-synchronous resonant frequency. Frequency scan provides the characteristic impedance of the wind farm and of the transmission system as a function of frequency. For the SSO screening, we perform separate frequency scans on the wind farm and on the transmission system sides from the point of interconnection (POI), as depicted in Figure 4-2.

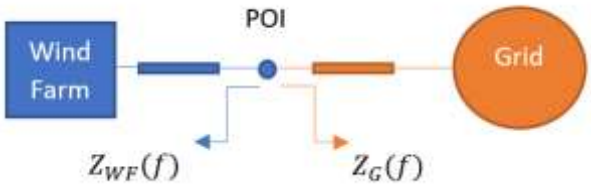

Figure 4-2 Wind farm connected to grid through a POI

For the frequency range of 5-55 Hz in a 60 Hz system;

$$Z_{WF}(f) = R_{WF}(f) + jX_{WF}(f) \tag{4.14}$$

$$Z_G(f) = R_G(f) + jX_G(f) \tag{4.15}$$

The results of the wind farm frequency scan in conjunction with the grid side frequency scan are used to calculate the cumulative resistance and reactance over the entire range of sub-synchronous frequency. The cumulative resistance at a cross-over frequency (zero reactance) is an index of SSCI risk [4]. To find the cross-over frequency (resonant frequency), we define:

$$R_{Cumulative}(f) = R_{WF}(f) + R_{G}(f) \tag{4.16}$$

$$X_{Cumulative}(f) = X_{WF}(f) + X_{G}(f) \tag{4.17}$$

f_{Co} is considered the cross-over frequency if:

$$X_{Cumulative}(f_{Co}) = 0 \;\&\; d(X_{Cumulative})/df > 0 \tag{4.18}$$

In other words, the zero-reactance frequency while reactance is crossing the frequency axis from negative to positive is considered the cross-over frequency [11]. Here, cumulative resistance represents the damping of the system at the resonant frequency.

If $R_{Cumulative}(f_{Co}) \leq 0$ or marginally positive, then there is SSCI risk and,

$f_{Co} = f_{ssr}$.

Hence, in the first step, the results of the frequency scan can be used to comment on the need for a detection algorithm. However, as it was mentioned earlier, the frequency of oscillation and corresponding damping are not fixed and can be affected by various system operating condition. In this regard, a sensitivity analysis around the operating condition of wind farm and transmission system is performed to determine the range of sub-synchronous resonance for possible incident.

Wind farm side scans will be performed across the following conditions:

- Varying active power dispatch levels for the project
- Varying number of turbines assumed to be online

On the system side, the characteristic impedance of the transmission system can significantly be affected by the compensation level of series-compensated lines and the status of switch shunts between the POI of the wind farm and the series-compensated line of interest. Therefore, a sensitivity analysis with different compensation levels and statuses of switch shunts is required to be performed.

Performing a comprehensive frequency scan screening for all above-mentioned scenarios provides valuable input for the SSCI detection algorithm. These outputs include the range of sub-synchronous resonant frequencies and corresponding damping factors. These data are very critical for the preprocessing and decision-making blocks of the detection algorithm. Therefore, it is highly recommended to validate the results of frequency scans by performing a detailed EMT simulation for the all scenarios. It is expected that the results from the EMT simulation match with the ones from the frequency scan analysis. Detail of different scenarios of operation are elaborated in the case study.

Next subsections elaborate the application of frequency scan results in preprocessing and decision-making block.

4.3.2 Pre-Processing Block

The pre-processing block includes three functions:

1) d-q transformation: This block is used to remove the power frequency from the measured signals such as POI current and voltage. This function is bypassed, If the input signal does not include 60 Hz (such as active power).

2) Recursive DC blocker: The use of the active power as the input signal leads to a presence of a main DC component instead of a 60Hz component in the processed signal. This filter is used to remove the DC component in a very fast rate.

3) Butterworth bandpass filter: This filter eliminates high order harmonics, noise and other unwanted frequencies outside the range defined after the frequency scan screening step. A first-order Butterworth filter is able to provide the necessary roll-off at the same time that it prevents over-delays and magnitude distortion in the frequency range of interest.

4.3.3 Monitoring Block

As shown in Figure 4-1, this block utilizes three parallel and independent methods to monitor the frequency and magnitude of the SSCI mode under real-time conditions. A moving window is refreshed for every input sample for all methods. Two of the algorithms, Eigensystem Realization Algorithm (ERA) and Prony, are modal analysis techniques that process system outputs to extract the frequency and magnitude of the signal modes.

The third algorithm is a moving-window FFT, which is able to capture the frequency and magnitude of the SSCI signal in every refreshing window. While FFT has a very good frequency determination, it does not have the time localization capability. However, by implementing the windowing FFT the algorithm can capture the time when the SSCI mode start the oscillation. The input/output and features of monitoring is summarized in Figure 4-3.

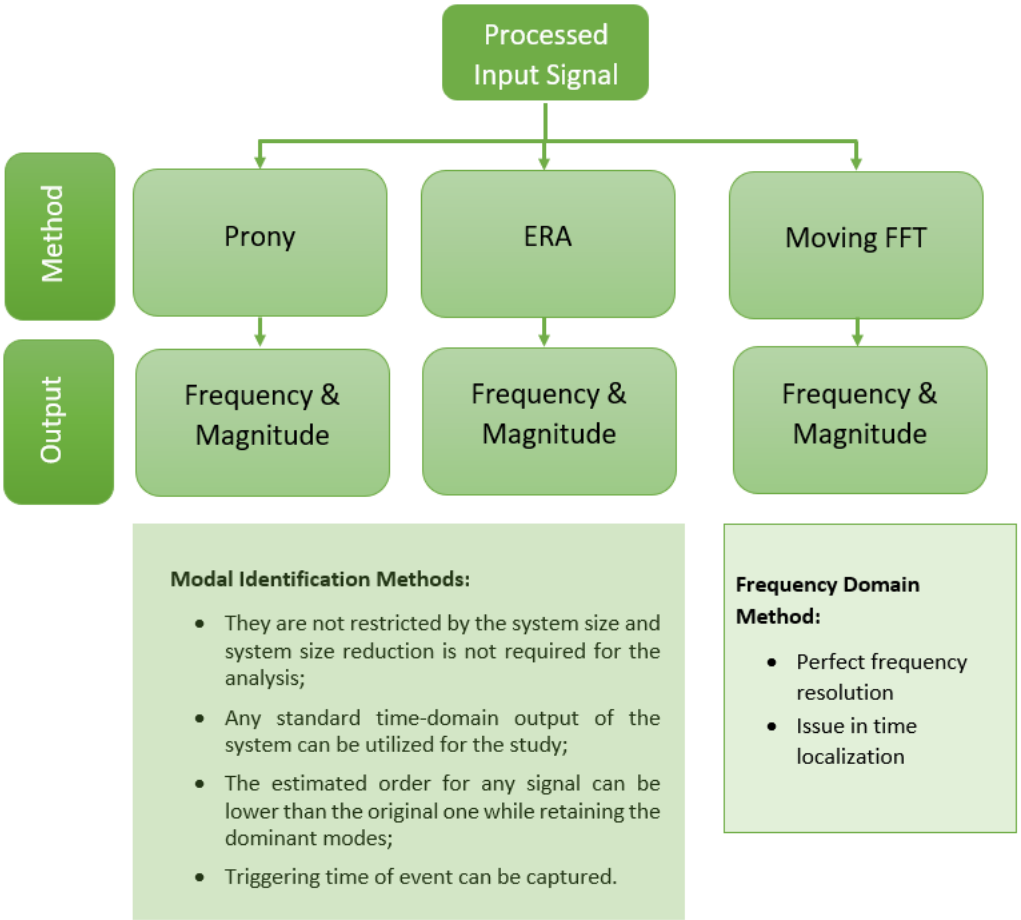

Figure 4-3 Monitoring Block characteristic

The outcomes of the monitoring block, i.e. magnitude and frequency, serve as inputs for the decision-making block. Figure 4-1 shows the details only in the FFT sub-block due to space limitations, but the same method is applied in the ERA and Prony decision-making blocks.

4.3.4 Decision-Making Block

The decision-making block evaluates the frequency and magnitude captured in the online monitoring section. Three criteria should be fulfilled to detect an undamped SSCI oscillation. These constraints are listed as below:

1) Frequency range: The captured frequency should be within the sub-synchronous frequency range, which normally is considered as 10% to 90% of the nominal frequency. In this work, for a 60Hz system, the interval is considered as 5-55Hz.

2) Magnitude of Oscillation: A threshold (M_t) is considered for the magnitude of oscillation. This threshold depends on the cumulative resistance (damping) of the plant and transmission system at the resonance frequency. The larger the negative damping, the larger the threshold that can be selected. The cumulative frequency scan results of the plant and transmission system at the point of interconnection can be utilized to set M_t.

3) Derivative of Magnitude: To issue the trip signal we need to make sure that the sub-synchronous oscillation is undamped. In order to check this constraint,

the derivative of magnitude is calculated in every window. A positive derivative represents a growing oscillation.

4) Minimum Detection time: The three methods use a pre-specified number of samples to build the analyzing window in each iteration. After the initiation of an SSCI event, a transition period containing both pre-SSCI and SSCI modes with a duration equal to the duration of the analyzing window is expected. Hence, in order to issue a reliable trip signal, a minimum detection time equal or greater than the transition period (i.e. analyzing window) is chosen to allow sufficient time for analyzing the measured signal, therefore preventing misoperation. Stated differently:

$$t_{trip} = t_d + t_{\min} \tag{4.19}$$

where: t_{min} is the minimum detection time equal or greater than analyzing window, t_d is the actual detection time of SSCI based on the decision-making criteria one to three, and t_{trip} is the total time to issue the trip command.

All methods output their own decision to the last criterion. In order to increase the reliability and prevent the mis-operation, if only at least two out of three methods detect an SSCI condition for the minimum detection time, the protection algorithm issue the trip signal. At the same time, different methods may

have different response times. Hence, not requiring all three methods to detect SSCI is also expected to reduce the detection time.

4.4 Implementation and Test of the Detection Algorithm on Real time Target Device and ERCOT Case Study

4.4.1 ERCOT Case Study

In order to test the proposed algorithm, the portion of the ERCOT grid with relatively higher penetration of wind generation which exports power through a series-compensated line is selected. The ERCOT grid portion is depicted in Figure 4-4. A 200MW wind farm is connected to the 345kV station #3 (POI) through 34.5kV/345kV step-up transformers and a gen-tie line. The impedance data relating to the collection system, transformers and gen-tie lines are given in Table 2-1 .

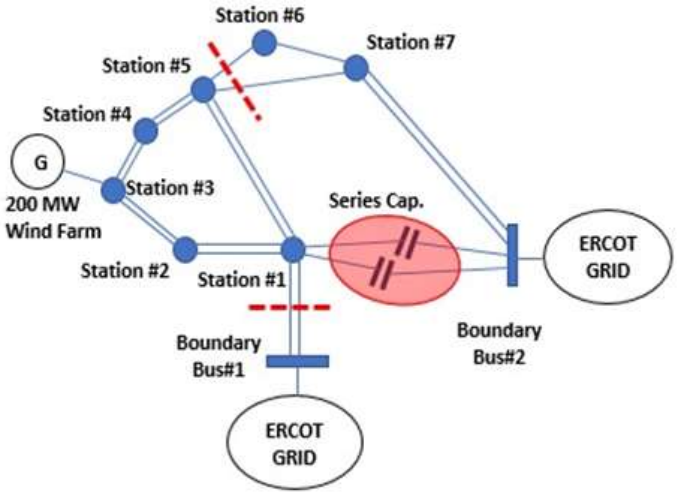

Figure 4-4 ERCOT grid portion with series compensated line

Any contingency that results in radial condition between the wind farm and the series-compensated line can lead to an SSCI event. For this portion of the ERCOT grid, N-4 is the minimum contingency rank that can result in radial condition and SSCI risk. The N-4 contingency definitions which is considered for this study purpose is provided in Table 4-1.

Table 4-1 N-4 Contingency definition

Item	Element	From	To	Circuit No.
1	Transmission Line	Station #5	Station #6	Circuit #1
2	Transmission Line	Station #5	Station #7	Circuit #1
3	Transmission Line	Station #1	Boundary #1	Circuit #1
4	Transmission Line	Station #1	Boundary #1	Circuit #2

The pictorial definition of this contingency is shown by dashed red lines in Figure 4-4 In this situation, the only path to export the wind farm power from the selected ERCOT grid portion is the series-compensated line between station #1 and boundary bus #2.

4.4.2 Detail SSCI Analysis

As a first step of the detection scheme design, a comprehensive frequency scan is performed to extract the sub-synchronous resonant frequency range and corresponding damping of the case study at the POI (Station #3). In order to have wide-ranging assessment on SSCI susceptibility of the wind farm and determination of frequency range, the following scenarios are considered for the frequency scan of the wind farm side and transmission system side.

The wind farm side frequency scan scenarios are:

- All turbines are in service (100% turbines) and the wind farm with 100% dispatch;
- All turbines are in service (100% turbines) and the wind farm with 10% dispatch (situation when wind speed drops);
- 10% of turbines are in service and they are in 100% dispatch (this situation occurs during the startup of the wind farm).

For the transmission side a sensitivity analysis with different compensation levels and statuses of switch shunts are performed as follows:

- Different compensation levels of the transmission system;
- Transmission system with all switch shunts in service;
- Transmission system with all switch shunts out of service.

In this case, the series capacitor has only one stage. So, there is no scenario around the compensation level of series capacitor. The cumulative scan results are depicted in Figure 4-5 and the summary of the resonant frequency and associated damping at the POI for different scenarios of operation are provided in Table 4-2.

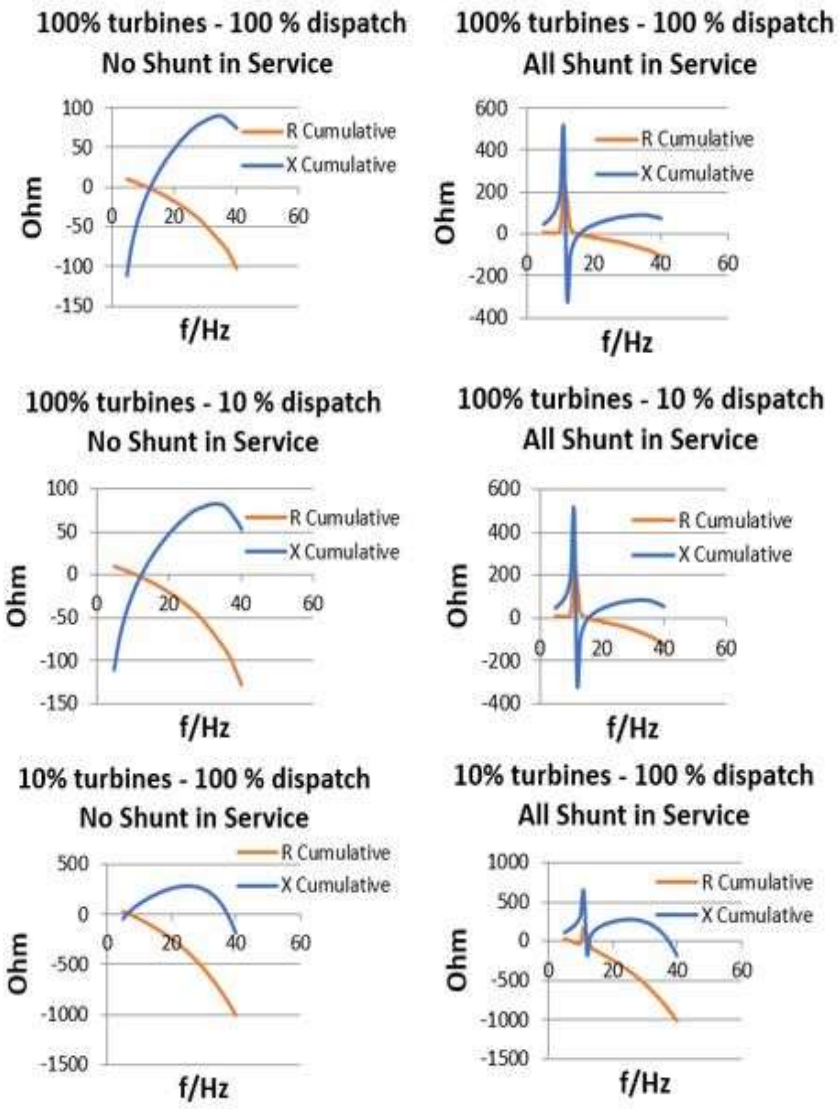

Figure 4-5 Cumulative frequency scan results at POI

Table 4-2 Frequency scan results for different operational conditions of wind farm and transmission system

Wind Farm Operation Scenario	Transmission Side Scenario	Cross-over Frequency for Cumulative X (Hz)	Cumulative R (Ohm)	Observation
100% turbines at 100% Dispatch	No Shunt	12	-2.75	Undamped SSCI
	All Shunt	15	-3.39	Undamped SSCI
100% turbines at 10% Dispatch	No Shunt	12	-4.24	Undamped SSCI
	All Shunt	15	-5.46	Undamped SSCI
10% turbines at 100% Dispatch	No Shunt	6	0.78	Damped Oscillation
	All Shunt	12	-67.4	Undamped SSCI

The frequency scan results are summarized as below:

- Negative cumulative resistance at the POI for different scenarios are indicative of severe SSCI concern for the proposed wind farm. Therefore, the SSCI protection scheme is required to avoid damage of turbines and the series capacitor;
- Table 4-2 shows that the SSCI resonant frequency can range from 6 Hz to 15 Hz for different scenarios of wind farm operation and status of switch shunts in the grid. This range of frequency with reasonable margin is utilized in the pre-processing block for the filters;
- All scenarios, except the scenario of 10% turbine with no shunt in service, show negative cumulative resistance at the cross-over frequency. These

negative damping factors are indicative of undamped SSCI oscillation for these scenarios;

- The marginally negative damping for the scenario of 100% turbines at 100% dispatch shows that for this scenario the SSCI grows more slowly compared to the other scenarios. Therefore, a small threshold is suggested for the decision-making block;
- The 10% turbine at 100% dispatch scenario with no shunts in service has a marginally positive resistance at the cross-over frequency, which leads to a damped oscillation.

Detailed Electro-Magnetic Transient (EMT) simulations are performed for all scenarios to validate the outcomes of the frequency scan analysis. EMT simulations are performed as per sequences outlined below:

- The transmission lines between stations #5 and #6 and stations #5 and #7 are assumed to be out of service for maintenance;
- Simulations are executed until 6 seconds, so that the steady state of the wind farm is achieved;
- In the case of simulations with no faults applied, a double-circuit line between station #1 and the boundary bus #1 is tripped at 6.065 seconds as per the contingency definition;

- In the case of fault-based simulations, a solid three-phase-to-ground fault is applied on the transmission system at 6 seconds and the double-circuit line between station #1 and boundary bus #1 is tripped in 4 cycles to clear the fault. As per the contingency definition this trip leads to a radial condition.

The active power and FFT results for all scenarios are shown in Figure 4-6 to Figure 4-8. In accordance with the frequency scan results, the EMT simulation outcomes also confirm the occurrence of SSCI and the frequencies of oscillation captured by FFT match with the frequency scan results.

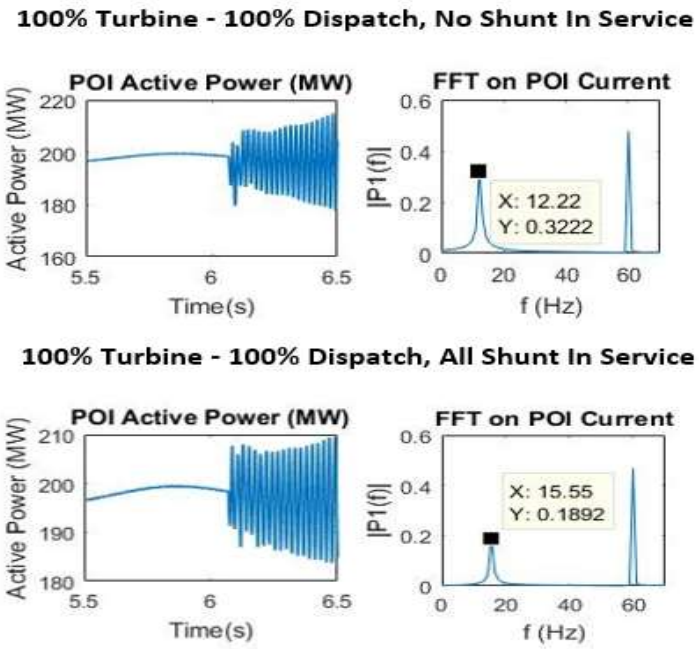

Figure 4-6 EMT Simulation results for 100% turbines at 100% dispatch

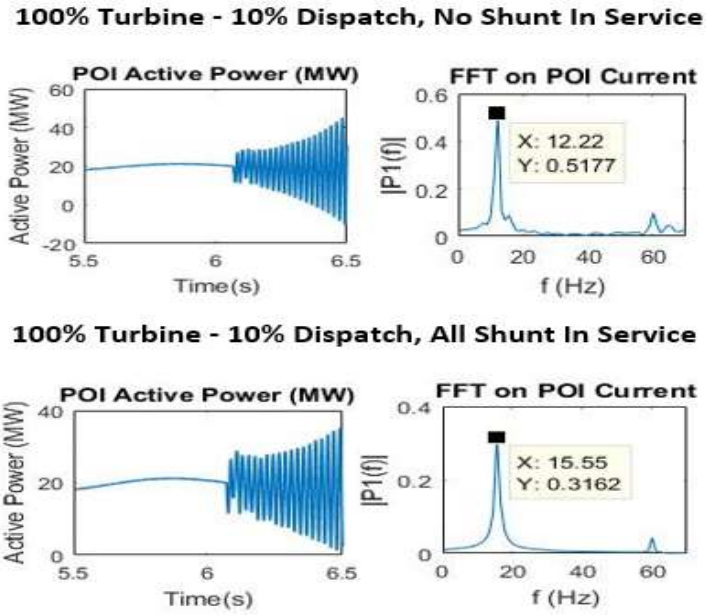

Figure 4-7 EMT Simulation results for 100% turbines at 10% dispatch

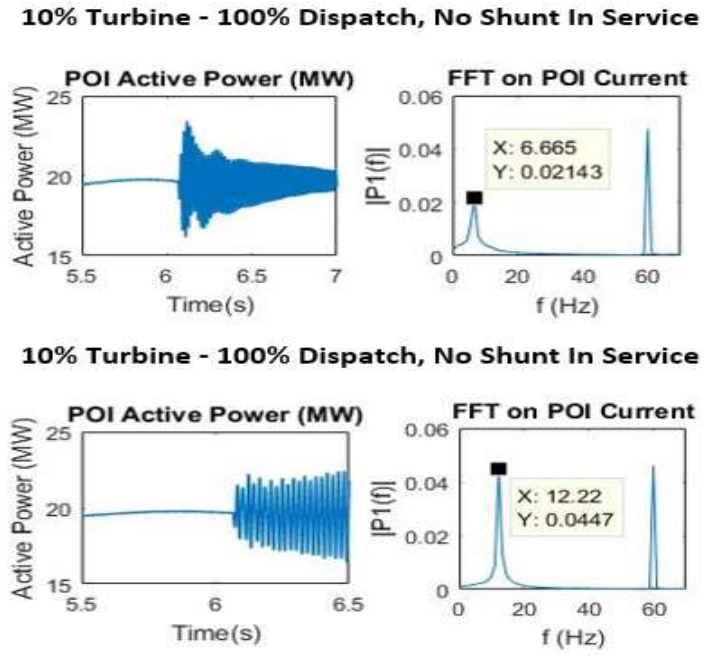

Figure 4-8 EMT Simulation results for 10% turbines at 100% dispatch

4.4.3 Real-Time Target Device

The algorithm was implemented in a real-time device with a 1.91 GHz quad-core processor, 16GB nonvolatile storage, and 2GB DDR3 memory [55], as shown in Figure 4-9. With a real-time device, we are able to achieve determinism due to time constraints in real-time operation. According to the Nyquist criterium, the sampling rate needs to be at least two times the highest detectable frequency. A 55Hz highest desired frequency would result in a minimum of 110 samples per second. A sampling rate of 1000 per second is used herein, which provides better accuracy in the sub-synchronous range of frequency, while not overloading the processor and maintaining time determinism. All three detection methods use a 45ms window as to provide good accuracy also without overloading the processor, and the window is updated every new sample received.

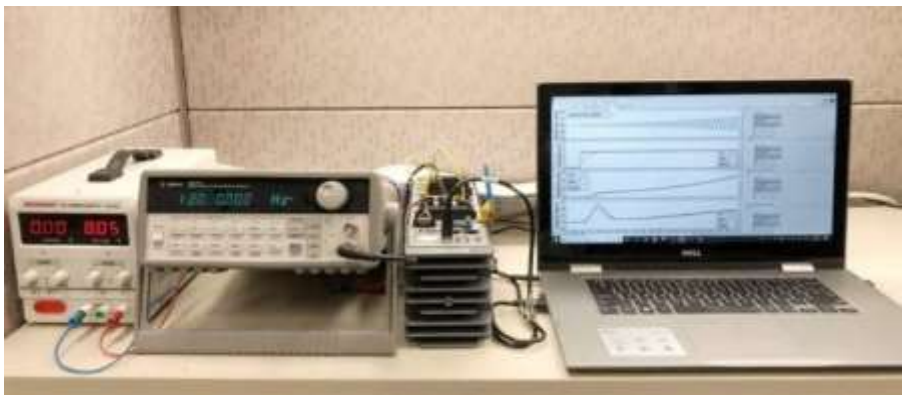

Figure 4-9 Laboratory setup with the real-time device where the algorithm was tested

The hardware realization of the proposed method is depicted in Figure 4-10.

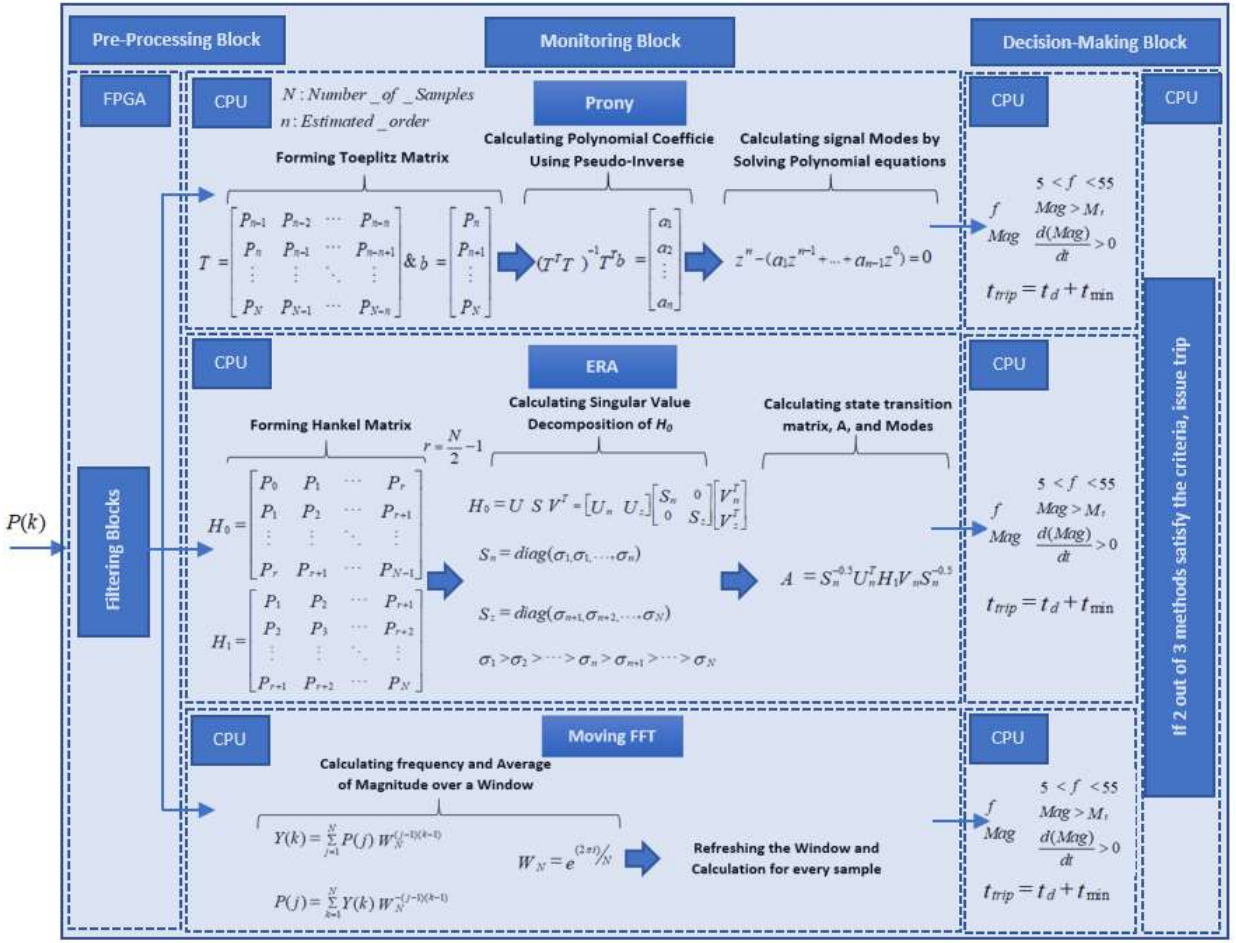

Figure 4-10 Hardware realization of proposed algorithm

4.4.4 Real-Time Target Simulation Results

The 100% turbines at 100% dispatch scenario for both all shunt and no shunt operating conditions is utilized to test the algorithm. The capability and performance of the proposed method was tested under real-time operating condition in the monitoring and detection modes. Finally, the algorithm is also tested under fault-based conditions. The details of scenarios and simulation steps for no-fault/fault-based situations were elaborated in the EMT simulation section.

1) Monitoring Mode: in this mode, the trip unit is disabled, and the algorithm is just monitoring the active power of the wind farm as an input signal. This mode is introduced to show the resolution of the proposed algorithm on capturing the SSCI frequency, magnitude and derivative of the magnitude. The active power of the wind farm, SSCI frequency, magnitude of the SSCI signal and its derivative are captured by the detection algorithm, being depicted in Figure 4-11 and Figure 4-12, for the cases of 100% turbines and 100% dispatch, with no shunts connected and all shunts connected, respectively.

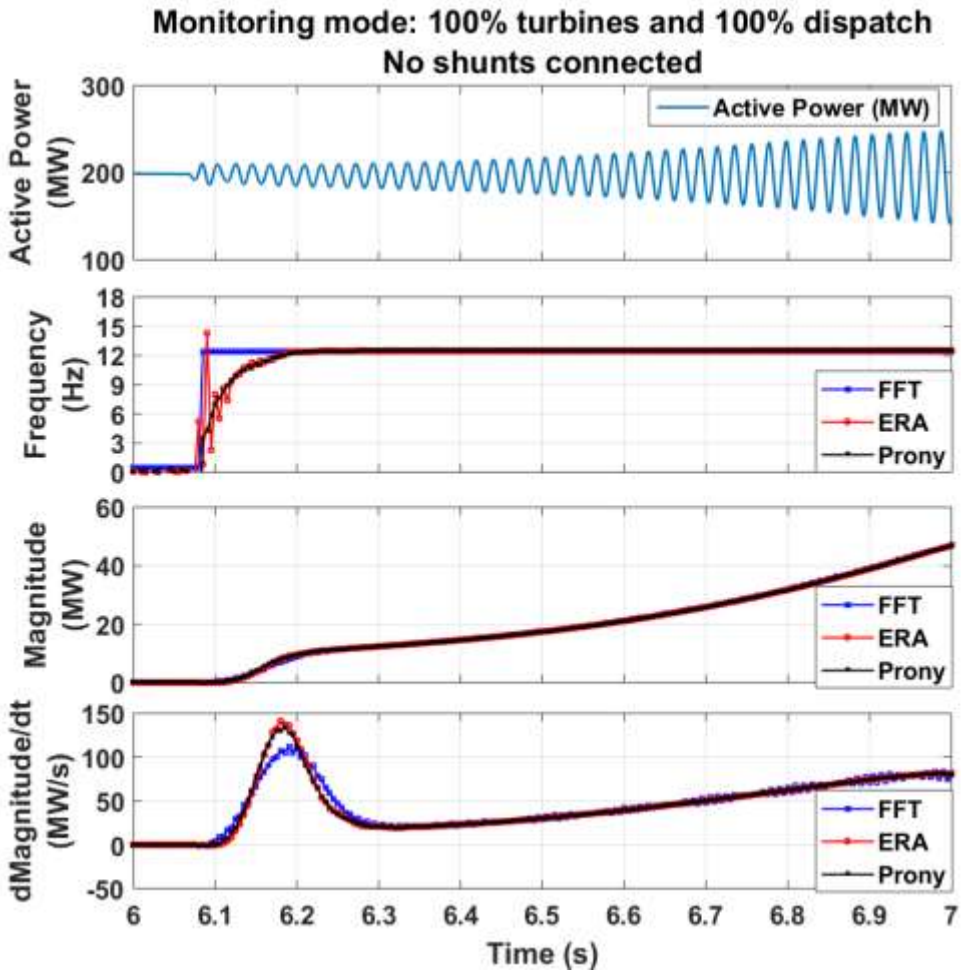

Figure 4-11 Monitoring mode – no shunts: active power; frequency, magnitude and its derivative for time-domain and frequency-domain algorithms.

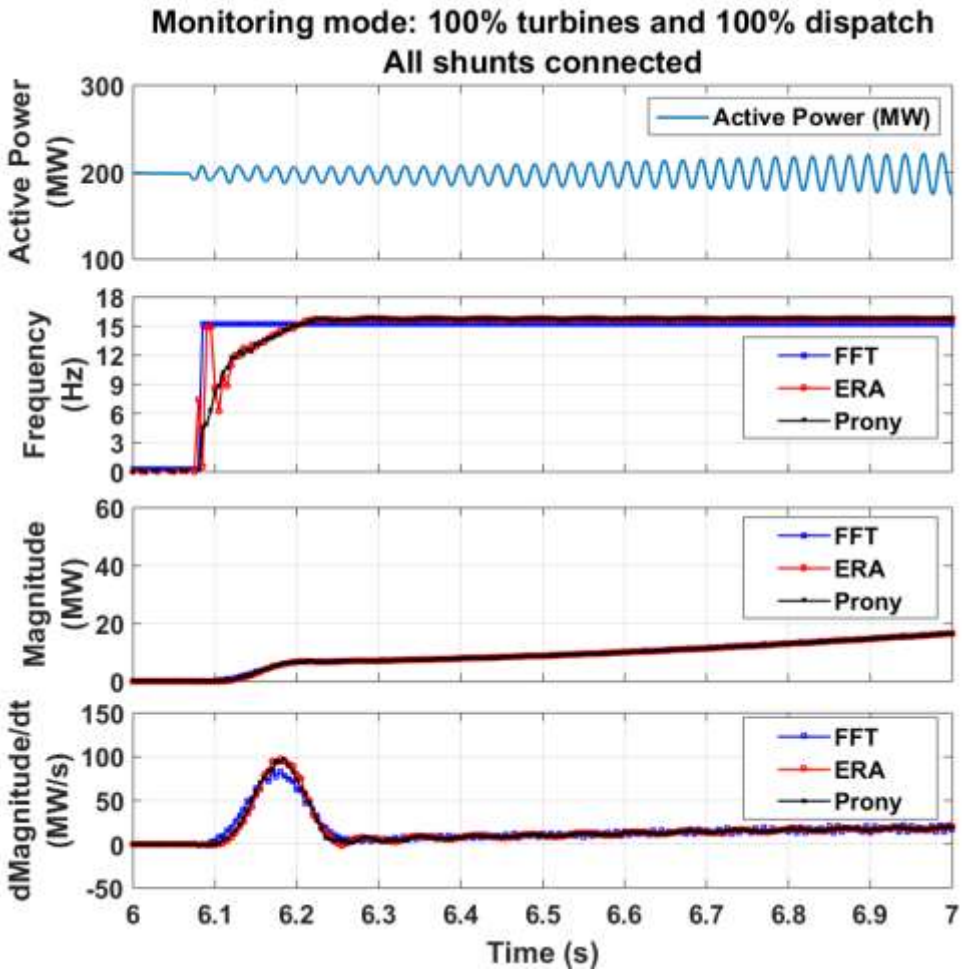

Figure 4-12 Monitoring mode – all shunts: active power; frequency, magnitude and its derivative for time-domain and frequency-domain algorithms

Profound analysis of the results clarifies the following points:

- The radial condition between wind farm and series compensated line occurs at t=6.065 s. So, the output of the monitoring block before this time is zero for all three algorithms;
- A transition period is observed right after the start of the phenomenon for close to 45ms, which is the window size. During this period, the signal includes the SSCI mode and pre-SSCI modes, so we can observe some transients in the captured frequency. However, gradually, with the increase of the energy of the SSCI mode, which becomes dominant, the outcomes of all three methods get aligned and reach the same value of frequency and magnitude;
- The frequency of oscillations is detected at 12 Hz and 15 Hz for the no-shunt and all-shunt scenarios, respectively. This is in line with the results of the frequency scan and EMT simulation;
- The calculated magnitude through Prony and ERA methods are almost a perfect match. Even though the response is different from the FFT method during the transition interval, all methods converge to the same solution;
- The positive derivative of magnitude assures the undamped SSCI and avoid unnecessary trip command for any SSCI mode with sufficient damping.

2) Protective Mode: In this mode, the trip unit is enabled, and the minimum detection time is set to 50ms. The results show that the proposed algorithm detects the undamped SSCI oscillation and issues the trip command in less than the desired 95ms time interval (analyzing window plus minimum detection time). Figure 4-13 and Figure 4-14 depict the SSCI frequency, SSCI mode amplitude and corresponding derivative.

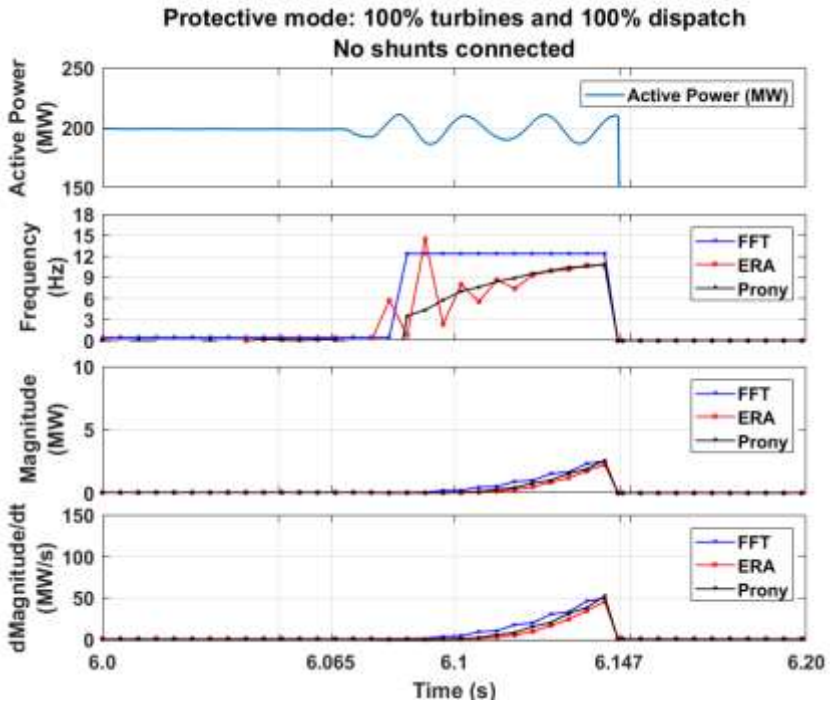

Figure 4-13 Protective mode – no shunts: active power; frequency, magnitude and its derivative for time-domain and frequency-domain algorithms.

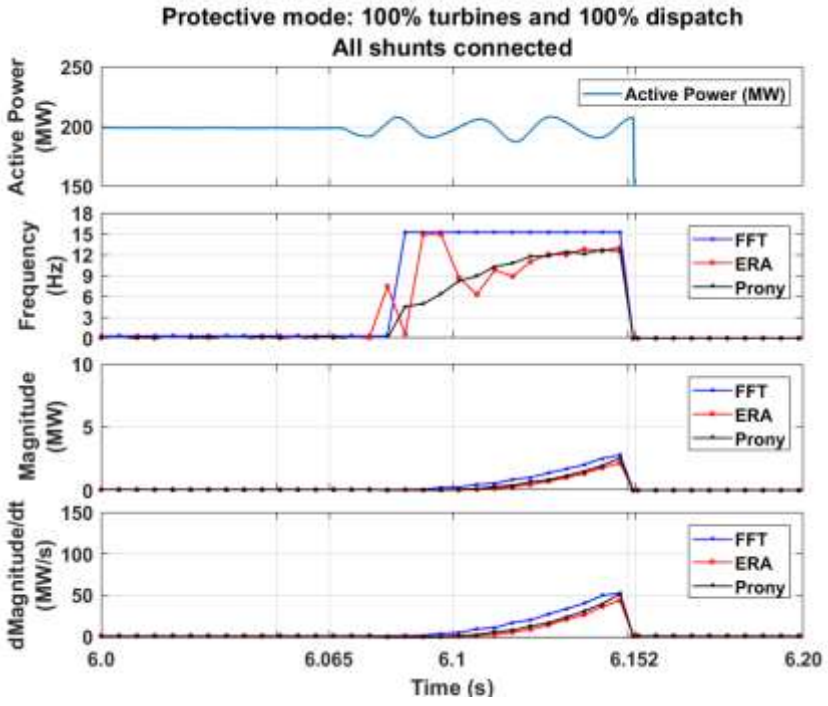

Figure 4-14 Protective mode – all shunts: active power; frequency, magnitude and its derivative for time-domain and frequency-domain algorithms.

As mentioned earlier, during a transition period equal to the window size, which is 45ms, SSCI mode has low energy and is not the dominant mode of the system. This transition phase mainly shows up in the calculated frequency. However, the transition quickly disappears as the SSCI mode gets stronger. The following notes should be taken into account for the protection mode.

- It can be seen that any of the single algorithms has the capability to detect the SSCI within the first 45ms, analyzing window after SSCI incidence. However, waiting for the three cycles from the criteria to trip makes the system more reliable. These three cycles, 50ms in this case, is enough to

stabilize the response of all three methods while not over-increasing the detection time;

- The detection time and trip time for no shunt and all shunt scenarios are as below:

  No shunt scenario: t_d =32ms and t_{trip}=82ms

  All shunt scenario: t_d =37ms and t_{trip}=87ms

- As it is evident, the moving FFT has better resolution and accuracy on the frequency of oscillation. Hence, the result of this method is suggested for the report of SSCI oscillation frequency.

3) Fault-Based Scenario: In this scenario, a solid three-phase-to-ground fault is applied in the vicinity of the POI at t=6s. The trip commend is issued within 4 cycles to open the double-circuit line between station #1 and boundary bus #1. This scenario is implemented to show the capability of the method to detect the SSCI under disturbances. The monitoring mode and detection mode results of no-shunt operating conditions under the fault are depicted in Figure 4-15 and Figure 4-16. The results indicate that the proposed algorithm can rapidly detect the SSCI under the fault -based scenario.

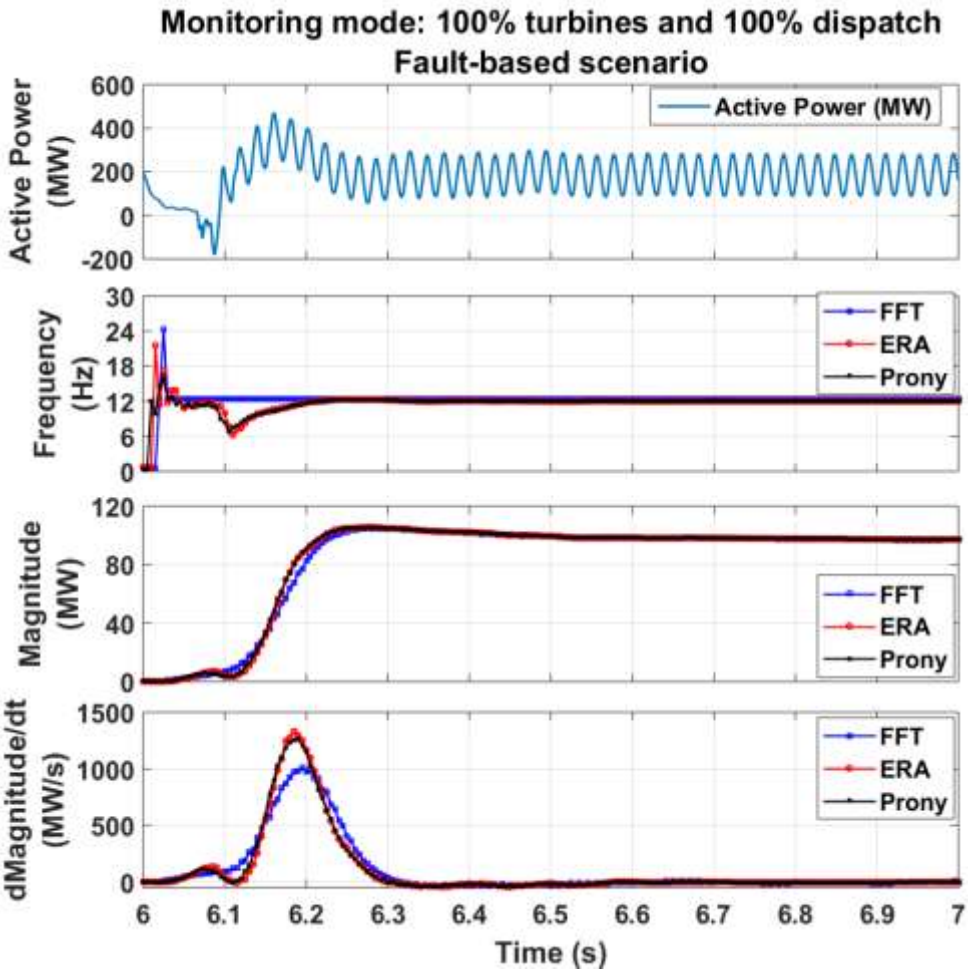

Figure 4-15 Fault base scenario monitoring – No shunts: active power; frequency, magnitude and its derivative for time-domain and frequency-domain algorithms

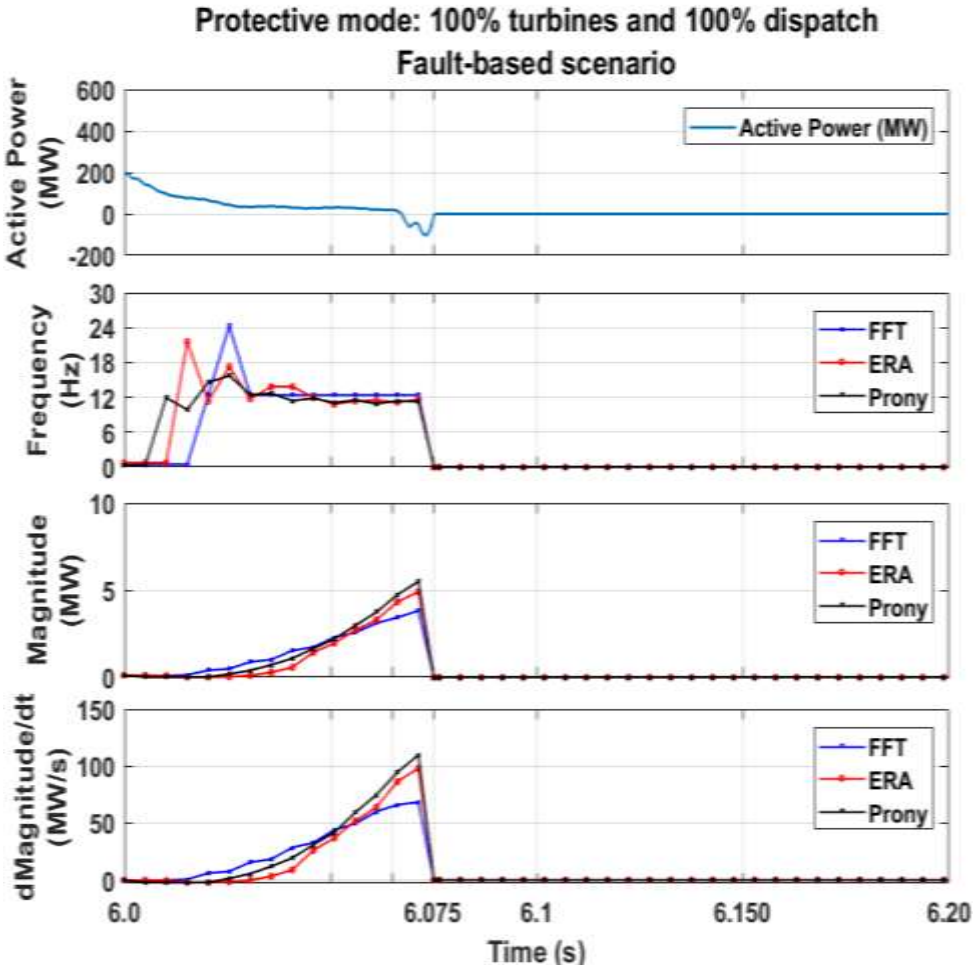

Figure 4-16 Fault base scenario detection – No shunts: active power; frequency, magnitude and its derivative for time-domain and frequency-domain algorithms.

The following discussion can be made about this scenario:

- The characteristic impedance of the network under the fault-based scenario cannot be estimated through frequency scan. Therefore, the fault-based scenarios should be evaluated by performing detailed EMT simulation;

- Compared to the no-fault scenarios, the magnitude of the SSCI oscillation is much larger and can lead to serious damage on transmission elements and leading to cascading outage;
- Contrarily to the no-fault condition, right after the fault and even before the line trips and radial condition happens, the SSCI mode is triggered and shows up in the system. The algorithm detects 12 Hz with very small magnitude between 6.025s and 6.05s. This proves that the proposed model is effective to even detect the SSCI while it has just been triggered with very low energy;
- Herein, the transition is observed at two points: one at the beginning, which is a result of the fault in the system, and the other at the faulted line tripping time, at t=6.065s. The plot shows that all three methods are robust and can quickly converge to the correct responses after any disturbance;
- In the fault-based scenario, the trip command is issued at an earlier time than in the no-fault scenario. The protective mode shows that the final trip is at 6.075s, which is 50ms after the SSCI mode is first being detected according to the detection criteria.

4.5 Conclusion

An innovative detection algorithm based on the combination of modal identification methods and moving FFT is proposed, which is able to detect the SSCI oscillation within 95ms. The algorithm was implemented in a real-time target device and was extensively tested with signals from EMT simulation of SSCI in the portion of ERCOT grid for different scenarios of system operation and conditions. The results show that the algorithm is capable to detect the frequency and magnitude of SSCI oscillation with remarkable accuracy within an acceptable time frame, even during a large disturbance in the system. Since there is trade-off between the number of parallel algorithms and the detection time, three parallel and independent methods of monitoring are utilized to guarantee the reliability of the proposed algorithm and avoid any false trip.

Chapter 5

Conclusion and Future Work

Recently, increasing penetration of renewable generation resources and power electronic based control devices has stunningly changed the dynamic of power system and consequently the grid code requirements. Complex and multi-layer controllers associated with renewable resources have introduced new challenges in transmission and distribution networks. One of these challenges is Sub-Synchronous Control Interaction (SSCI) which has received increasing attention by researchers in recent times. This research is aimed to address the detail modeling of DFIG with respect to SSCI phenomena and also propose an algorithm to reliably detect the SSCI and send the trip command.

Firstly, a unique *d-q* state space modeling methodology was proposed which allows for the inclusion of PLL dynamic in detail *d-q* state-space model of DFIG. Using the proposed modeling approach, the impact of PLL control loop on SSCI was investigated through Eigenvalue analysis and time domain transient simulation. The Eigenvalue analysis results show that faster PLL parameters lead to larger negative damping which exacerbate the risk of SSCI. To further corroborate the modeling approach and findings, the *d-q* impedance model of DFIG consisting of proposed PLL closed loop transfer function is developed for different

PLL parameters. In line with Eigenvalue analysis and transient time domain simulation results, impedance analysis shows that faster PLL parameters lead to lower phase margin and higher SSCI risk.

Moreover, an innovative detection algorithm based on the combination of modal identification methods and moving FFT is proposed, which is able to detect the SSCI oscillation within 45ms and generates reliable trip signal within 95ms. A comprehensive SSCI analysis is suggested to improve the preprocessing of the measured signal, this allows the application of shorter window lengths for each processing cycle of the algorithm, in this case 45ms, enabling faster detection times while maintaining accuracy. The algorithm was implemented in a real-time target device and was extensively tested with SSCI signal in the portion of ERCOT grid for different scenarios of system operation and conditions. The results show that the algorithm is capable to detect the frequency and magnitude of SSCI oscillation with remarkable precision within an acceptable time frame, even during a large disturbance in the system. Since there is trade-off between the number of parallel algorithms and the detection time, three parallel and independent methods of monitoring are utilized to guarantee the reliability of the proposed algorithm and avoid any false trip.

Future works may focus on evaluating the impact of nearby renewable generation resources on sub-synchronous interaction, possibility of SSCI for

HVDC lines and also development of a field-testing equipment to assess the risk of SSCI.

References

[1] J. Miller, M. B. Watson, J. Leighfield and PSC North America, " Review of series compensation for transmission lines," *Southwest Power Pool*, May. 2014.

[2] H. Liu, X. Xie, C. Zhang, Y. Li, H. Liu, Y. Liu, "Quantitative SSR analysis of series-compensated DFIG-based wind farms using aggregated RLC circuit model," *IEEE Trans. Power Systems*, vol. 32, no. 1, pp. 474-483, Jan. 2017.

[3] A. E. Leon, "Integration of DFIG-based wind farms into series-compensated transmission systems," *IEEE Trans. Sustainable Energy*, vol. 7, no. 2, pp. 451-459, Apr. 2016.

[4] H. K. Nia, F. Salehi, M. Sahni, N. Karnik and H. Yin, "A filter-less robust controller for damping SSCI oscillations in wind power plants," *2017 IEEE Power & Energy Society General Meeting*, Chicago, IL, 2017, pp. 1-1.

[5] L. Wang, X. Xie, Q. Jiang, H. Liu, Y. Li, Y. Li, H Liu, "Investigation of SSR in practical DFIG-Based wind farms connected to series compensated power system," *IEEE Trans. Power Systems*, vol. 30, no. 5, pp. 2772-2779, Sep. 2015.

[6] A. E. Leon, J. A. Solsona, "Sub-synchronous interaction damping control for DFIG wind turbines," *IEEE Trans. Power System*, vol. 30, no. 1, pp. 419-428, Jan. 2015.

[7] U. Karaagac, S. O. Faried, J. Mahseredjian, A. Edris, "Coordinated control of wind energy conversion systems for mitigation subsynchronous interaction in DFIG-based wind farms," *IEEE Trans. Smart Grid*, vol. 5, no. 5, pp. 2440-2449, Sep. 2014.

[8] P. Huang, M. S. El-Moursi, W. Xiao, J. L. Kirtley, "Subsynchronous resonance mitigation for series compensated DFIG-based wind farm by using two-degree-of-freedom control strategy," *IEEE Trans. Power Systems*, vol. 30, no. 3, pp. 1442-1454, May. 2015.

[9] P. Dattaray, D. Chakravorty, P. Wall, J. L. Kirtley, " A Novel Control Strategy for Subsynchronous Resonance Mitigation Using 11 kV VFD-Based Auxiliary Power Plant Loads," *IEEE Trans. Power Delivery*, vol. 33, no. 2, pp. 728-740, April. 2018.

[10] A. Moharana, R. K. Varama, R. Seethapathy, "SSR alleviation by STATCOM in induction-generator-based wind farm connected to series compensated line," *IEEE Trans. Sustainable Energy*, vol. 5, no. 3, pp. 947-957, Jul. 2014.

[11] F. Huang and J. Billo, " ERCOT nodal protocol for sub-synchronous resonance (NPRR562)," *ERCOT nodal protocols*, June. 2017.

[12] D. H. R. Suriyaarachchi, U. D. Annakkage, C. Karawita and D. A. Jacobson "A procedure to study sub-synchronous interactions in wind integrated power systems," *IEEE Trans. Power System*, vol. 28, no. 1, pp. 377-384, Feb. 2013.

[13] Y. Song and F. Blaabjerg, "Analysis of middle frequency resonance in DFIG system considering phase locked loop," *IEEE Trans. Power Electronic*, in press., Feb. 2017

[14] L. Fan, R. Kavasseri, Z. L. Miao, C. Zhu, "Modeling of DFIG-based wind farms for SSR analysis," *IEEE Trans. Power Delivery*, vol. 25, no. 4, pp. 2073-2082, Oct. 2010.

[15] H. Khalilinia, N. Karnik, H. Yin and M. Sahni, "Power system sub-synchronous oscillation damper," U.S. Patent 20 160 141 991, 2016.

[16] DAVARIKIA, Hamzeh, and Masoud BARATI. "A tri-level programming model for attack-resilient control of power grids." *Journal of Modern Power Systems and Clean Energy* (2018): 1-12.

[17] Znidi, Faycal, Hamzeh Davarikia, and Kamran Iqbal. "Modularity clustering based detection of coherent groups of generators with generator integrity indices." *In Power & Energy Society General Meeting*, 2017 IEEE, pp. 1-5. IEEE, 2017.

[18] Davarikia, Hamzeh, Faycal Znidi, Mohammad Reza Aghamohammadi, and Kamran Iqbal. "Identification of coherent groups of generators based on synchronization coefficient." *In Power and Energy Society General Meeting (PESGM)*, 2016, pp. 1-5. IEEE, 2016.

[19] Sharafi Masouleh, Mahmoud, Farshid Salehi, Fatima Raeisi, Mojtaba Saleh, Azade Brahman, and Abdollah Ahmadi. "Mixed-integer programming

of stochastic hydro self-scheduling problem in joint energy and reserves markets." *Electric Power Components and Systems* 44, no. 7 (2016): 752-762.

[20] Dehghanian, Pooria, Semih Aslan, and Payman Dehghanian. "Maintaining Electric System Safety through An Enhanced Network Resilience." *IEEE Transactions on Industry Applications* (2018).

[21] Dehghanian, Pooria, Semih Aslan, and Payman Dehghanian. "Quantifying power system resiliency improvement using network reconfiguration." *In IEEE 60th International Midwest Symposium on Circuits and Systems (MWSCAS)*, pp. 1-4. 2017.

[22] F. Salehi, A. Brahman, R. Keypour and Wei-jen Lee, "Reliability assessment of automated substation and functional integration," *2016 IEEE Industry Applications Society Annual Meeting, Portland*, OR, 2016, pp. 1-7.

[23] A. Sahami, R. Yousefian and S. Kamalasadan, "An approach based on potential energy balance for transient stability improvement in modern power grid," *2018 IEEE Power and Energy Conference at Illinois (PECI)*, Champaign, IL, 2018, pp. 1-7.

[24] F. Salehi, M. Sahni and W. Lee, "Arc Flash Study in large scale industrial plant with internal generation and complex interconnected network," *2017 IEEE IAS Electrical Safety Workshop (ESW)*, Reno, NV, 2017, pp. 1-1.

[25] R. Yousefian, A. Sahami and S. Kamalasadan, "Hybrid Transient Energy Function-Based Real-Time Optimal Wide-Area Damping Controller," in *IEEE Transactions on Industry Applications*, vol. 53, no. 2, pp. 1506-1516, March-April 2017.

[26] Y. Song and F. Blaabjerg, "Analysis of middle frequency resonance in DFIG system considering phase locked loop," *IEEE Trans. Power Electronic*, in press., Feb. 2017

[27] Y. Song, X. Wang, F. Blaabjerg, "High Frequency Resonance Damping of DFIG based Wind Power System under Weak Network," *IEEE Trans. Power Electron.*, vol. 32, no. 3, pp. 1927-1940, March 2017.

[28] I. Vieto, and J. Sun, “Small-Signal Impedance Modeling of Type-III Wind Turbine,” *in Proc. Power & Energy Society General Meeting* (PESG), pp. 1-5, 2015.

[29] I. Vieto, and J. Sun, “Real-time Simulation of Subsynchronous Resonance in Type-III Wind Turbines,” *in Proc. Control and Modeling for Power Electronics* (COMPEL), pp. 1-8, 2014

[30] J. Hu, Y. Huang, D. Wang, H. Yuan and X. Yuan, “Modeling of grid connected DFIG-based wind turbines for DC-link voltage stability analysis," *IEEE Trans. Sustainable Energy*, vol. 6, no. 4, pp. 1325-1336, Oct. 2015.

[31] H. A. Mohamadpour, E. Santi, "Modeling and control of gate-controlled series capacitor interfaced with a DFIG-based wind farm," *IEEE Trans. Industrial Electronic*, vol. 62, no. 2, pp. 1022-1033, Feb. 2015.

[32] G. Abad, J. Lopez, M. A. Rodriguez, L. Marroyo, G. Lwanski, *Doubly Fed Induction Machine*, IEEE Press, 2011, p. 147.

[33] F. Hans, W. Schumacher, L. Harnefors, “Small-Signal Modeling of Three-Phase Synchronous Reference Frame Phase-Locked Loops,” *IEEE Trans. Power Electronics*, vol. 33, no. 7, pp. 5556-5560, July 2018.

[34] P. C. Krause, *Analysis of Electric Machinary*, New York: McGraw-Hill, 1995, p. 81.

[35] F. Richard, *Power System Dynamics and Stability*, CRC Press, 2001.

[36] L. Xu, Y. Wang, "Dynamic modeling and control of DFIG-based wind turbines under unbalanced network conditions," *IEEE Trans. Power System*, vol. 22, no. 1, pp. 314-323, Feb. 2007.

[37] J. B. Ekanayake, L. Holdsworth, X. Wu and N. Jenkins, "Dynamic modeling of doubly fed induction generator wind turbines," *IEEE Trans. Power System*, vol. 18, no. 2, pp. 803-809, May. 2003.

[38] F. Wilches-Bernal, "Application of wind generation for power system frequency control, inter-area oscillation damping and parameter identification,"

Ph.D. dissertation, Graduate Faculty of Rensselaer. Electrical Eng., Rensselaer Polytechnic institute, 2015.

[39] N. W. Miller, J. J. Sanchez-Gasca, W. W. Price, and R. W. Delmerico, “Dynamic modeling of GE 1.5 and 3.6 MW wind turbine-generators for stability simulations,” in *Proc. 2003 IEEE Power Eng. Soc. GeneralMeeting*, 2003, vol. 3, pp. 1977–1983.

[40] B. Wen, D. Boroyevich, R. Burgos, P. Mattavelli, and Z. Shen, “Analysis of D-Q small-signal impedance of grid-tied inverters,” *IEEE Trans. Power Electron.*, vol. 31, no. 1, pp. 675–687, Jan. 2016.

[41] Z. Miao, “Impedance-model-based SSR analysis for type3 wind generator and series-compensated network,” *IEEE Trans. Energy Convers.*, vol. 27, no. 4, pp. 984–991, Dec. 2012.

[42] R. K. Varma and R Salehi "SSR mitigation with a new control of PV solar farm as STATCOM (PV-STATCOM)," *IEEE Trans. Sustainable Energy*, vol. 8, no. 4, pp. 1473-1483, Oct. 2017.

[43] F. Bizzarri, A Brambilia and F milano "Simplified model to study the induction generator effect of the sub-synchronous resonance phenamenon," *IEEE Trans. Energy Conversion*, DOI 10.1109/TEC.2018.2799479.

[44] W. Du, Q. Fu and H. F. Fang, "Sub-synchronous oscillations caused by open-loop modal coupling between VSC-based HVDC line and power system," *IEEE Trans. Power Systems*, DOI 10.1109/TPWRS.2017.2771764.

[45] W. Du, Q. Fu and H. Wang, " Method of Open-Loop Modal Analysis for Examining the Subsynchronous Interactions Introduced by VSC Control in an MTDC/AC System," IEEE Trans. Power Delivery, vol. 33, no. 2, pp. 840-850, April. 2018.

[46] W. Du, C. Chen and H. F. Fang, "Sub-synchronous interactions induced by DFIGs in power system without series compensated lines," *IEEE Trans. Sustainable Energy*, DOI 10.1109/TSTE.2017.2781289.

[47] L. Zhao, I. Matsuo, F. Salehi, Y. Zhou and W. Lee, "Development of a Real-Time Web-Based Power Monitoring system for the substation of petrochemical

facilities," *2018 IEEE/IAS 54th Industrial and Commercial Power Systems Technical Conference (I&CPS),* Niagara Falls, ON, 2018, pp. 1-6.

[48] F. Salehi, I. B. Matsuo, W. J. Lee "Detection of Sub-Synchronous Control Interaction (SSCI) Using Modal Identification Analysis and FFT," *2018 50th North American Power Symposium,* Fargo, ND. 2018

[49] Z. Zhang, S. Liu, G. Zhu and Z. Lu, "SSCI detection and protection in doubly fed generator based on DTFT," *Journal of Engineering,* Nov. 2017.

[50] M. Orman, P. Balcerek and M. Orkisz, "Effective method of subsynchronous resonance detection and its limitations," *Journal of Electrical power and Energy System,* pp. 915-920 Jul. 2012.

[51] L. C. Gross, " Sub-Synchronous grid conditions: New event, New problem, and New solutions," 37th annual western protective relay conference., Spokane, Washington, Oct. 2010.

[52] H. Khalilinia and V. Venkatasubramanian, "Subsynchronous resonance monitoring using ambient high-speed sensor data," *IEEE Trans. Power Power System,* vol. 31, no.2, pp. 1073-1083, March. 2016.

[53] Y. Xia, B. K. Johnson and H. Xia, "Application of Modern Techniques for Detecting Subsynchronous Oscillation in Power System," *in Proc. Power & Energy Society General Meeting* (PESG), Nov. 2013.

[54] J. J. Sanchez-Gasca, " Identification of electromechanical modes in power systems," IEEE PES, Tech Rep. PES-TR15, June. 2012.

[55] National Instruments, "cRIO-9039 CompactRIO Controller", Available: http://www.ni.com/en-us/support/model.crio-9039.html . [Accessed: 23-Jul-2018]

Appendix A

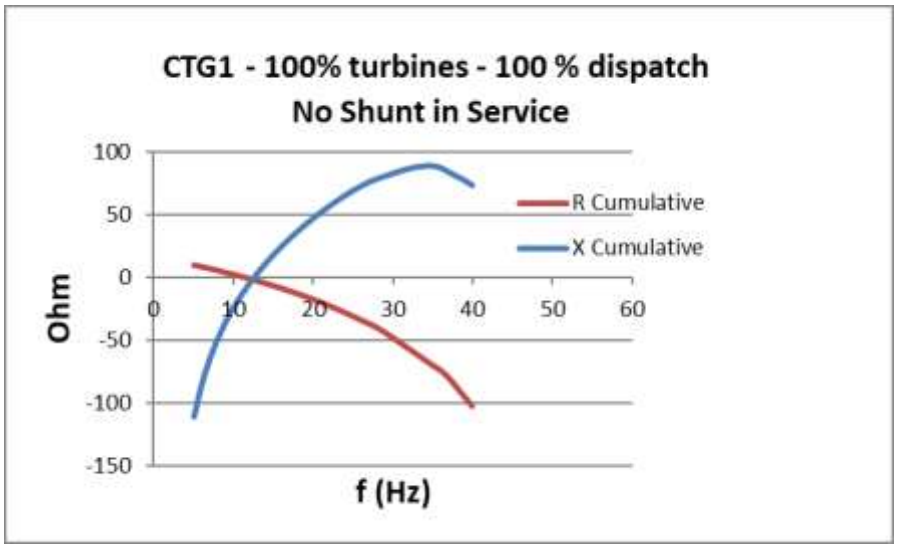

Figure A-1 Detail Screening – Contingency#1, All Shunts out of service (100% turbines & 100% dispatch)

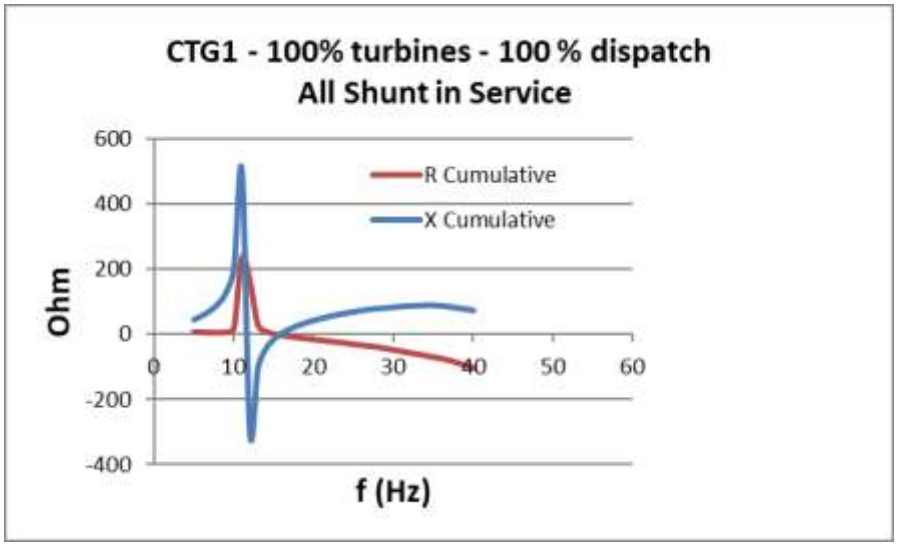

Figure A-2 Detail Screening – Contingency#1, All Shunts in service (100% turbines & 100% dispatch)

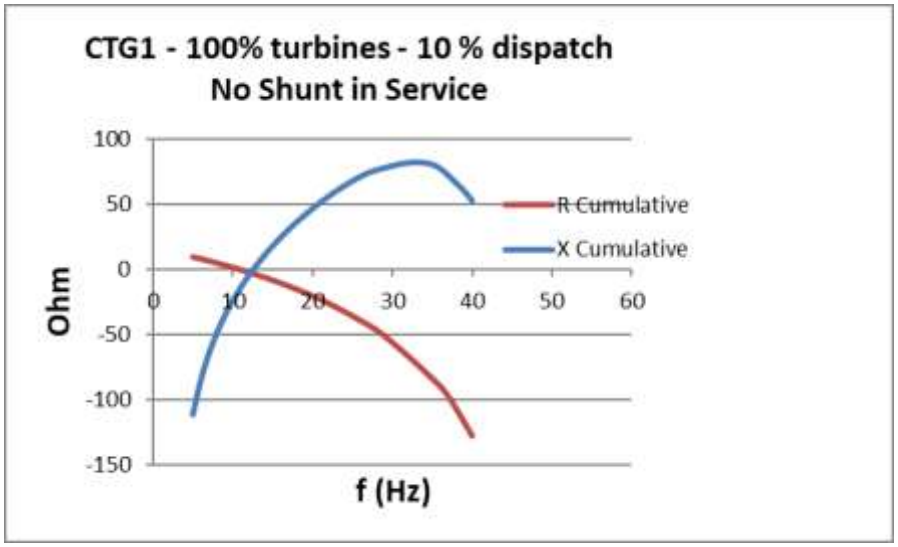

Figure A-3 Detail Screening – Contingency#1, All Shunts out of service (100% turbines & 10% dispatch)

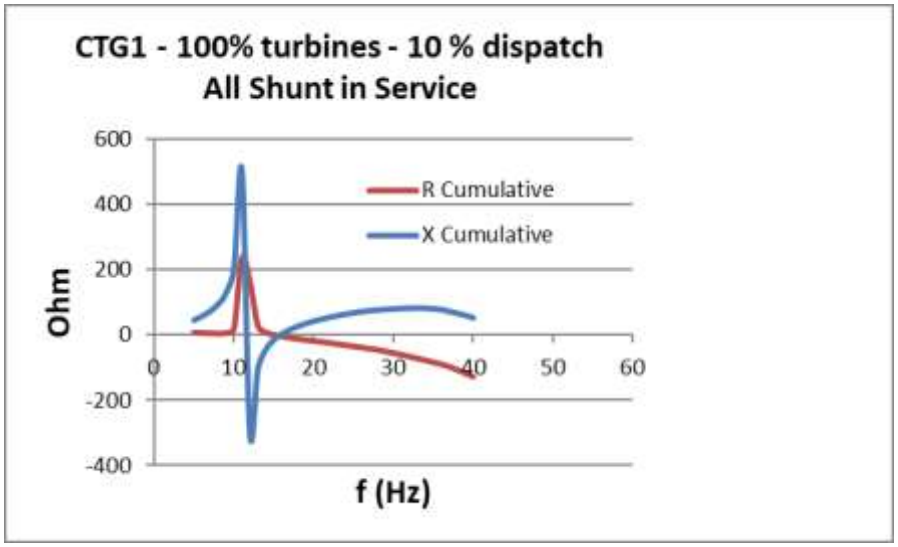

Figure A-4 Detail Screening – Contingency#1, All Shunts in service (100% turbines & 10% dispatch)

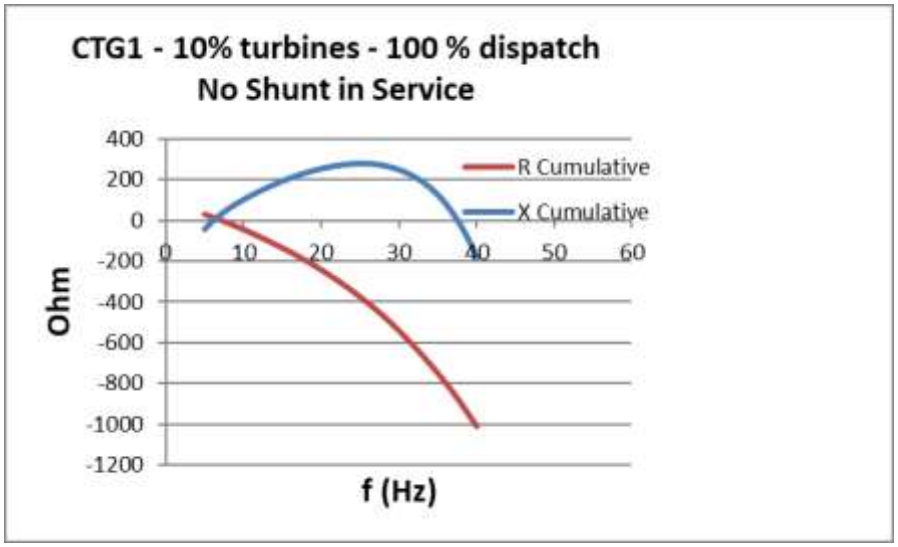

Figure A-5 Detail Screening – Contingency#1, All Shunts out of service (10% turbines & 100% dispatch)

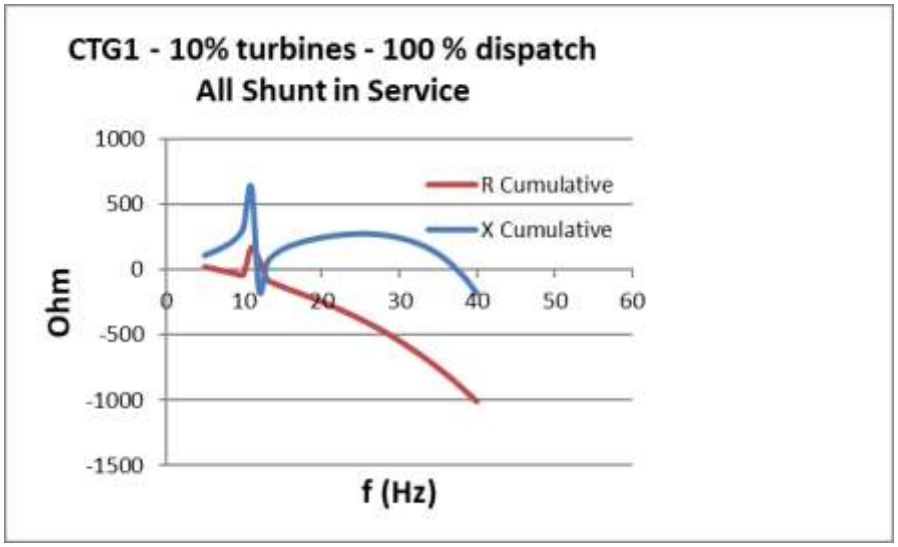

Figure A-6 Detail Screening – Contingency#1, All Shunts in service (10% turbines & 100% dispatch)

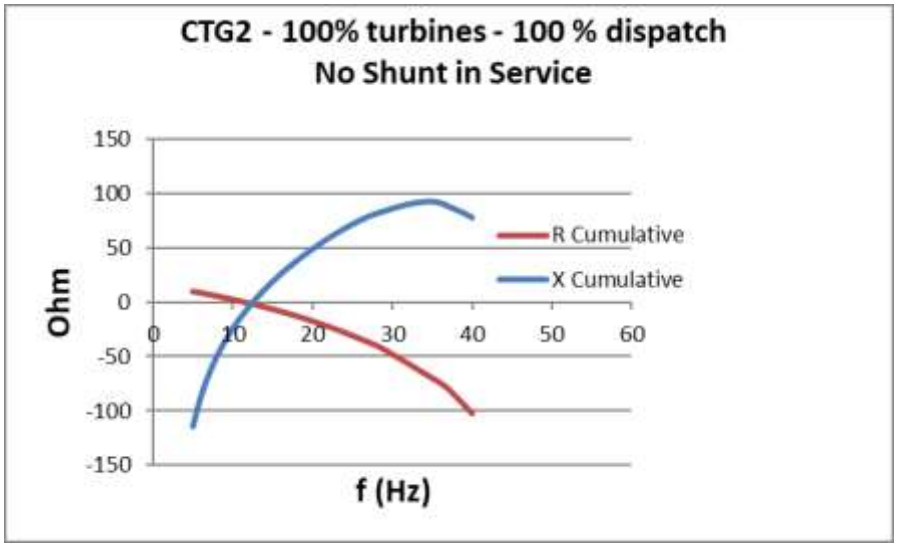

Figure A-7 Detail Screening – Contingency#2, All Shunts out of service (100% turbines & 100% dispatch)

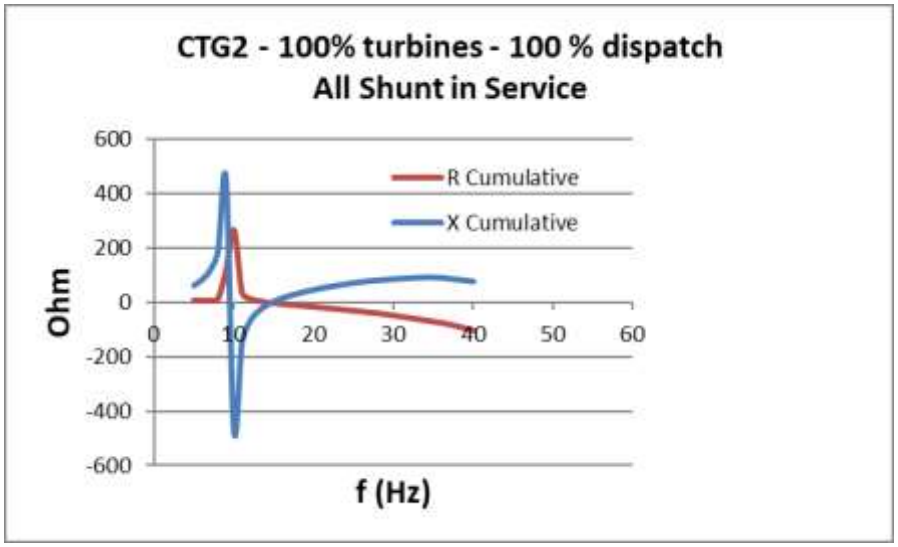

Figure A-8 Detail Screening – Contingency#2, All Shunts in service (100% turbines & 100% dispatch)

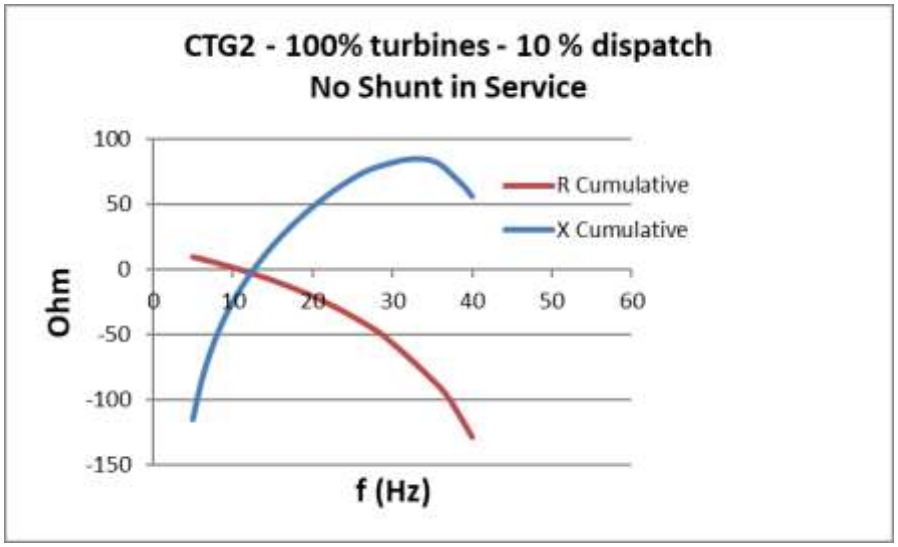

Figure A-9 Detail Screening – Contingency#2, All Shunts out of service (100% turbines & 10% dispatch)

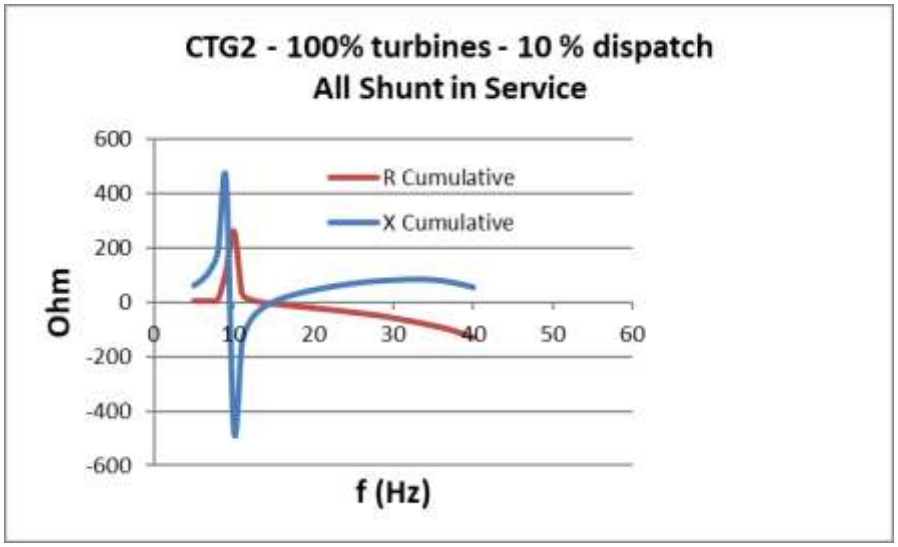

Figure A-10 Detail Screening – Contingency#2, All Shunts in service (100% turbines & 10% dispatch)

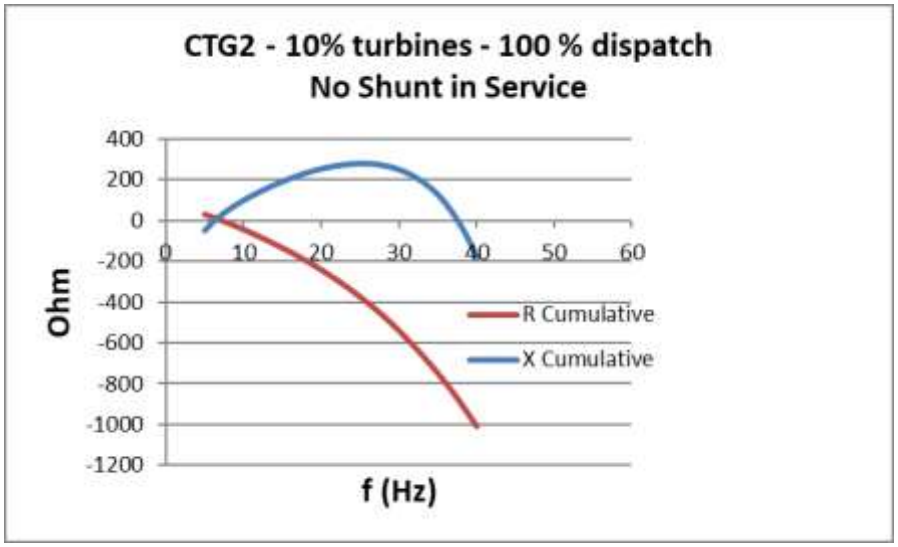

Figure A-11Detail Screening – Contingency#2, All Shunts out of service (10% turbines & 100% dispatch)

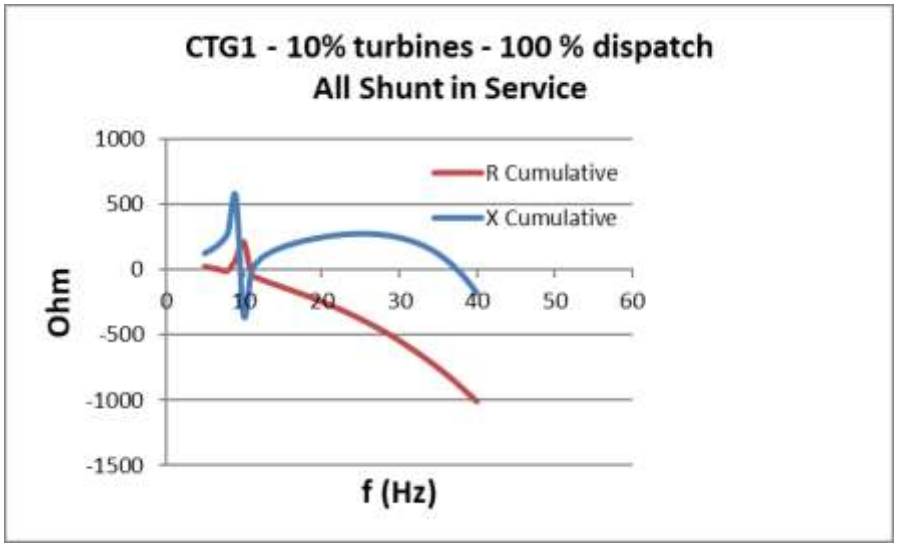

Figure A-12 Detail Screening – Contingency#2, All Shunts in service (10% turbines & 100% dispatch)

Appendix B

CTG1-D100T100-NoShunt-Fault

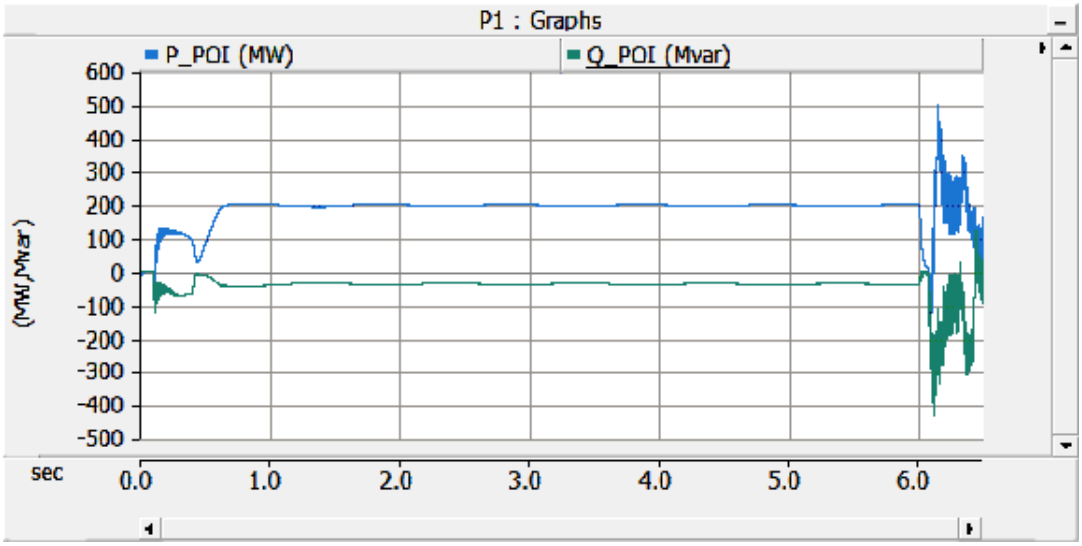

Figure B-1 EMT Simulation, SC1, POI Active & Reactive Power

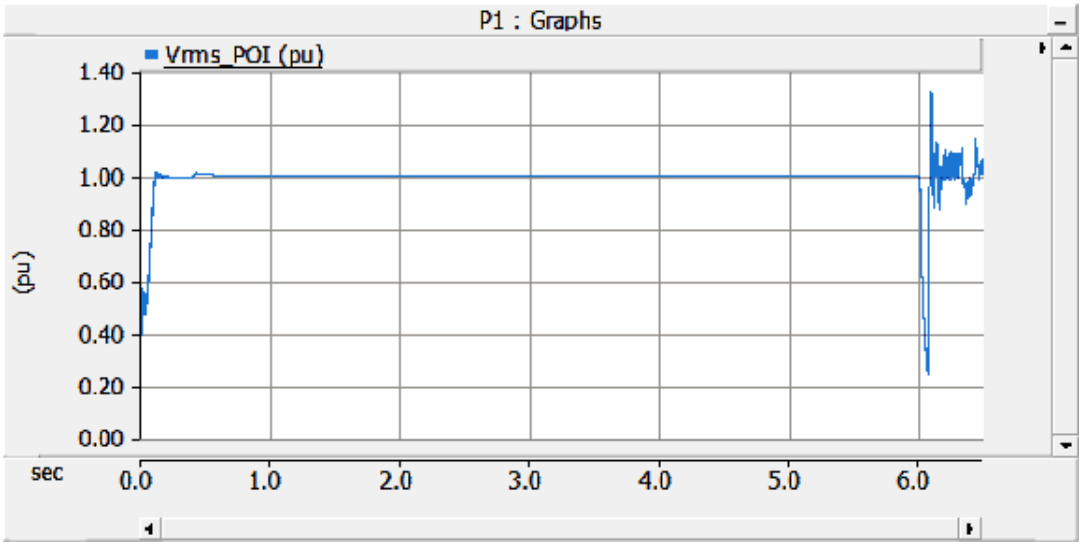

Figure B-2 EMT Simulation, SC1, POI rms voltage

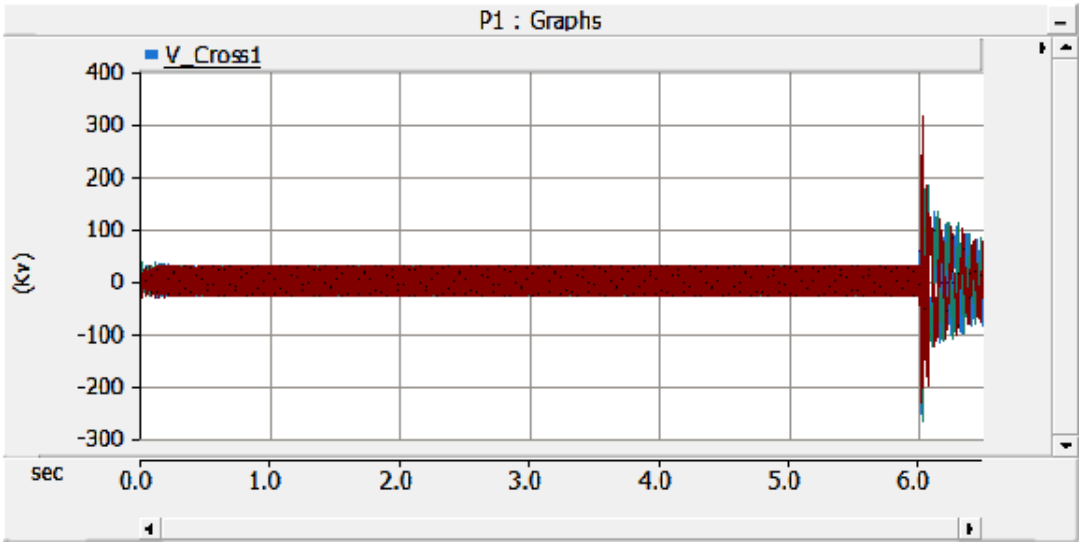

Figure B-3 EMT Simulation, SC1, series capacitor voltage

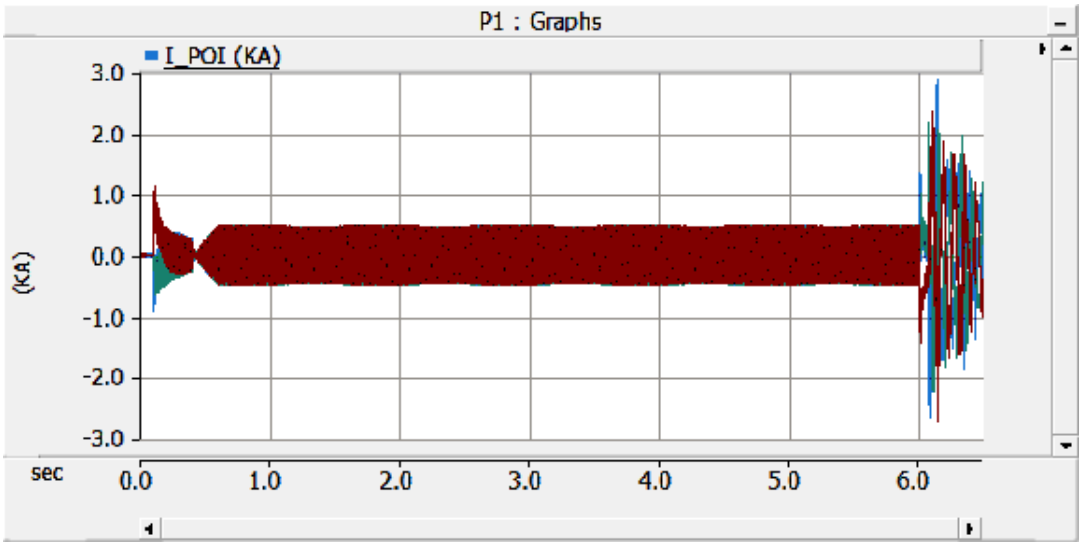

Figure B-4 EMT Simulation, SC1, POI instantaneous current

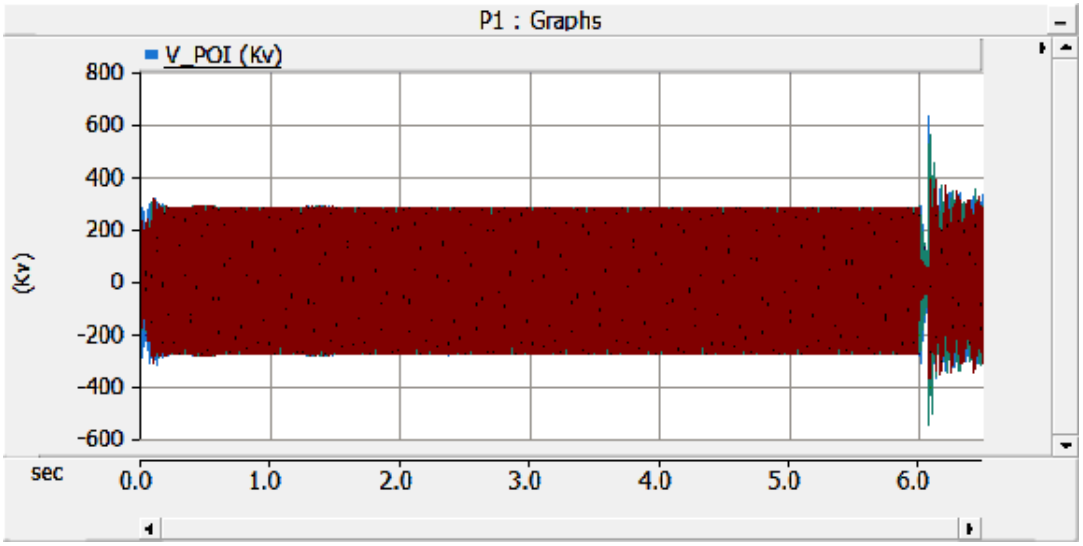

Figure B-5 EMT Simulation, SC1, POI instantaneous voltage

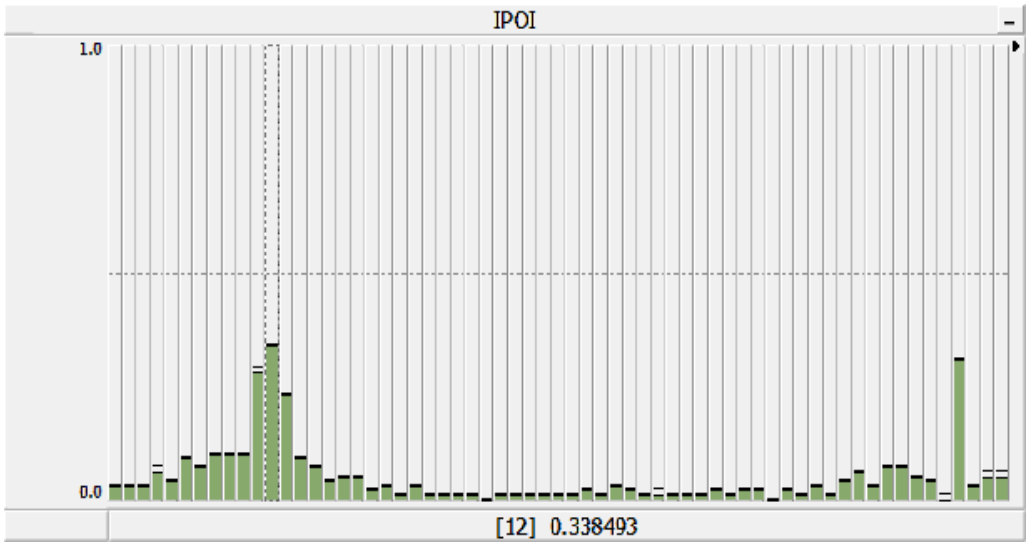

Figure B-6 EMT Simulation, SC1, POI current FFT

SC2: CTG1-D100T100-AllShunt-Fault

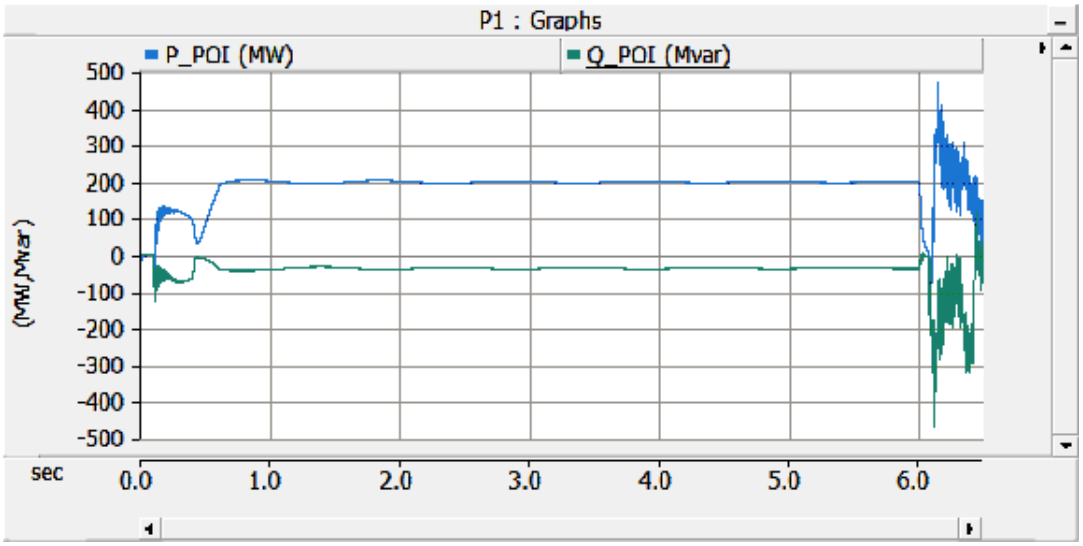

Figure B-7 EMT Simulation, SC2, POI Active & Reactive Power

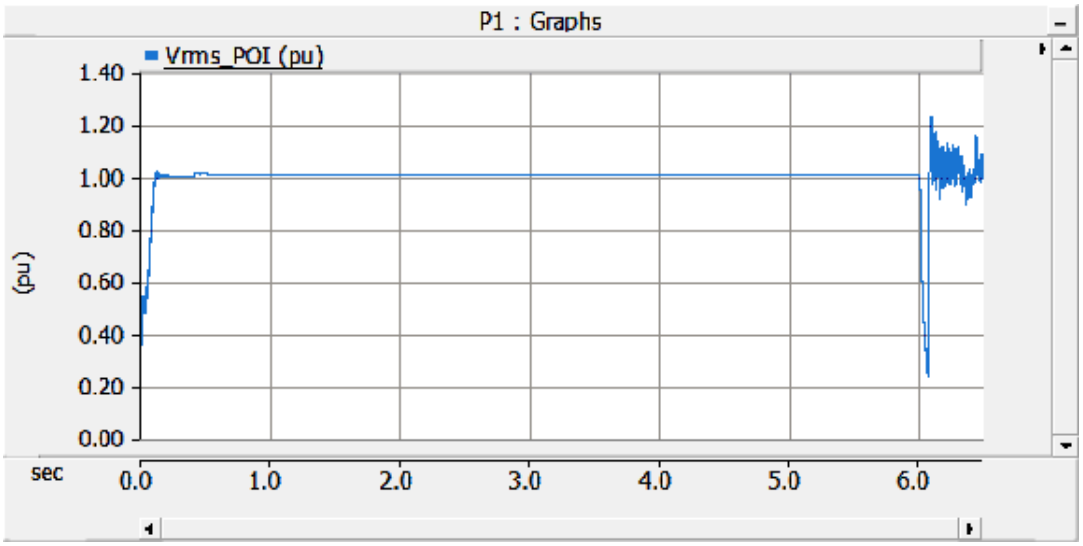

Figure B-8 EMT Simulation, SC2, POI rms voltage

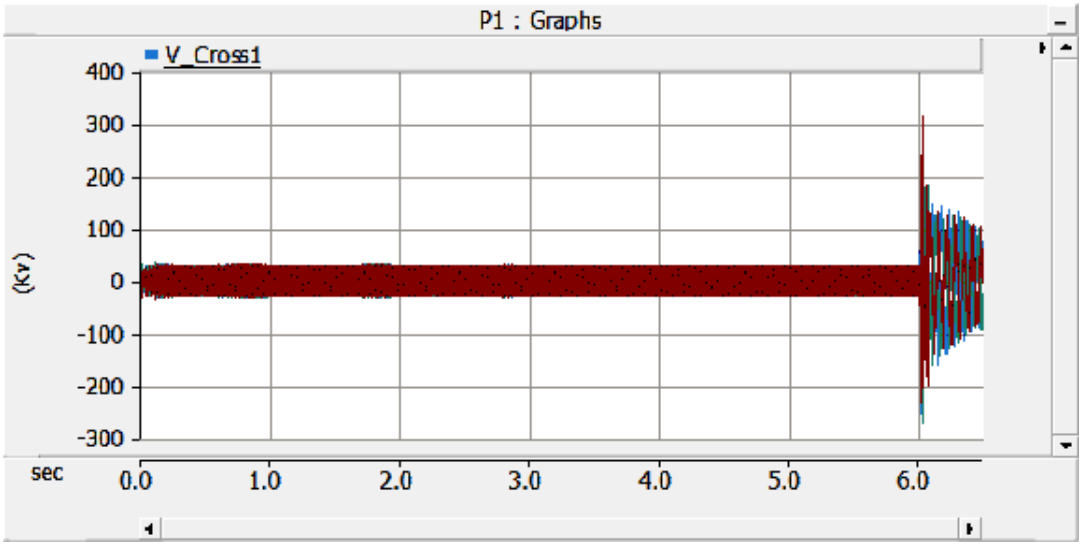

Figure B-9 EMT Simulation, SC2, series capacitor voltage

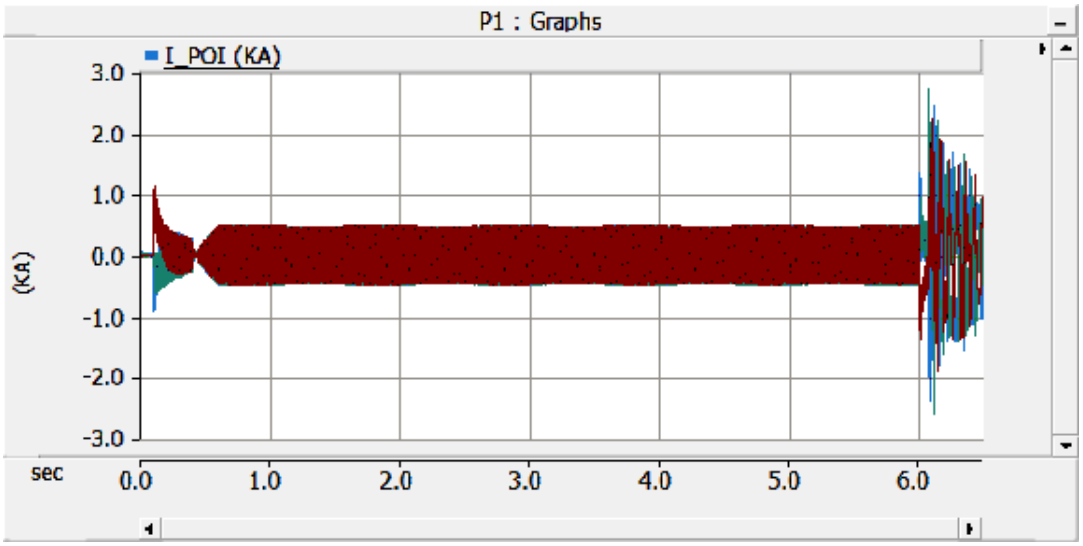

Figure B-10 EMT Simulation, SC2, POI instantaneous current

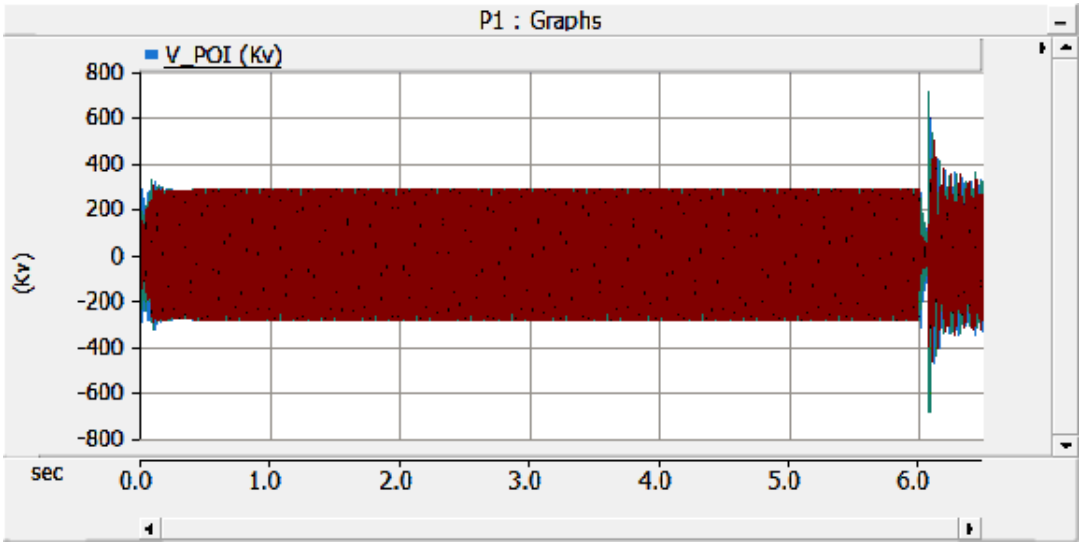

Figure B-11 EMT Simulation, SC2, POI instantaneous voltage

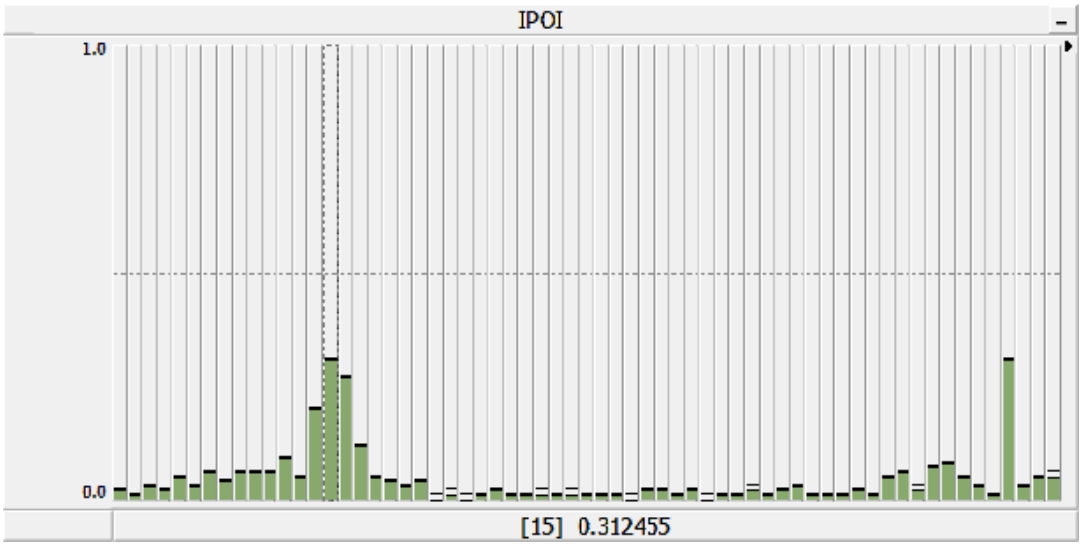

Figure B-12 EMT Simulation, SC1, POI current FFT

SC3: CTG1-D100T100-NoShunt-NoFault

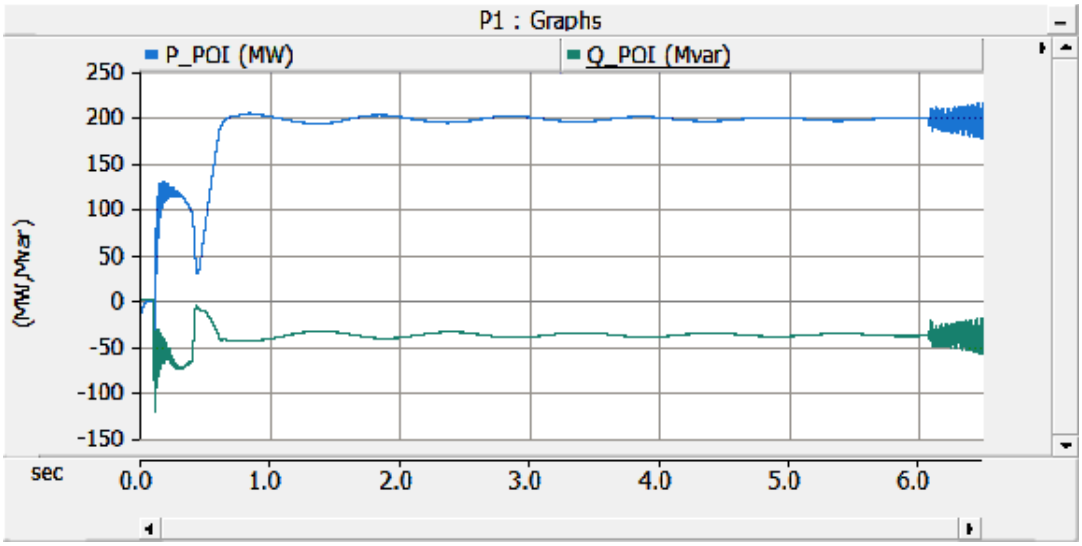

Figure B-13 EMT Simulation, SC3, POI Active & Reactive Power

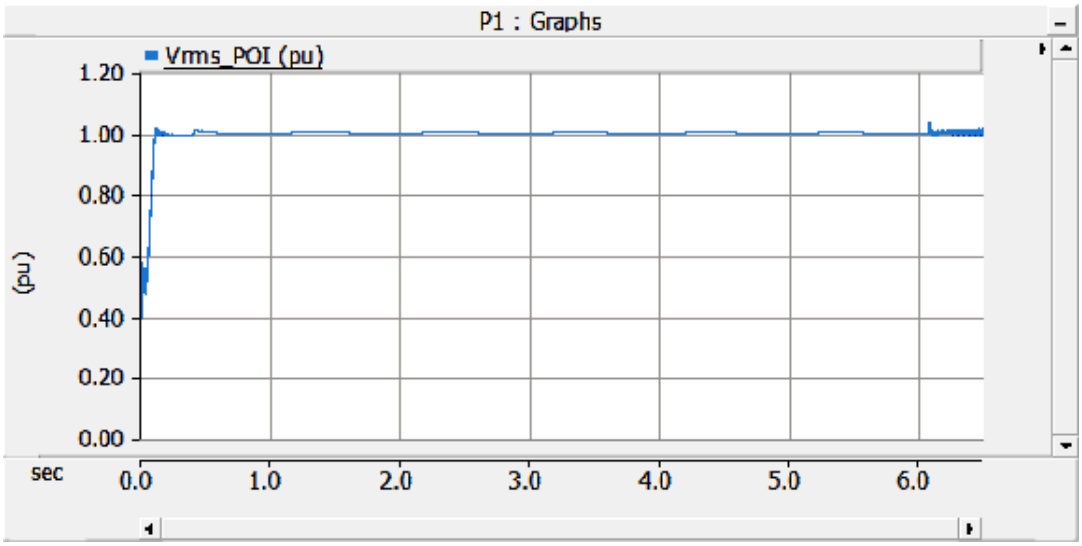

Figure B-14 EMT Simulation, SC3, POI rms voltage

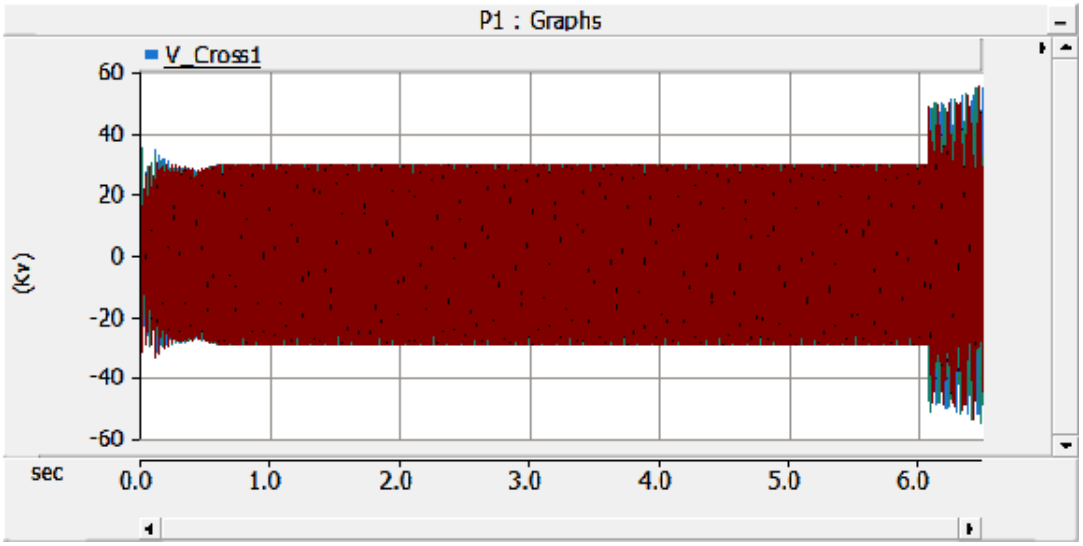

Figure B-15 EMT Simulation, SC3, series capacitor voltage

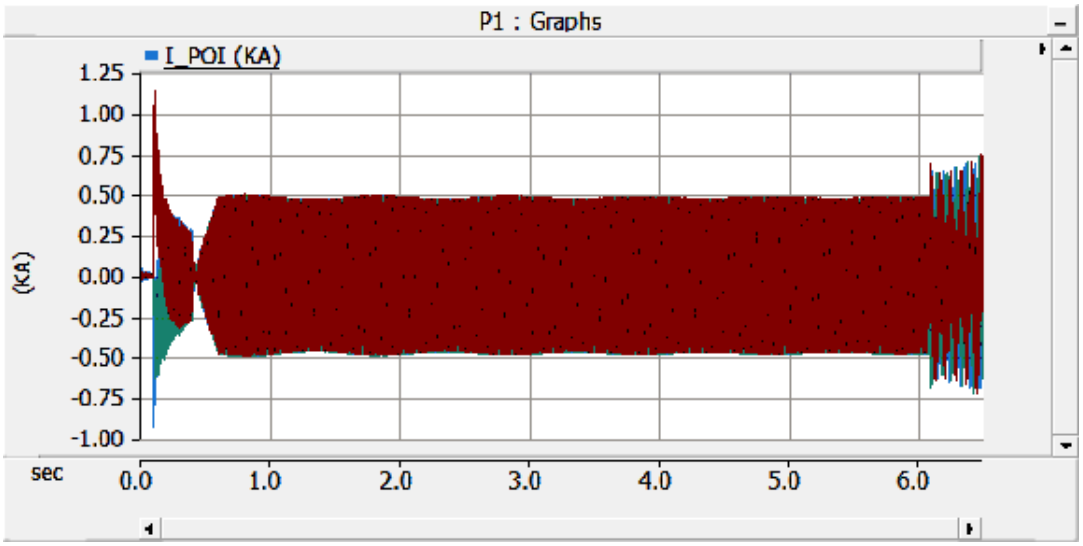

Figure B-16 EMT Simulation, SC3, POI instantaneous current

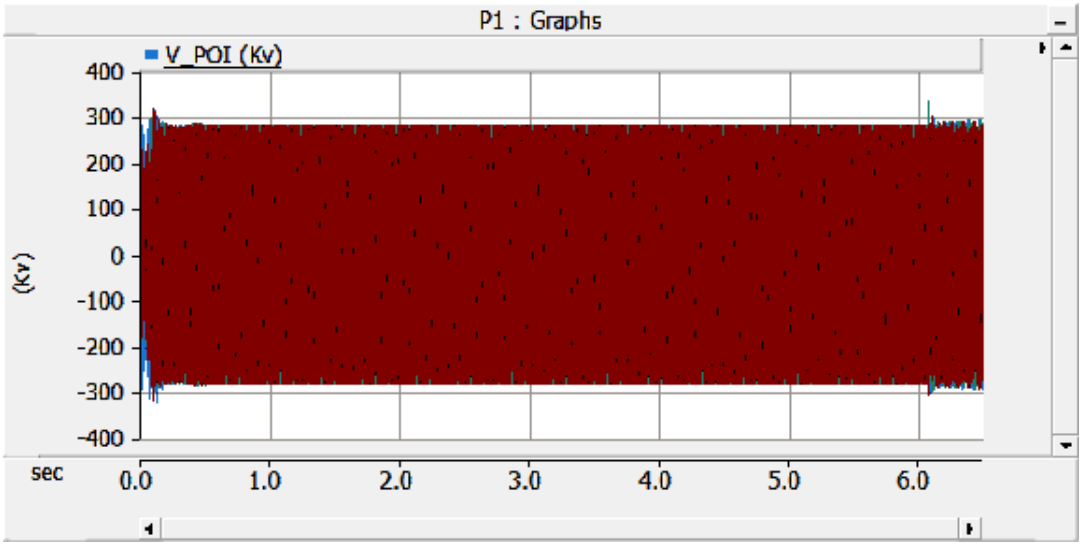

Figure B-17 EMT Simulation, SC3, POI instantaneous voltage

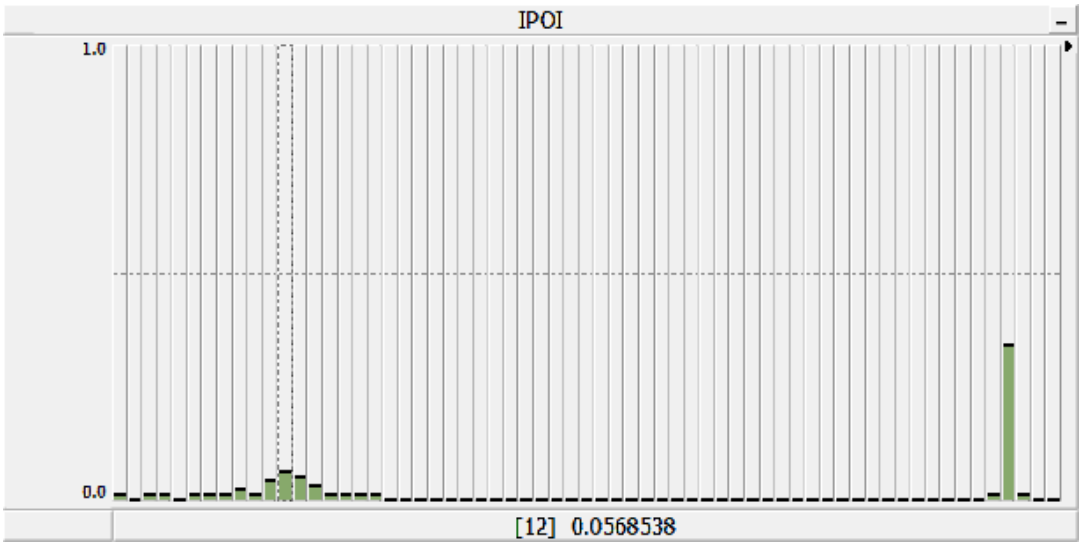

Figure B-18 EMT Simulation, SC3, POI current FFT

SC4: CTG1-D100T100-AllShunt-NoFault

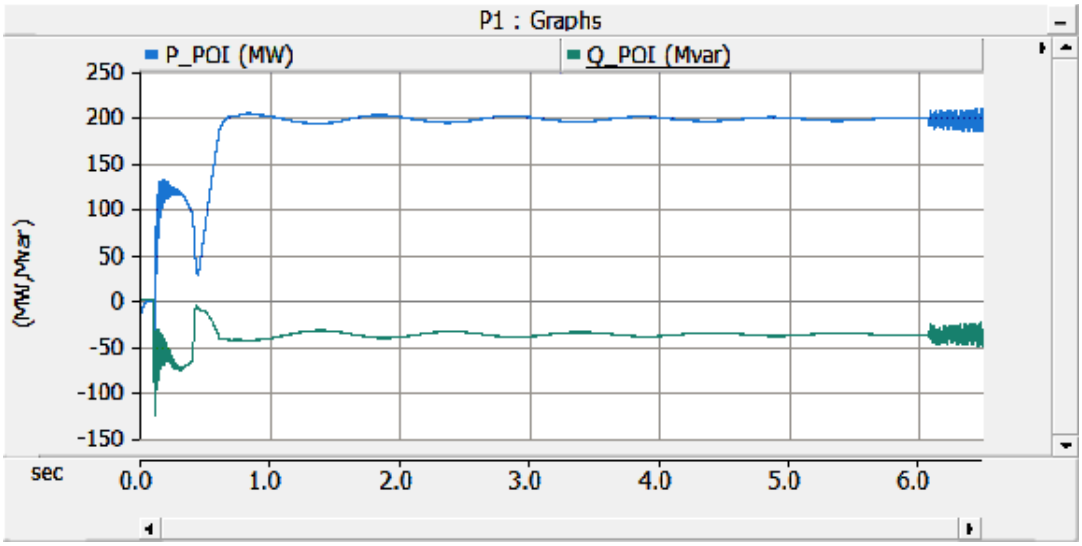

Figure B-19 EMT Simulation, SC4, POI Active & Reactive Power

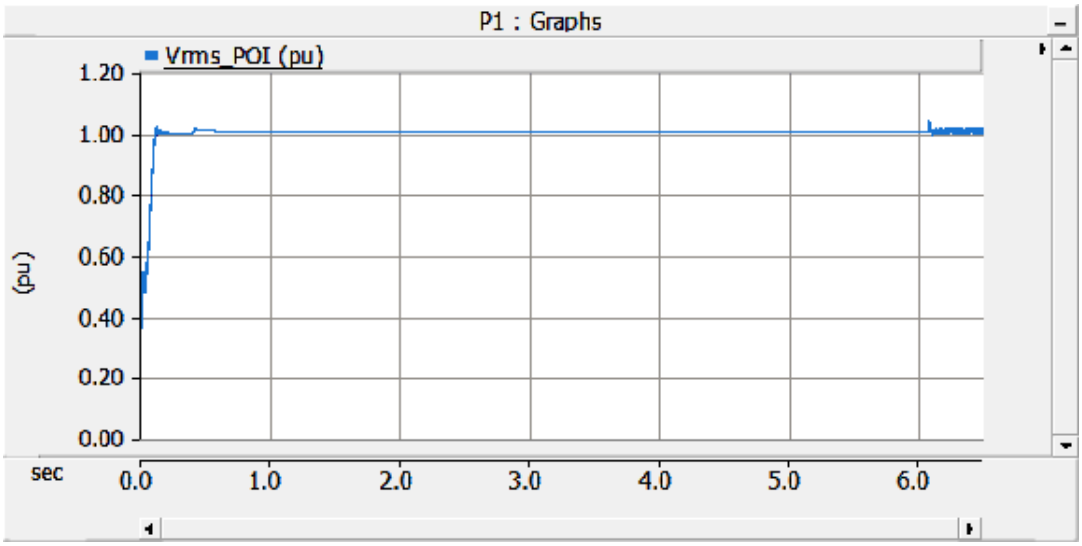

Figure B-20 EMT Simulation, SC4, POI rms voltage

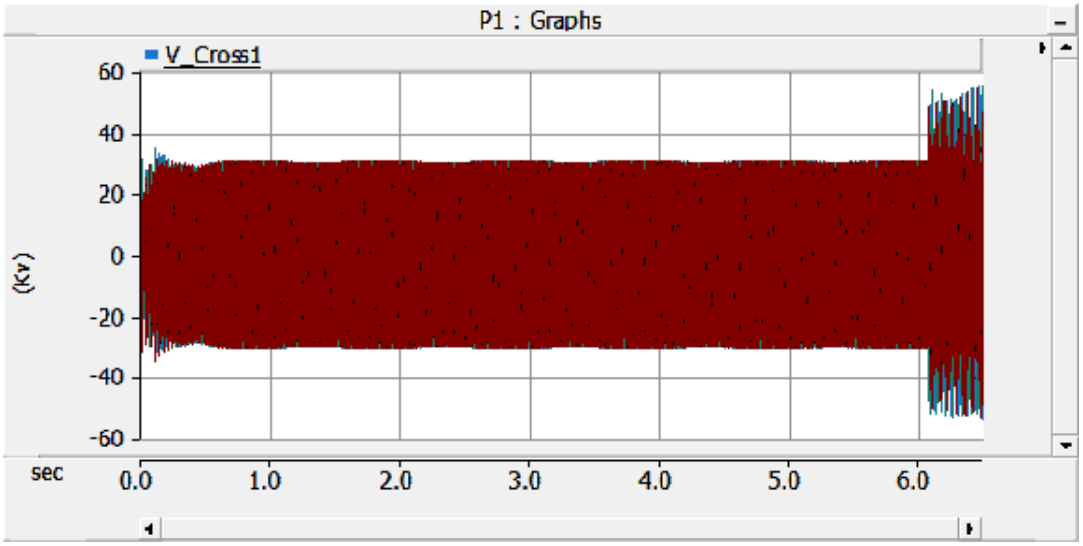

Figure B-21 EMT Simulation, SC4, series capacitor voltage

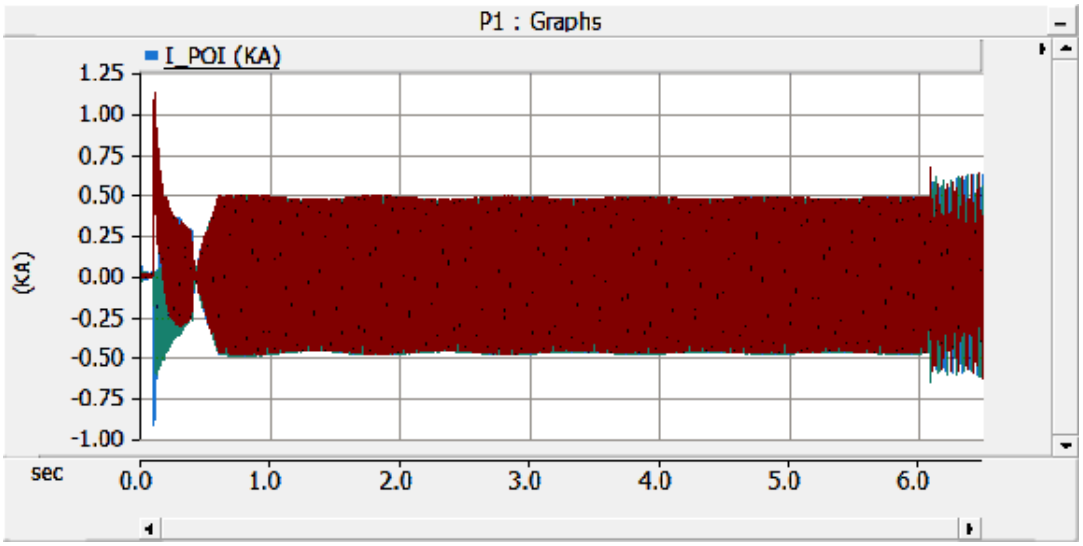

Figure B-22 EMT Simulation, SC4, POI instantaneous current

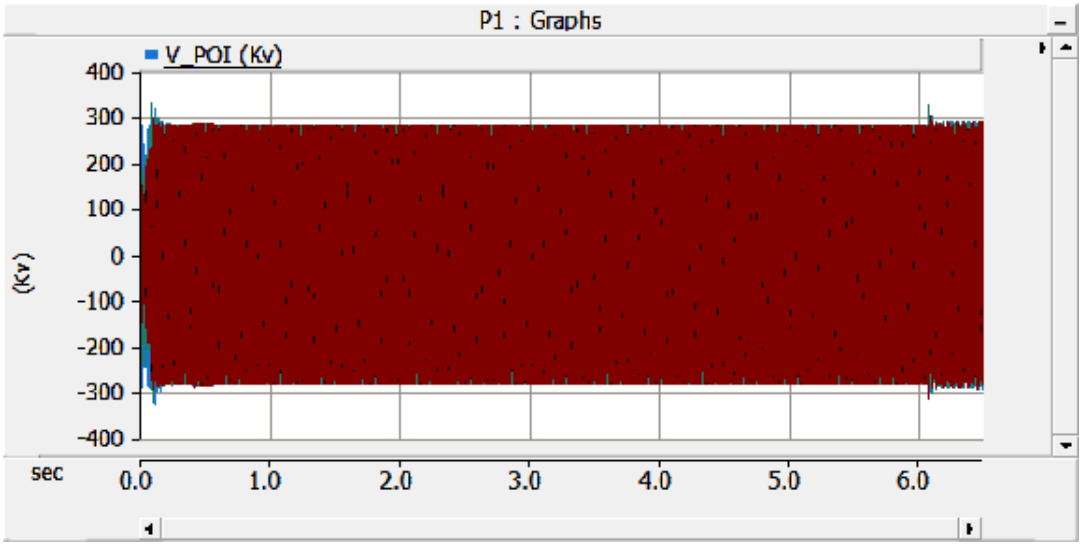

Figure B-23 EMT Simulation, SC4, POI instantaneous voltage

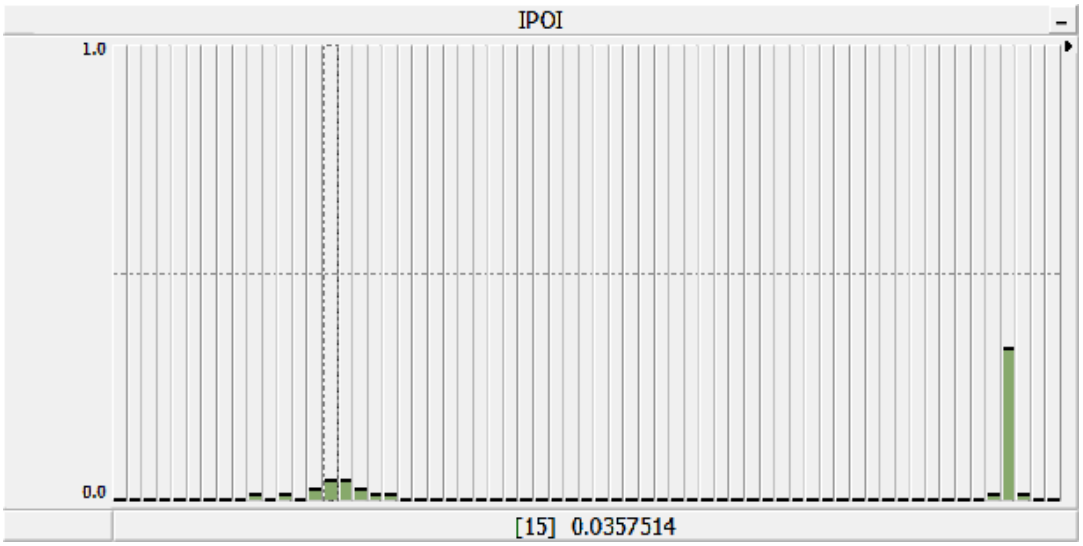

Figure B-24 EMT Simulation, SC1, POI current FFT

SC5: CTG1-D10T100-NoShunt-Fault

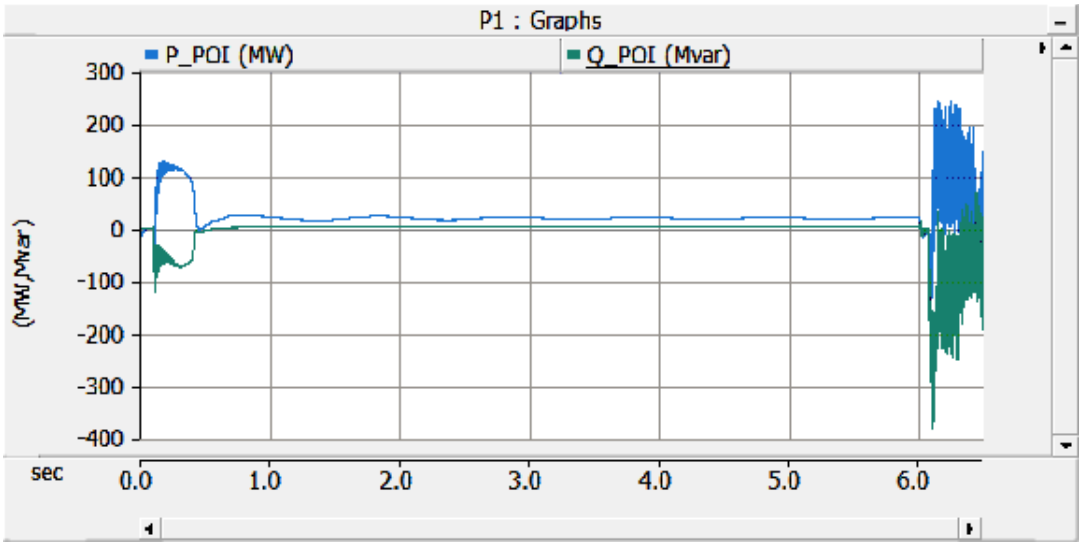

Figure B-25 EMT Simulation, SC5, POI Active & Reactive Power

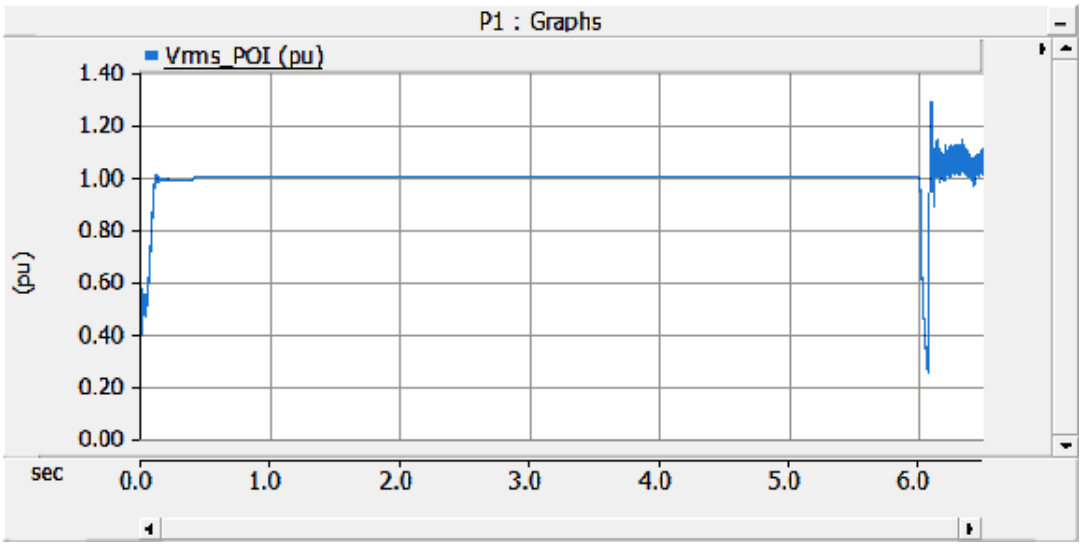

Figure B-26 EMT Simulation, SC5, POI rms voltage

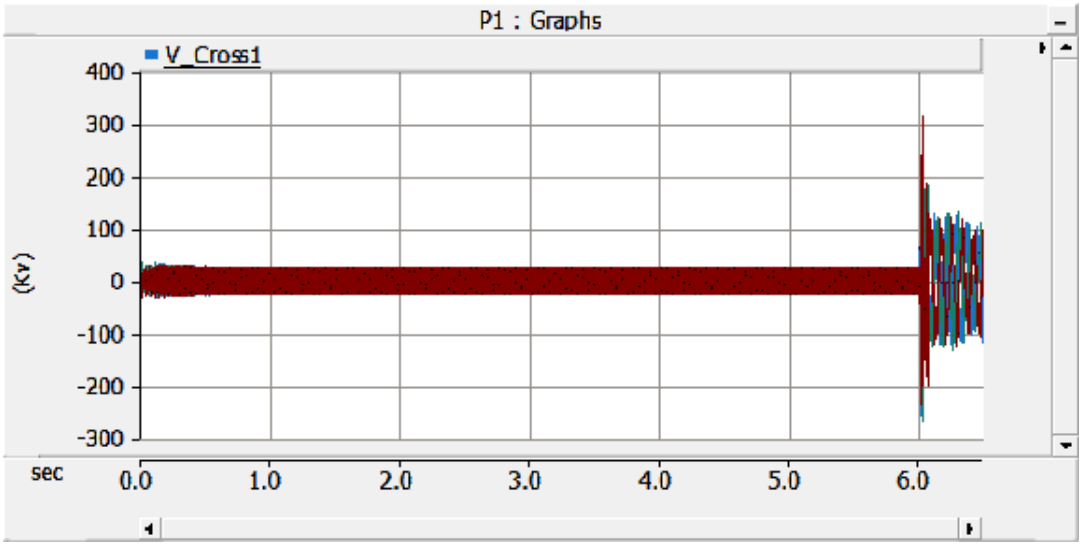

Figure B-27 EMT Simulation, SC5, series capacitor voltage

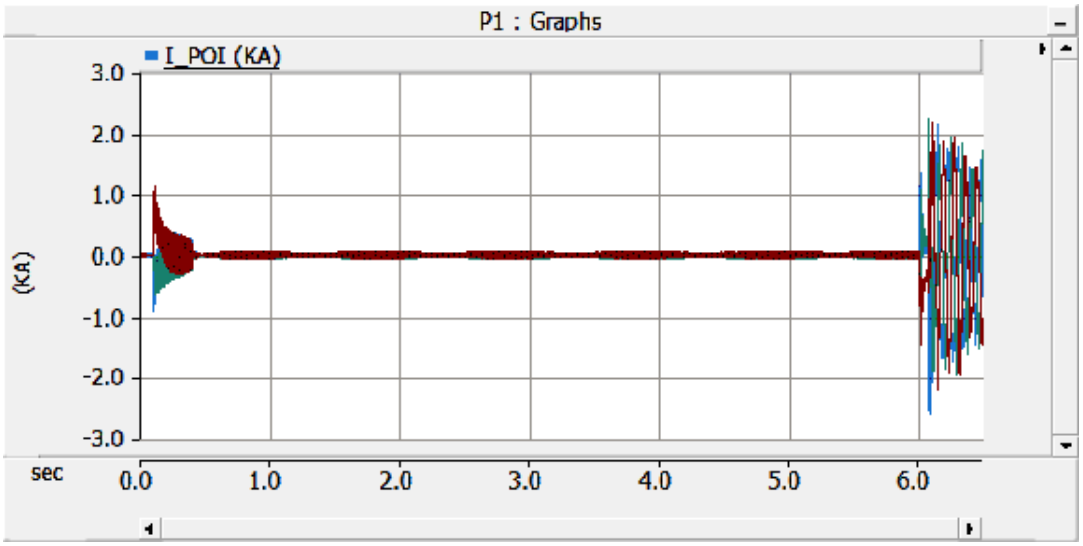

Figure B-28 EMT Simulation, SC5, POI instantaneous current

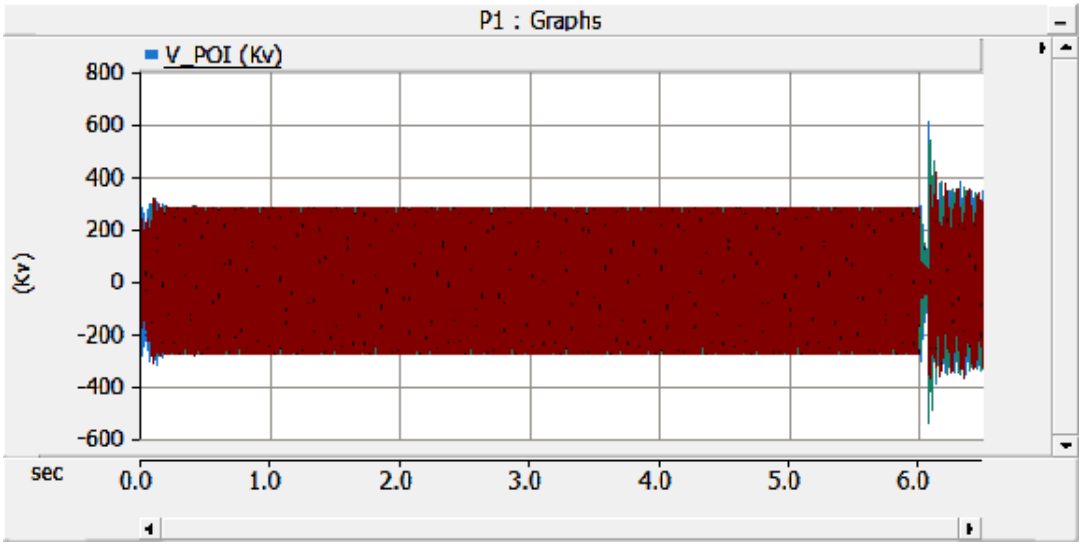

Figure B-29 EMT Simulation, SC5, POI instantaneous voltage

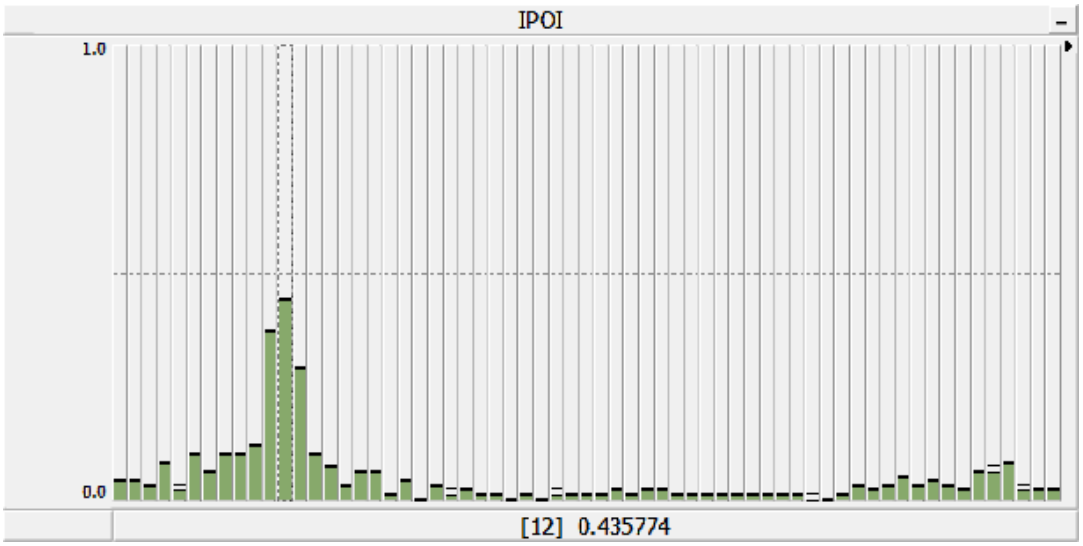

Figure B-30 EMT Simulation, SC5, POI current FFT

CTG1-D10T100-AllShunt-Fault

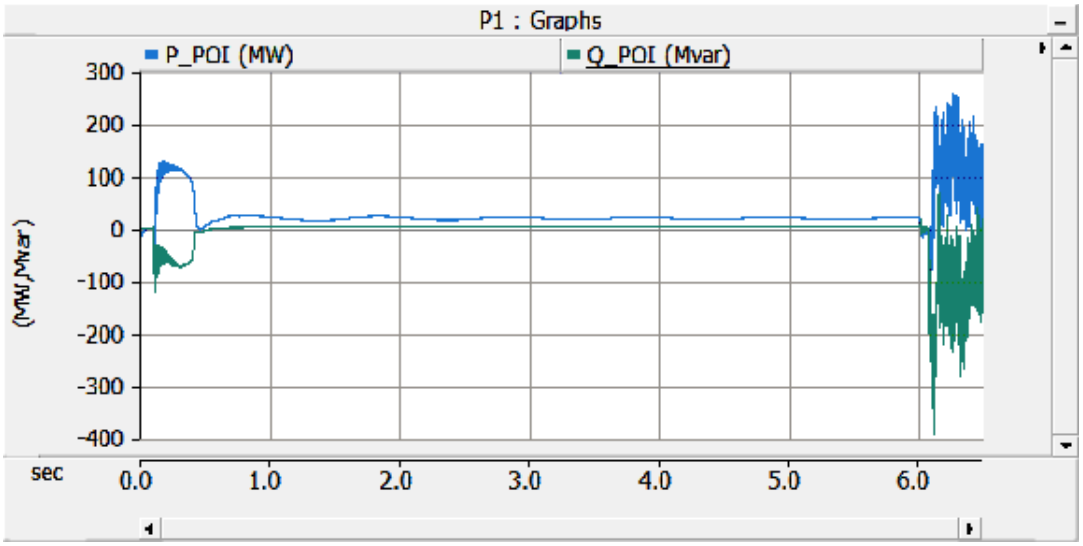

Figure B-31 EMT Simulation, SC6, POI Active & Reactive Power

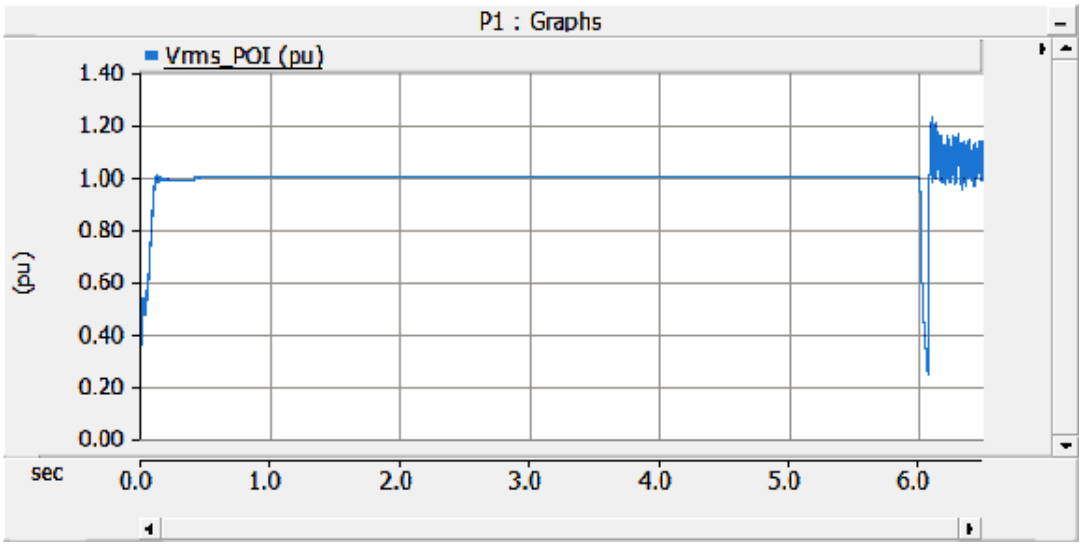

Figure B-32 EMT Simulation, SC6, POI rms voltage

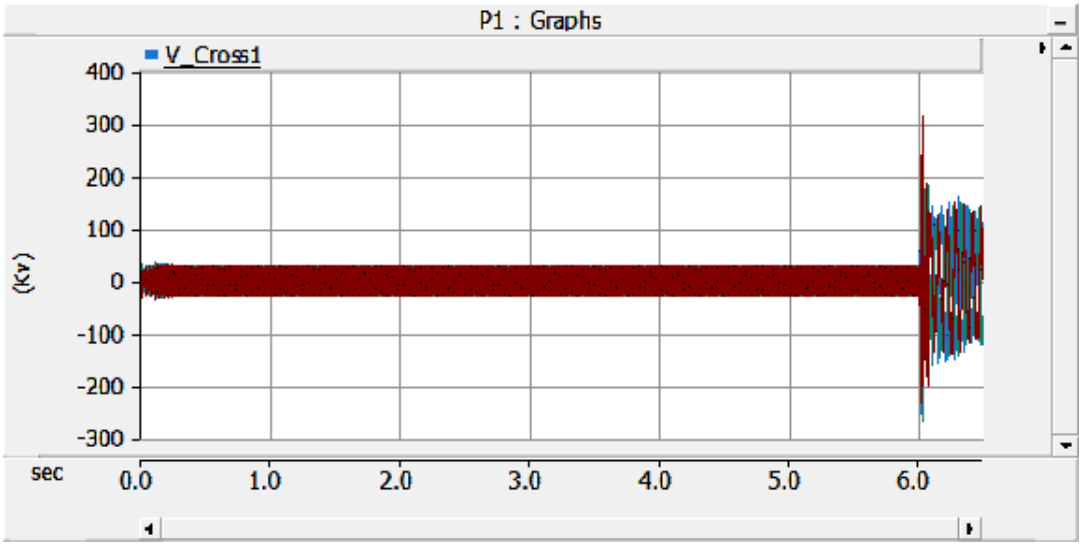

Figure 0-33 EMT Simulation, SC6, series capacitor voltage

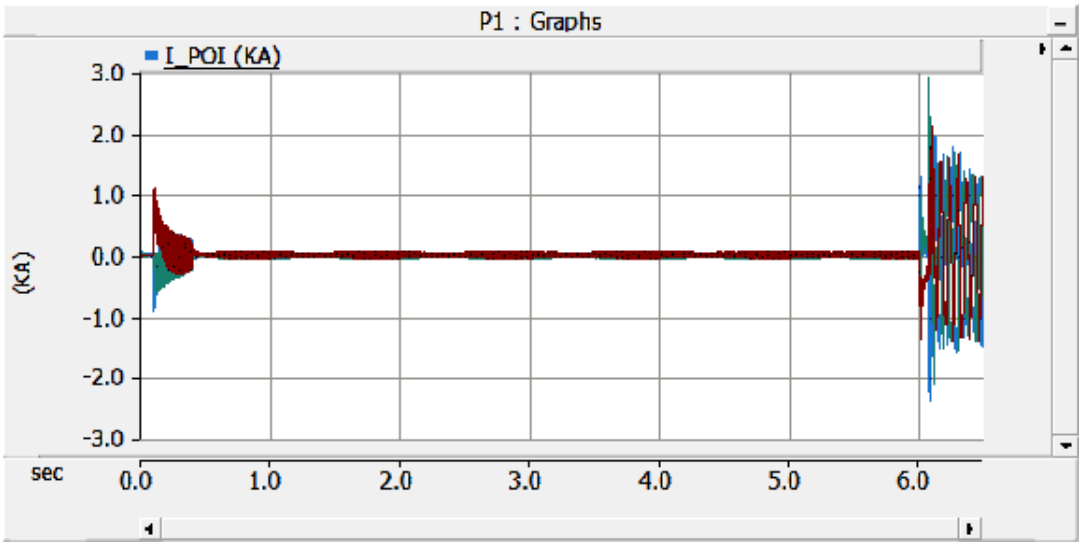

Figure B-34 EMT Simulation, SC6, POI instantaneous current

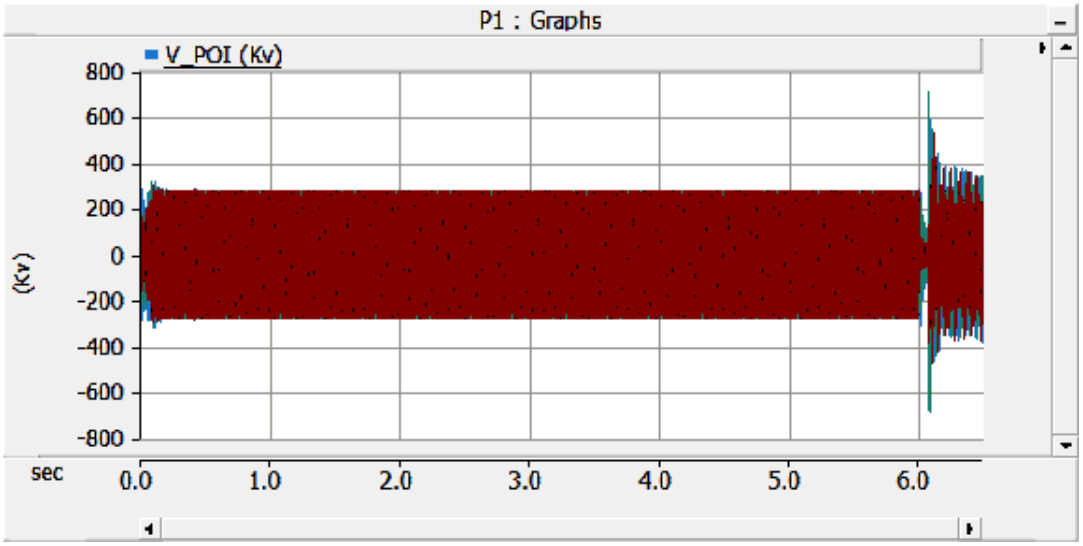

Figure B-35 EMT Simulation, SC6, POI instantaneous voltage

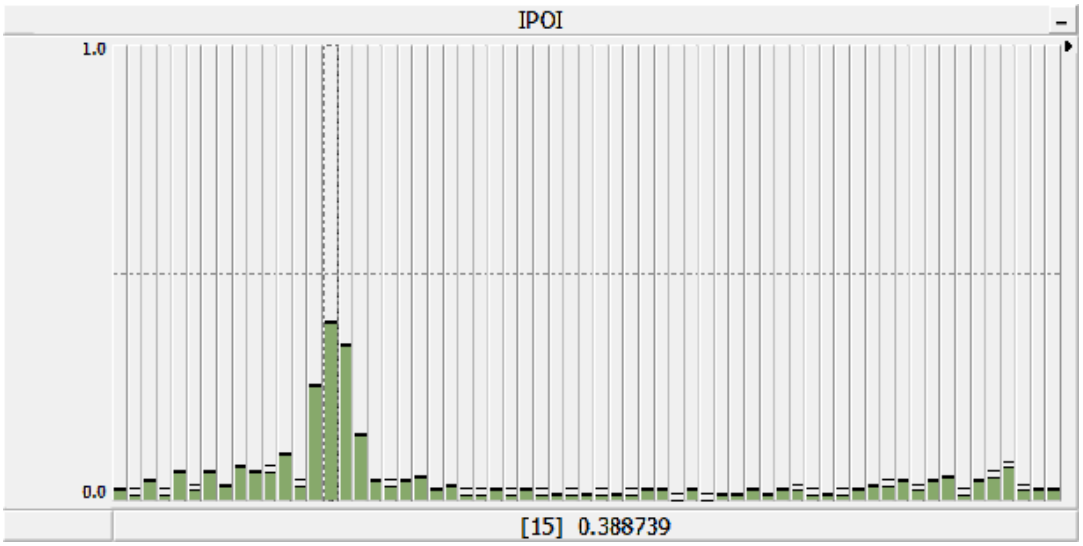

Figure B-36 EMT Simulation, SC, POI current FFT

SC7: CTG1-D10T100-NoShunt-NoFault

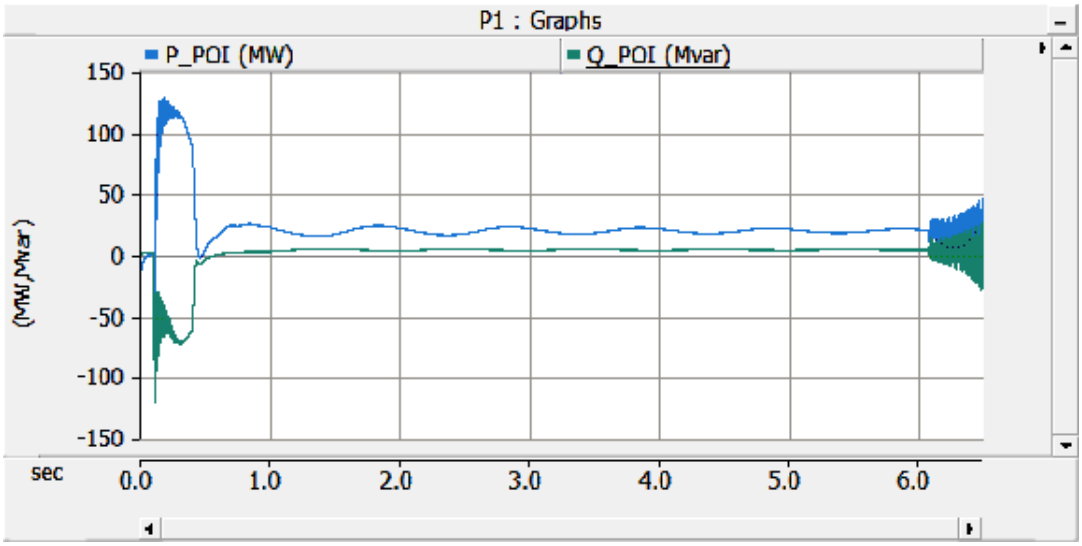

Figure B-37 EMT Simulation, SC7, POI Active & Reactive Power

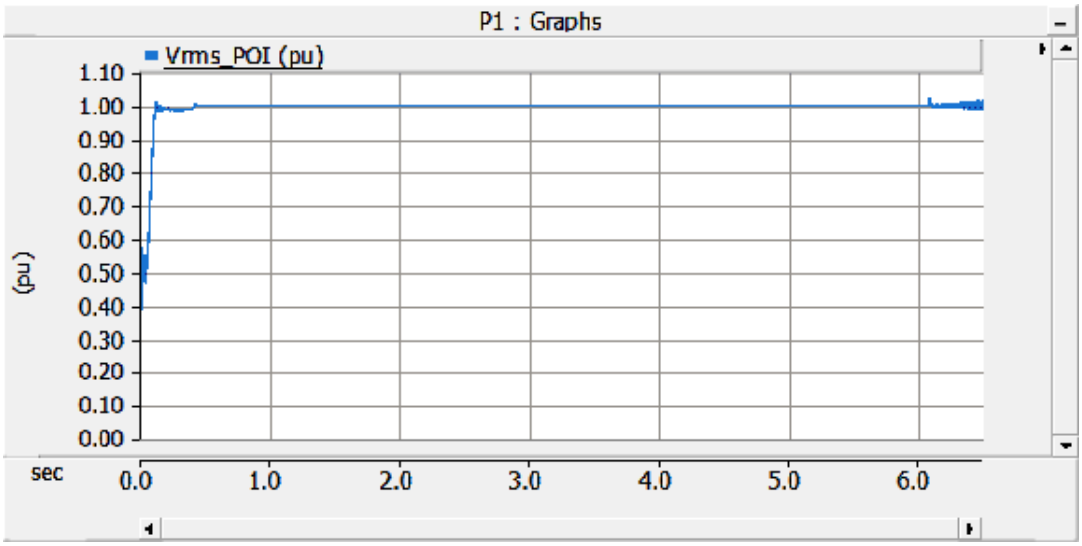

Figure B-38 EMT Simulation, SC7, POI rms voltage

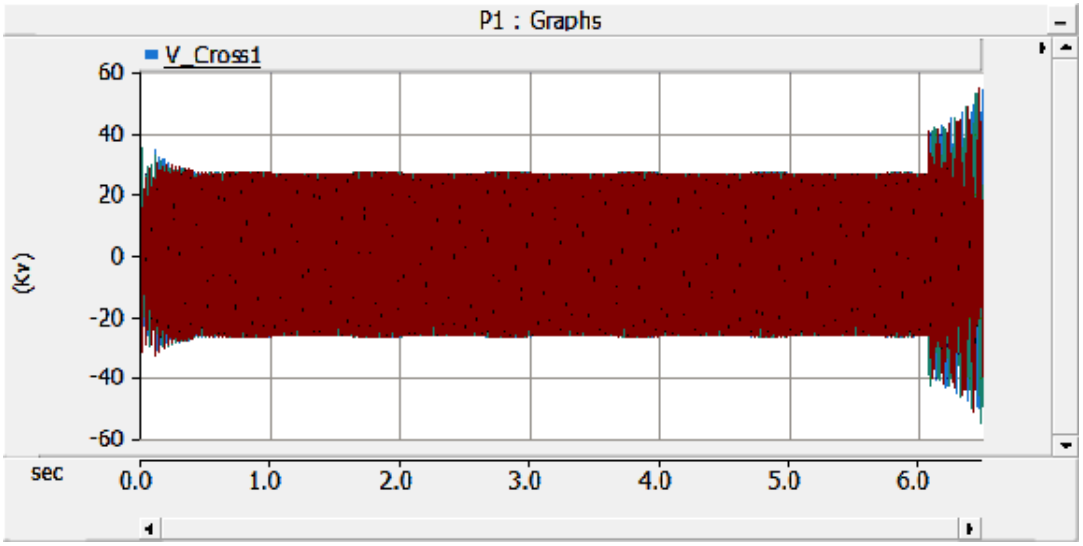

Figure B-39 EMT Simulation, SC7, series capacitor voltage

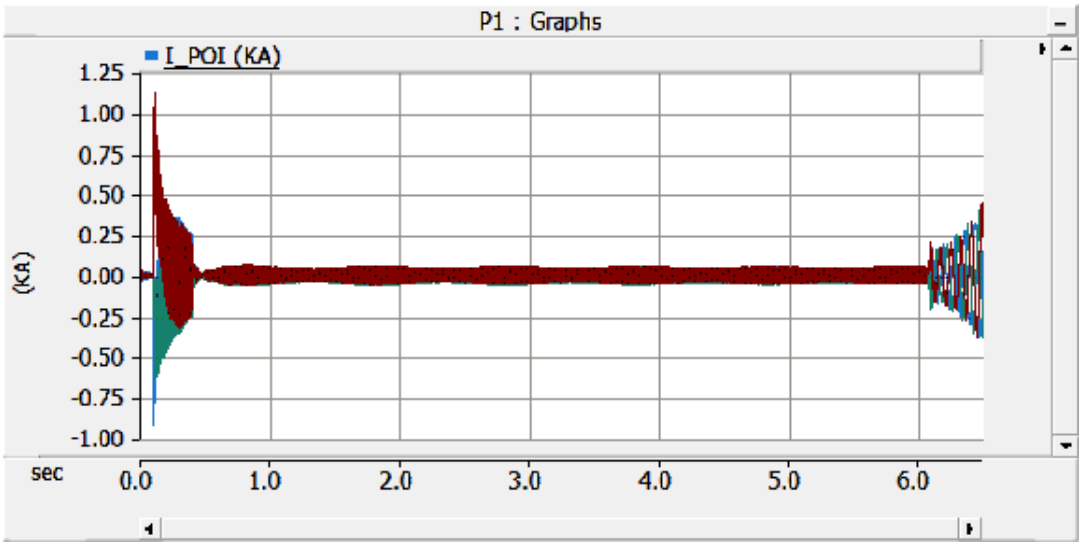

Figure B-40 EMT Simulation, SC7, POI instantaneous current

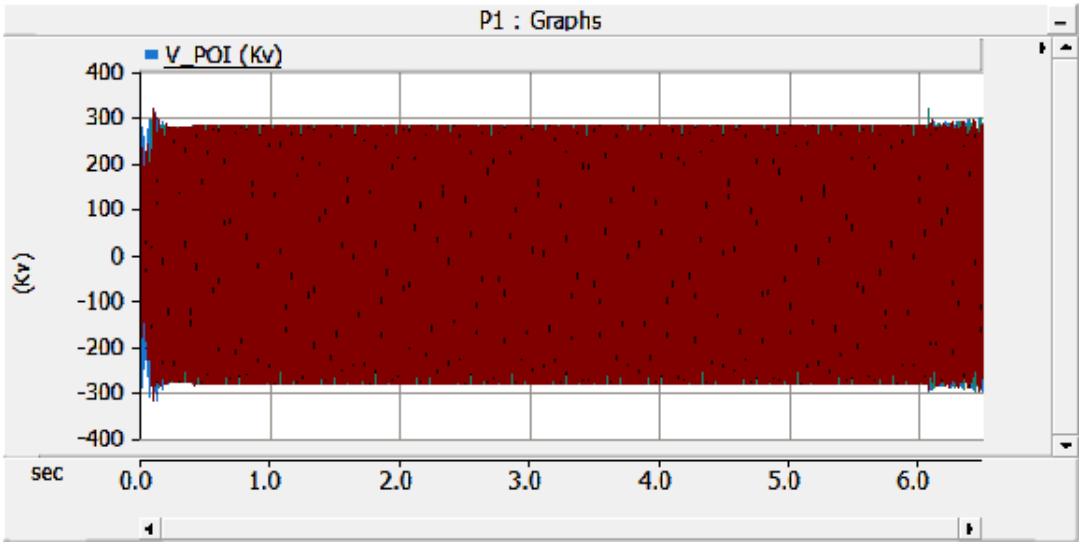

Figure B-41 EMT Simulation, SC7, POI instantaneous voltage

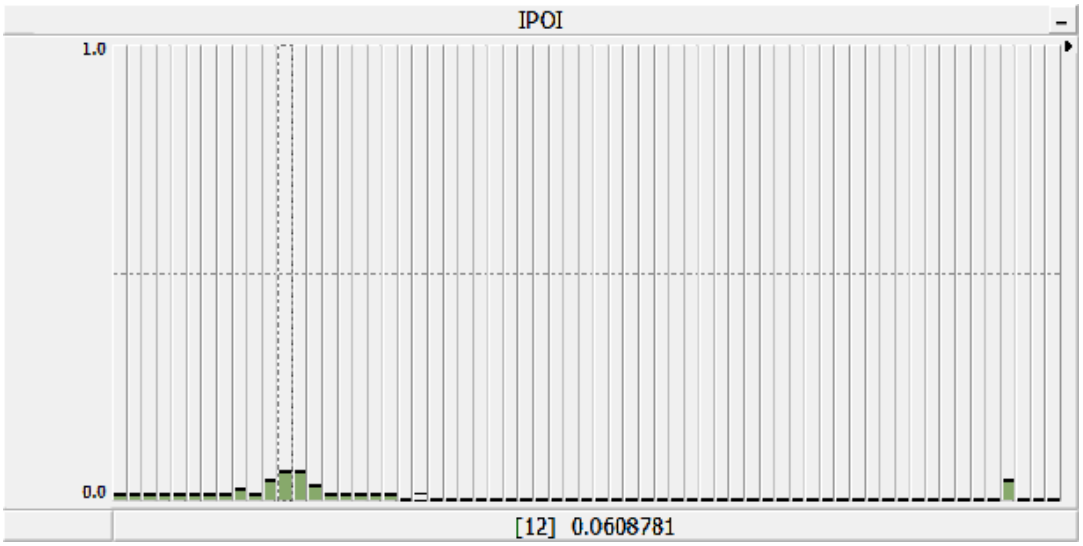

Figure B-42 EMT Simulation, SC7, POI current FFT

SC8: CTG1-D10T100-AllShunt-NoFault

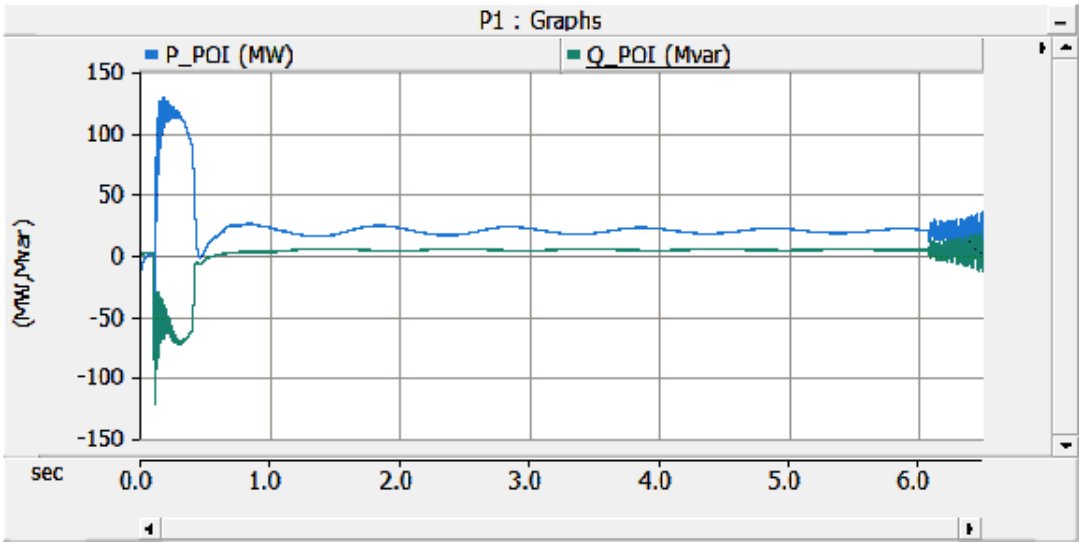

Figure B-43 EMT Simulation, SC8, POI Active & Reactive Power

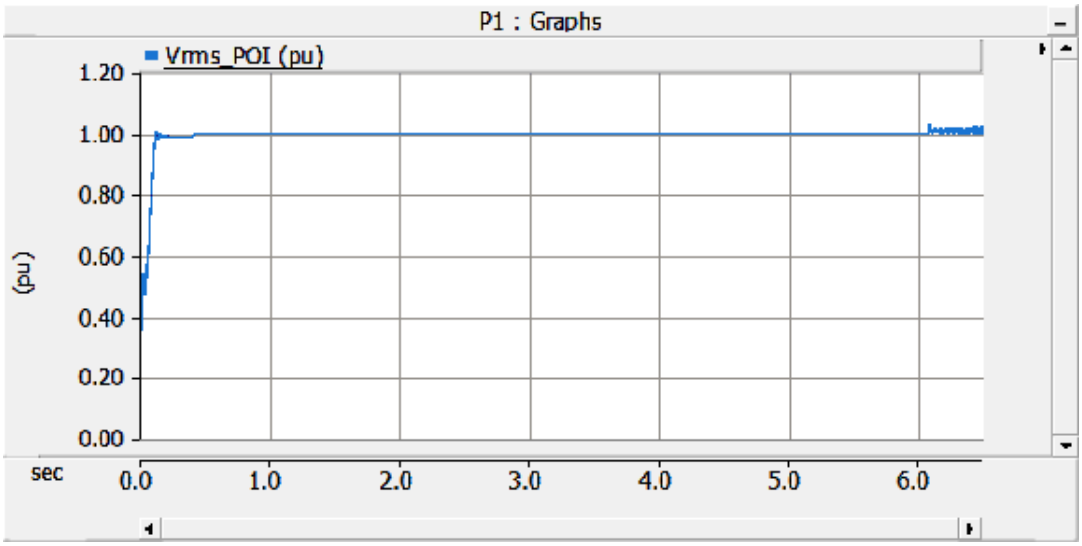

Figure B-44 EMT Simulation, SC8, POI rms voltage

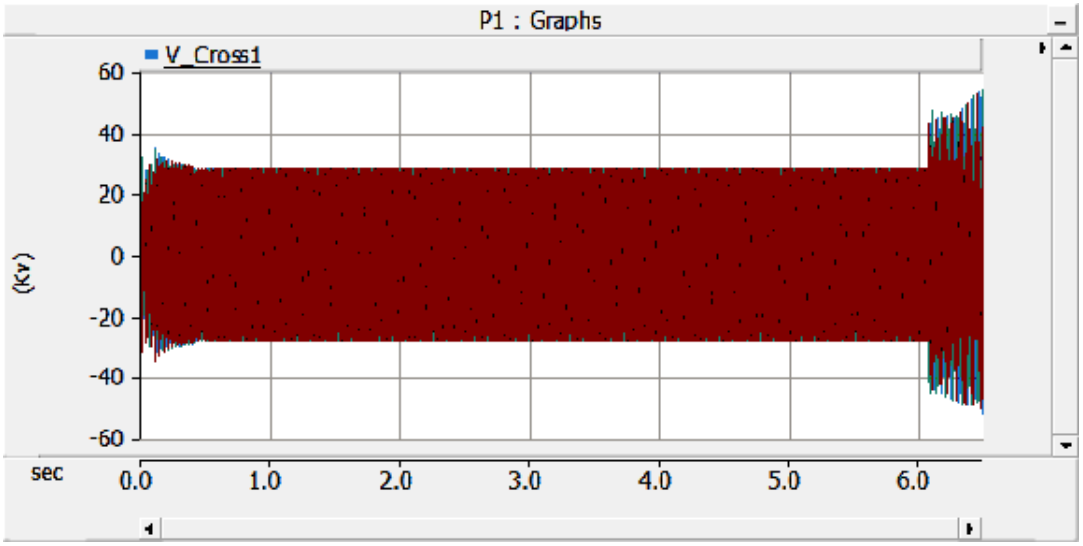

Figure B-45 EMT Simulation, SC8, series capacitor voltage

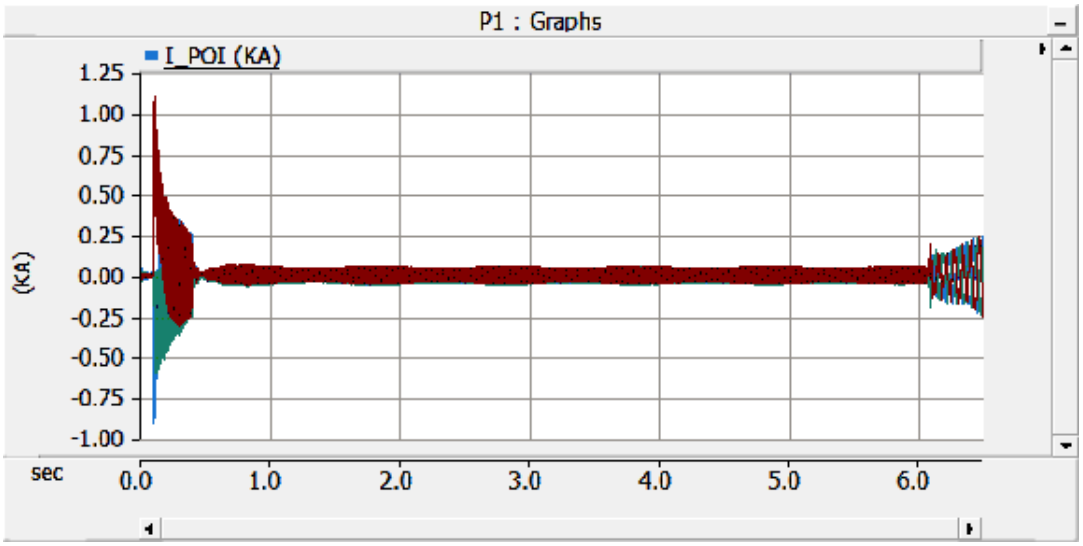

Figure B-46 EMT Simulation, SC8, POI instantaneous current

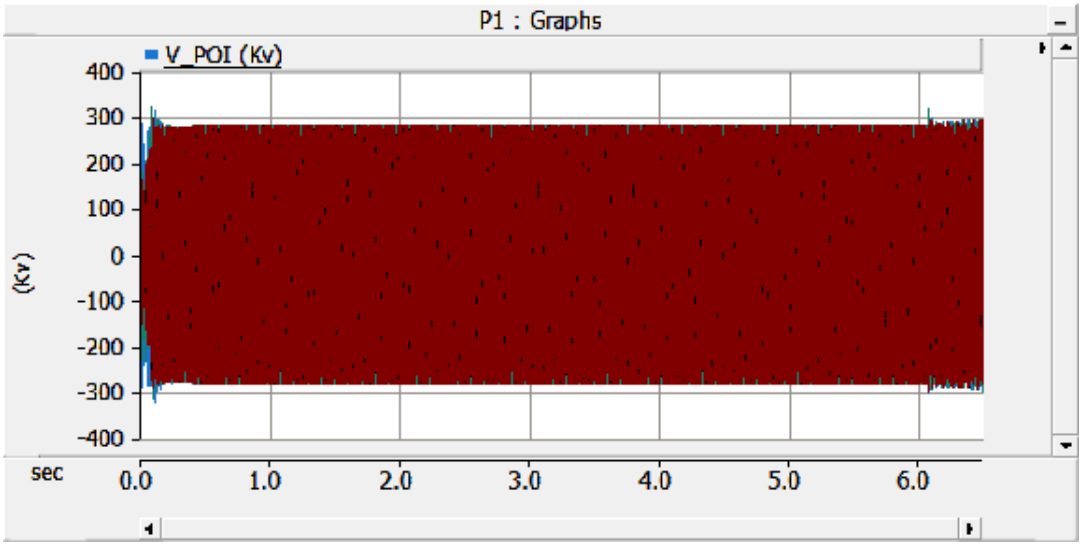

Figure B-47 EMT Simulation, SC8, POI instantaneous voltage

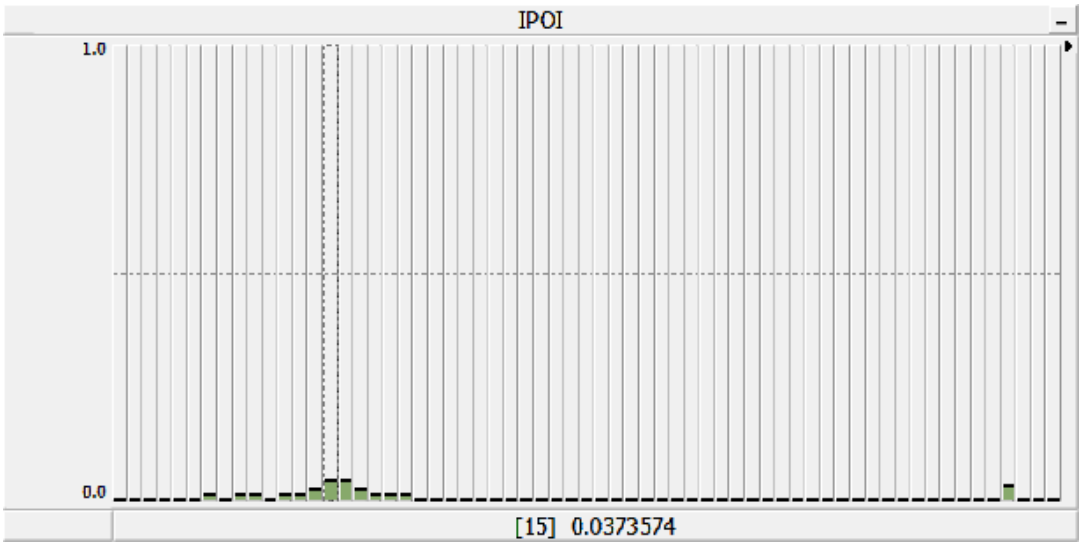

Figure B-48 EMT Simulation, SC8, POI current FFT

SC9: CTG1-D100T10-NoShunt-Fault

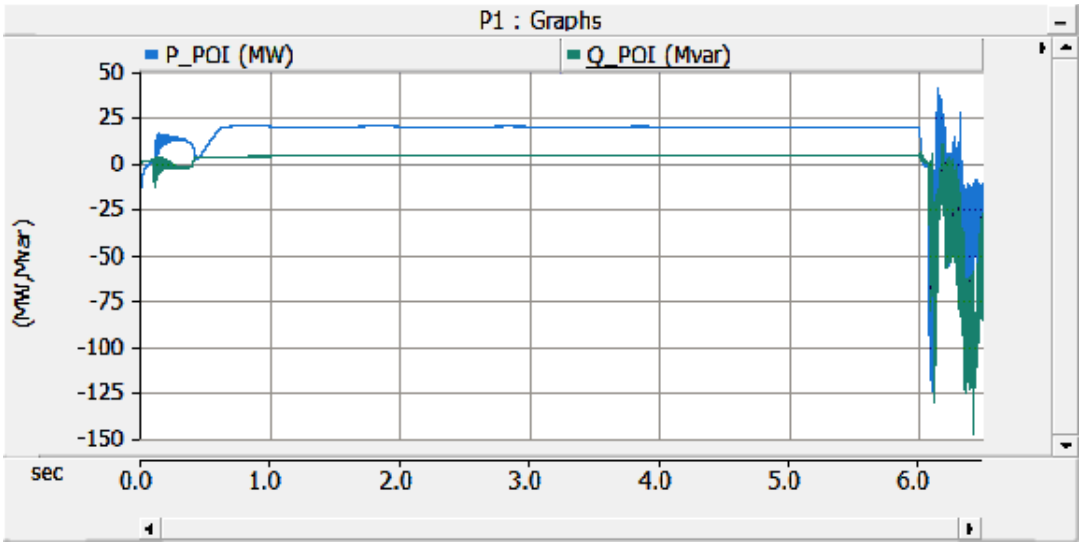

Figure B-49 EMT Simulation, SC9, POI Active & Reactive Power

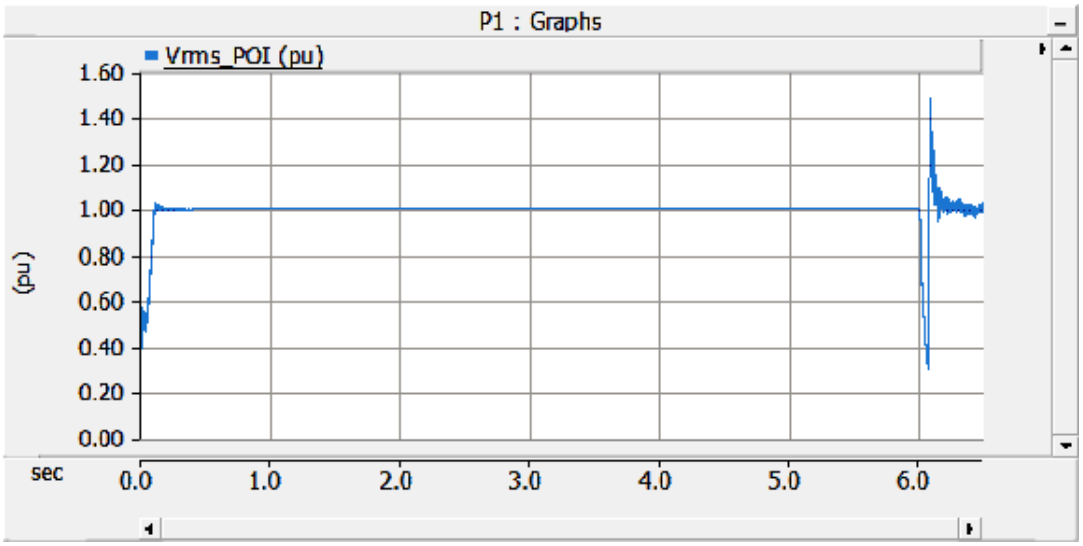

Figure B-50 EMT Simulation, SC9, POI rms voltage

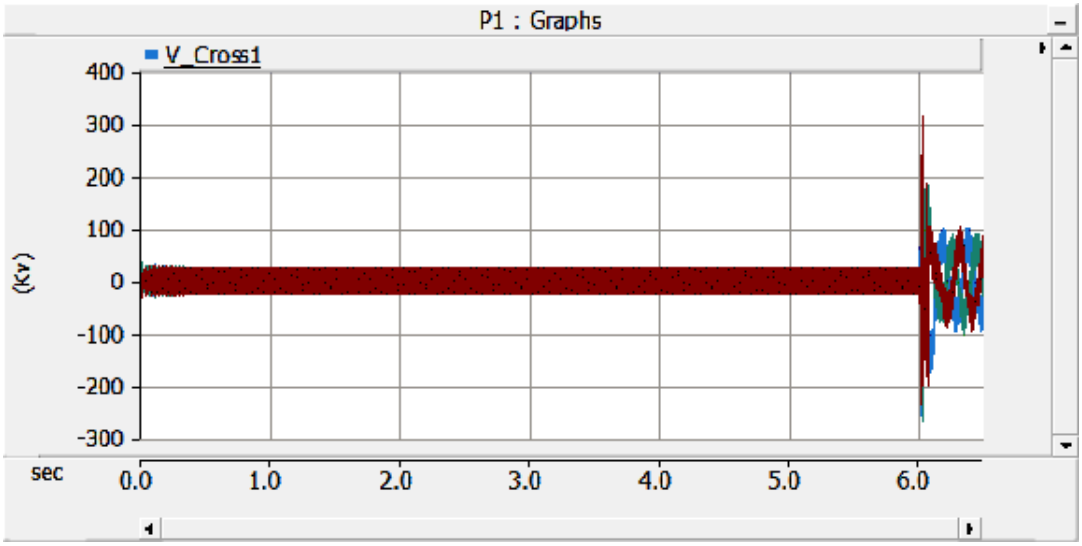

Figure B-51 EMT Simulation, SC9, series capacitor voltage

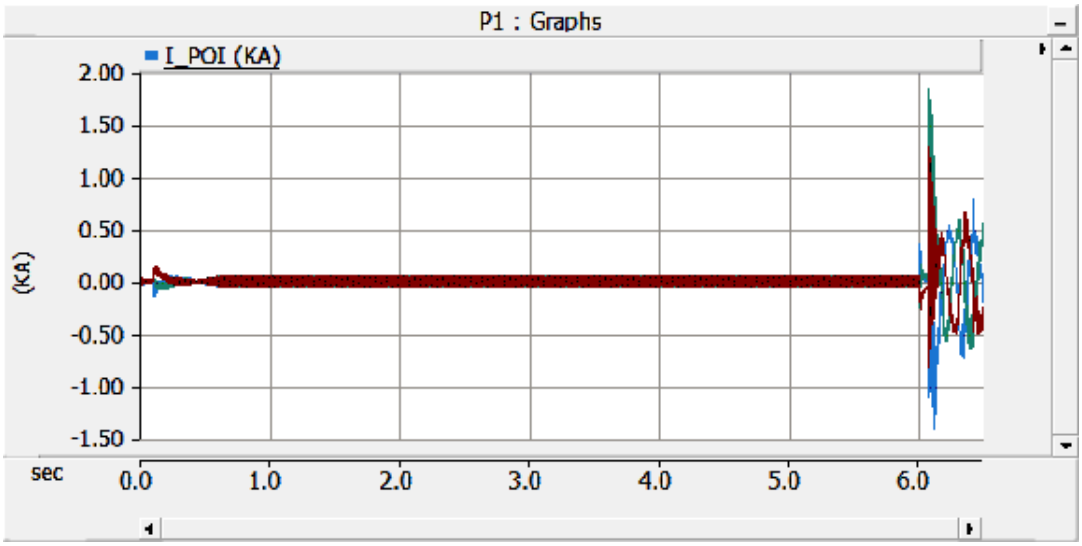

Figure B-52 EMT Simulation, SC9, POI instantaneous current

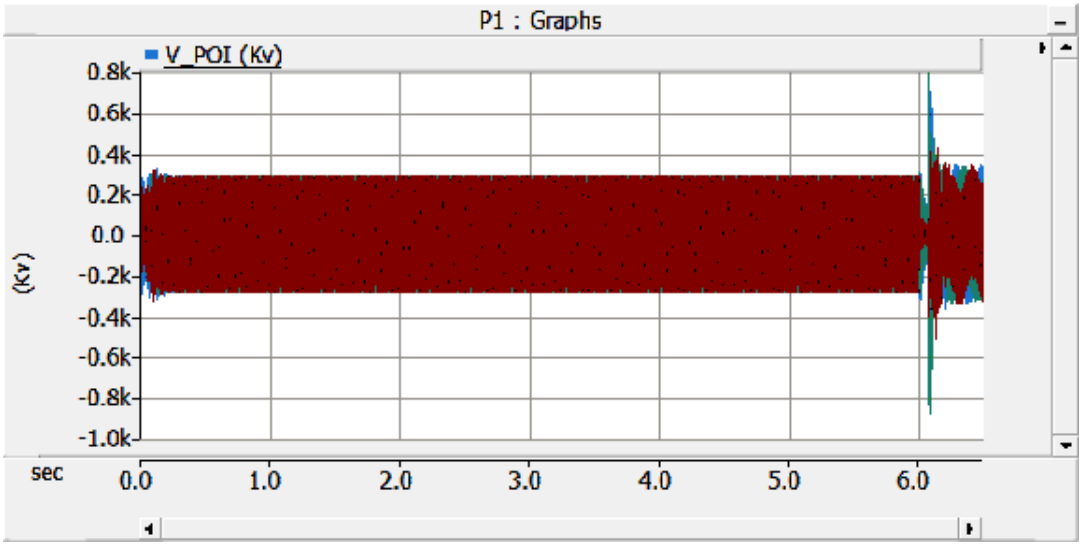

Figure B-53 EMT Simulation, SC9, POI instantaneous voltage

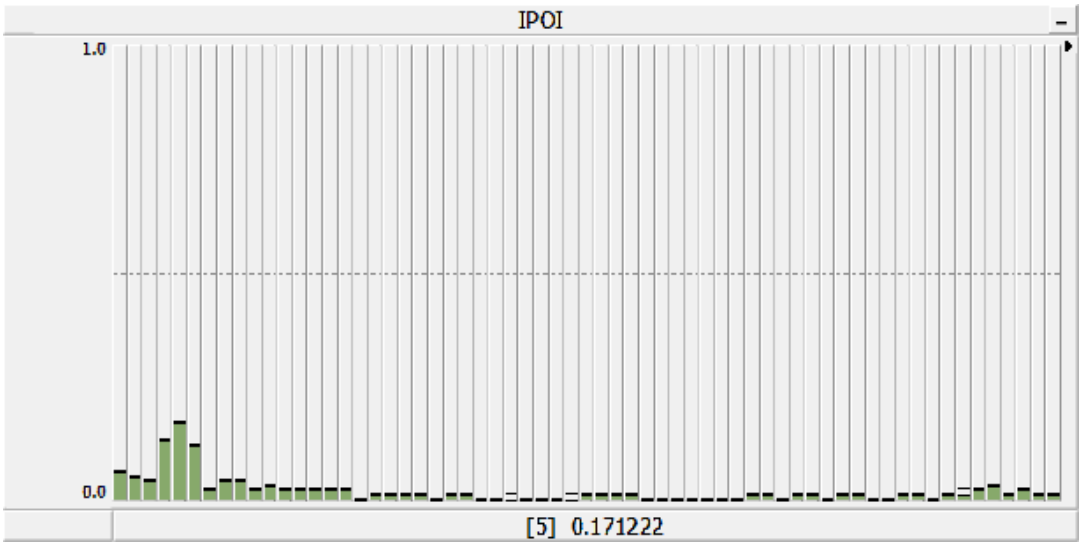

Figure B-54 EMT Simulation, SC9, POI current FFT

SC10: CTG1-D100T10-AllShunt-Fault

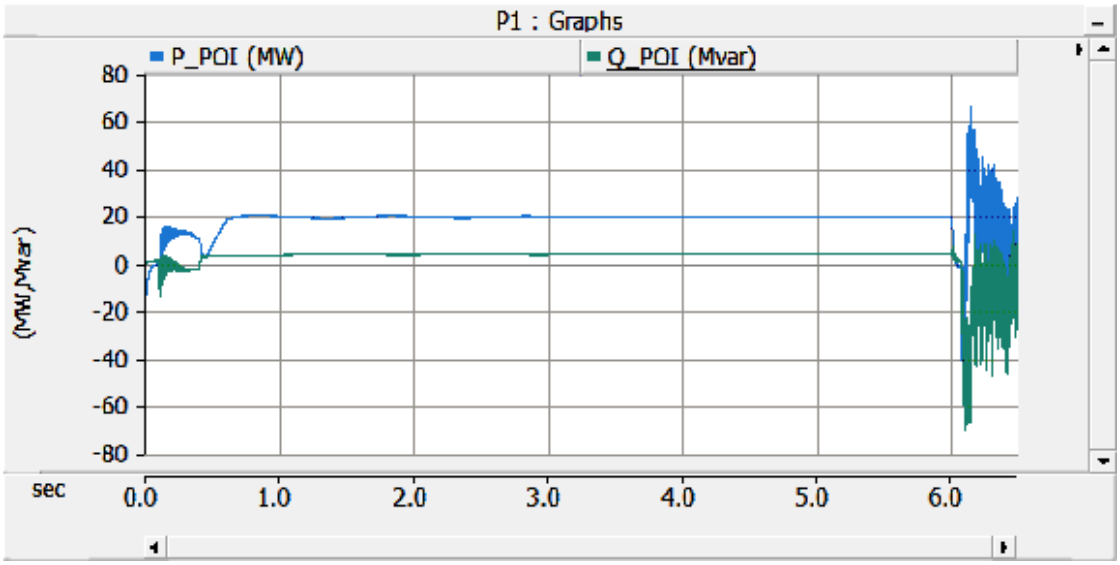

Figure B-55 EMT Simulation, SC10, POI Active & Reactive Power

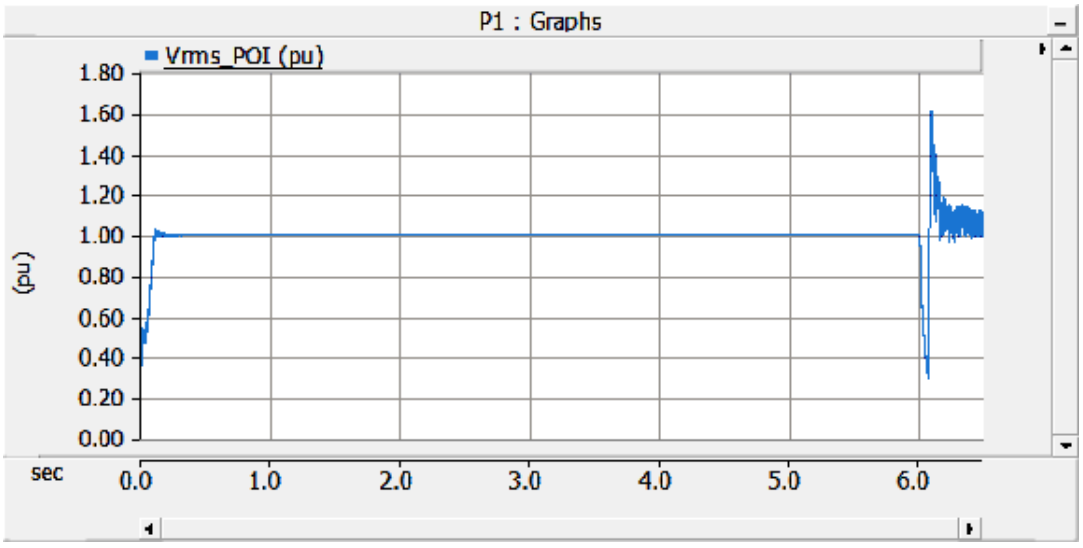

Figure B-56 EMT Simulation, SC10, POI rms voltage

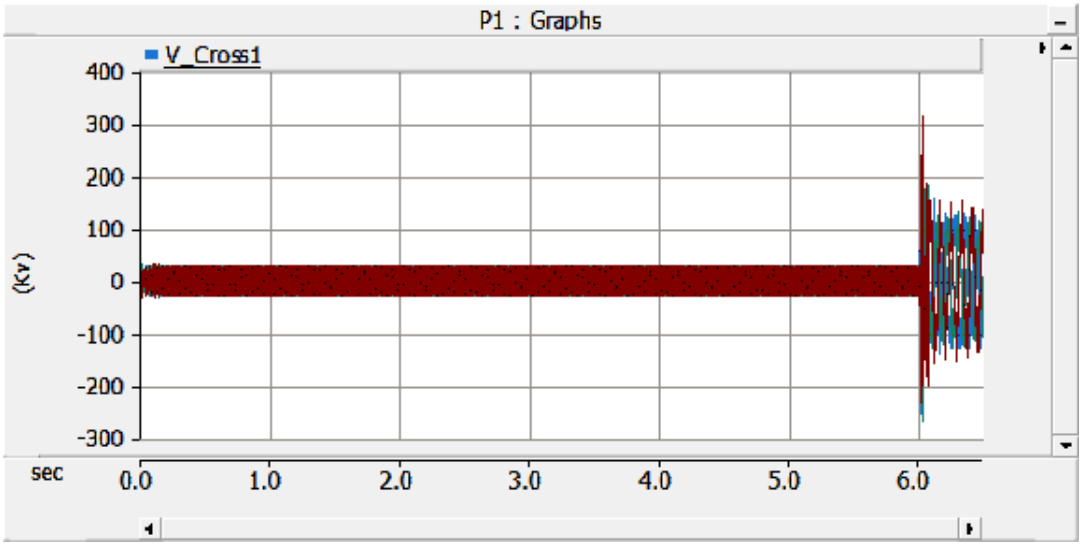

Figure B-57 EMT Simulation, SC10, series capacitor voltage

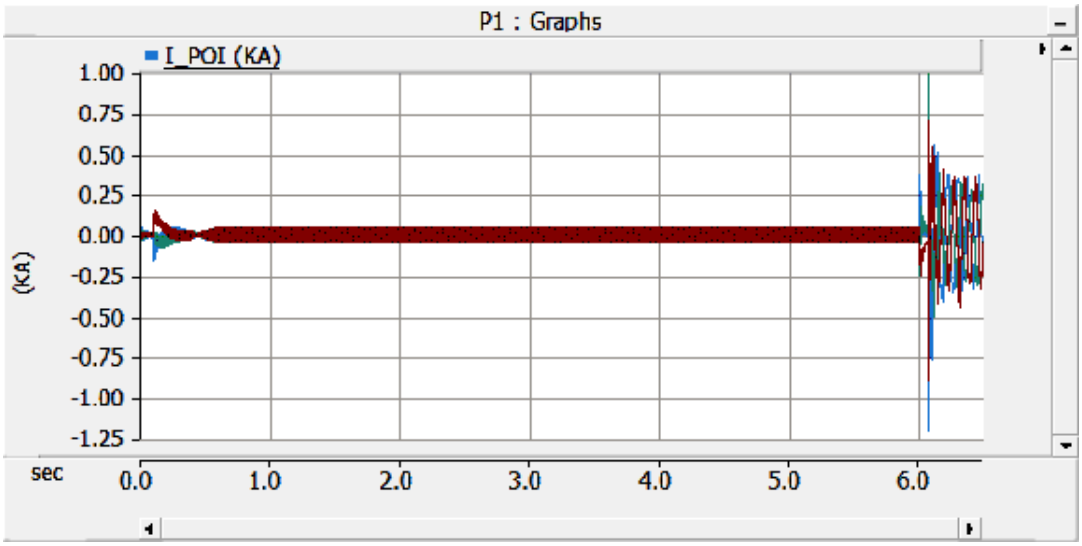

Figure B-58 EMT Simulation, SC10, POI instantaneous current

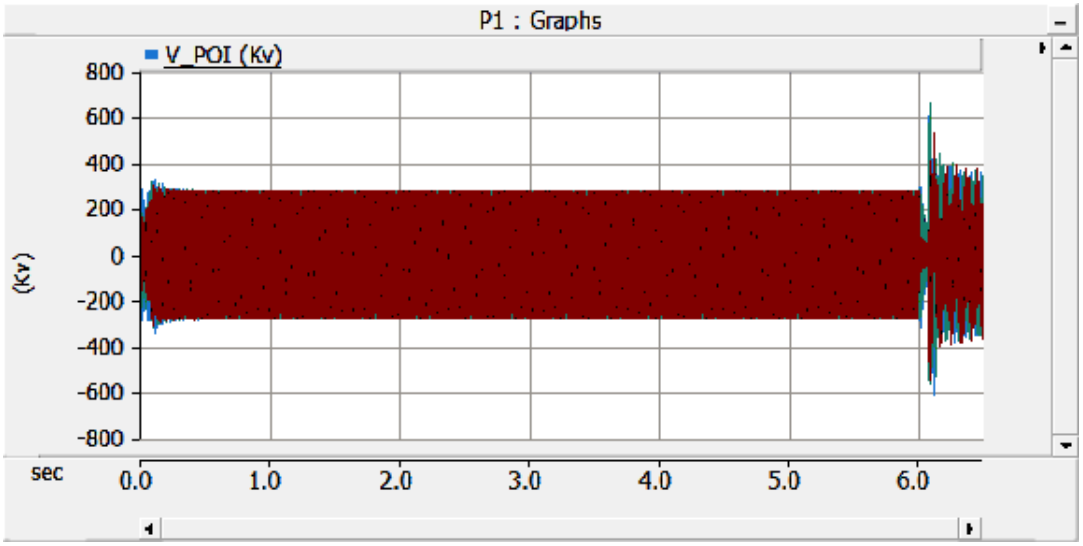

Figure B-59 EMT Simulation, SC10, POI instantaneous voltage

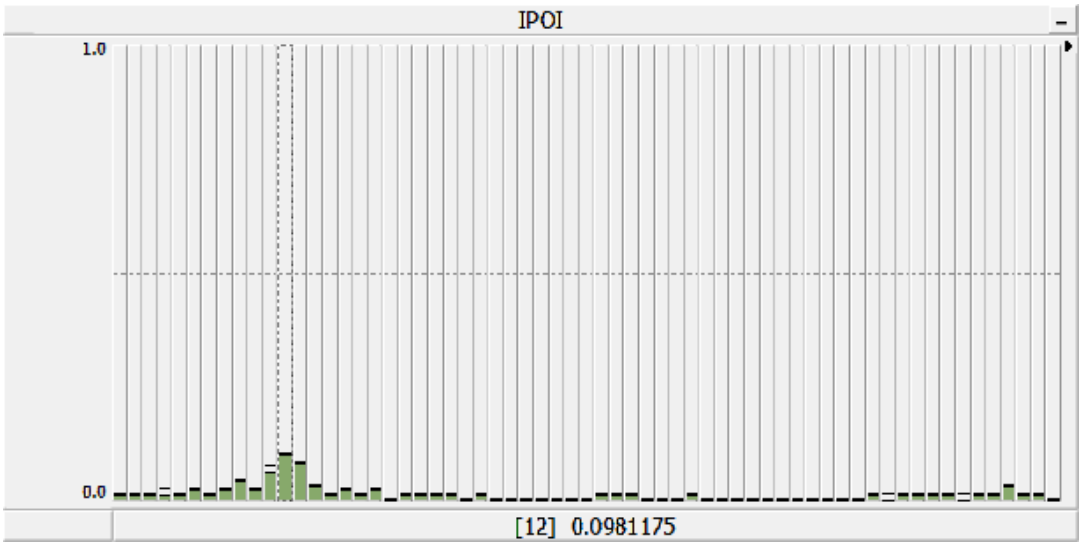

Figure B-60 EMT Simulation, SC10, POI current FFT

SC11: CTG1-D100T10-NoShunt-NoFault

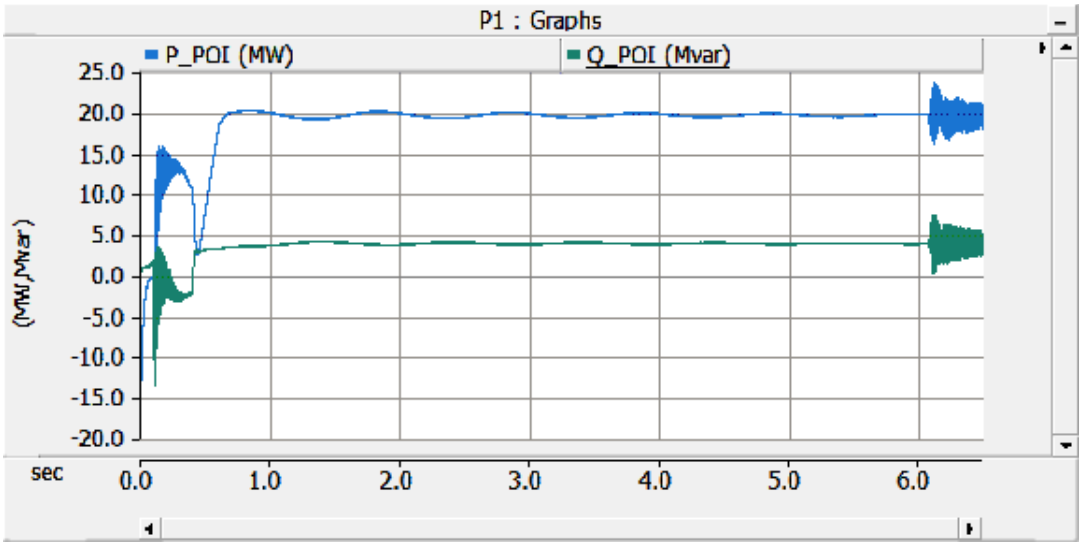

Figure B-61 EMT Simulation, SC11, POI Active & Reactive Power

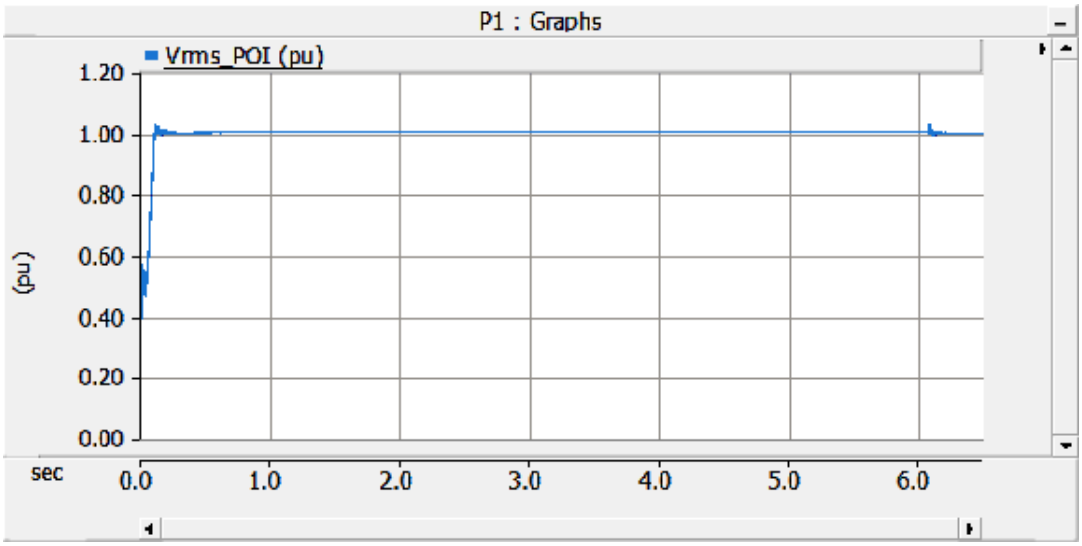

Figure B-62 EMT Simulation, SC11, POI rms voltage

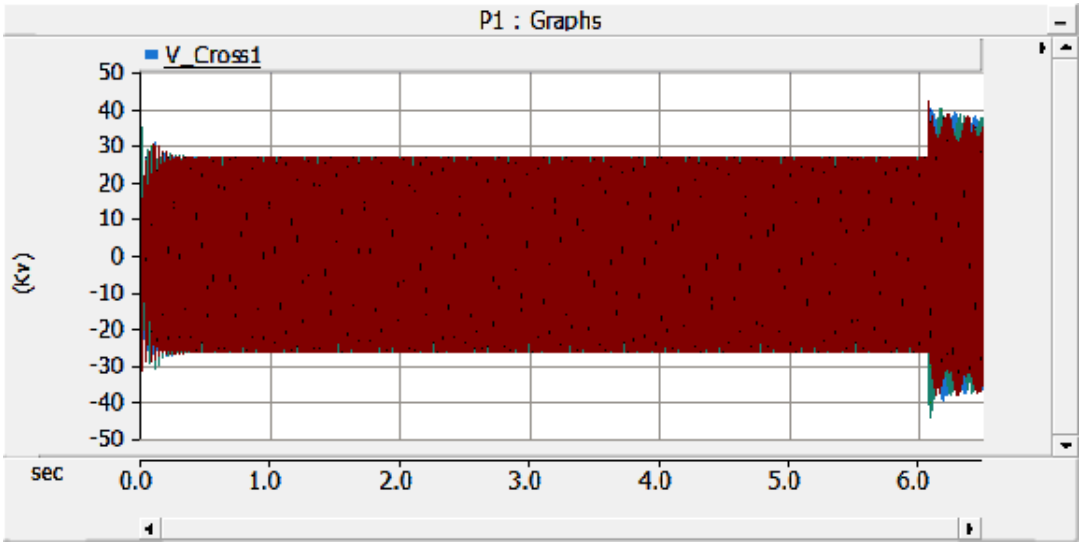

Figure B-63 EMT Simulation, SC11, series capacitor voltage

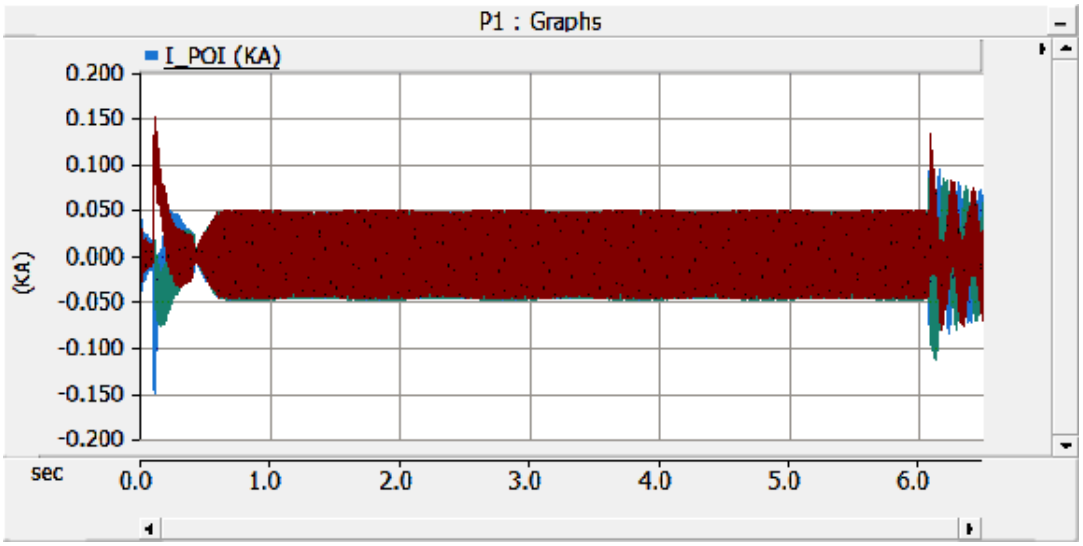

Figure B-64 EMT Simulation, SC11, POI instantaneous current

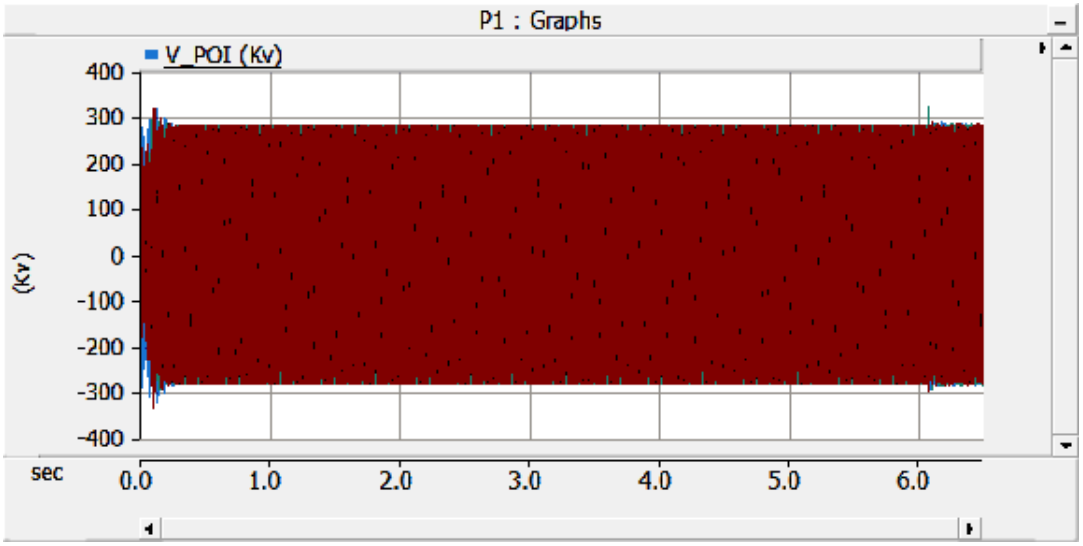

Figure B-65 EMT Simulation, SC11, POI instantaneous voltage

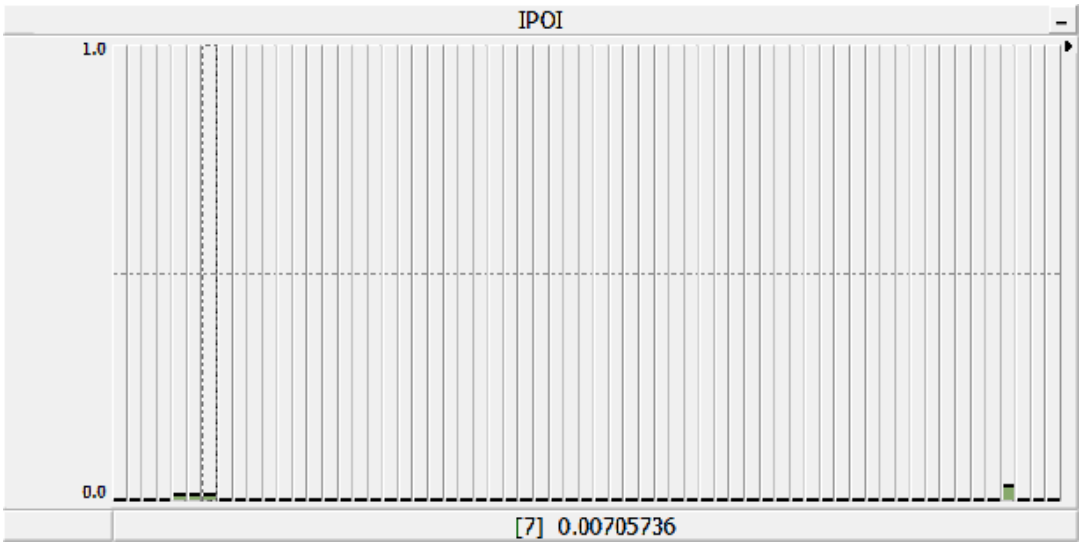

Figure B-66 EMT Simulation, SC11, POI current FFT

SC12: CTG1-D100T10-AllShunt-NoFault

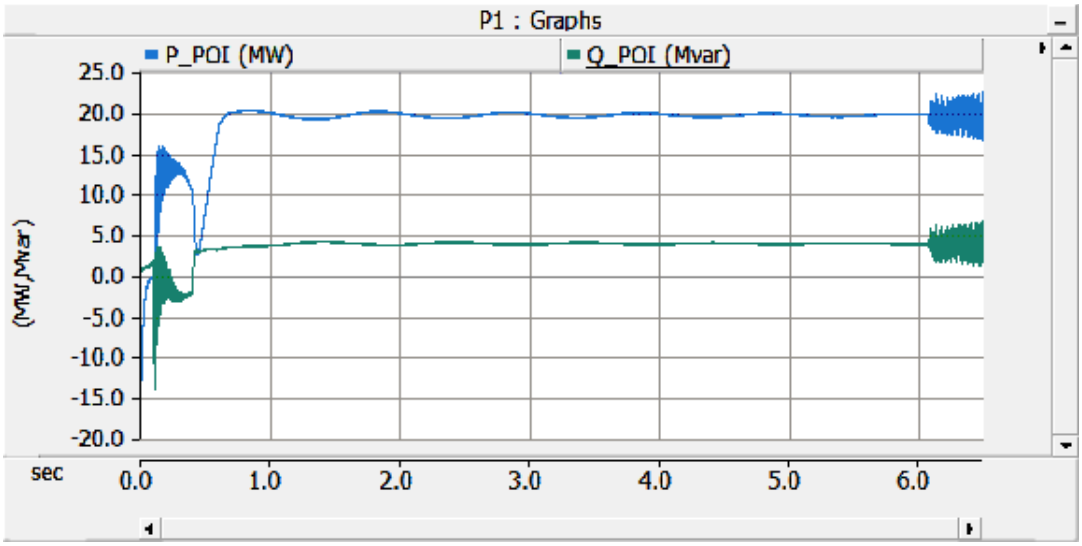

Figure B-67 EMT Simulation, SC12, POI Active & Reactive Power

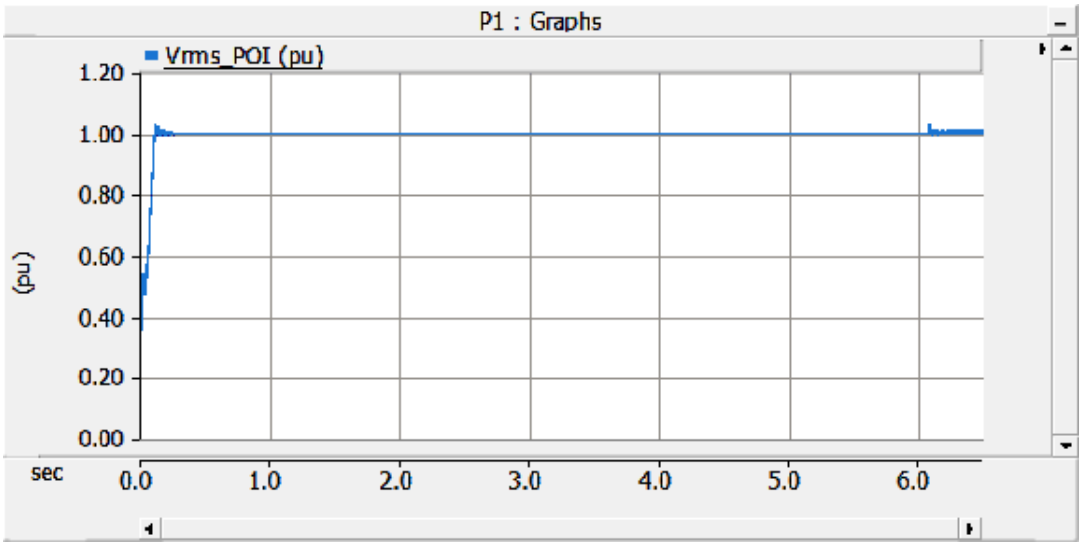

Figure B-68 EMT Simulation, SC12, POI rms voltage

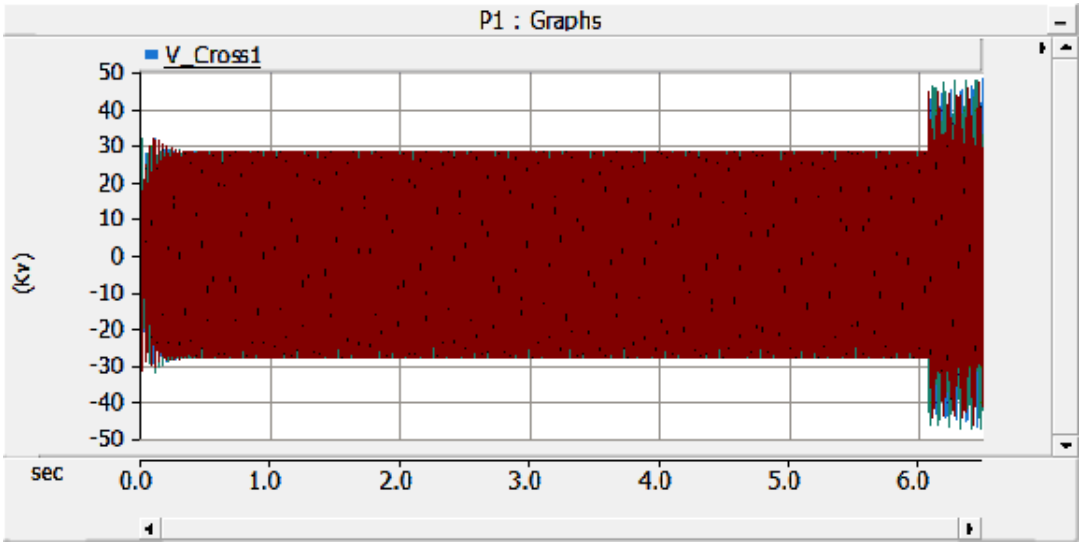

Figure B-69 EMT Simulation, SC12, series capacitor voltage

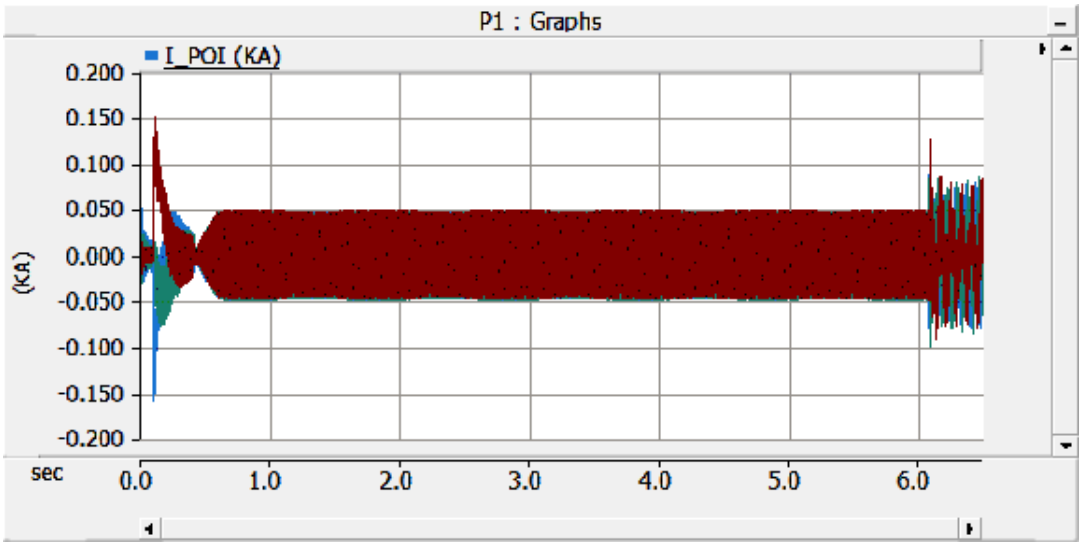

Figure B-70 EMT Simulation, SC12, POI instantaneous current

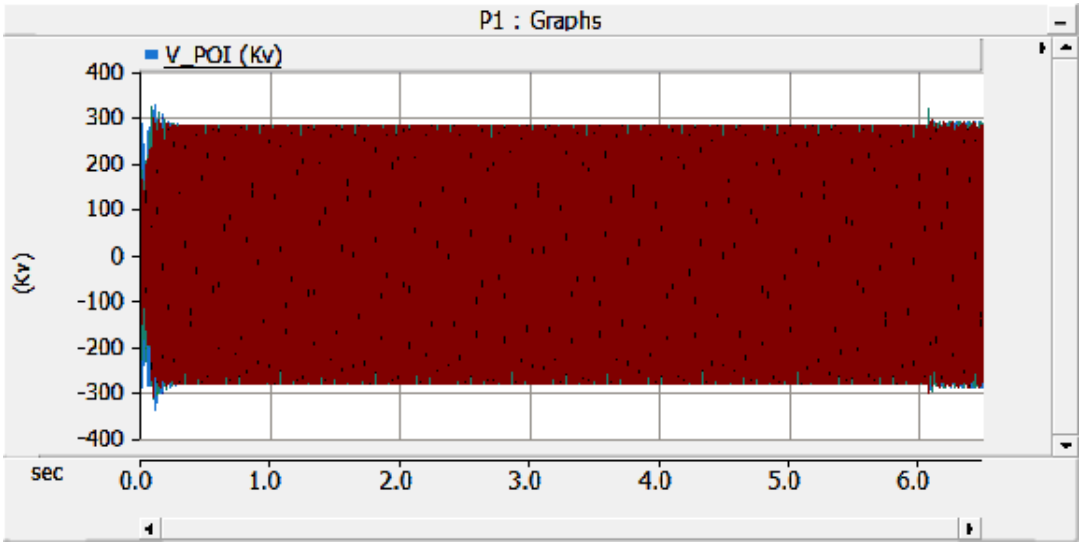

Figure B-71 EMT Simulation, SC12, POI instantaneous voltage

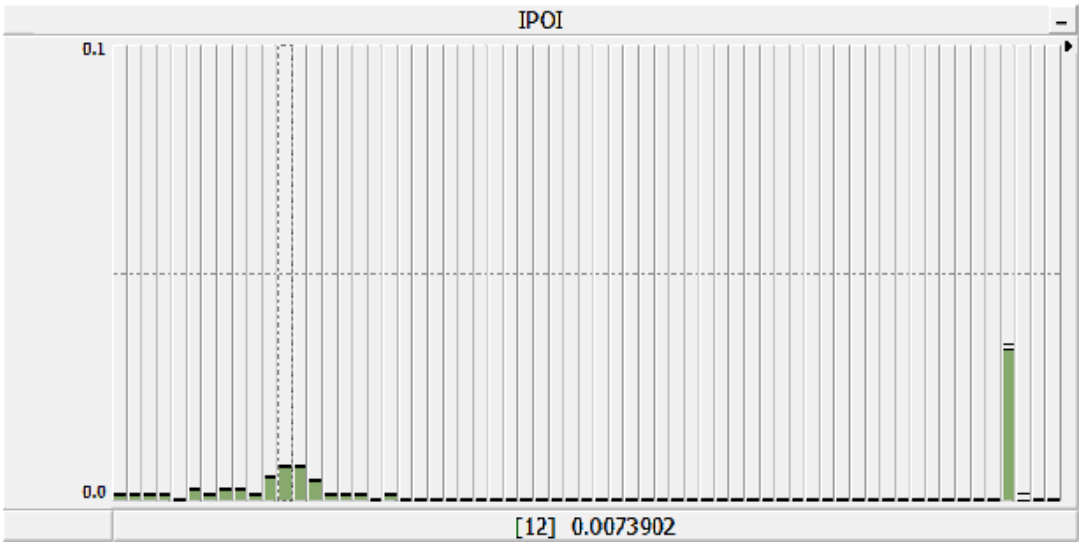

Figure B-72 EMT Simulation, SC12, POI current FFT

SC13: CTG2-D100T100-NoShunt-Fault

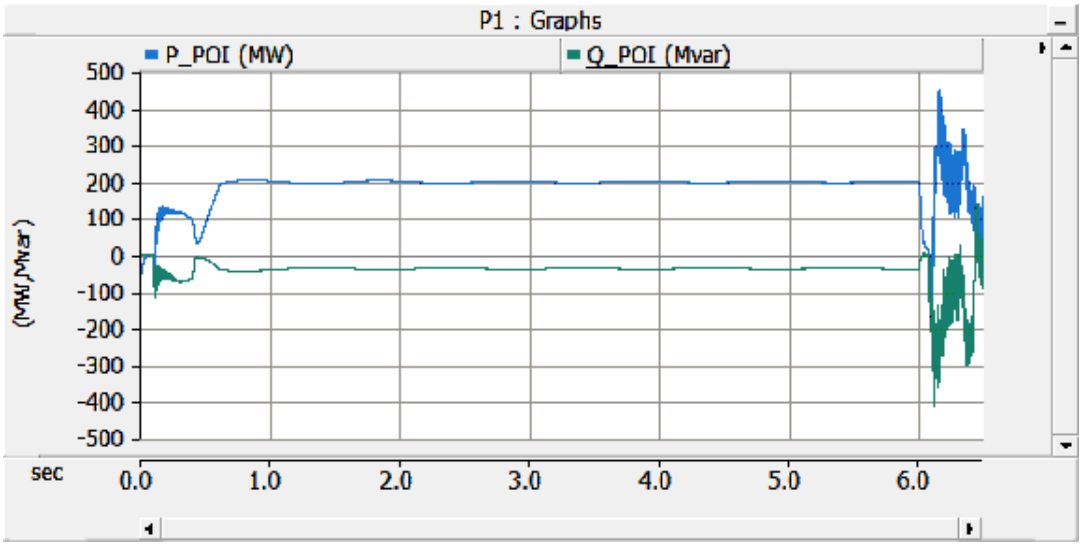

Figure B-73 EMT Simulation, SC13, POI Active & Reactive Power

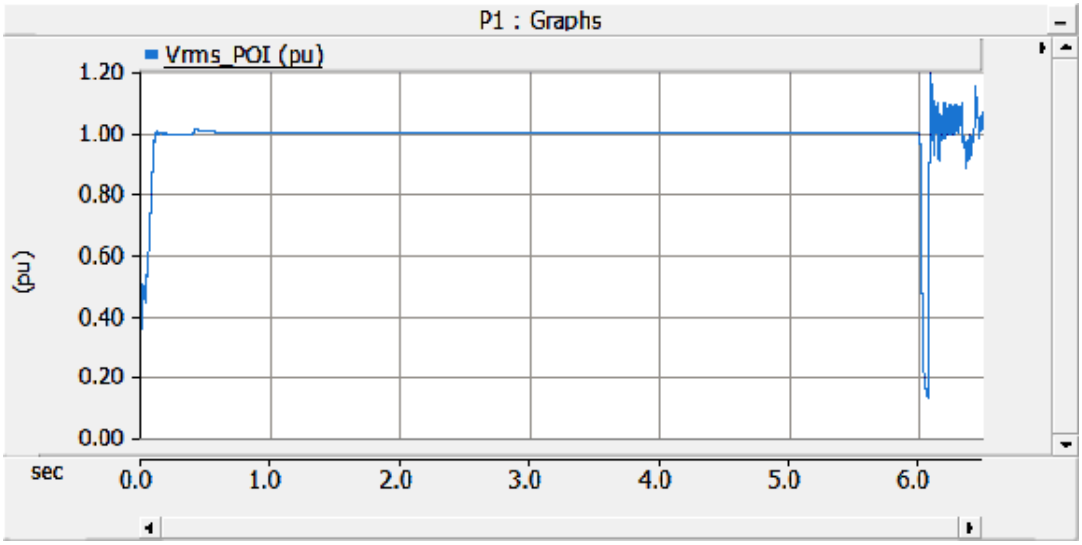

Figure B-74 EMT Simulation, SC13, POI rms voltage

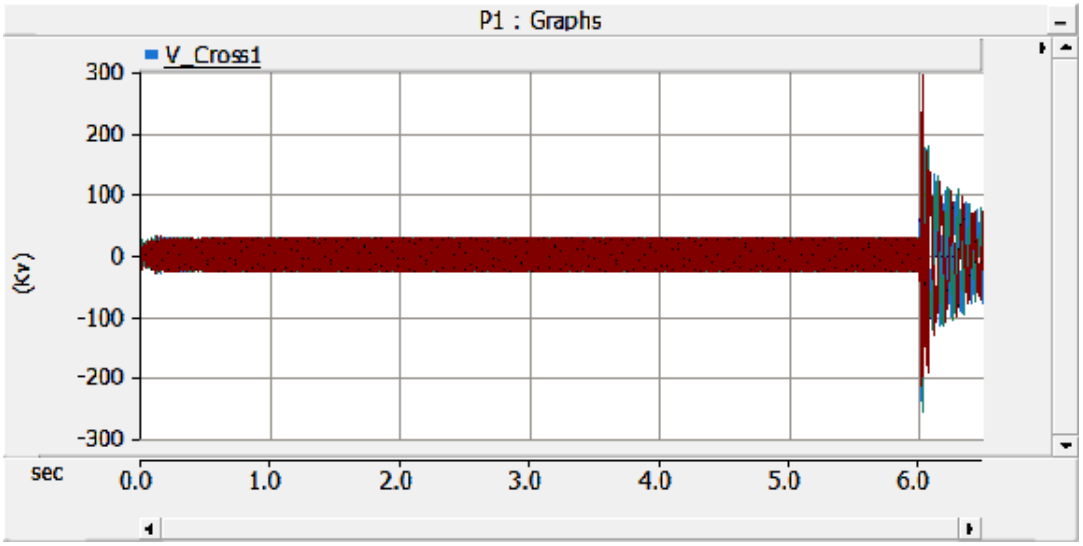

Figure B-75 EMT Simulation, SC13, series capacitor voltage

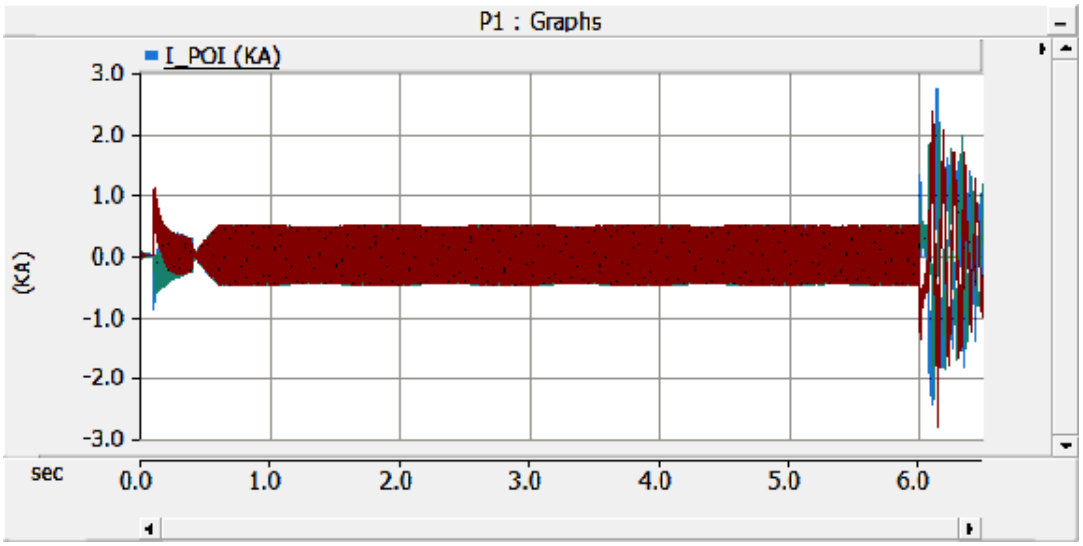

Figure B-76 EMT Simulation, SC13, POI instantaneous current

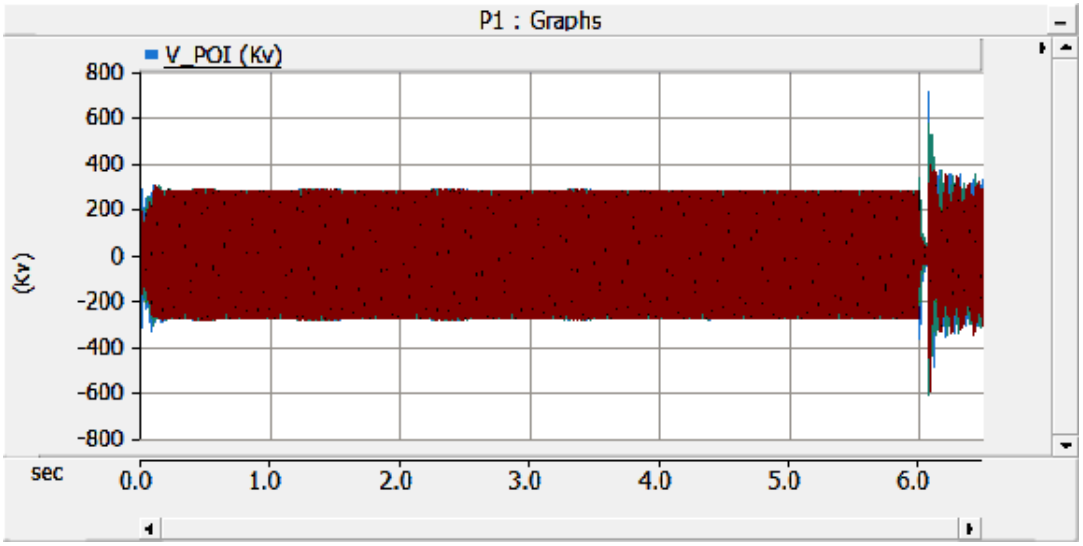

Figure B-77 EMT Simulation, SC13, POI instantaneous voltage

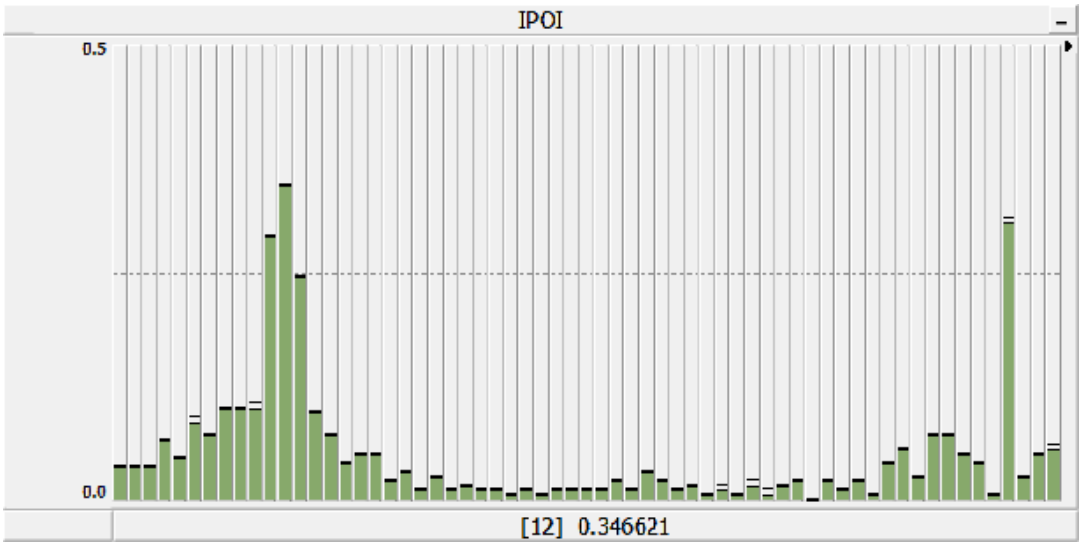

Figure B-78 EMT Simulation, SC13, POI current FFT

SC14: CTG2-D100T100-AllShunt-Fault

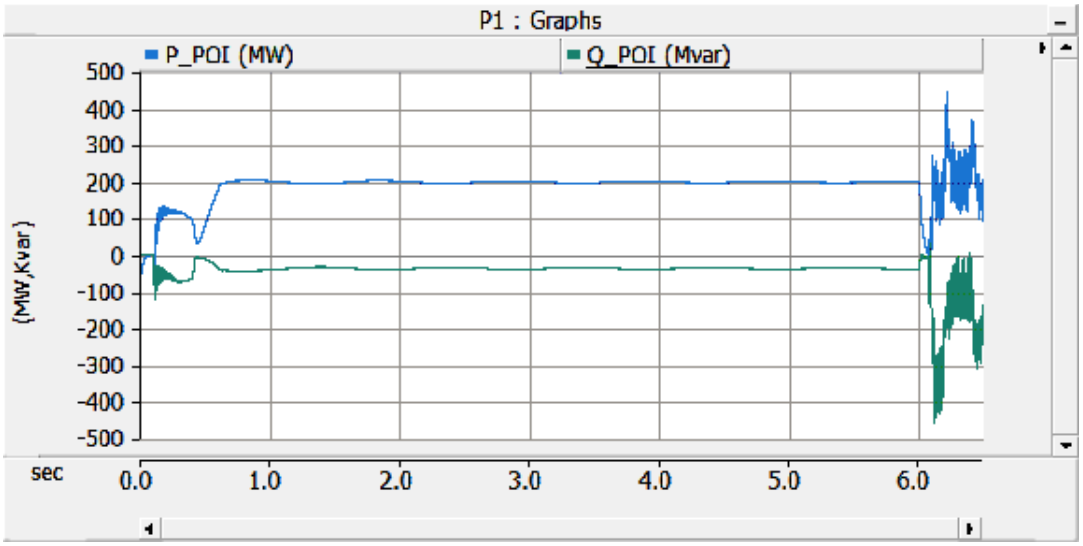

Figure B-79 EMT Simulation, SC14, POI Active & Reactive Power

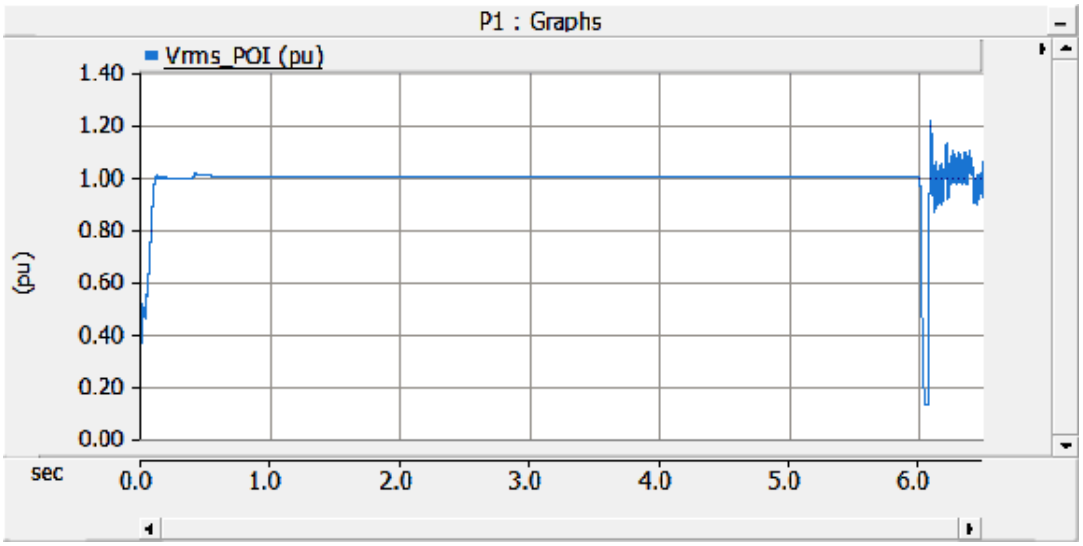

Figure B-80 EMT Simulation, SC14, POI rms voltage

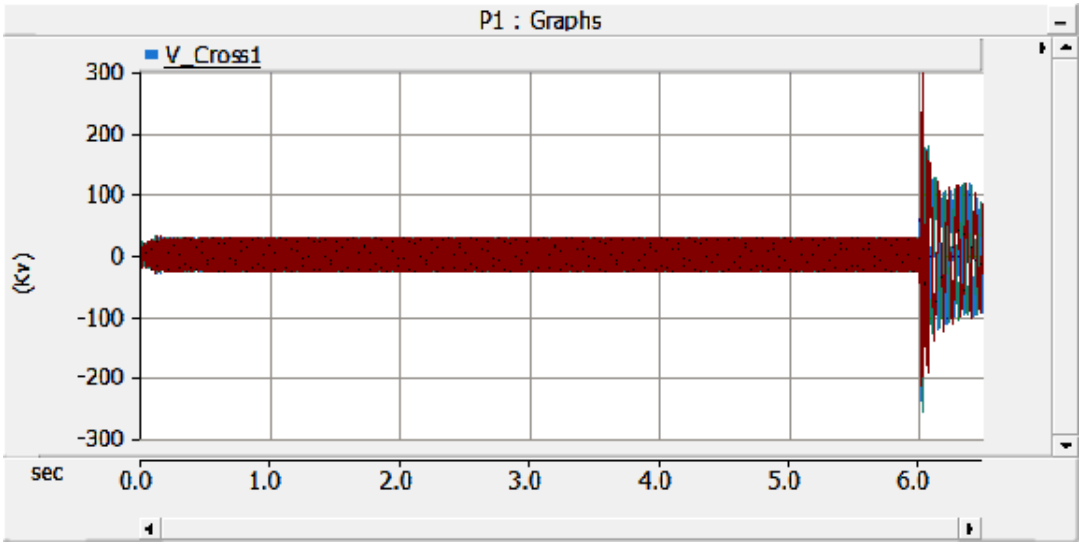

Figure B-81 EMT Simulation, SC14, series capacitor voltage

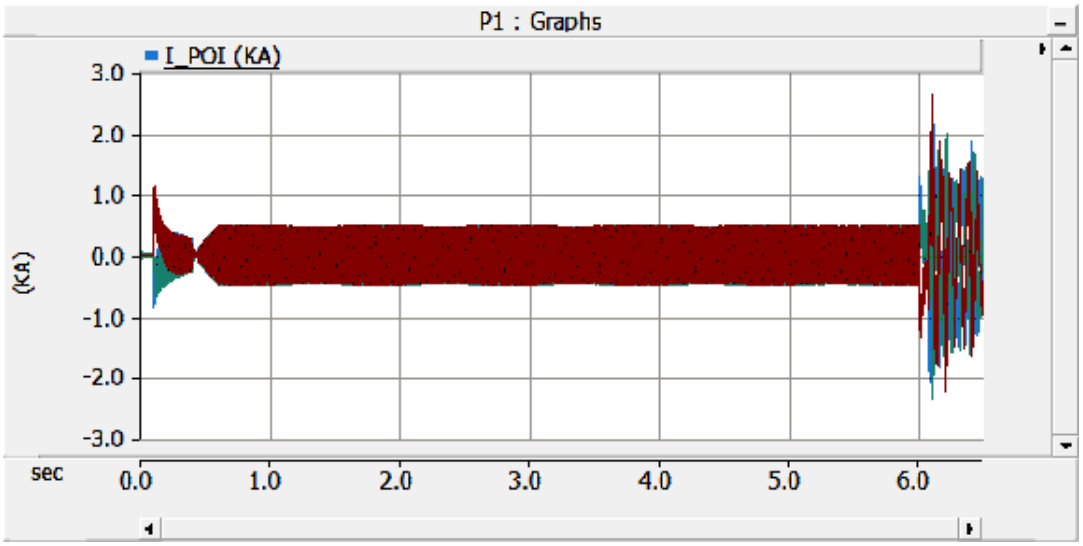

Figure B-82 EMT Simulation, SC14, POI instantaneous current

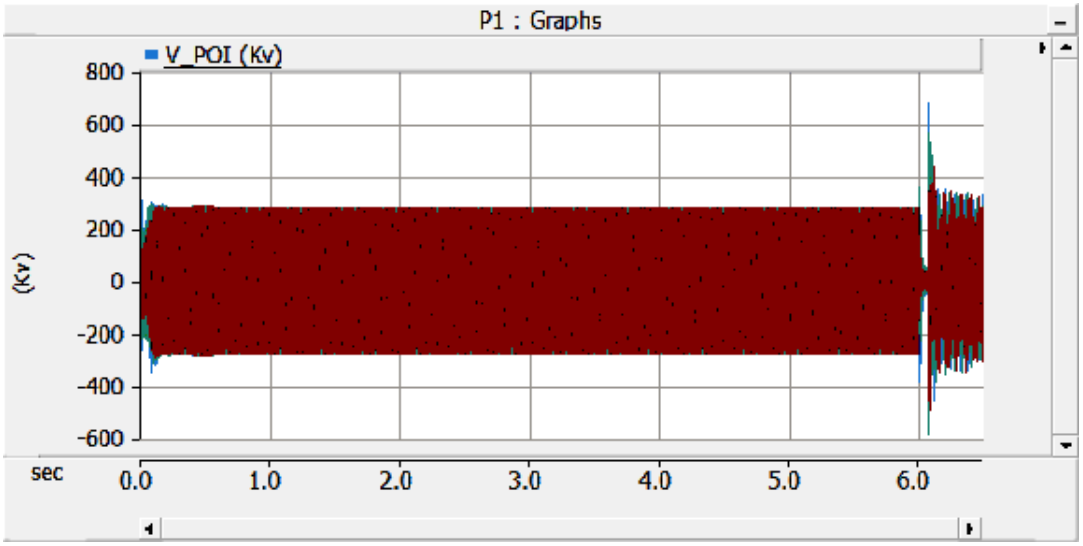

Figure B-83 EMT Simulation, SC14, POI instantaneous voltage

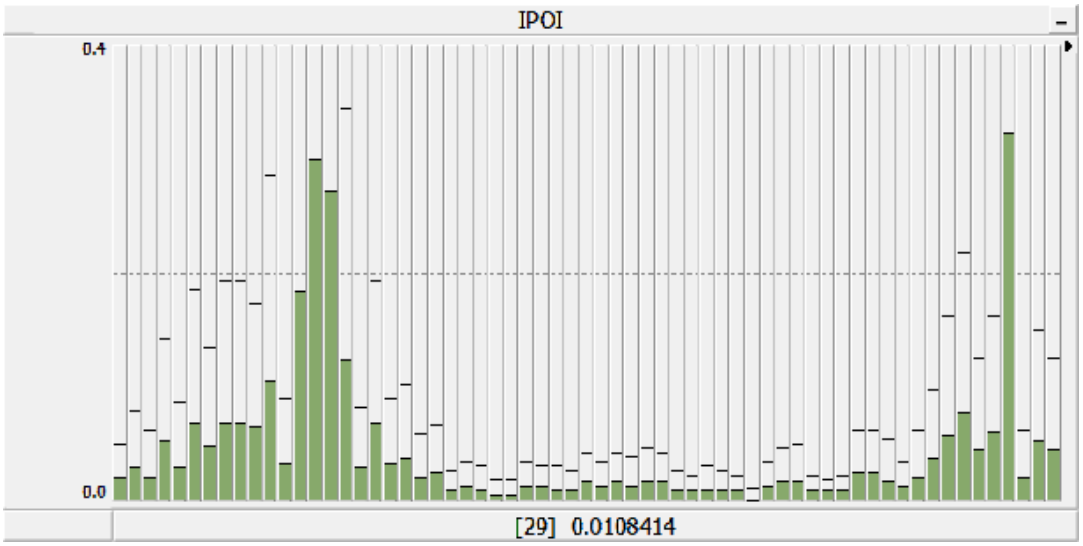

Figure B-84 EMT Simulation, SC14, POI current FFT

SC15: CTG2-D100T100-NoShunt-NoFault

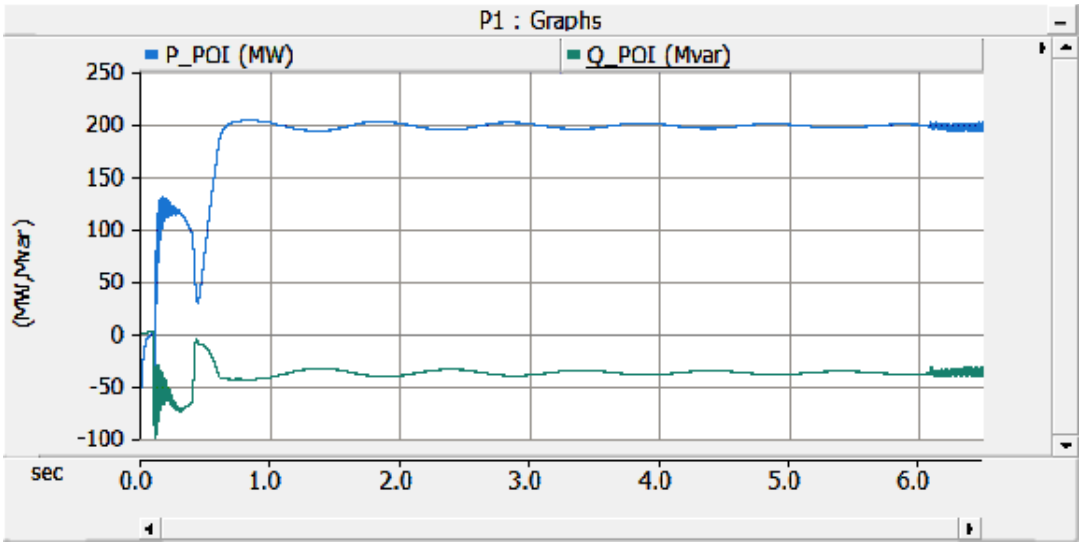

Figure B-85 EMT Simulation, SC15, POI Active & Reactive Power

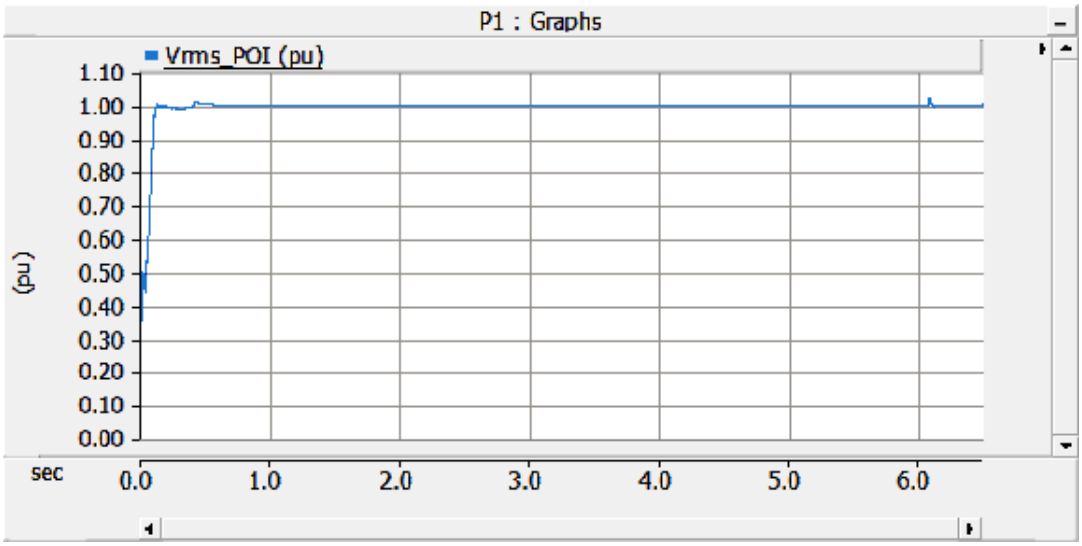

Figure B-86 EMT Simulation, SC15, POI rms voltage

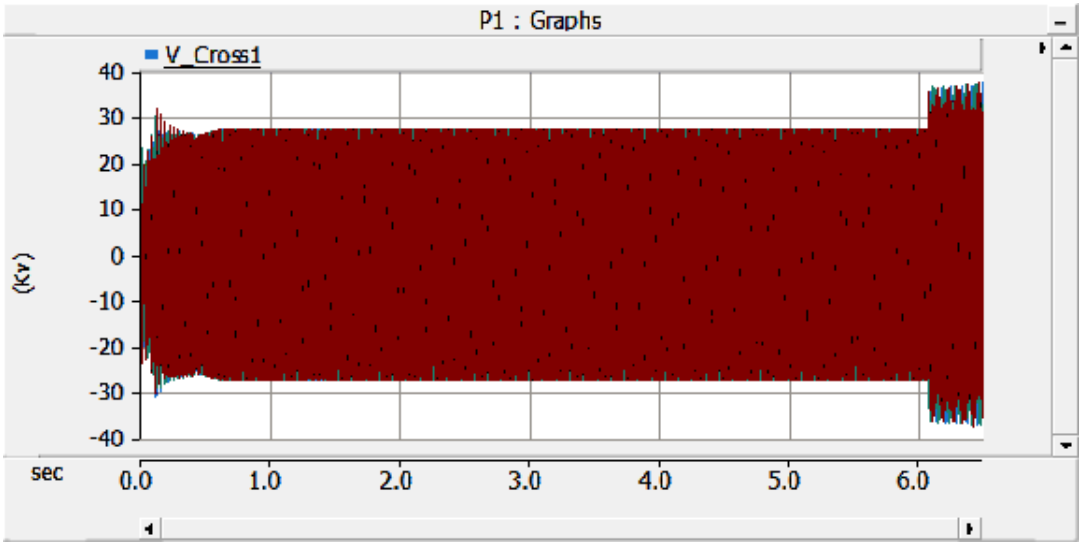

Figure B-87 EMT Simulation, SC15, series capacitor voltage

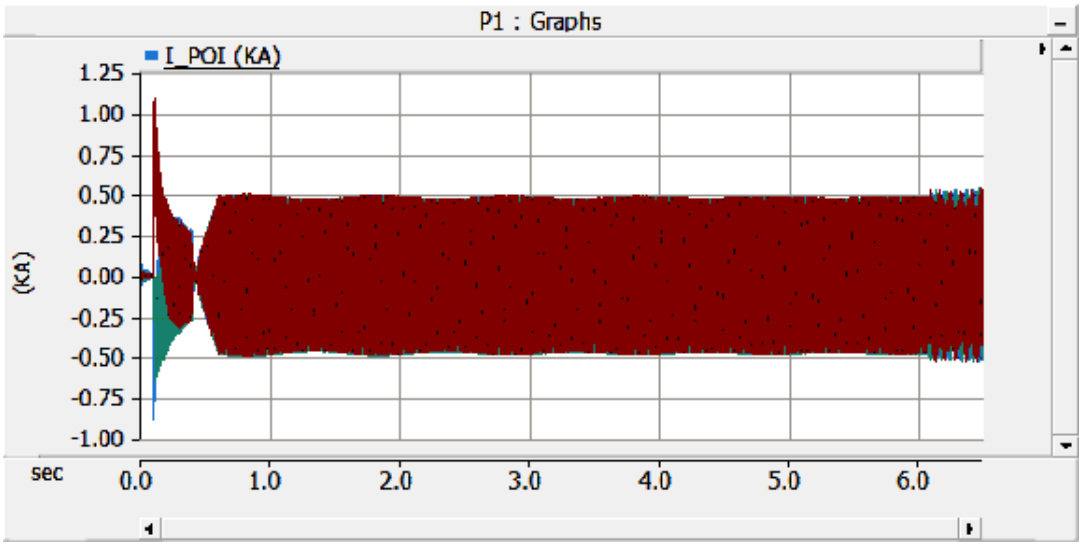

Figure B-88 EMT Simulation, SC15, POI instantaneous current

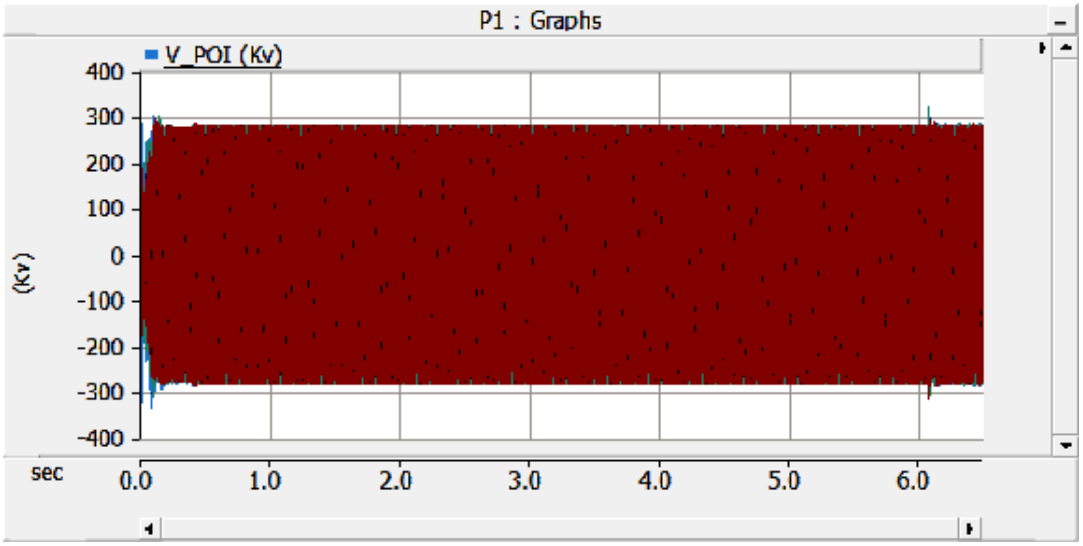

Figure B-89 EMT Simulation, SC15, POI instantaneous voltage

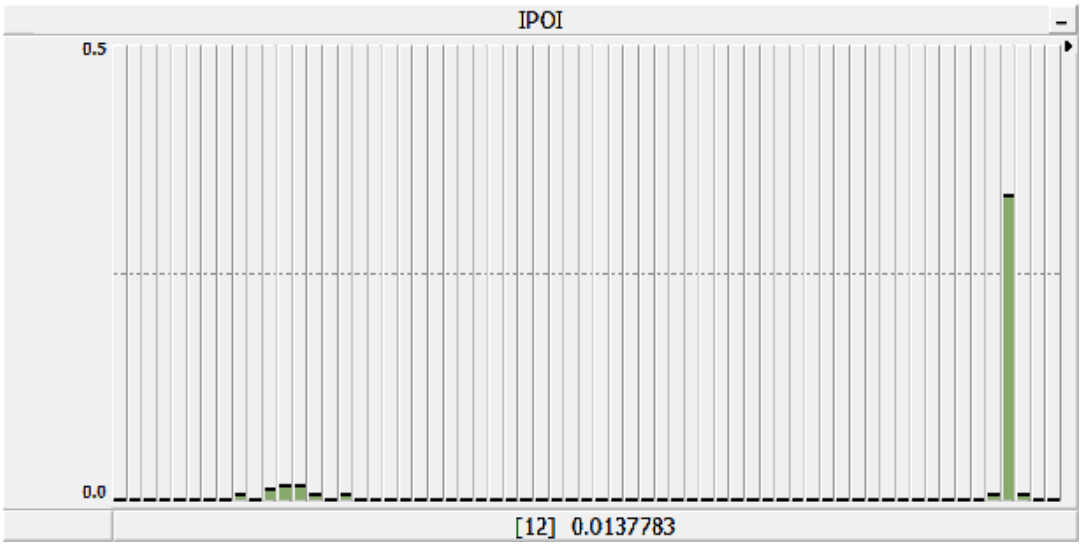

Figure B-90 EMT Simulation, SC15, POI current FFT

SC16: CTG2-D100T100-AllShunt-NoFault

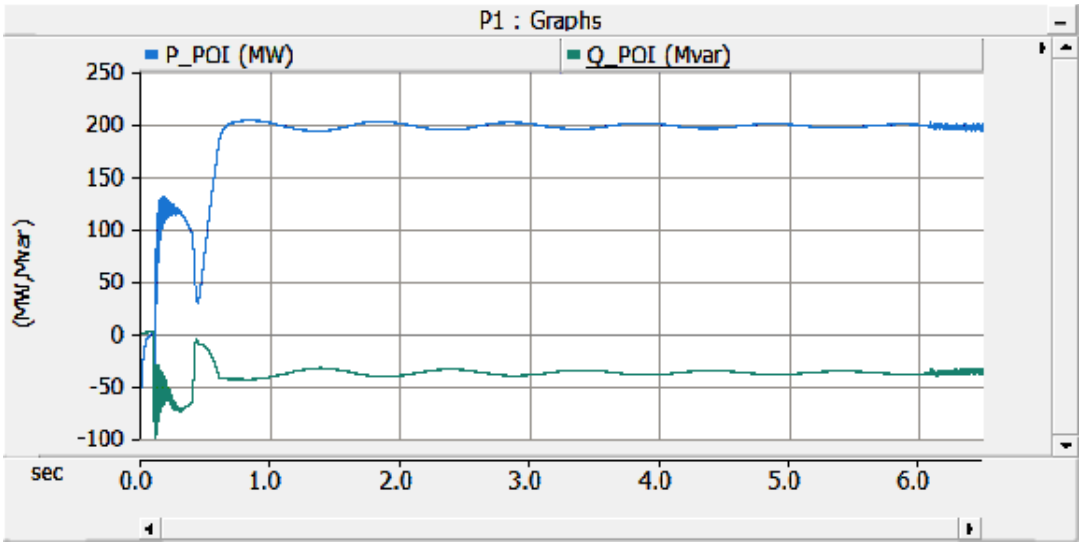

Figure B-91 EMT Simulation, SC16, POI Active & Reactive Power

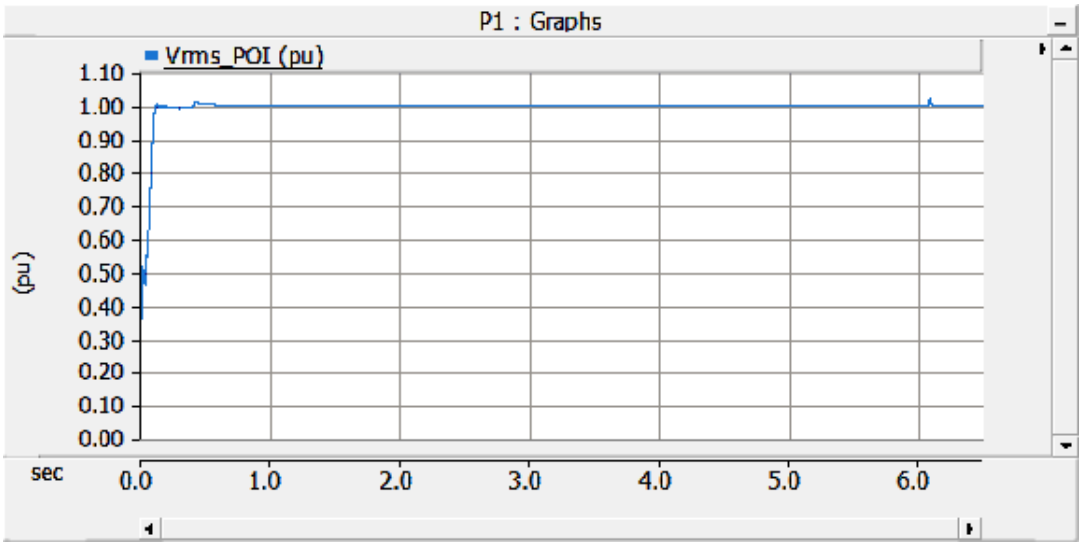

Figure B-92 EMT Simulation, SC16, POI rms voltage

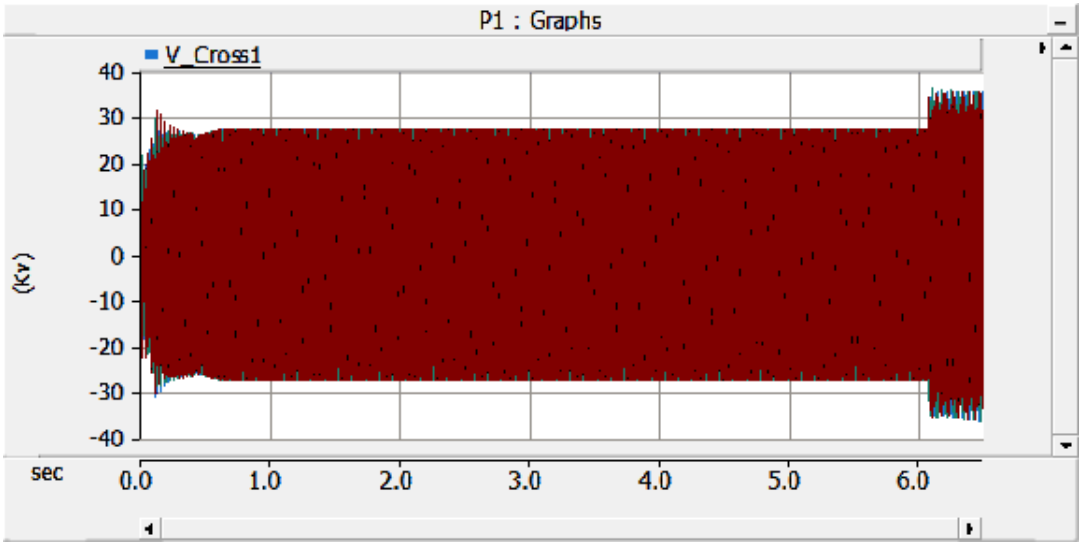

Figure B-93 EMT Simulation, SC16, series capacitor voltage

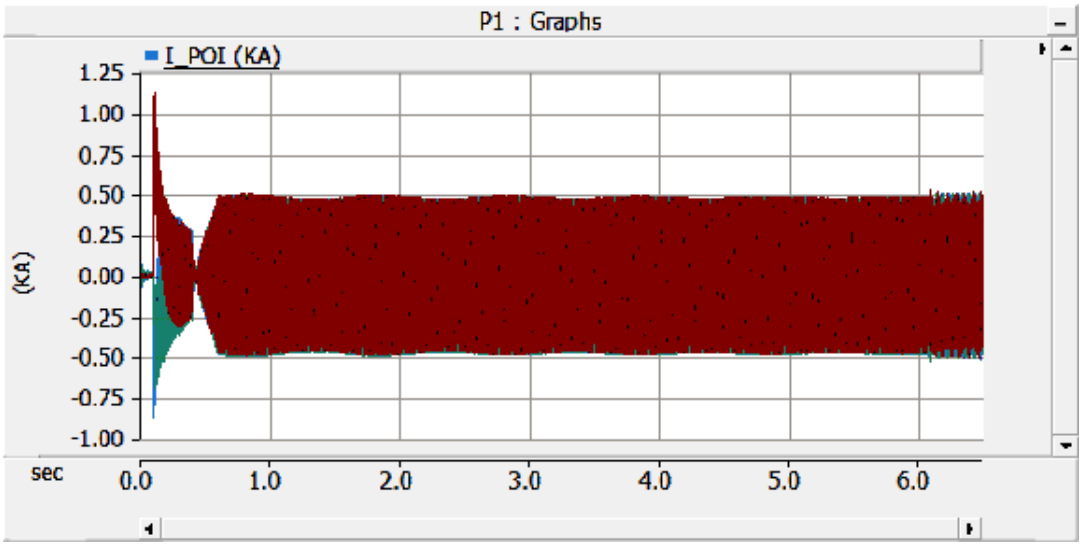

Figure B-94 EMT Simulation, SC16, POI instantaneous current

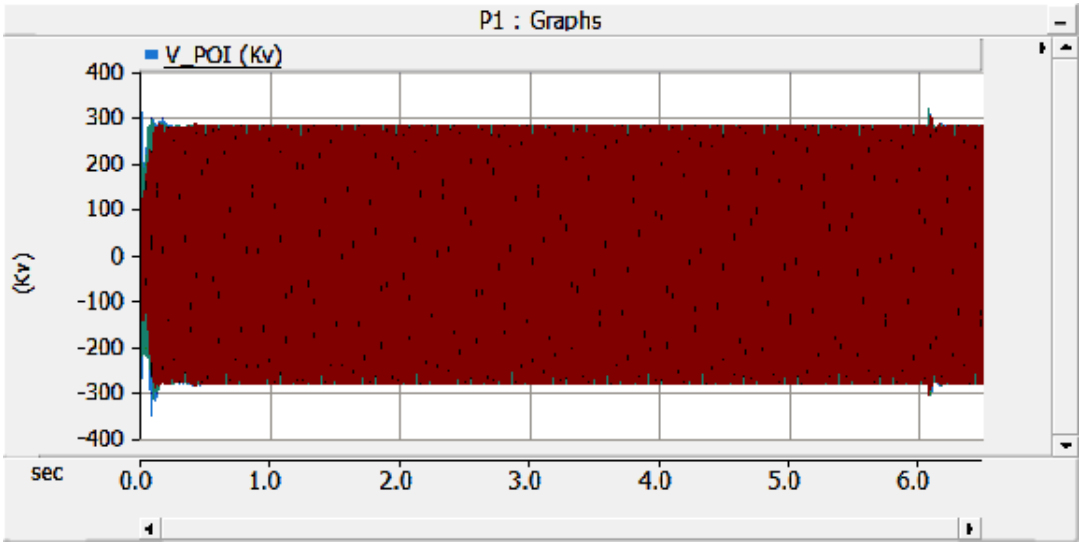

Figure B-95 EMT Simulation, SC16, POI instantaneous voltage

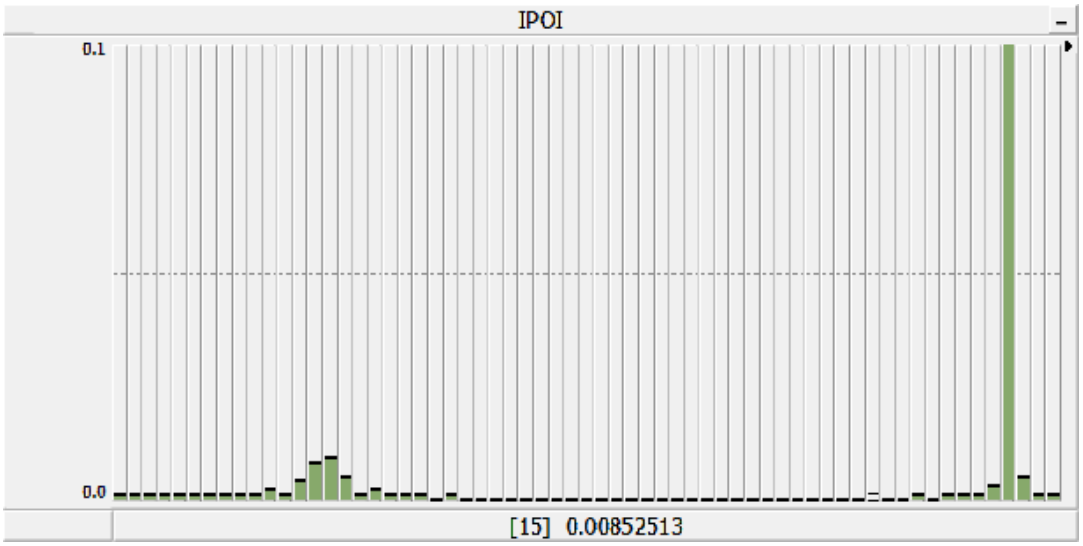

Figure B-96 EMT Simulation, SC1, POI current FFT

SC17: CTG2-D10T100-NoShunt-Fault

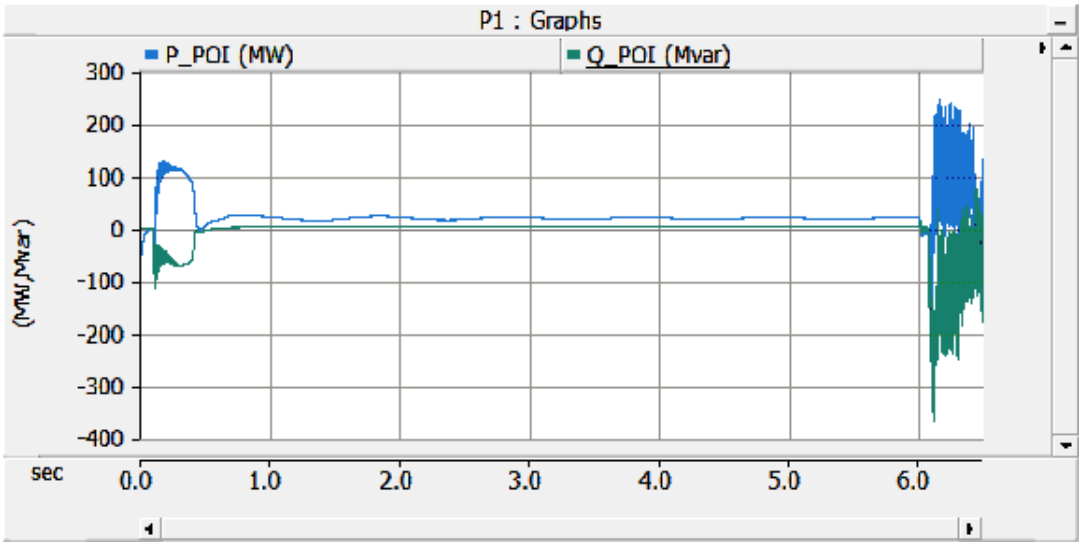

Figure B-97 EMT Simulation, SC17, POI Active & Reactive Power

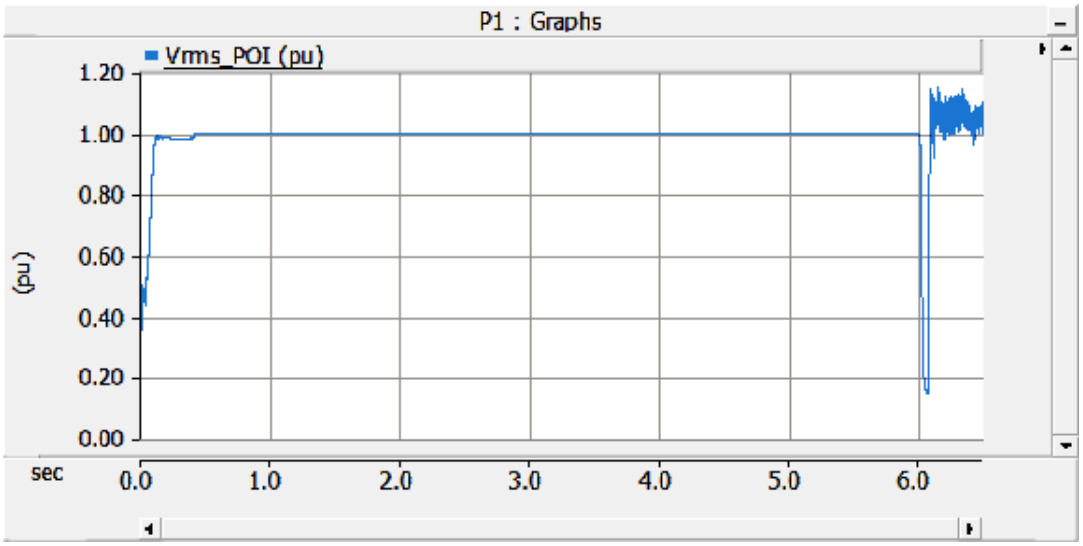

Figure B-98 EMT Simulation, SC17, POI rms voltage

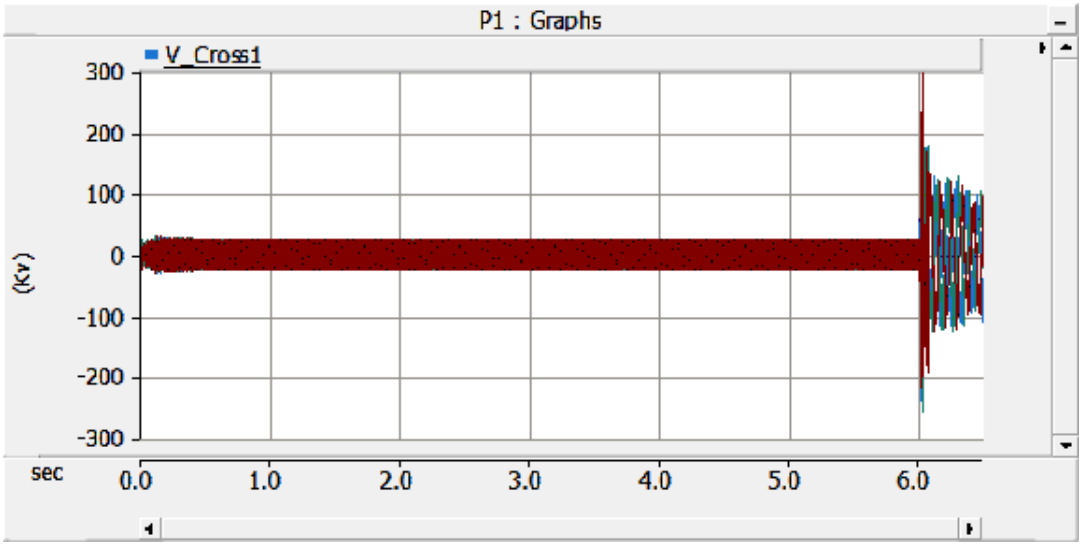

Figure B-99 EMT Simulation, SC17, series capacitor instantaneous voltage

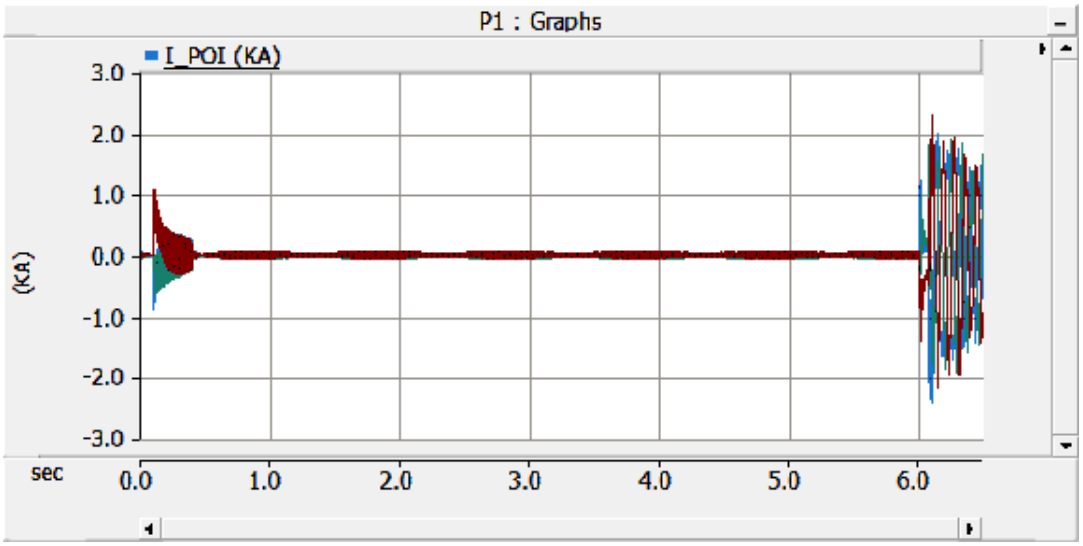

Figure B-100 EMT Simulation, SC17, POI instantaneous current

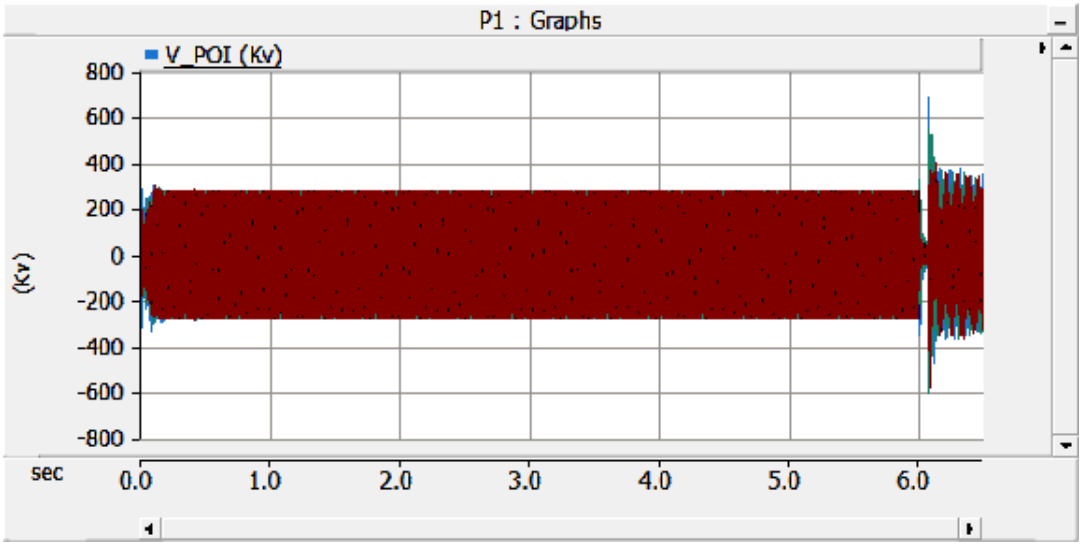

Figure B-101 EMT Simulation, SC17, POI instantaneous voltage

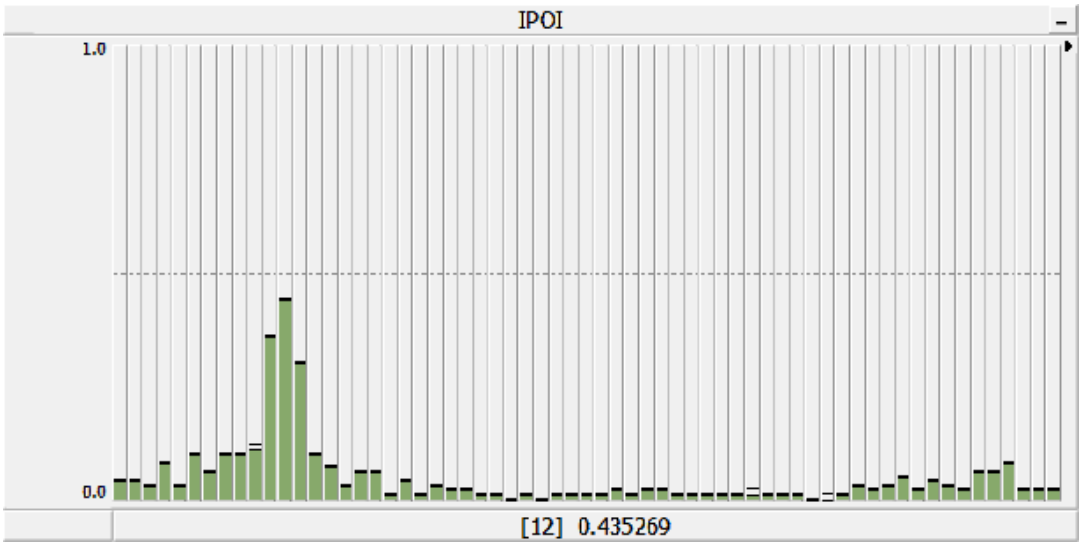

Figure B-102 EMT Simulation, SC17, POI current FFT

SC18: CTG2-D10T100-AllShunt-Fault

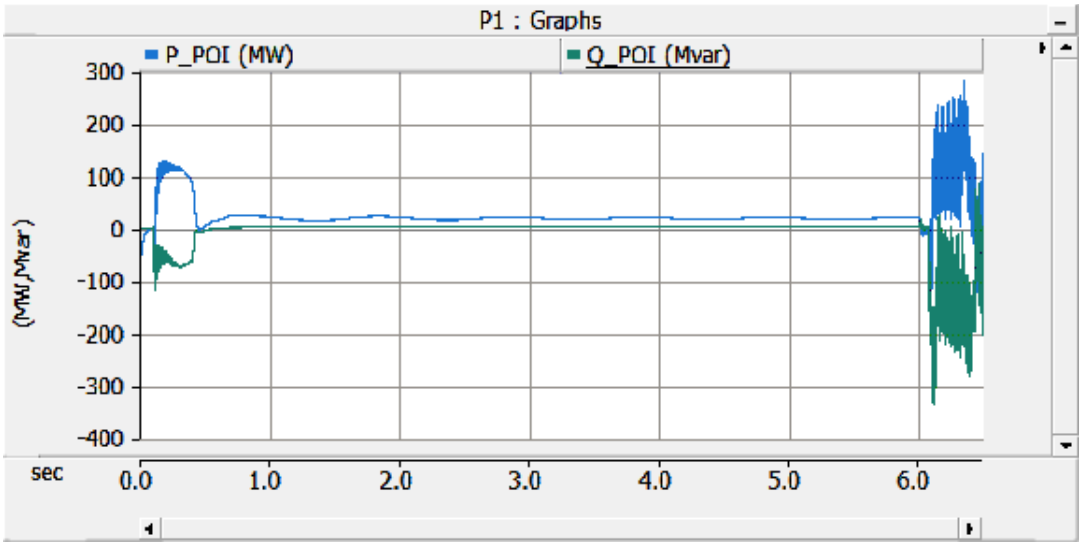

Figure B-103 EMT Simulation, SC18, POI Active & Reactive Power

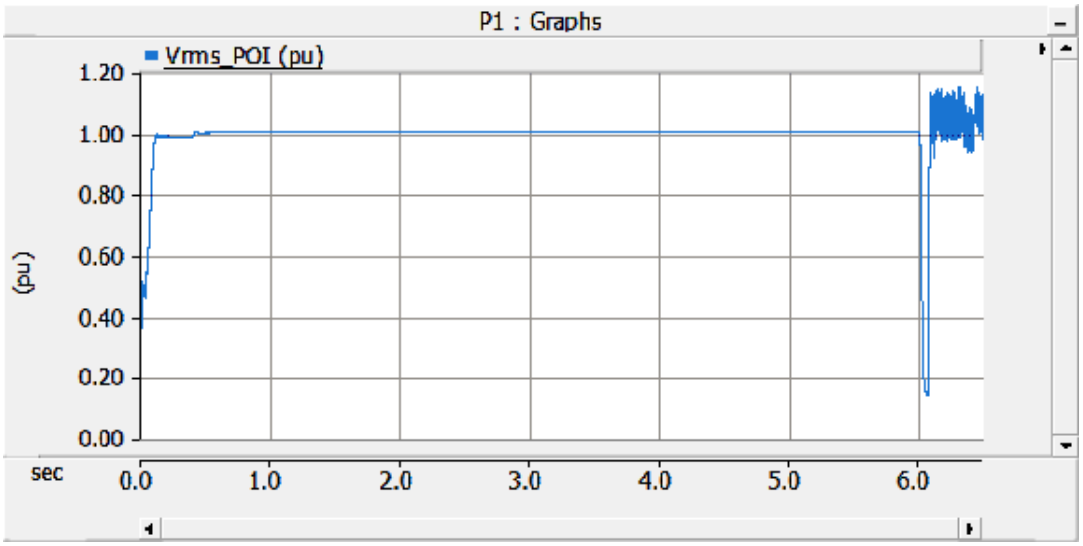

Figure B-104 EMT Simulation, SC18, POI rms voltage

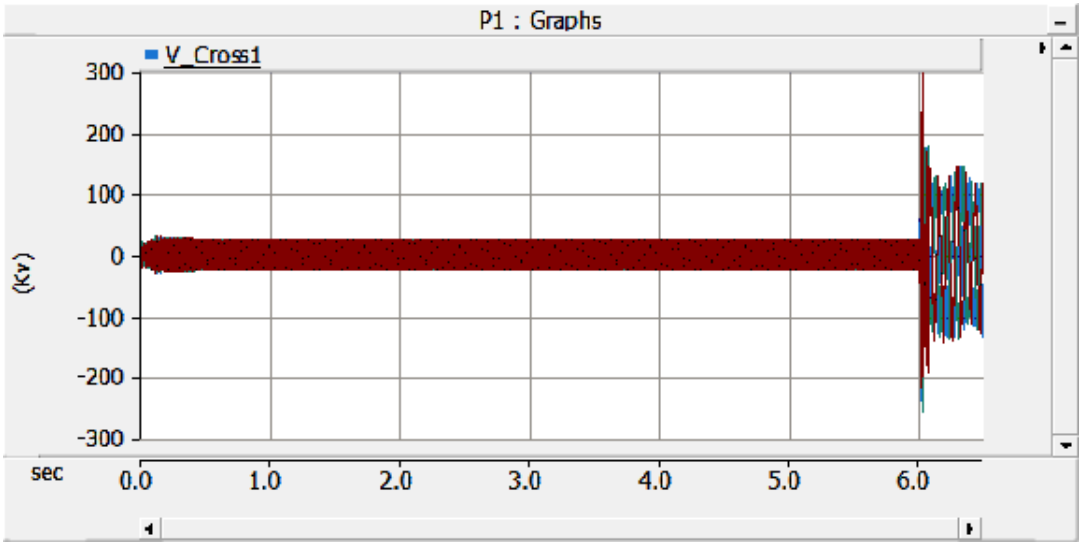

Figure B-105 EMT Simulation, SC18, series capacitor voltage

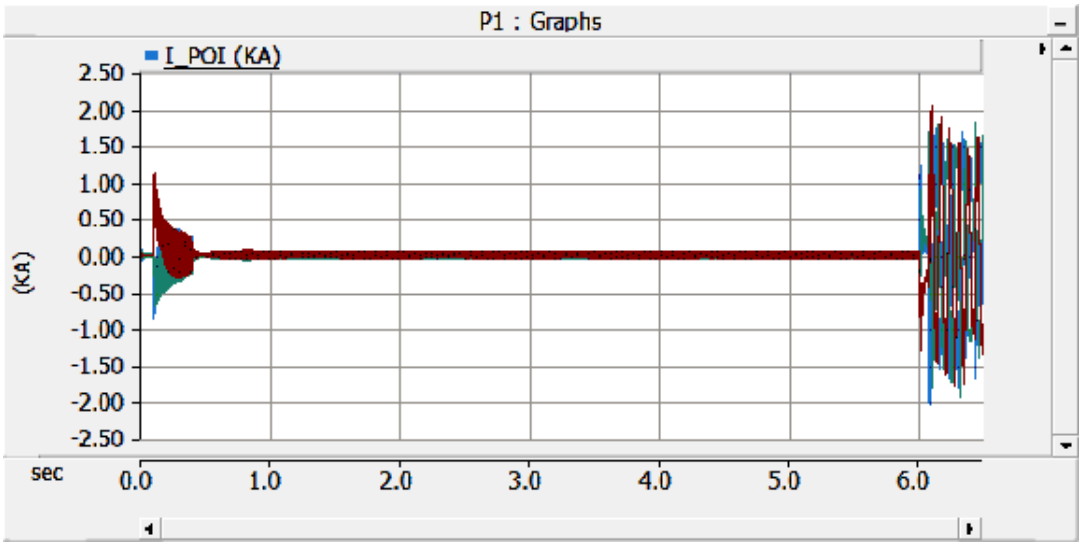

Figure B-106 EMT Simulation, SC18, POI instantaneous current

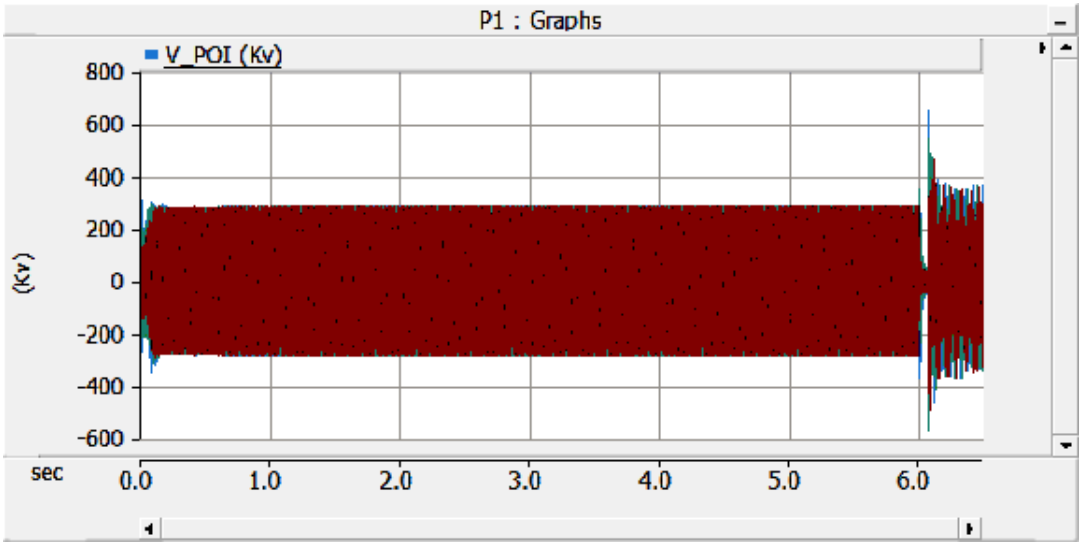

Figure B-107 EMT Simulation, SC18, POI instantaneous voltage

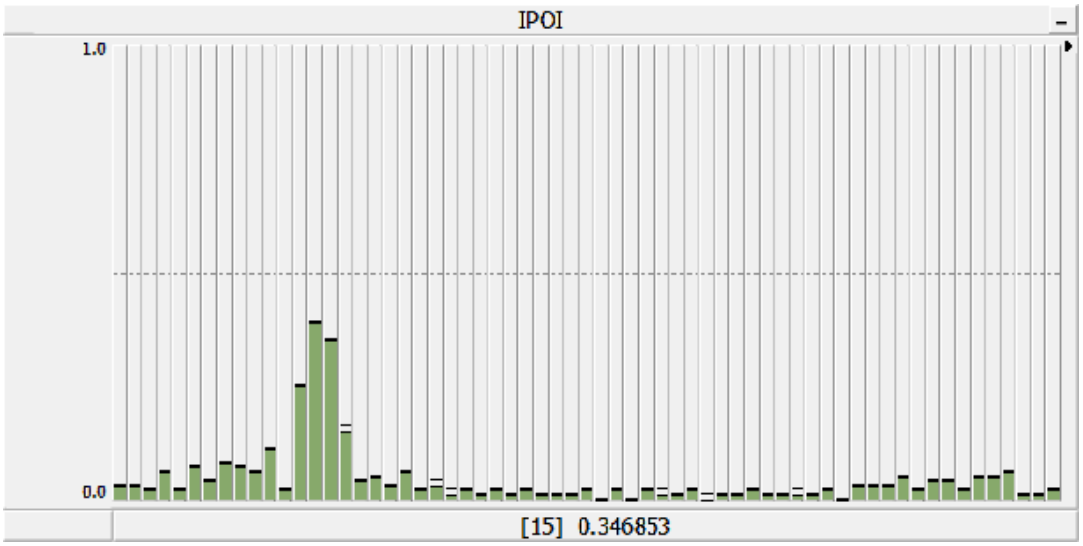

Figure B-108 EMT Simulation, SC18, POI current FFT

SC19: CTG2-D10T100-NoShunt-NoFault

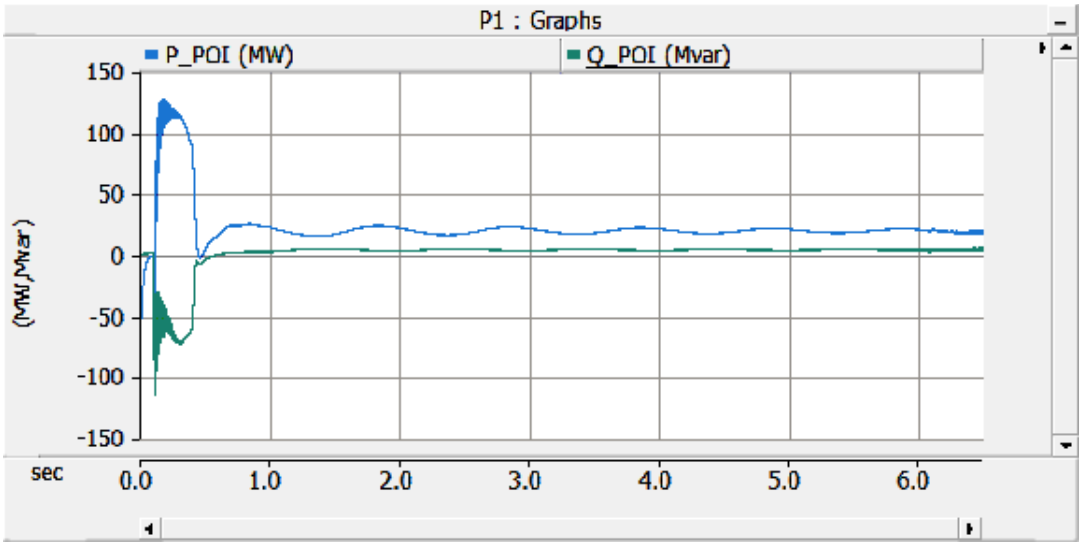

Figure B-109 EMT Simulation, SC19, POI Active & Reactive Power

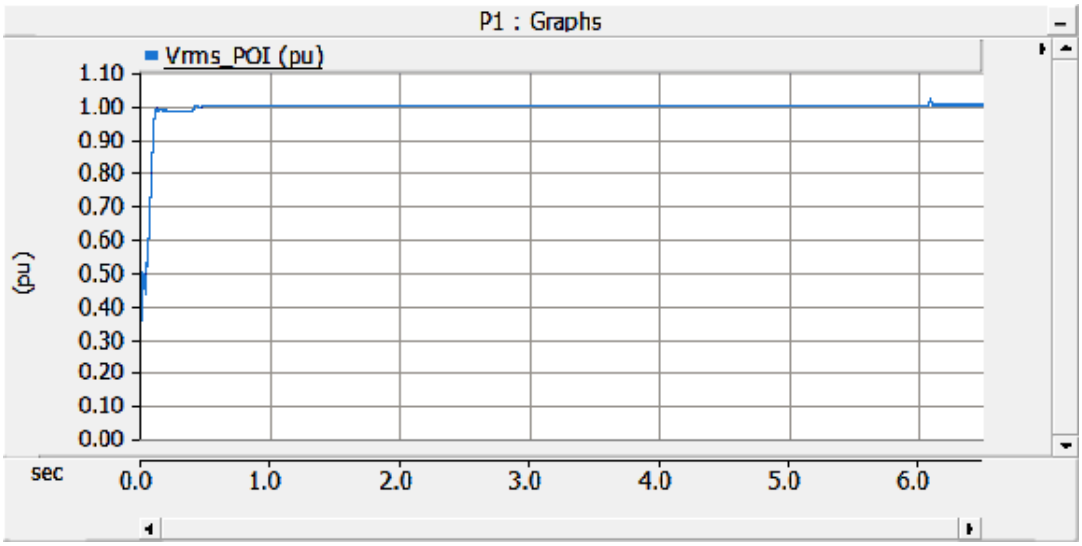

Figure B-110 EMT Simulation, SC19, POI rms voltage

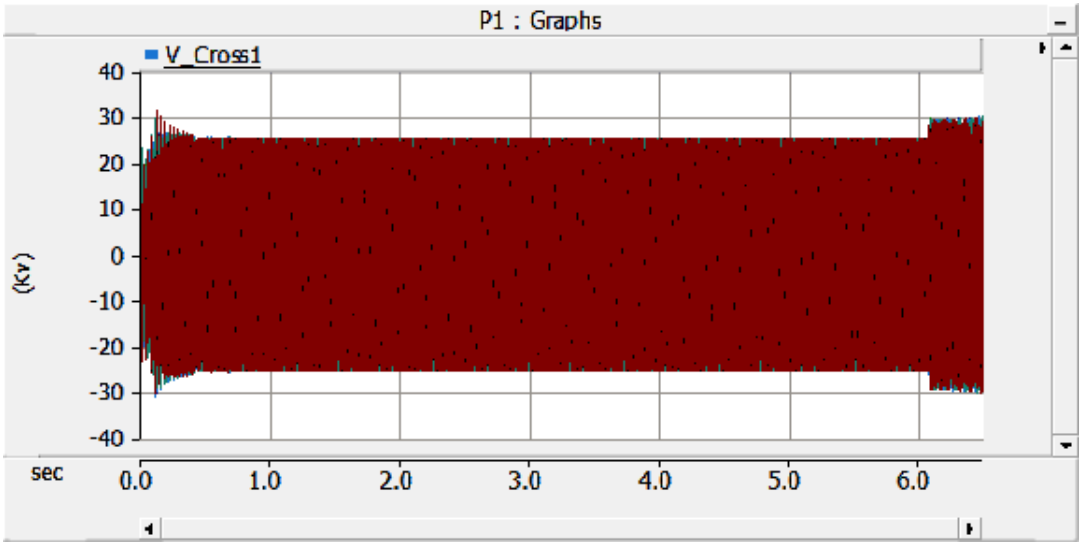

Figure B-111 EMT Simulation, SC19, series capacitor voltage

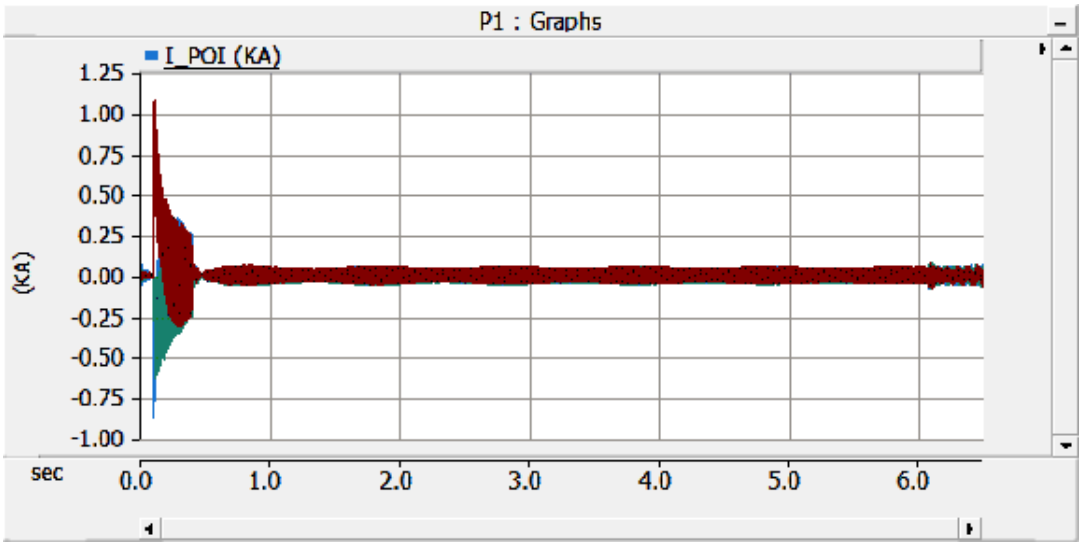

Figure B-112 EMT Simulation, SC19, POI instantaneous current

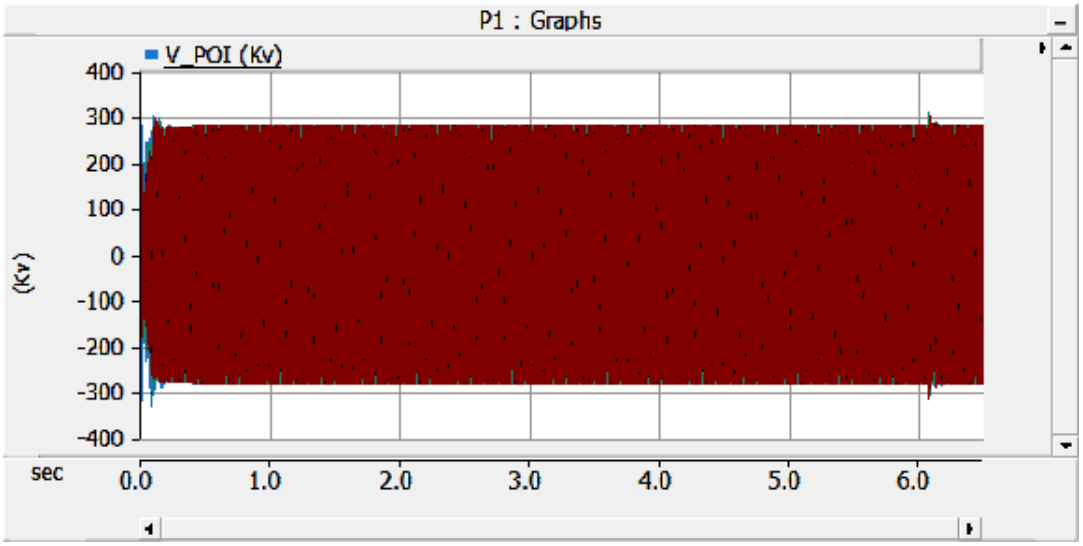

Figure B-113 EMT Simulation, SC19, POI instantaneous voltage

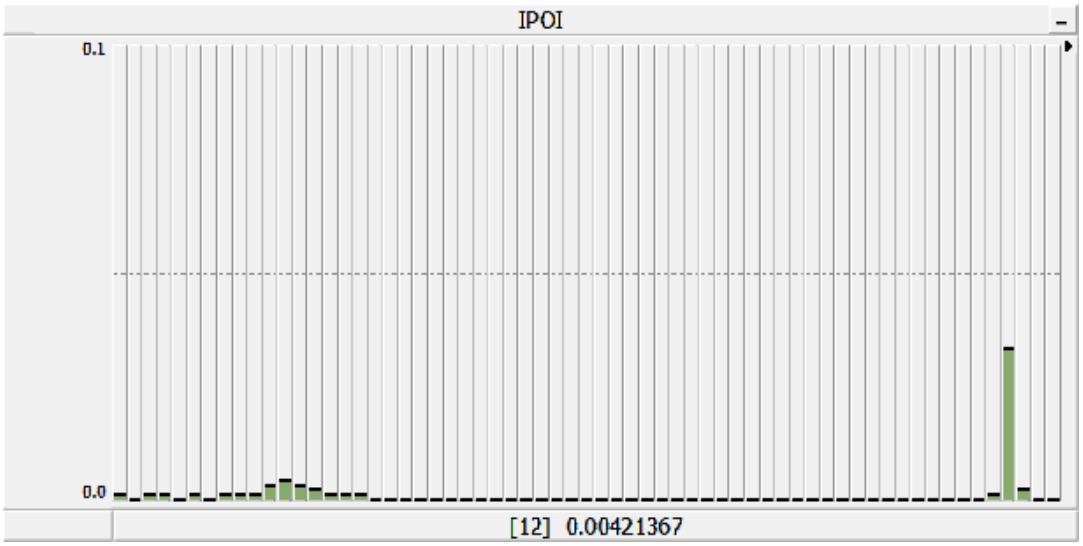

Figure B-114 EMT Simulation, SC19, POI current FFT

SC20: CTG2-D10T100-AllShunt-NoFault

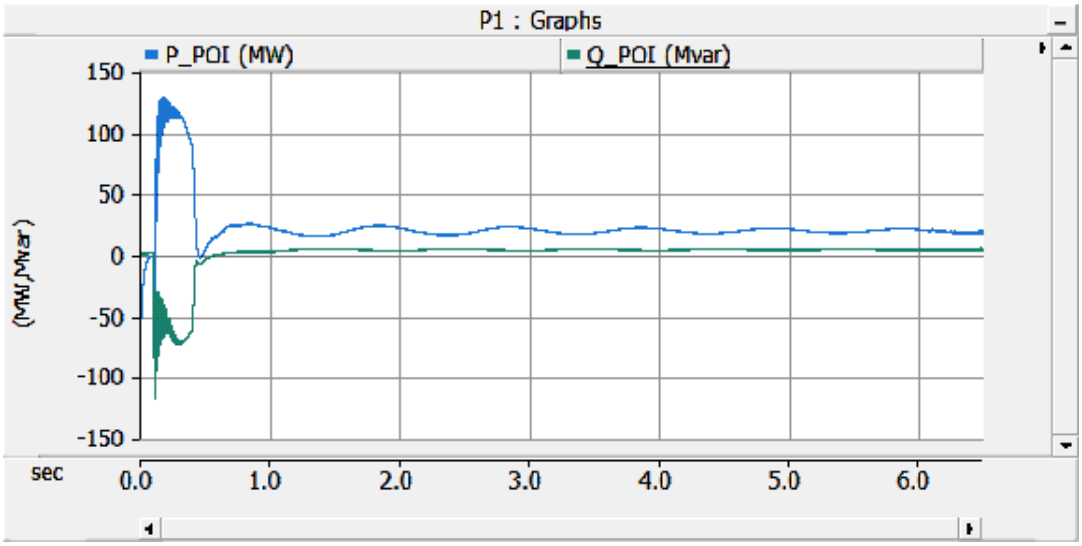

Figure B-115 EMT Simulation, SC20, POI Active & Reactive Power

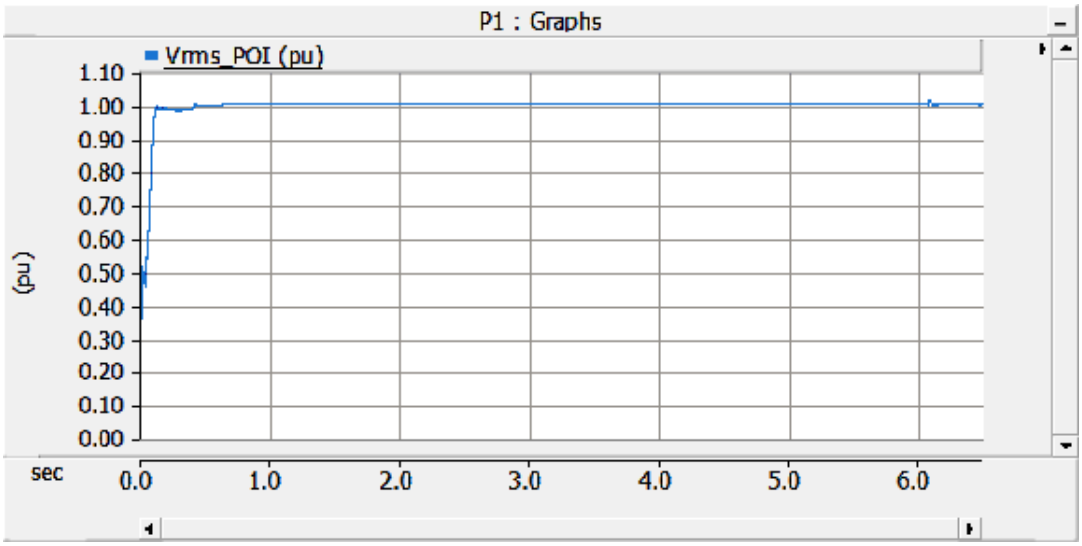

Figure B-116 EMT Simulation, SC20, POI rms voltage

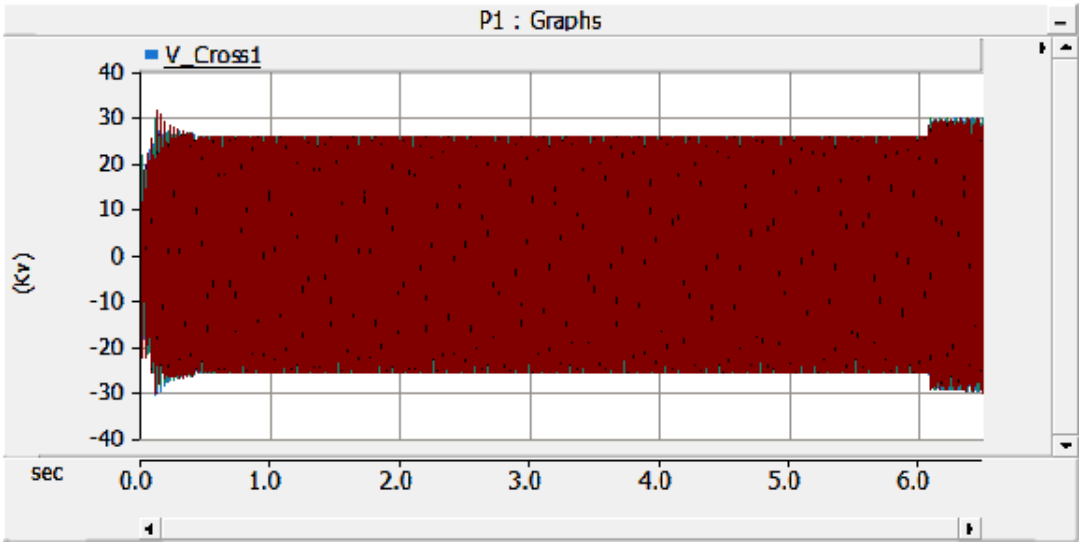

Figure B-117 EMT Simulation, SC20, series capacitor voltage

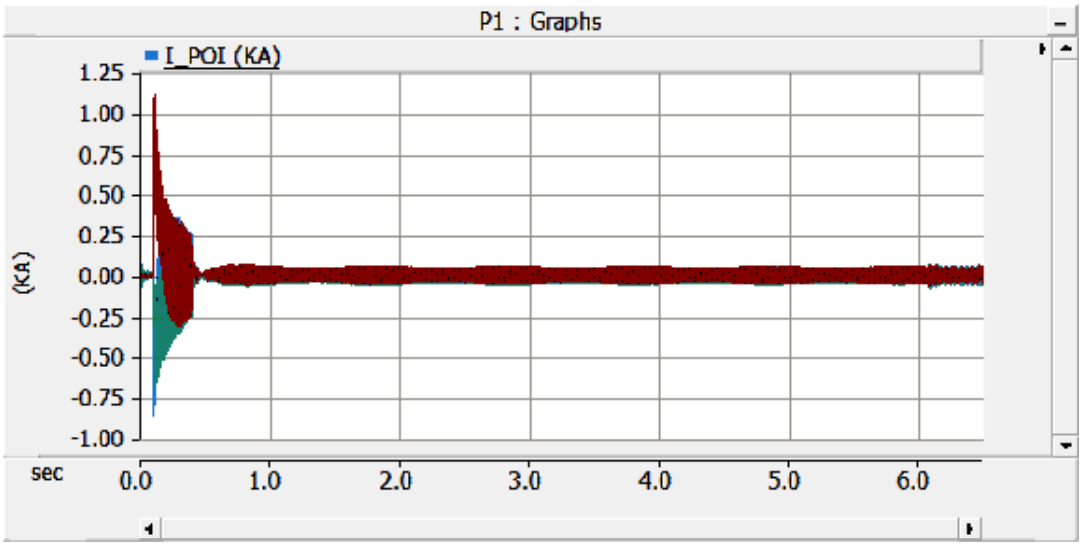

Figure 0-118 EMT Simulation, SC20, POI instantaneous current

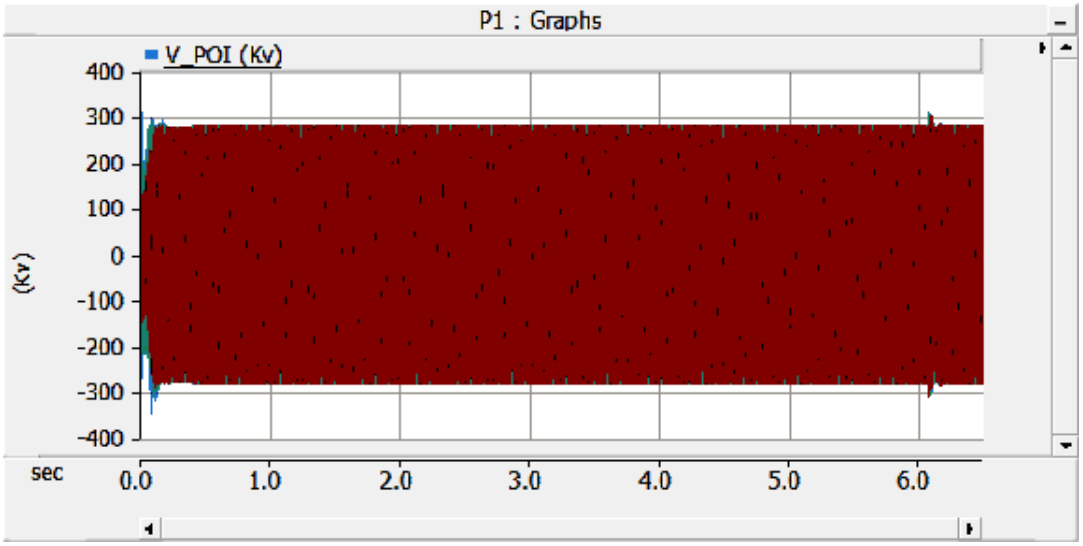

Figure B-119 EMT Simulation, SC20, POI instantaneous voltage

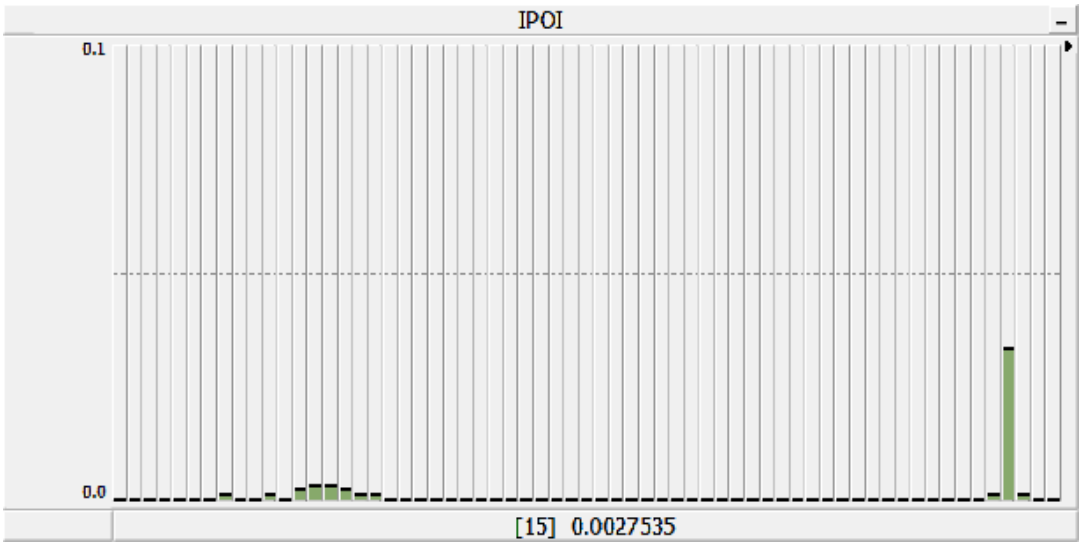

Figure B-120 EMT Simulation, SC20, POI current FFT

SC21: CTG2-D100T10-NoShunt-Fault

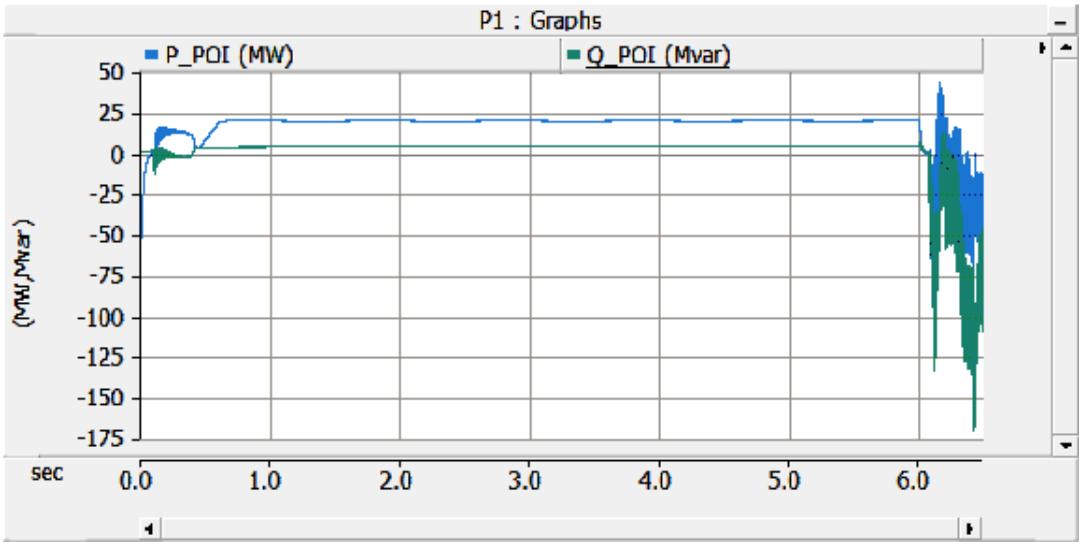

Figure B-121 EMT Simulation, SC21, POI Active & Reactive Power

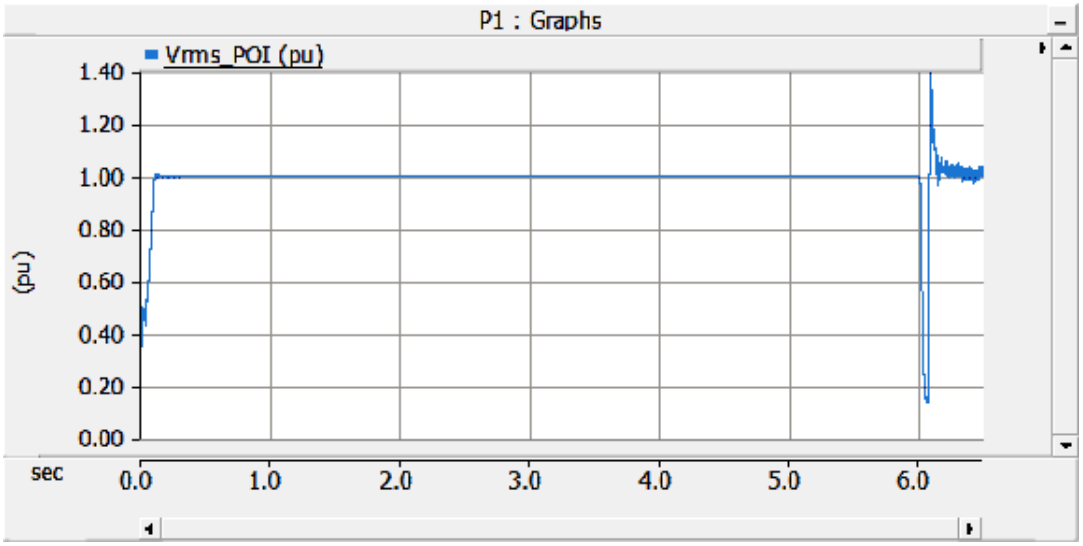

Figure B-122 EMT Simulation, SC21, POI rms voltage

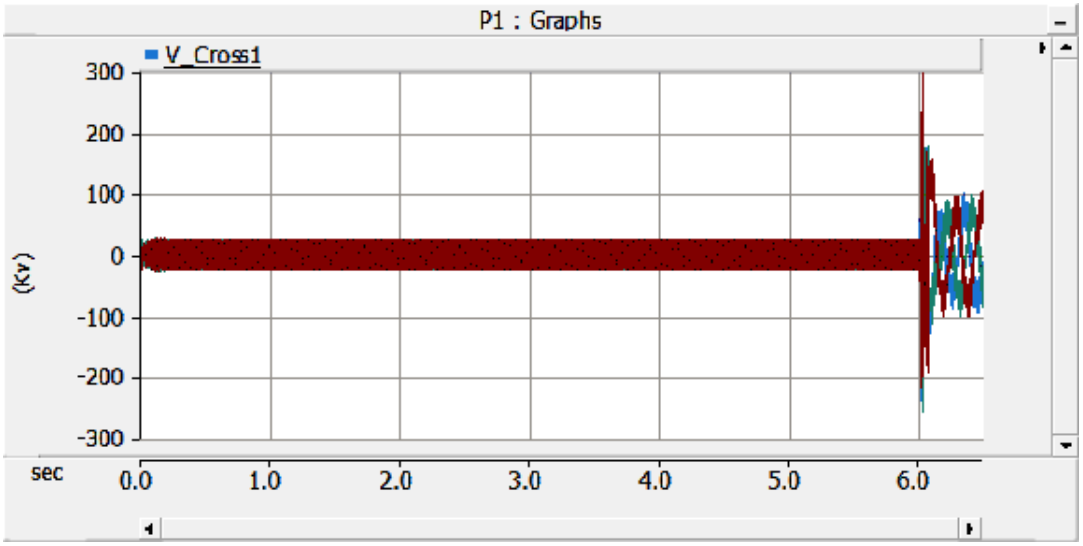

Figure B-123 EMT Simulation, SC21, series capacitor voltage

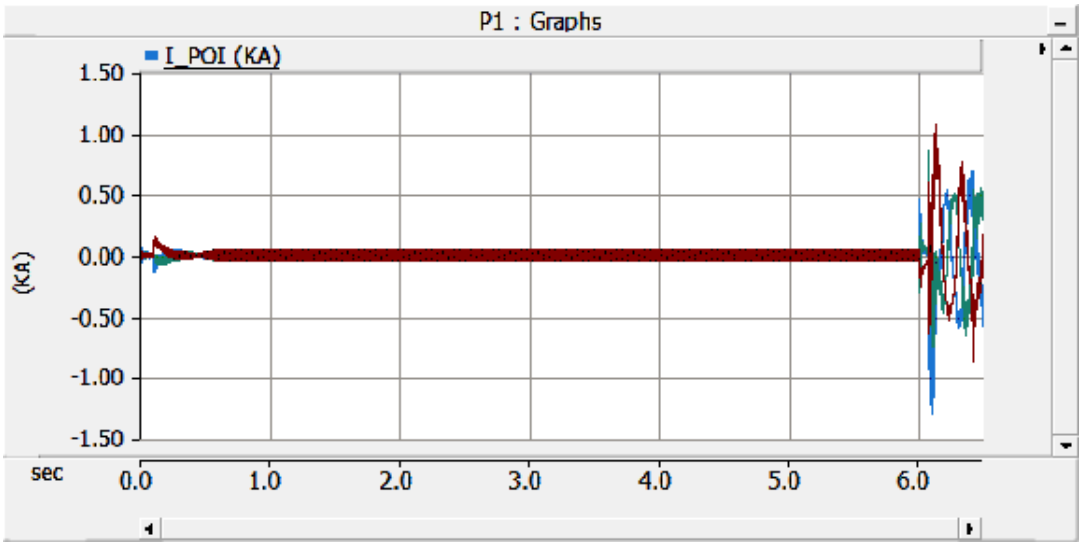

Figure B-124 EMT Simulation, SC21, POI instantaneous current

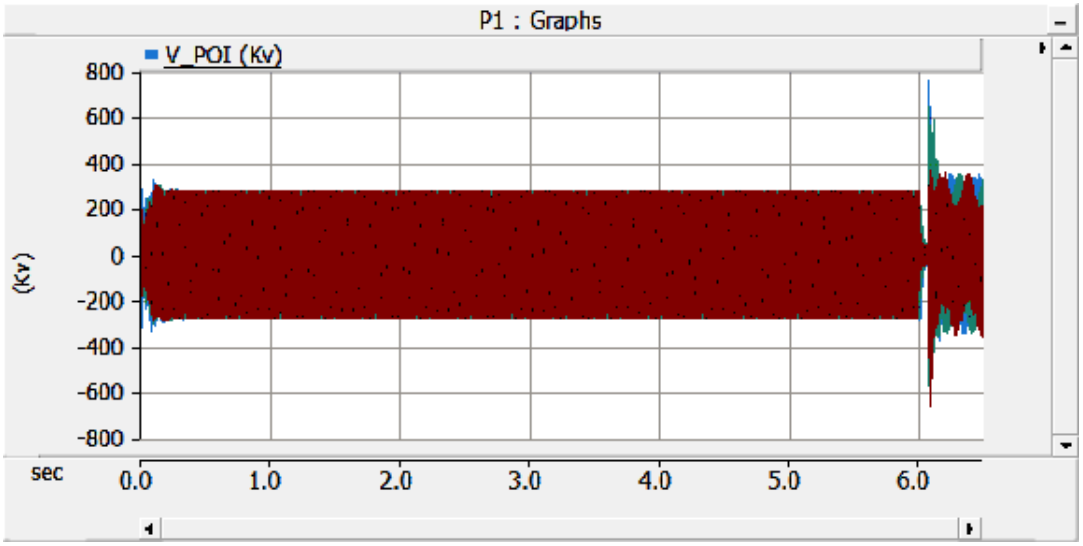

Figure B-125 EMT Simulation, SC21, POI instantaneous voltage

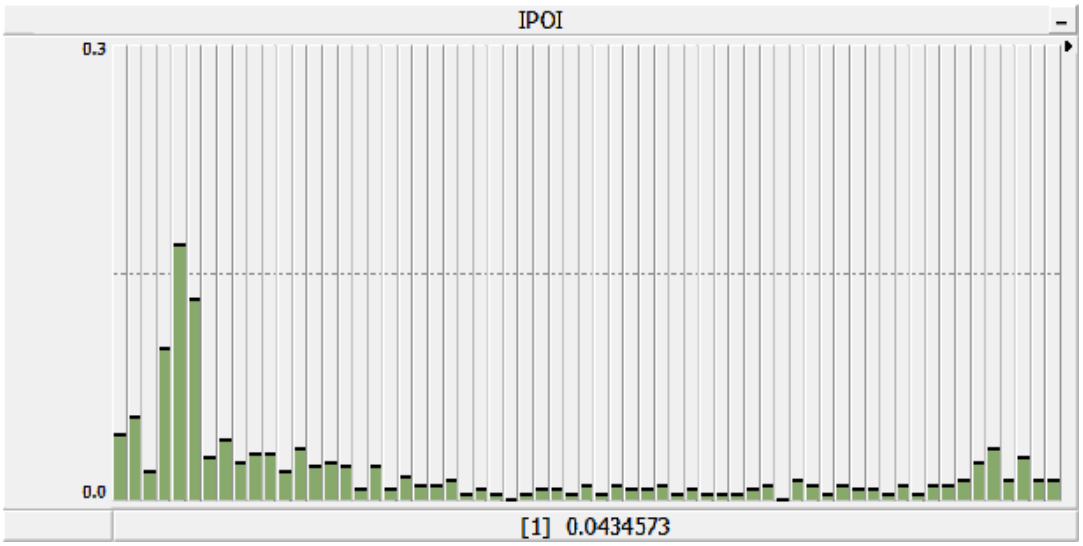

Figure B-126 EMT Simulation, SC21, POI current FFT

SC22: CTG2-D100T10-AllShunt-Fault

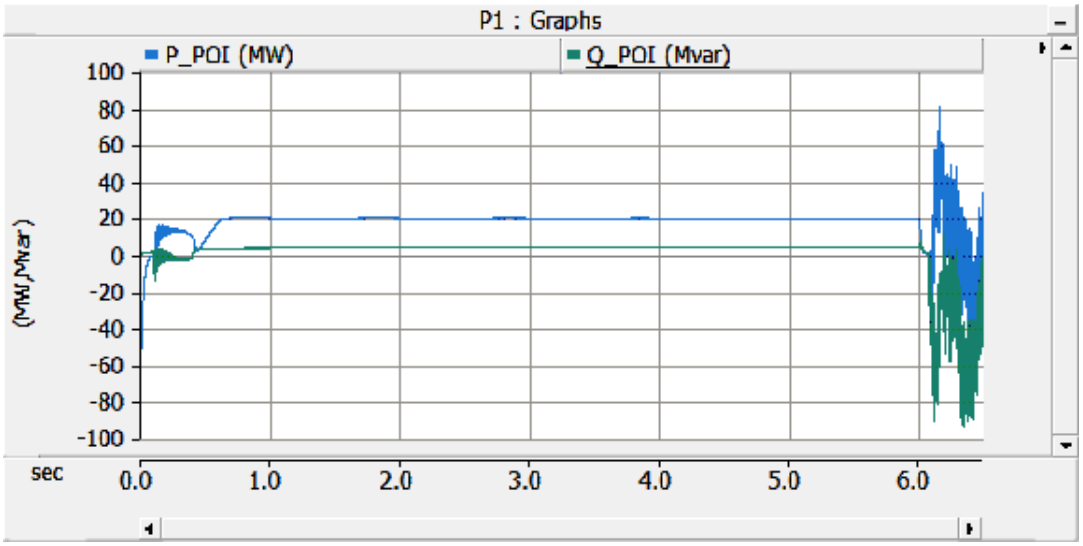

Figure B-127 EMT Simulation, SC22, POI Active & Reactive Power

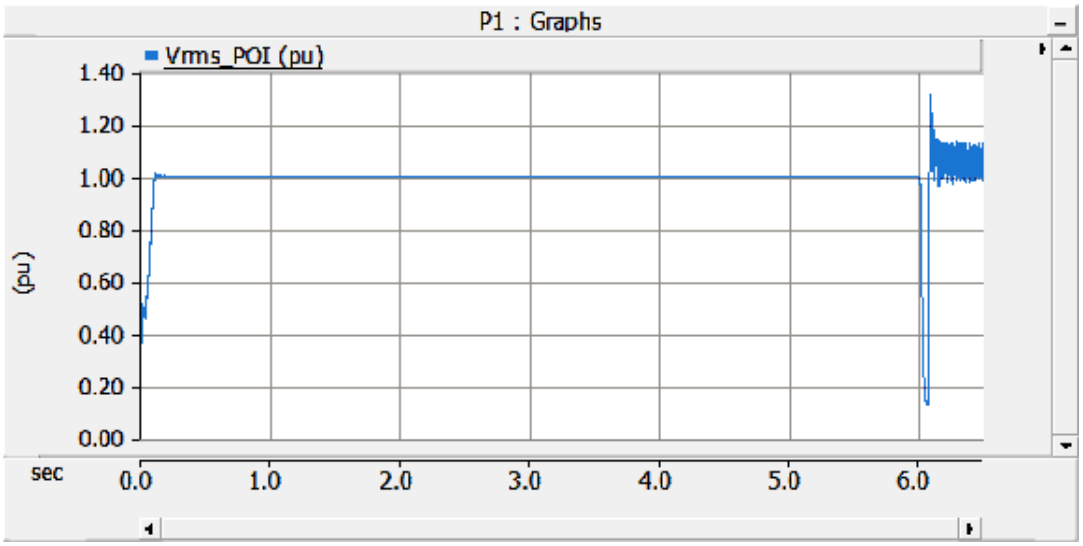

Figure B-128 EMT Simulation, SC22, POI rms voltage

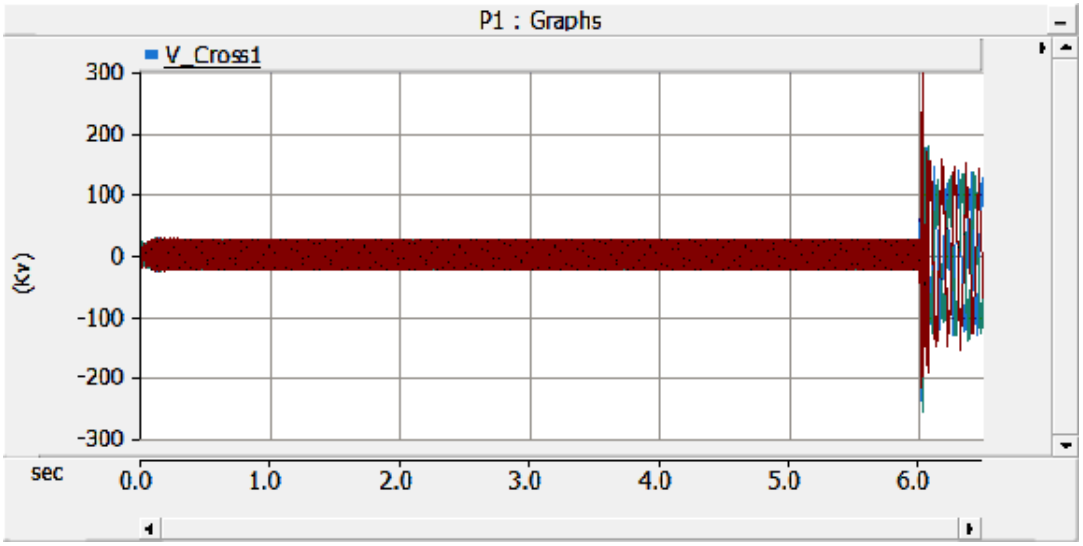

Figure B-129 EMT Simulation, SC22, series capacitor voltage

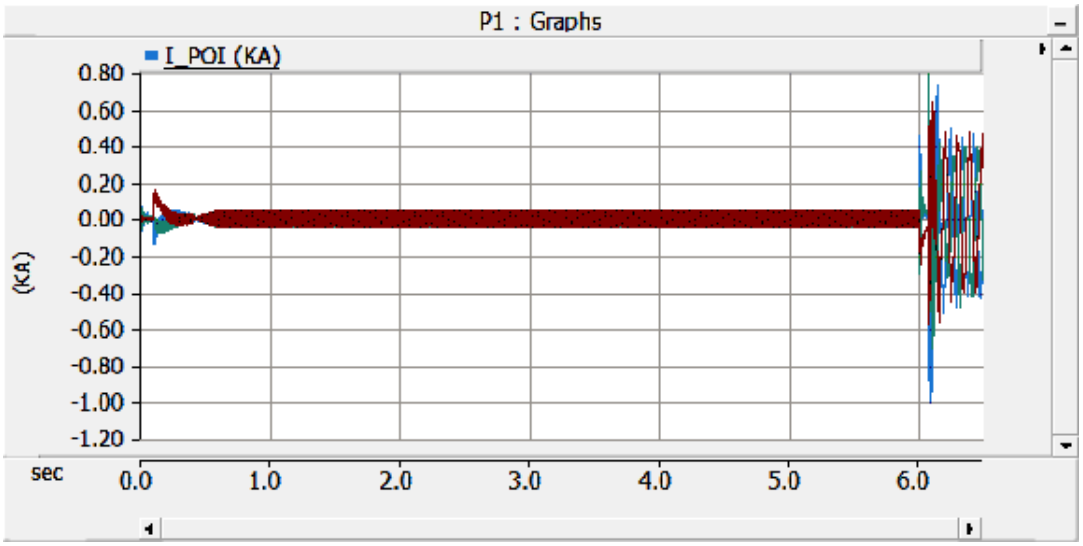

Figure B-130 EMT Simulation, SC22, POI instantaneous current

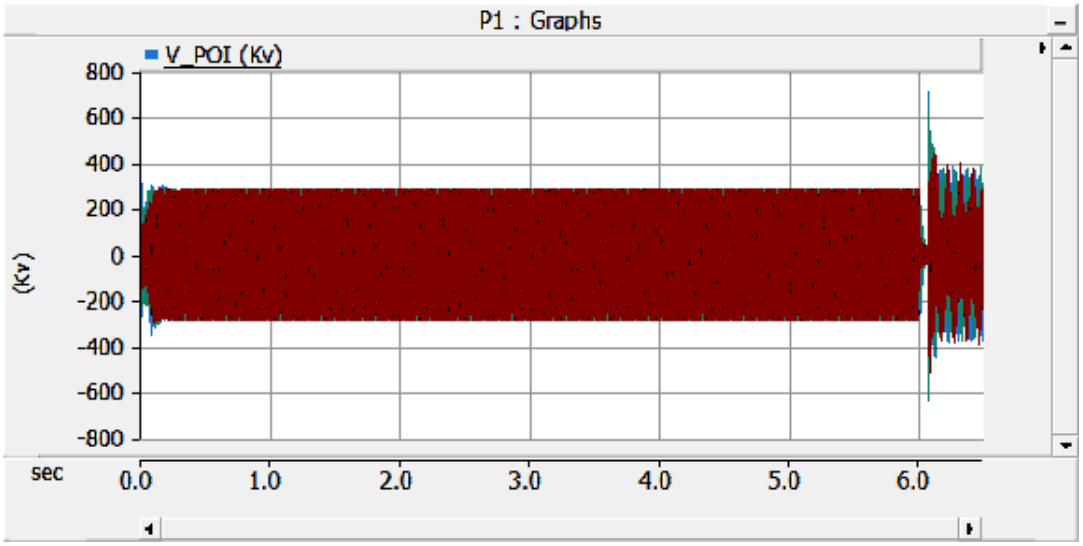

Figure B-131 EMT Simulation, SC22, POI instantaneous voltage

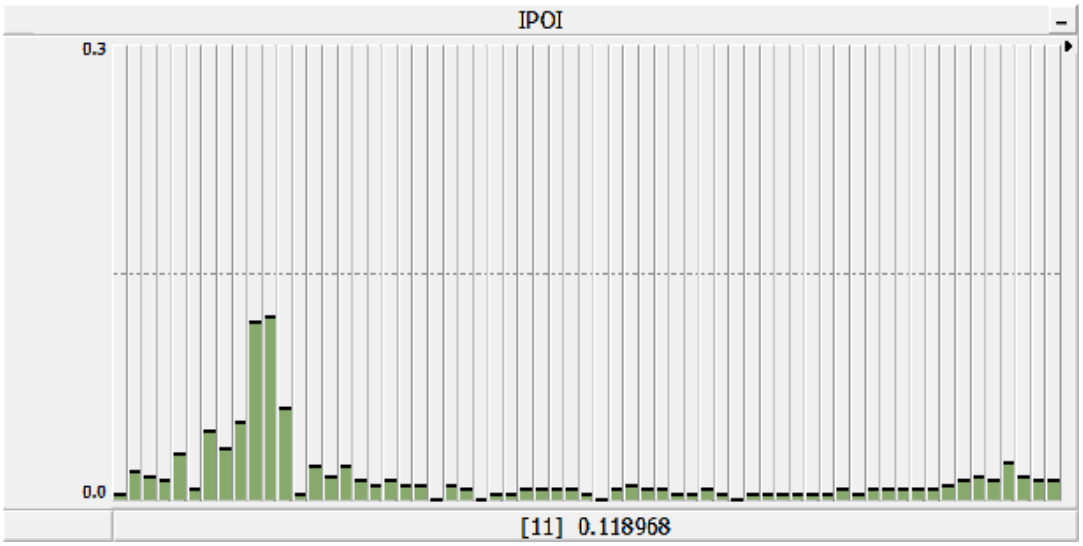

Figure B-132 EMT Simulation, SC22, POI current FFT

SC23:CTG2-D100T10-NoShunt-NoFault

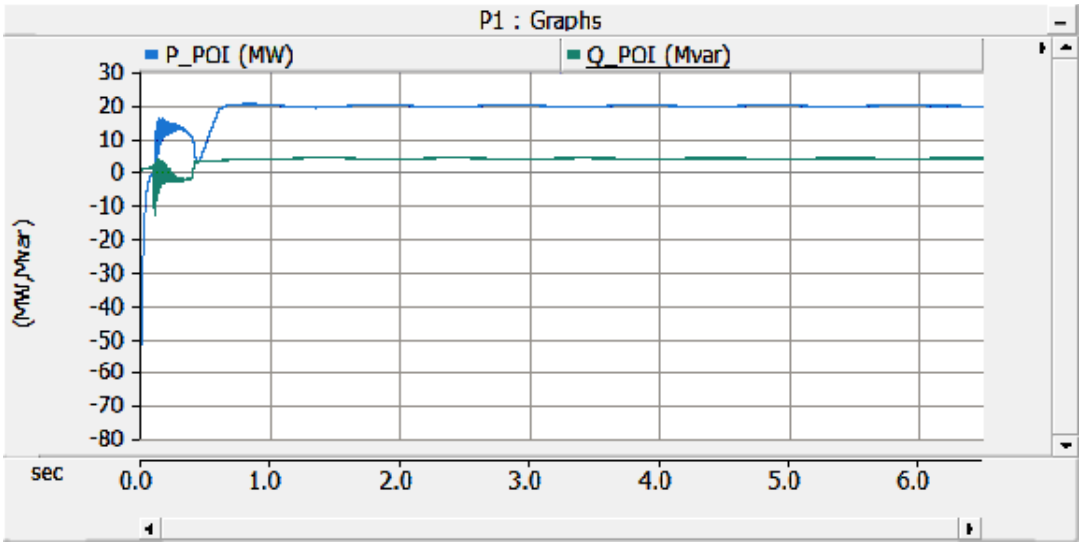

Figure B-133 EMT Simulation, SC23, POI Active & Reactive Power

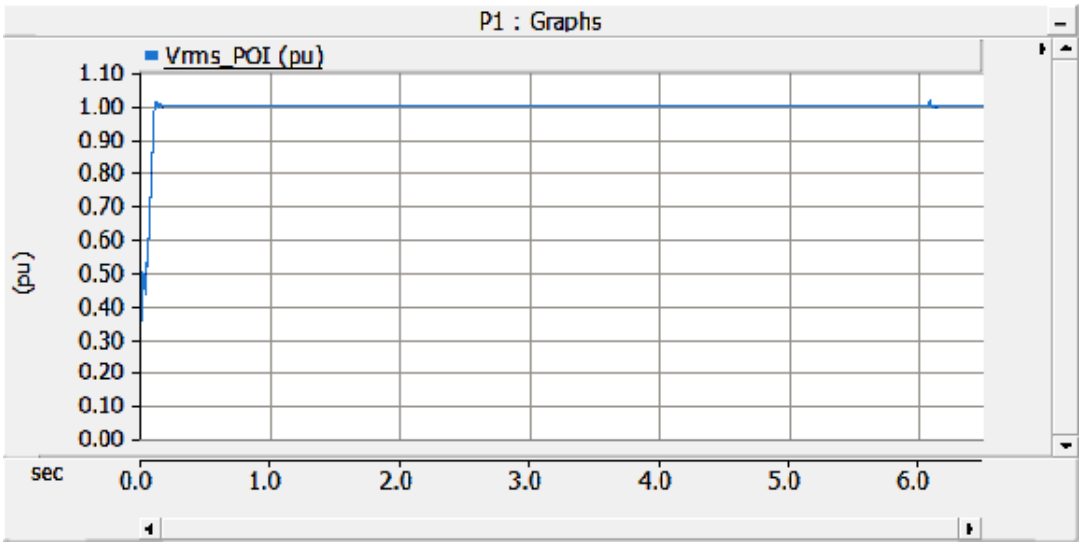

Figure B-134 EMT Simulation, SC23, POI rms voltage

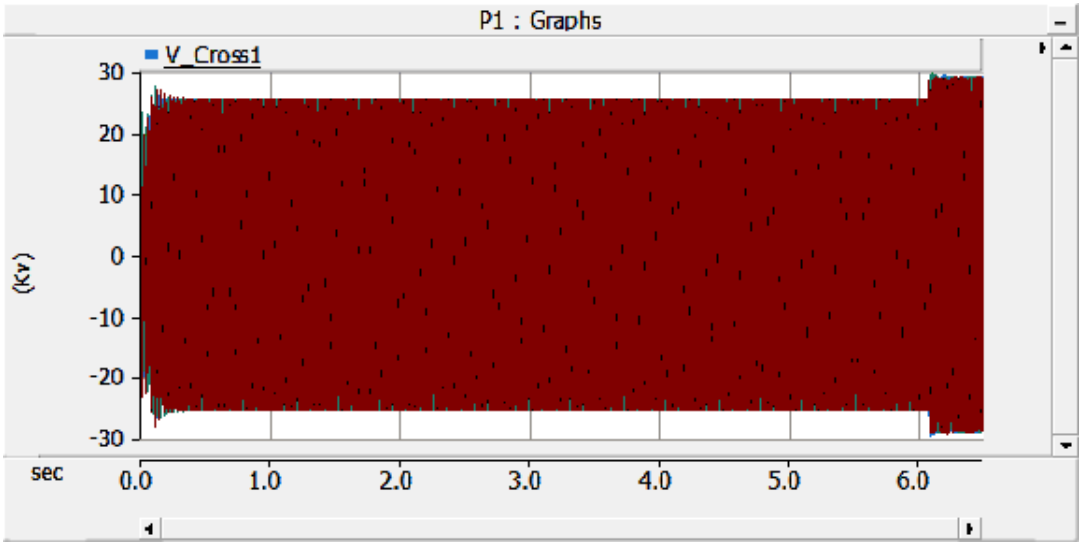

Figure B-135 EMT Simulation, SC23, series capacitor voltage

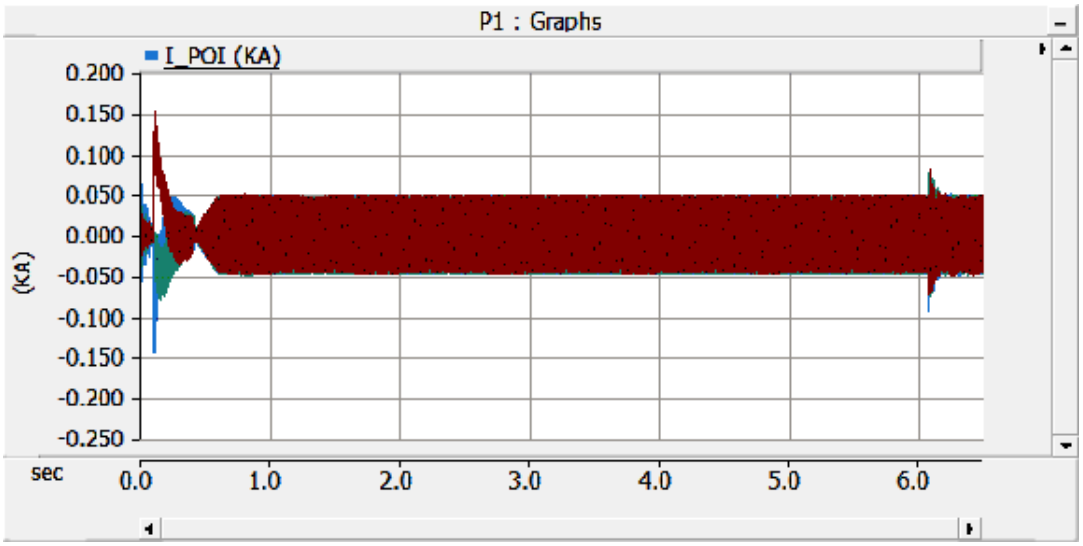

Figure B-136 EMT Simulation, SC23, POI instantaneous current

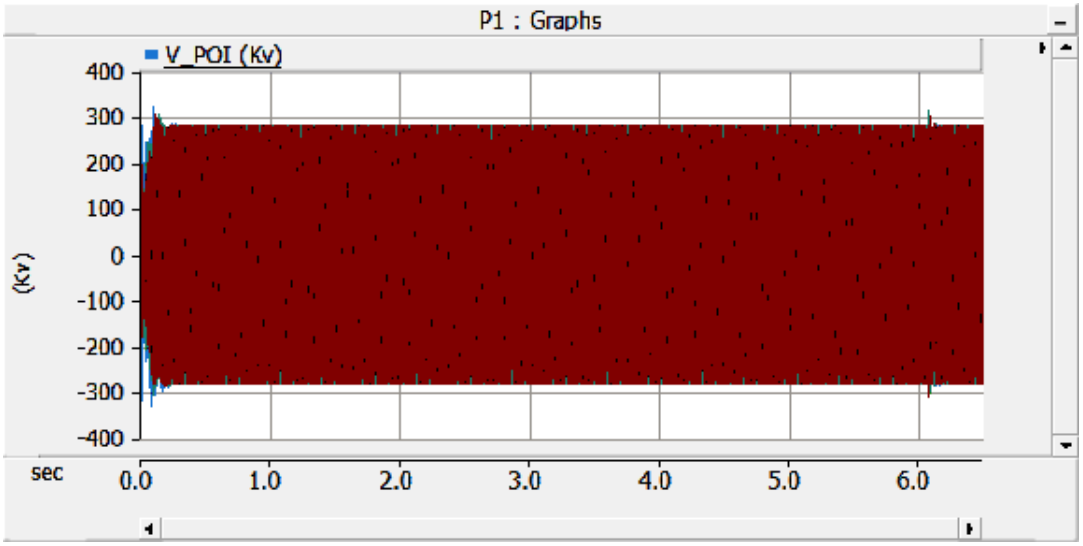

Figure B-137 EMT Simulation, SC23, POI instantaneous voltage

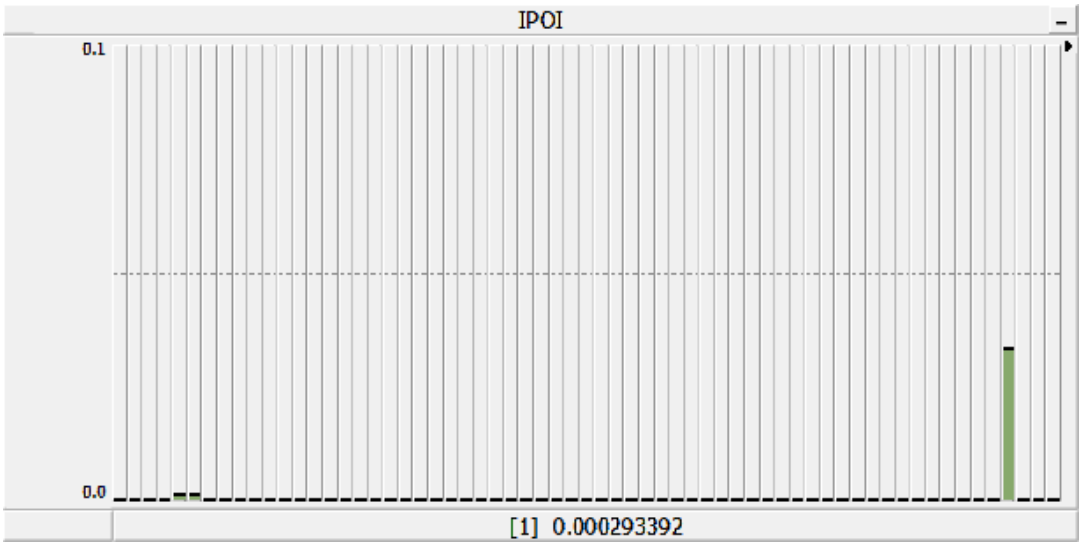

Figure B-138 EMT Simulation, SC23, POI current FFT

SC24: CTG2-D100T10-AllShunt-NoFault

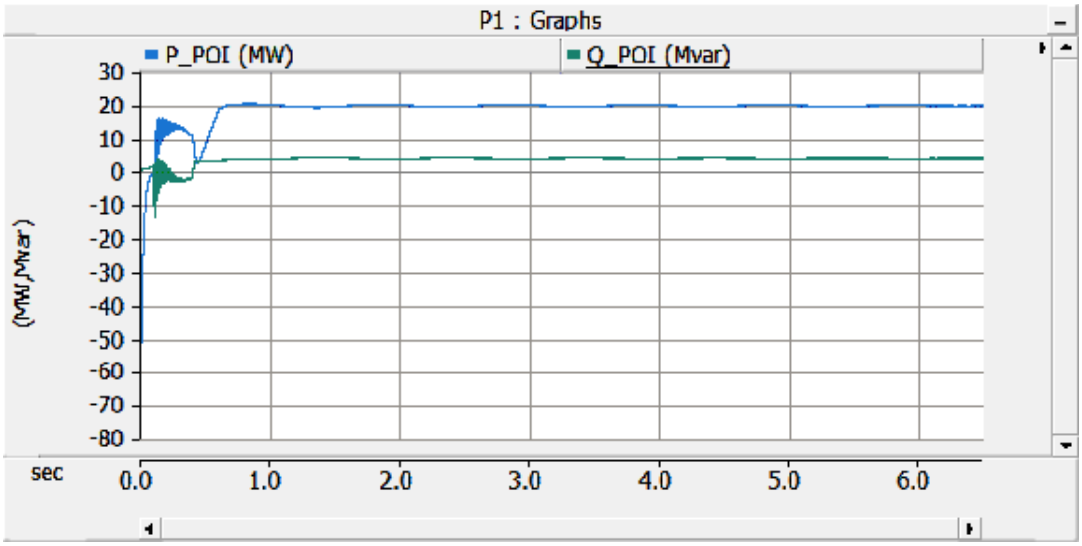

Figure B-139 EMT Simulation, SC24, POI Active & Reactive Power

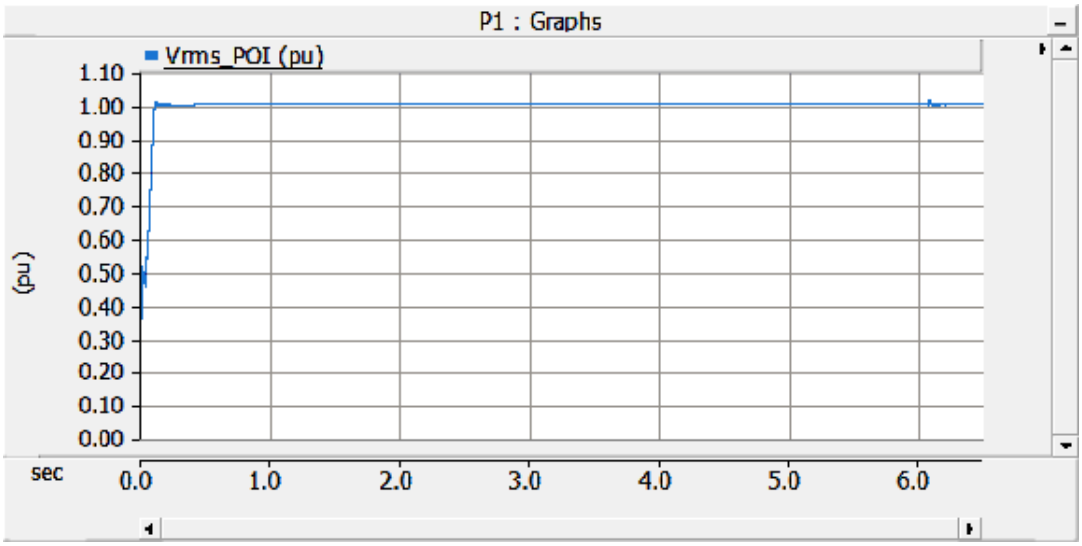

Figure B-140 EMT Simulation, SC24, POI rms voltage

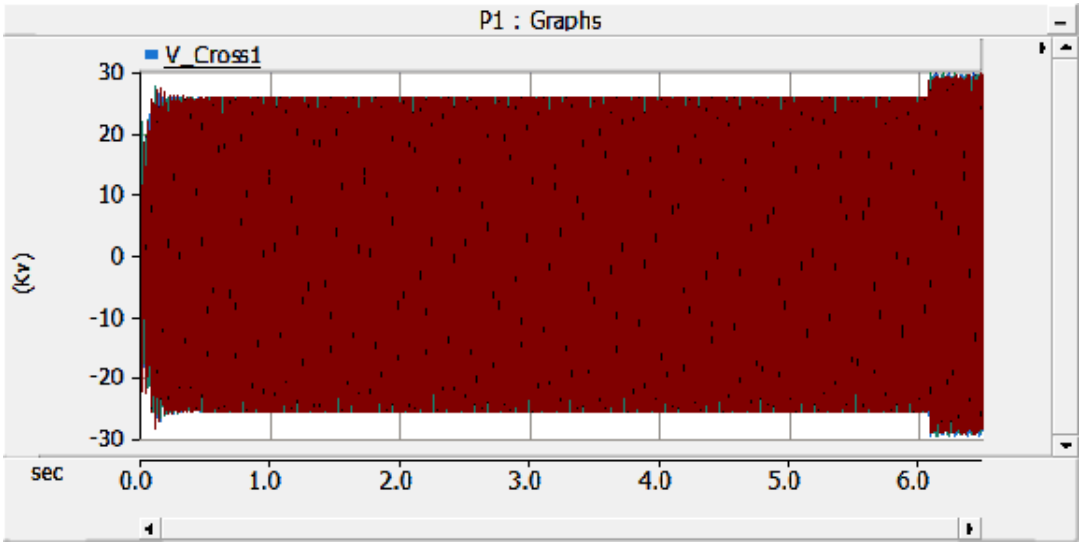

Figure B-141 EMT Simulation, SC24, series capacitor voltage

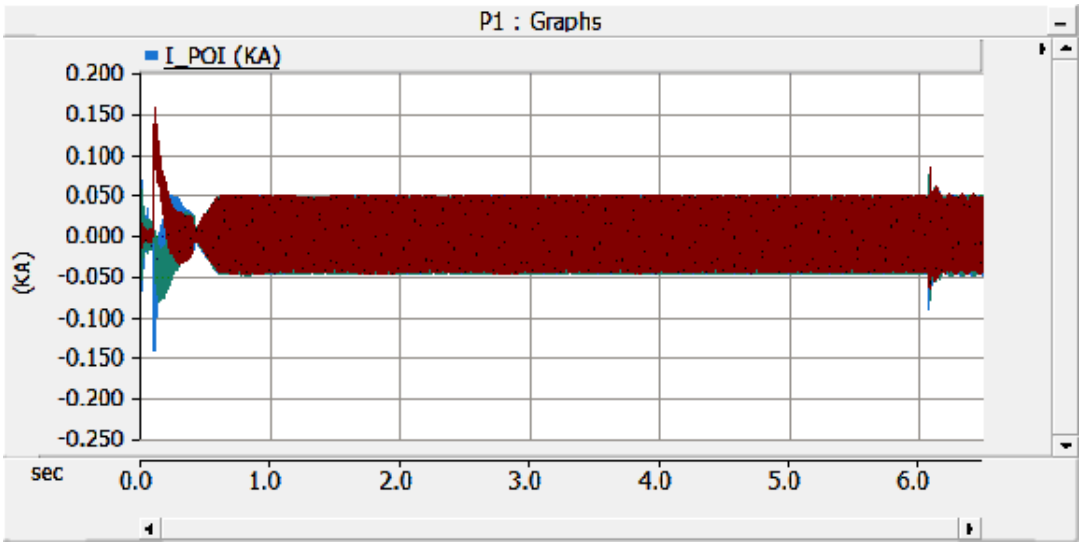

Figure B-142 EMT Simulation, SC24 POI instantaneous current

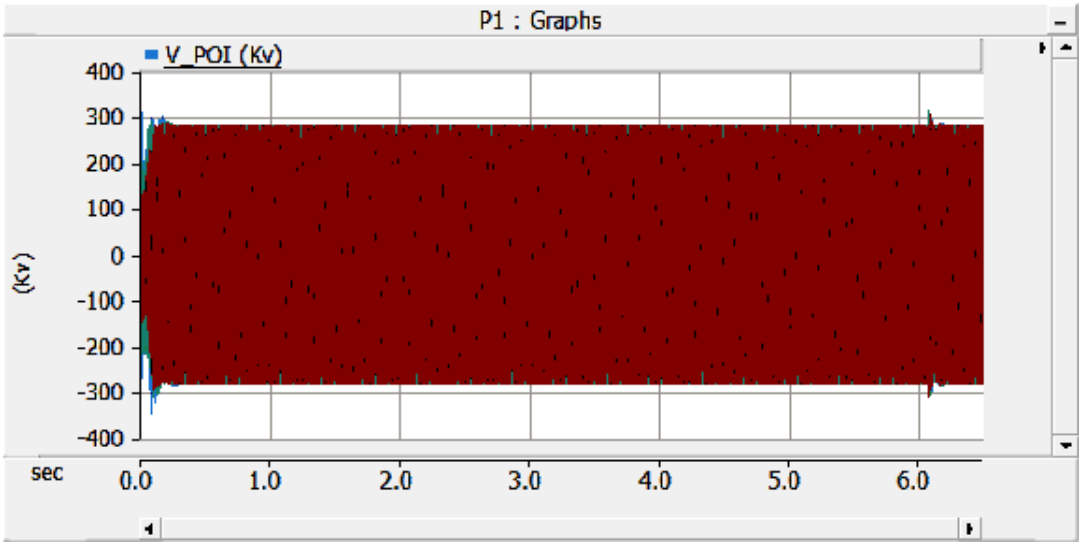

Figure B-143 EMT Simulation, SC24, POI instantaneous voltage

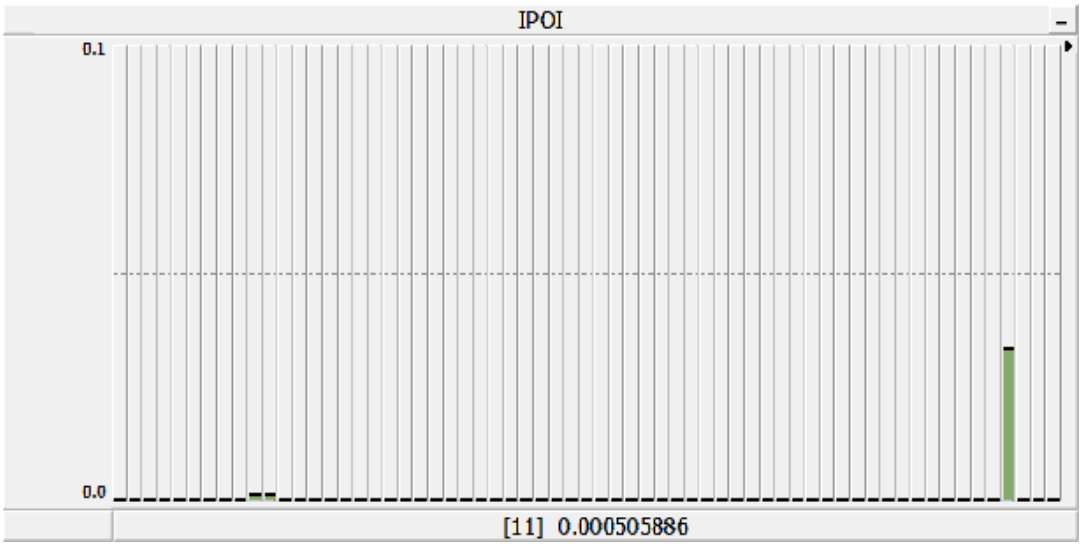

Figure B-144 EMT Simulation, SC24, POI current FFT